A Hybrid Deformation Model of Ventricular Myocardium

Zur Erlangung des akademischen Grades eines

DOKTOR-INGENIEURS

von der Fakultät für

Elektrotechnik und Informationstechnik

der Universität Fridericiana Karlsruhe

genehmigte

DISSERTATION

von

Dipl.-Ing. Matthias B. Mohr
aus Bad Dürkheim

Tag der mündlichen Prüfung: 16. Februar 2006
Hauptreferent: Prof. Dr. rer. nat. Olaf Dössel
Korreferent: Prof. Dr.-Ing. Karl Schweizerhof

Contents

1

Introduction

Computer models have become an essential tool in areas where simulations prior to real life experiments save time, resources and do not conflict with ethical objections in contrast to certain in-vivo experiments. Furthermore, simulations can be performed, which are beyond the capability of physical experiments.

In the medical environment, computer models support medical doctors in diagnostics, surgery planning and serve educational purposes. The simulation of soft and hard tissue is a key interest in modern medicine. In craniofacial surgery, a computer model of the skull is created by medical imaging techniques and a soft tissue model represents the patients skin, muscle and fat layer. Virtual bone surgery is performed and computer programs allow to estimate the deformation of facial expression of the patient. Hence, the surgeon can conduct a thorough operational planing and may present estimated results to the patient [1, 2].

In the field of cardiology until now only imaging techniques that result in 2D visualization (including temporal change) support medical doctors for surgery planning. This work contributes a step towards 4D modeling of the heart by proposing a mechanical model representing the behavior of myocardial tissue. It was applied to compute the deformation of ventricular models including intraventricular pressure.

Acquiring information about anatomy and physiology is one part in mechanically modeling the heart. The other part consists in modeling blood pressure, valve function, and blood flow.

The initiation of mechanical contraction of the heart is the result of a series of biological processes. The heart consists of cells, which inhibit specialized functions. These functions can be differentiated into three main categories: excitation initiation, excitation propagation, and contraction. The sinus node is a self exciting region of cells, where a rhythmic electrical stimulus is created. This stimulus is propagated to neighboring tissue at a certain rate. An excited contractile cell, contracts upon this stimulus. The cells forming the conduction system propagate the stimulus to far regions of the heart and allow a temporally and spatially differentiated excitation and thus contraction of the whole heart. Only the interaction of these processes and the anatomical setup result in a pumping

action. Any disturbance of this interaction or of the underlying physiological function leads to a reduced supply of blood to the body and hence reduced oxygen and nutrients.

The heart's pumping function is dependent on the vitality of the heart muscle, which is mostly composed of contractile cells, so-called myocytes. The orientation of these myocytes throughout the muscle results in a unique profile of contraction allowing the pumping process to be possible. Knowledge about arrangement and physiological properties of the myocyte lead to a better understanding of diseases and pathologies of the heart.

The heart consists of cavities, which enclose an incompressible fluid, blood. Due to the contraction, a pressure change inside the cavities arises. This pressure change also results from opened and closed valves, which regulate the flow of blood. Furthermore, the blood dynamics play a role in the mechanical modeling of the heart.

In this work myocardial structure as well as lamination and orientation of myocytes were considered as anatomical model. Electrophysiology and excitation propagation were applied to achieve a temporal and spatial excitation pattern, which represents experimental results. The contraction modeling reproduces myocardial properties and results in a deformation of the geometry. Blood pressure inside the cavity was modeled depending on contraction phases and parameters were used to describe the opening and closing of valves. Fluid dynamics was not applied in this work, however the pressure due to blood dynamics was considered during the ejection phase.

1.1 Objectives of the Thesis

The objectives of this thesis lay in the creation, implementation, and application of an elasto-mechanical model to describe biologically active contracting muscle tissue of the heart. An investigation of anatomy and physiology has been conducted to understand the basic biological processes leading to a heart beat. Models of electrophysiology, excitation propagation and force development were chosen to reproduce biologically behavior. These models were coupled and applied to geometrical models representing muscular tissue. The resulting temporal and spatial force distributions were input to the created elasto-mechanical model.

Various approaches can be found in the literature for mechanical modeling. Anisotropy, non-linearity, and isovolumic behavior are the main issues to be addressed, when modeling muscular tissue. Only a few models meet all of these requirements and are either computationally expensive or allow only to model muscles as macroscopic patches.

In this work a spring-mass system, based upon the proposals of Bourguignon et al. [3], was created discretizing a geometrical model in regular cubic elements. Various methods were used to adapt the model to anisotropy, non-linearity and isovolumic behavior with a major focus on computational efficiency. Furthermore, intraventricular pressure was implemented yielding realistic boundary conditions found in the heart.

Simulations with varying geometrical models are presented. Pathological tissue behavior with and without pressure load were examined. Deformation of a ventricular model created from measured data were compared with a 4D MRI sequence of a patient.

1.2 Organization of the Thesis

The thesis consists of four parts. In the first part the anatomy and physiology of the heart and corresponding modeling techniques are described. In chapter 2 the macroscopic anatomical structures of the heart are introduced and an explanation of structures e.g. cavities, valves, vessels and the conduction system is given. The anatomy of the heart wall as the main tension generating element of the cavity is presented down to the cellular level. A brief introduction with respect to imaging techniques used to acquire data for modeling anatomical structures including basic preprocessing steps prior to model generation is given. Furthermore, some analytical ventricle models are presented. In chapter 3 the macroscopic and microscopic functionality of structural components of the heart and their interaction resulting in a heart beat are explained. The cardiac cycle (contraction and relaxation of the heart) and the resulting intraventricular pressure are presented, whose modeling is subject of this work. A brief introduction on electrical activity, its initiation and propagation throughout the hearts tissue as initiation of contraction is presented. The sliding filament theory as mechanism of microscopic mechanical contraction is discussed. The process of modeling electrophysiology, excitation propagation and force development is explained. For each step, one model is described, which was applied in this thesis. Furthermore, models of intraventricular pressure are introduced representing boundary conditions for mechanical modeling.

In the second part a brief overview of mechanical modeling techniques is given. In chapter 4 different models using physical and non physical principles are presented. Mechanical models applied for tissue and muscle simulation are outlined.

In the third part the hybrid deformation model created and the methodology of simulation is presented. In chapter 5 the hybrid deformation model, which is based on a spring-mass system in conjunction with continuum mechanical methods is described. The applied springs, their setup, model creation and continuum mechanical enhancements are presented and explained. Furthermore, the applied numerical method for mechanical deformation is described and numerical problems are addressed. In chapter 6 the methodology used for deformation simulation of a ventricular model is explained. Details of model creation, implementation of contraction initiation forces, and boundary conditions e.g. intraventricular pressure are given.

In the fourth part the application of the hybrid deformation model for various setups is addressed, chronologically. In chapter 7 deformation simulations of varying geometrical models, starting from basic study models, via ventricular models, and biventricular models , and a comparison with a real patient model created from MRI data are presented. In chapter 8 a discussion and suggestions for future work in the field of mechanical modeling of the heart are provided.

2

Anatomy of the Heart

For modeling the contraction of the heart a profound knowledge about the anatomy is necessary. The location and connection to surrounding tissue and structural components lead to boundary conditions relevant for modeling realistic contraction. Furthermore, the muscles structural properties as e. g. fiber orientation must be examined.

The following sections give an introduction into the anatomy of the heart, describing relevant structures for electrophysiological, mechano-electrical and contraction modeling down to the cellular level. Analytical ventricular models are presented derived from anatomical models.

2.1 Introduction

The heart is one of the vital organs in the human body. It is responsible for providing blood and hence oxygen and nutrients to the body and itself. This hollow muscular organ acts as a rhythmic working pump causing the blood to circulate through arteries and veins. Its weight ranges from 230 g to 350 g and it is approximately the size of a persons fist. The heart lies underneath the sternum (breastbone) and is surrounded by the lungs. The orientation of its apex is tilted to the left (fig. 2.1).

The heart consists of two atria, two ventricles, vessels and valves. The vessels split into two categories, one feeding blood to the cavities of the heart, the so called veins and the other transporting blood away from the heart, the so called arteries. The atria collect blood coming from the body and the lung circuit and are separated by the atrial septum to prevent blood passing between them. The valves control the flow of blood from the atria to the ventricles and furthermore restrict the backward flow from arteries into the ventricles. The ventricles are separated by the ventricular septum and pump the blood into the lung and body circuit. The anatomical proportion of the cavities closely resemble their functionality.
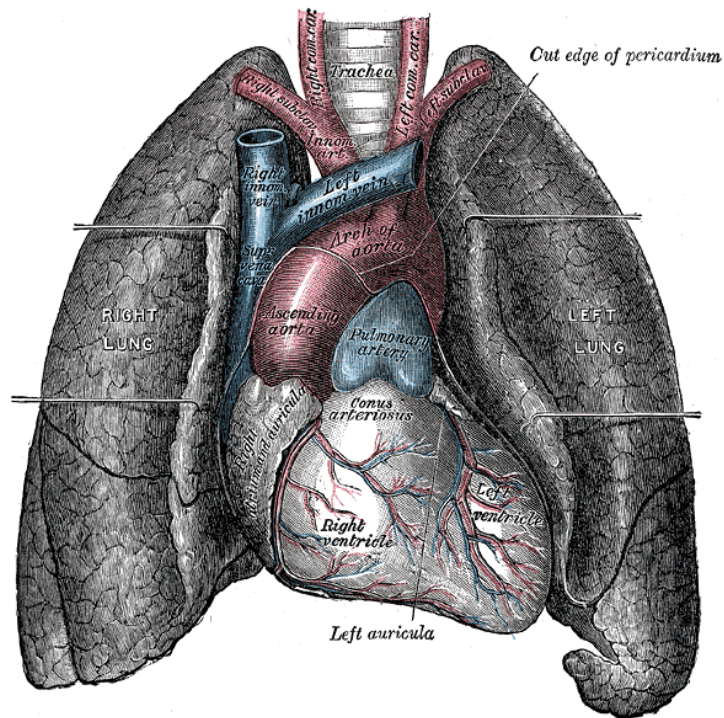
Figure 2.1. Historical drawing of anterior view of heart in thoracal position with lungs, cavities and vessels (fig. from [4]).

2.2 Macroscopic Structures

2.2.1 Cavity Structure

The heart lies inside a sac, the so called pericardium, which loosely connects to the epicardium (outer surface) of the atria and ventricles. The mid-wall tissue is called atrial or ventricular myocardium. The atria myocardium is a thin wall of up to 2 mm, whereas the ventricles have a thicker wall diameter. The left ventricle wall (diameter approx. 20 mm) is approximately three times the mass and twice the thickness of the right ventricle. Thus, the myocardium diameter resembles the force to be generated by the cavities. The endocardium (inside surface) of atria and ventricles consist of connective tissue.

The atrioventricular valves separate the atrial myocardium completely from the ventricles by the cardiac skeleton. The cardiac skeleton is a fibrous network formed by the rings of the four valves and connective tissue (fig. 2.2). It resembles an electrical insulation between atrial and ventricular myocardium. The only connective tissue penetrating the skeleton in a healthy heart is the atrioventricular bundle. The valve plane is also called the base of the ventricles.
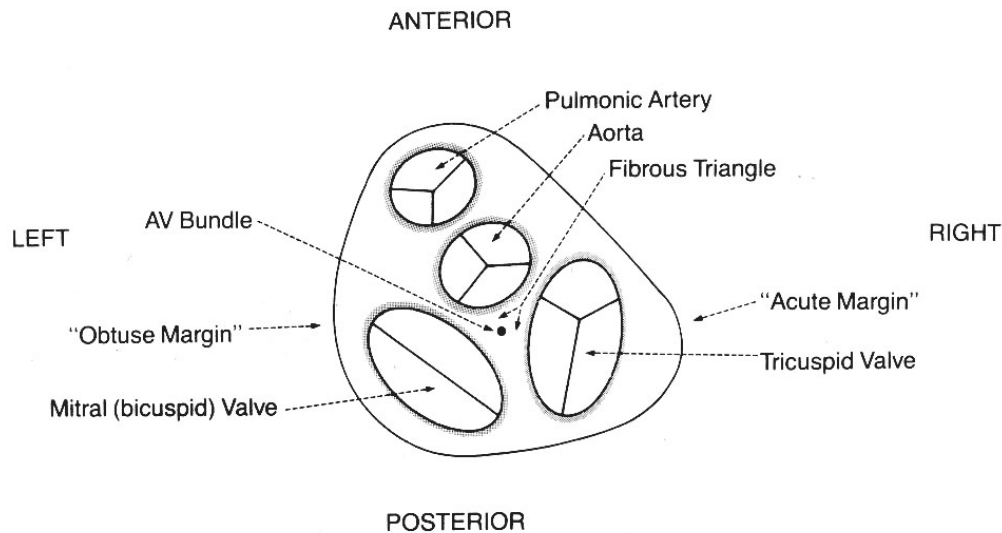
Figure 2.2. Schematic diagram of the fibrous skeleton of the heart, viewed from above with the atria removed (fig. from [5]).

2.2.2 Anatomical Trace of Blood-flow

The flow of blood through the anatomical landmarks of the heart is described below (fig. 2.3). Deoxygenated blood flows from the body circuit via the inferior and superior vena cava into the right atrium. The blood passes the tricuspid valve on its way to the right ventricle. The right ventricle pumps the blood via the pulmonary valve into the pulmonary artery, which commences the lung circuit. The blood is oxygenated in the lungs and returns via the pulmonary veins into the left atrium. The blood is then pumped into the left ventricle via the bicuspid valve. The left ventricle ejects the blood into the aorta and hence into the body circuit passing the aortic valve.

2.2.3 Conduction System

The conduction system consists of specialized tissues allowing for temporal and spatial differentiated activation of muscle cells and hence contraction of the myocardium. Involved specialized tissue structures are: The sinus atrial node, located between the vena cava superior and the right atrium; right atrial conduction pathway structures (e. g. crista terminalis, pectinate muscles and the Bachmann bundle); the atrioventricular (AV) node, which lays above the cardiac skeleton; the AV bundle or bundle of His, which penetrates the cardiac skeleton and splits into the Tawara bundle branches; the Purkinje fibers, which pursue the branches and reach further into the subendocardial myocardium. (fig. 2.4)
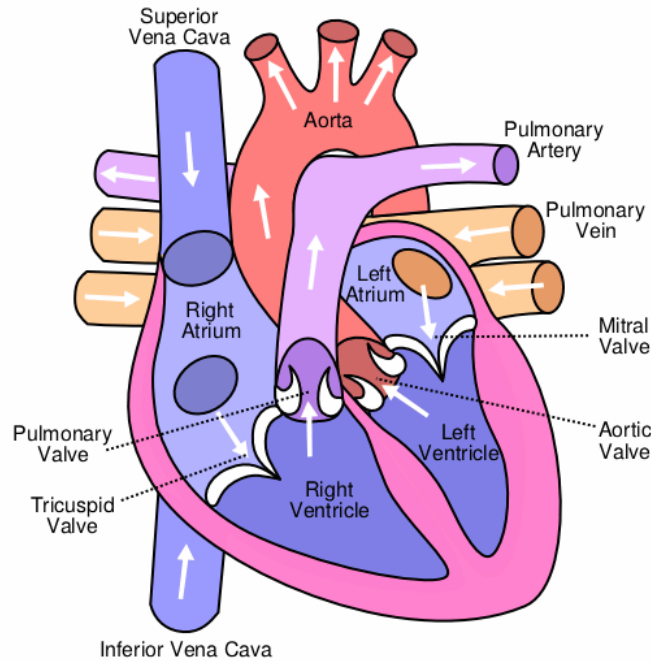
Figure 2.3. Schematic of cross-section of the heart with cavities, valves, and vessels. White arrows indicate normal blood flow (fig. from [6]).

2.3 Microscopic Structure

2.3.1 Anatomy of Myocardial Wall

The ventricular myocardium resides between endo- and epicardium and is the primary structural component of the wall. It consists of muscle bundles organized in overlapping sheets (fig. 2.5). The sheets are oriented into a spiral when followed from base to apex of the heart. The muscle fiber orientation in the ventricles is oriented and laminated [8, 9, 10, 11, 12]. In the human left ventricular myocardium the muscle fiber orientation varies from endo-$(55°)$ to epicardium$(-75°)$. The change of angle from endo- to epicardium is nearly linear, with $0°$ in the mid-myocardium. A similar structure can be found in canine myocardium (fig. 2.6). Apart from containing muscle fibers, the ventricular myocardium consists of fibroblasts, nerve cells, connective tissue, etc., which build up the muscular structure. The muscle bundles are composed of myocytes enclosed by a membrane.
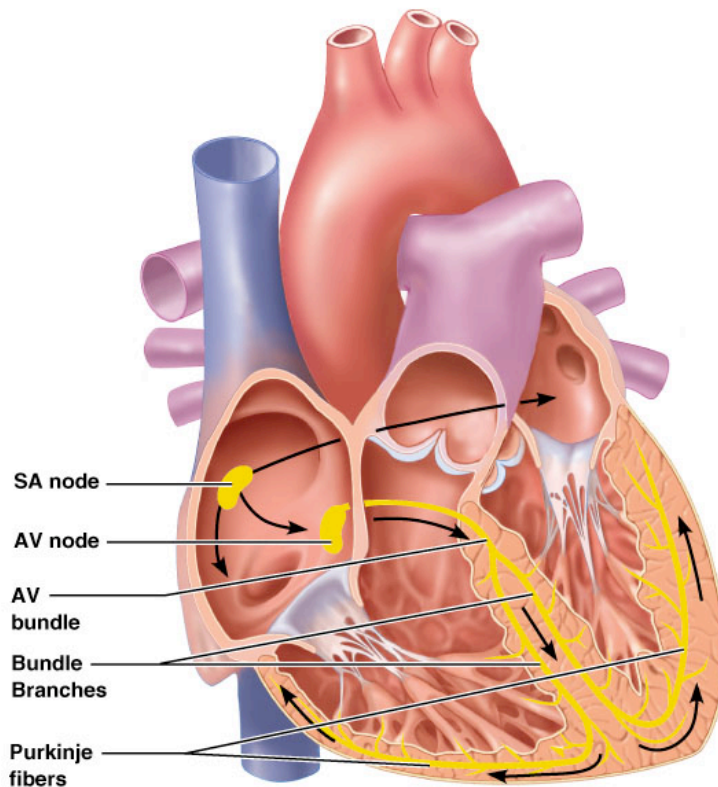
Figure 2.4. Outline of basic components of the conduction system. Black arrows show the way of excitation conduction (fig. from [7]).

2.3.2 Myocytes

2.3.2.1 Overview

Myocytes mainly fulfill either of two different functions depending on their structure and situation in the heart. Assigned to the working myocardium, they are responsible for development of tension and contraction. Assigned to the conduction system, they fulfill the task of fast excitation propagation. These cells vary in shape and cellular structure from those myocytes generating tension. The shape of a tension generating myocyte can be described as a cylinder. However, branching occurs (fig. 2.7). The size of a myocyte ranges from 50 to 120 μm with a diameter of approximately 5 to 25 μm.

2.3.2.2 Myocyte Ultra-structure

The myocyte is a specialized cell, whose structural layout will be described below. Details are given for the primary cell components.
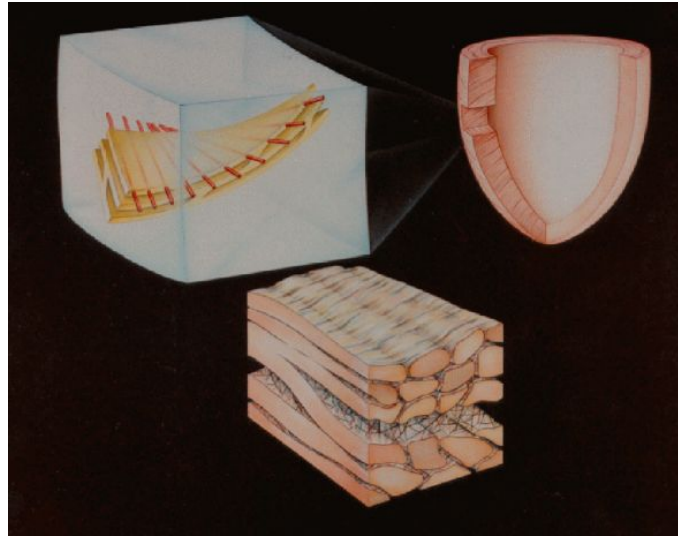
Figure 2.5. Schematic of ventricular wall with sheet and fiber orientation (fig. from [13]).
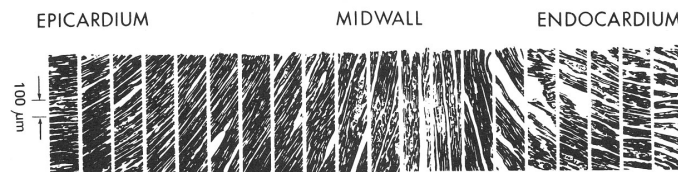
Figure 2.6. Reconstruction of fiber orientation of a canine left ventricular wall, prepared from a series of microphotographs, showing changing fiber angles at different depths (fig. from [5]).
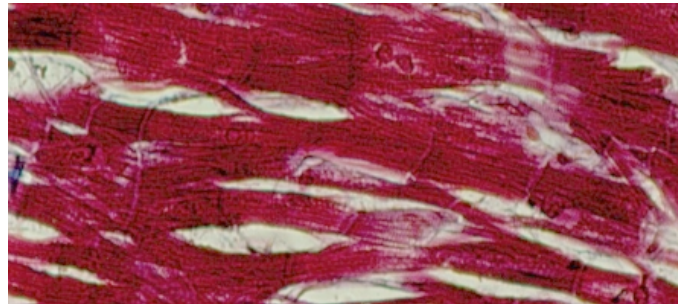
Figure 2.7. Microscopic picture of myocytes. The branching of myocytes is distinguishable (fig. from [13]).

The myofibrils examined with a light microscope reveal light and dark structures (fig. 2.8). These structures are differentiated into I-band, A-band, H-band, Z-disc, and M-line (fig. 2.9). The structures enclosed by two Z-discs are called sarcomere (fig. 2.10(a)). The myocyte is surrounded by the sarcolemma (cell membrane), which acts as a barrier between intra- and extracellular space.
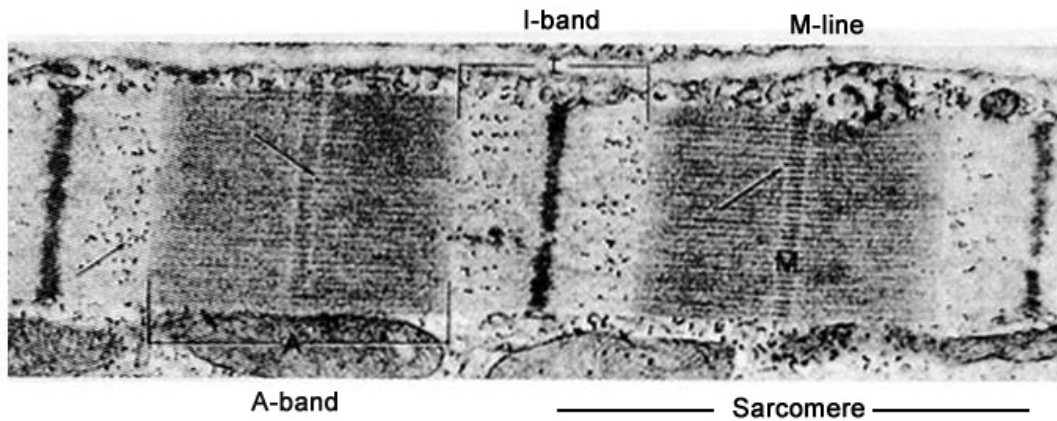
Figure 2.8. Longitudinal section of a myofibril of cat myocardium, showing the characteristic cross-striations (fig. from [5]).
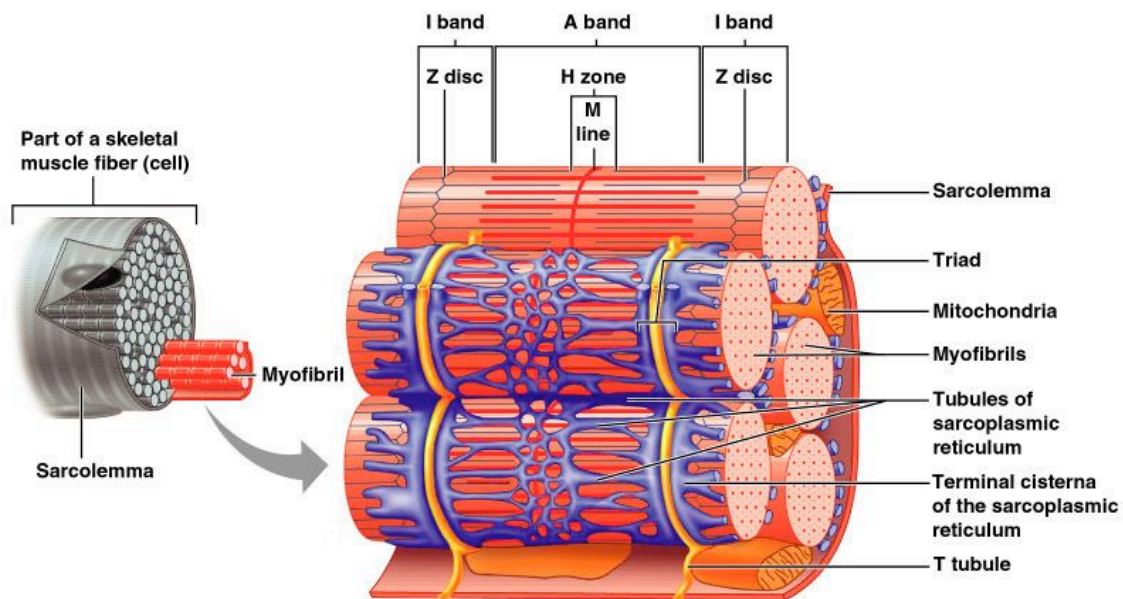
Figure 2.9. Schematic structure of a skeletal myocyte. Structure differs to myocardial myocyte by the triad, where only a diad is present. Cell organelles and band structure is illustrated (fig. from [7]).

The myofibril can be differentiated into the myofilaments, which is the term for the thin filament consisting of actin chains and for the thick filament consisting of myosin molecules (fig. 2.10(b)). These are the force generating structures.

(a)   (b)
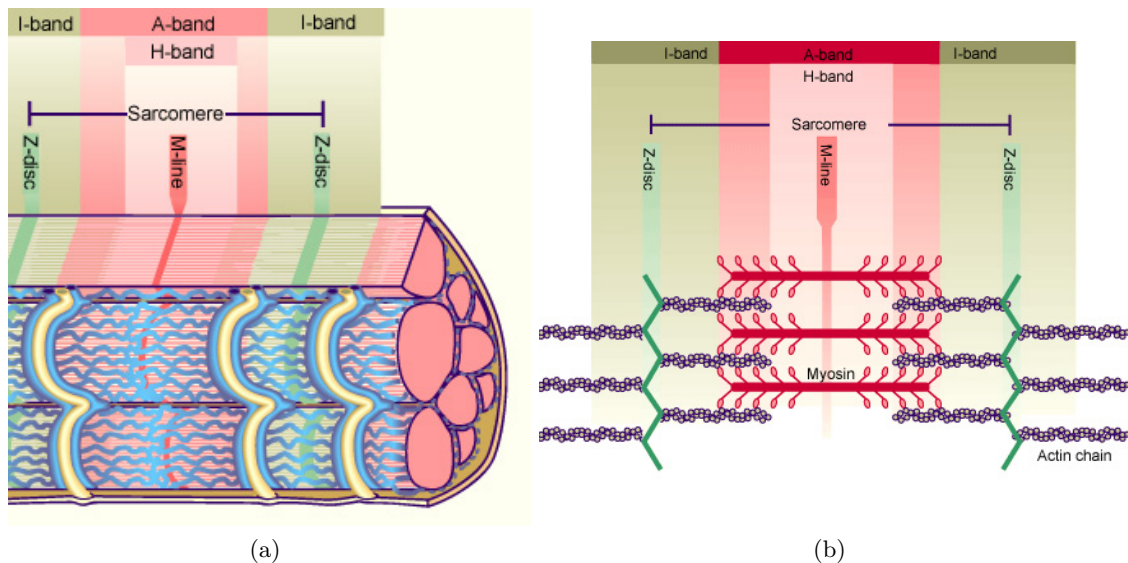
Figure 2.10. Schematic diagram of myofibril and myofibril ultra structure. (a) myofibril with band structure. (b) myofibril ultra structure with actin chains and myosin molecules (fig. adapted from [14]).

Sarcolemma

The myocytes consist of a semi permeable membrane the sarcolemma. It encloses the nucleus, the mitochondria, the myofibrils, the sarcoplasmic reticulum and the cytoskeleton. Furthermore, it is filled with sarcoplasm, which contains water, lipids, carbon-hydrates, salts and proteins. The sarcolemma consists of a phospholipid bilayer with embedded proteins on both, inside and outside surface, some of which tunnel the sarcolemma (fig. 2.11). Surface proteins are mainly responsible e. g. for signaling and cell bonding. The tunneling proteins serve as ion channels, exchangers and pumps. Specialized structures of the sarcolemma are the transversal tubuli, intercalated discs, and gap-junctions.

Transversal tubuli A specialization of the sacrolemma are the transversal tubuli or "T system" (fig. 2.9). They enter into the myocyte at the proximity of Z-discs and open freely to extracellular fluid. The "T system" wraps around the myofibrils and ends close to the sarcoplasmic reticulum, where they play a significant role for calcium handling.

Intercalated disc. The intercalated discs represent the part of the sarcolemma where a coupling of myocytes is achieved (fig. 2.12). These special regions enclose intercellular channels, so-called gap junctions, which are important for intercellular signaling. Desmosomes link the myocytes and stabilize their relative position and maintain a three dimensional structure of the tissue. The structure of the intercalated disc allows a direct electrical connection and a strong bond between two myocytes.
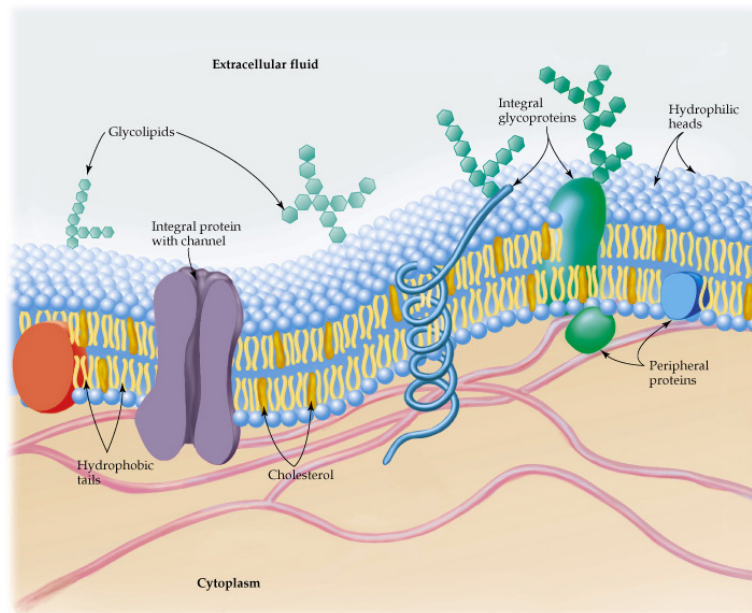
Figure 2.11. Schematic of a cross-section of a cell membrane consisting of a phospholipid layer. Cholesterol forms part of the membrane, proteins are embedded in the lipid bilayer, and the carbohydrate chains of glycoproteins and glycolipids extend into the extracellular space, where they act as receptors. Integral proteins form channels to the outside of the cell and also participate in transporting large molecules across the membrane (fig. from [15]).
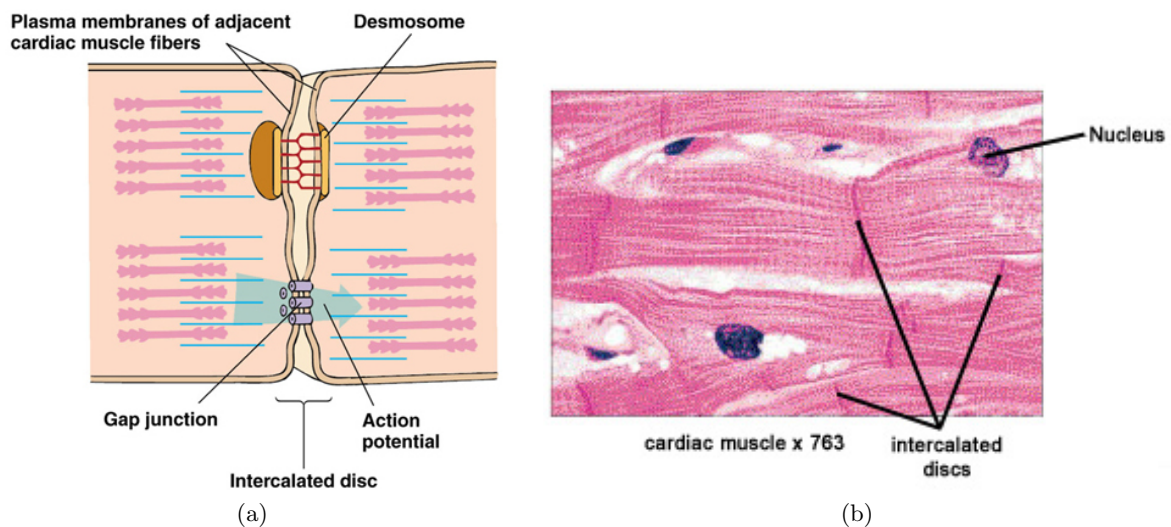
Figure 2.12. Schematic (a) and microscopy (b) of intercalated disc, with desmosomes and gap junction (fig. from [16] and [17]).

Gap Junctions The gap junctions are a means to connect intercellular space of myocytes. They are mainly located at the intercalated discs (fig. 2.12(a)). The gap junction has a cylindrical shape with a length of approx. $2 - 12$ nm and a diameter of $1.5 - 2.0$ nm. It allows the passage of nutrients, metabolites and ions etc. from one cell to another. This allows the electrical intercellular conductivity.

Mitochondria

The shape of a mitochondrion is formed like a rod, with a length of $0.3 - 1.7$ μm and a diameter of $0.2 - 1$ μm. Mitochondria are the generator of energy of a cell, converting nutrients and oxygen into adenosine triphosphate (ATP). ATP is the chemical energy form a cell can use to power its metabolic activities.

Myofibril

The myofibril is the contractile apparatus which consists of bundles of myofilaments. When viewed through a light microscope a characteristic repeating pattern of dark and light regions can be examined. The distinction of I, A, and H-band as well as Z-disc and M-line was based on the microscopic pattern (fig. 2.8). The sarcomere is defined as the region between two Z-discs. The Z discs are dense protein discs and are the anchoring area for actin filaments. The Z stands for the German word "zwischen" meaning "between".
The actin or thin filaments are build of actin, tropomyosin (Tm) and troponin (Tn) (fig. 2.13(a),(b)). The myosin or thick filament consists of mainly myosin II molecules, which can be differentiated into head, hinge and tail region (fig. 2.13(c),(d)) . The heads of myosin II molecule embeds an ATP and an actin binding site.
Myosin and actin are arranged in a parallel array. The examination with polarized light microscopy reveals optical properties of isotropy for actin (I-band) and anisotropy for myosin (A-band). The I- and A-bands overlap where actin and myosin filaments bind together. The unbound part of the A-band describes the H-band. The name of the H-bands resembles the German word "hell" meaning "light" as can be examined with light microscopy. During contraction the actin filament is pulled along the myosin toward the middle of the sarcomere. The I- and H-band is reduced as the filaments slide past each other. When the muscle is fully contracted the H-Band is no longer visible. Nevertheless neither actin nor myosin filaments are shortened in size. This is called the Sliding Filament theory (section 3.3.2).

Sarcoplasmic reticulum

The sarcoplasmic reticulum (SR) is a specialized form of the endoplasmic reticulum. It is completely separated from the myocytes intracellular space by its own membrane and acts as a calcium reservoir. The membrane encloses various ionic channels. Predominantly calcium release channels and calcium pumps are present. The SR can be differentiated into a network of intracellular tubules
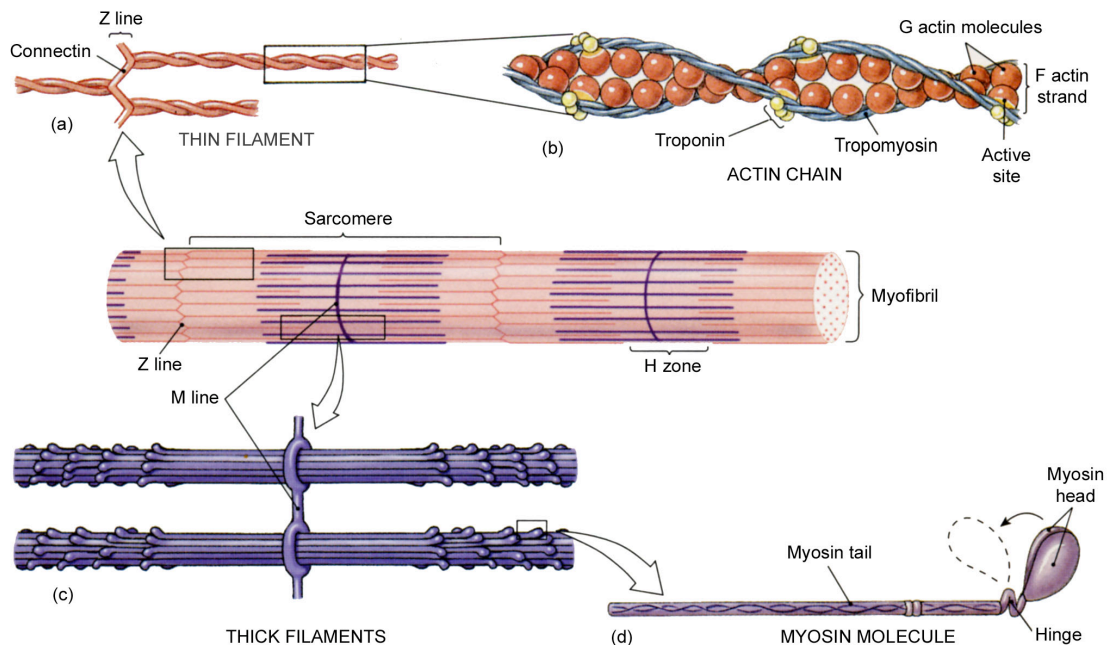
Figure 2.13. Schematic of actin and myosin filaments. The figure in the center shows a schematic of a myofibril with sarcomeres, H-zone, M zone and Z line. The subfigures show (a) the thin filament, which is connected by connectin. (b) a magnification of the thin filament with actin, troponin, tropomyosin and active binding site. Furthermore, (c) shows the thick filament and (d) a myosin molecule with myosin head, myosin tail, and the hinge (fig. from [17]).

(sarcotubular network) and into the terminal (subsarcolemmal) cisternae. The longitudinal tubes form a net between the Z-discs and reside in close proximity to the myofibrils. The terminal cisternae are located at the t-tubuli but do not fuse or establish intimate contact. The composite structure formed by terminal cisternae and the "T system" is called dyad for a myocardial cell and a triad for skeletal muscle. The narrow space remaining between the membranes is called the dyadic space. Ryanodine receptors enclosed in the terminal cisternae and the specialized Ca^{2+} channel (dihydropyridine receptor) of the "T system" bridge the dyadic space. This bridge constitutes the excitation-contraction coupling by releasing calcium into the myoplasm as result of an arriving action potential.

Cytoskeleton

Beside the contractile apparatus the myocyte consists of a structure called cytoskeleton. It is needed for structural integrity of the sarcomere and provides mechanical linkage to convey developed tension of the sarcomere to the surrounding structures and finally to the end of the muscle. The main proteins are nebulin and titin. Titin is a protein, which is associated with myosin. It is connected at the Z-discs and follows myosin towards the M-line. Titin controls the assembly of

muscle thick filaments, plays a role in muscle elasticity and generates passive tension on muscle strain.

Nebulin accompanies actin filaments and is also connected to the Z-disc. It is understood to form a molecular ruler to control the length of the thin filament, since the length of expressed nebulin corresponds to the length of the sarcomere.

2.4 Medical Image Acquisition

2.4.1 Overview

The macroscopic model of the anatomy of the heart is created from $3D/4D$ image data taken in a clinical environment. The images are filtered, segmented and classified into tissue classes describing different tissue types and properties. Thus, a suitable model for simulation is gained. Several medical imageing modalities exist, which can be used to capture in-vivo images of the heart. Imaging systems in medical environments are ultrasonography (US), magnetic resonance tomography (MRT), and computed tomography (CT). Furthermore, all imaging techniques can also be used for in vitro investigations. An example for an in vitro imaging technique is cryosection.

2.4.2 Imaging Techniques

Ultrasonography

The ultrasonography relies on the fact, that acoustic waves from a transmitter are reflected or scattered depending on acoustic impedance of traversed tissue. The time a wave travels from a transducer into the material and back is measured and utilized to compute the penetration depth. The strength of the echo depends on the difference between acoustic impedances of the structures. When the transducer is mechanically or electrically swiveled, the received data can be used to reconstruct 2D or even 3D images [18] (fig. 2.14(a)). The advantage of this method is its ability to produce 2D images in real time and its small size and hence mobility.
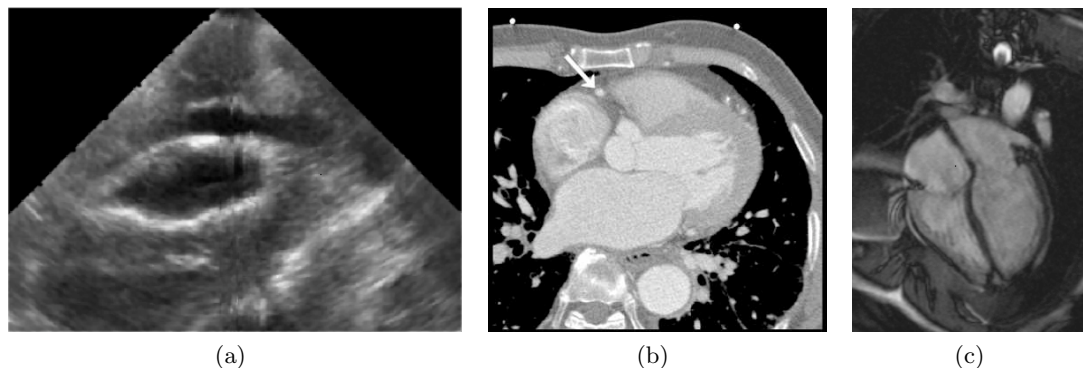

(a) (b) (c)

Figure 2.14. Images of the heart acquired by medical imaging techniques. (a) Ultrasonographic image of pig heart with EnSite catheter. Courtesy of Matthias Reumann, Karlsruhe. (b) Computed tomography of human heart with ECG-Based cardiac CT imaging (fig. from [19]). (c) Magnetic resonance tomography image of a human heart. Courtesy of Bernd Jung, Freiburg

Magnetic resonance tomography

The MRT is based on the relaxation properties of excited hydrogen nuclei of organic molecules. The object of interest is placed in a powerful uniform magnetic field B_0 with equilibrium magnetization M_0. Inside the tissue, the spins of the atomic nuclei align with an offset angle from the static field in parallel and anti-parallel direction. The percentage of parallel oriented nuclei outbalances those of anti-parallel direction [20]. In this configuration the spins are aligned in the longitudinal magnetization M_z equal to M_0. The tissue is then exposed to electromagnetic pulses (RF). As a result all hydrogen nuclei temporary leave their equilibrium state and a saturation of the spin system is possible resulting in $M_z = 0$. The spin lattice relaxation time (T1) describes the time constant how the spins magnetization M_z returns to the equilibrium value.

$$M_z = M_0(1 - e^{\frac{-t}{T1}}) \tag{2.1}$$

T1 is defined as the time required for the Z magnetization to change by the factor e. A time constant T2 can be defined for the spin-spin relaxation, which describes time needed to reduce the transverse magnetization due to dephasing by a factor of e. A localization of a voxel (3D-pixel) of the tissue is achieved by applying three orthogonal magnetic gradients.

In order to visualize tissue in a magnetic resonance image a contrast or difference in signal intensity must exist between adjacent tissue. The signal intensity depends on T1, T2, and ρ (spin density) which vary depending on tissue and pathology.

Further detail of MRT imaging technique is beyond the scope of this work and can be found in various publications e. g. [18, 20, 21].

Computed tomography

The computed tomography (CT) principles rely on an X-ray source that rotates around the object [18]. X-ray sensors are aligned at the opposite side of the circle. Progressively taken data scans of the object are needed to reconstruct a 2D image. The data acquired represents the radiographic intensity sensed by the detectors. Computers process this data to compute cross-sectional estimations of radiographic density (fig. 2.14(b)).

Cryosection

The cryosection is an imaging technique, where the object or sample is destroyed after taking the image. The sample is frozen in a block and a few micrometers are milled off. Then the slice is photographed and digitized (fig. 2.15). The milling and photographing is repeated until the sample is fully processed. This method was applied to acquire data for the Visible Human Project. It provides data of cross-sectional slices of the human body of a man and a woman corps [22]. This image data was processed at the Institute for Biomedical Engineering creating a 3D voxel data set of human corps [23].

Figure 2.15. Cryosection slice of Visible Human Male - thorax, including heart (with muscular left ventricle), lungs, spinal column, major vessels, musculature (from thorax subset) (fig. from [24])

2.5 Modeling of Anatomy

Images taken in clinical environments have to be pre-processed prior to creating a virtual anatomical model. The following sections describe briefly the pre-processional steps.

2.5.1 Image Processing

Depending on image quality further processing steps precede model creation [25]. A 3D anatomical model can be obtained by sequentially stacking 2D images acquired from any discussed source. The pre-processing of images starts with coordinate transformation, translation or scaling of images and filtering 2D images depending on the desired application and raw data. To enhance data, image filters can be applied e.g. to enhance borders, eliminate noise and artifacts. Furthermore, the stacking of pictures for a 3D model needs to be examined to eliminate misalignment of images. This is especially needed, when integrating e.g. CT and MTI images into a single model.

2.5.2 Segmentation

The next step in modeling is the segmentation of images. Starting out from a plane image, pixels belonging to a broader structure e.g. muscle tissue or blood, are grouped together into regions with common properties. A segmentation can also be done on 3D data sets represented e.g. by a stack of 2D images.

Manual as well as semi-automatic segmentation is widely used. An example for semi-automatic segmentation is the region growing algorithm [26] (fig. 2.16). For this method a seed point is set inside an image, which defined a starting gray value and a position inside the image. The automatic algorithm compares the surrounding pixels gray value and decides upon a threshold value (gray value) whether to incorporate the pixel to the region or not. The result of this very simple algorithm depends on the quality of the image data.
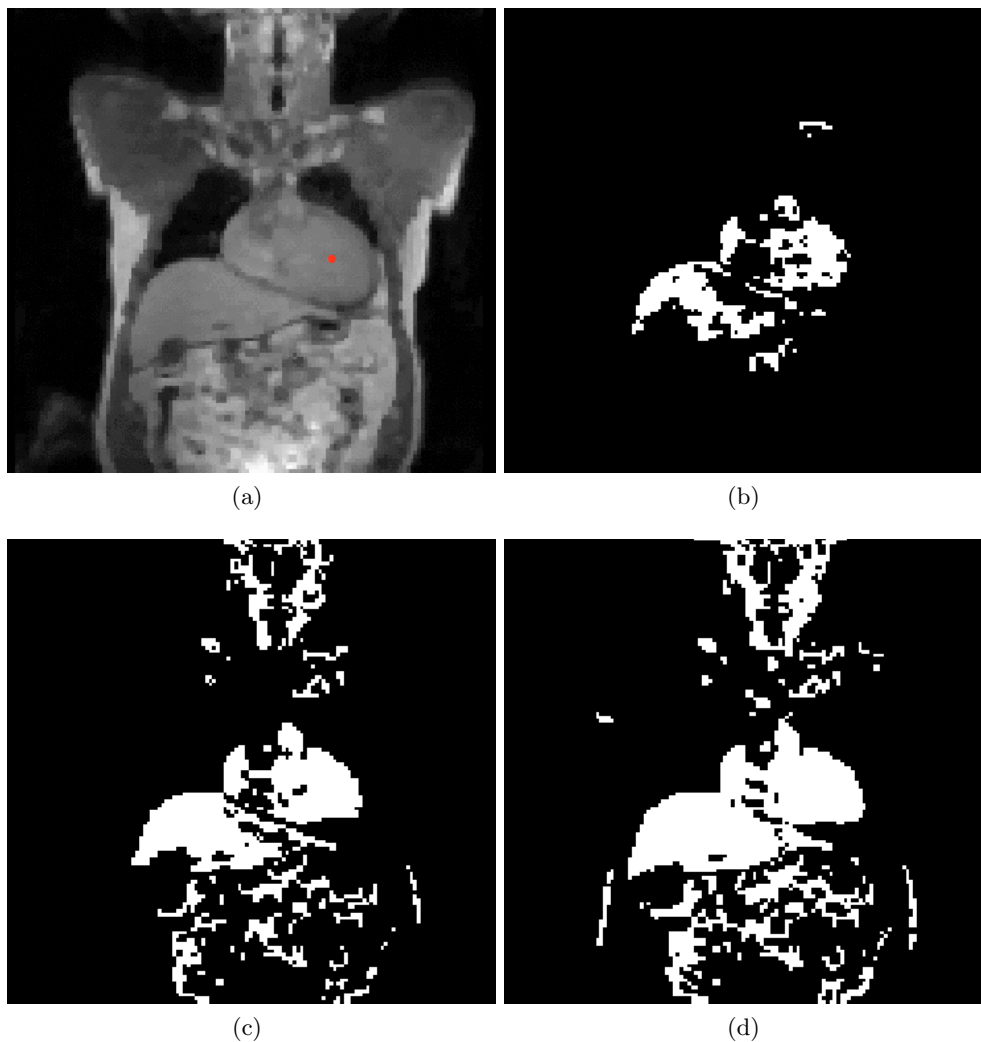
Figure 2.16. Illustration of semi-automatic 3D region growing segmentation on thorax image. Exemplary extraction of the human heart from a thoracal image by region growing. The red dot marks the seed point. (a) original image, (b) threshold value 5, (c) threshold value 10, (d) threshold value 15. It becomes obvious, that more sophisticated methods of semi-automatic segmentation or better pre-processing must be applied for extracting anatomical objects.

2.5.3 Classification

The segmented 3D data can be processed further by assigning specific properties to the regions which resulted from the segmentation process [26]. A classification can be done by e.g. color, texture or geometry (fig. 2.17). Physical properties can then be assigned to classified objects like elastic mmodules or electrical impedance.
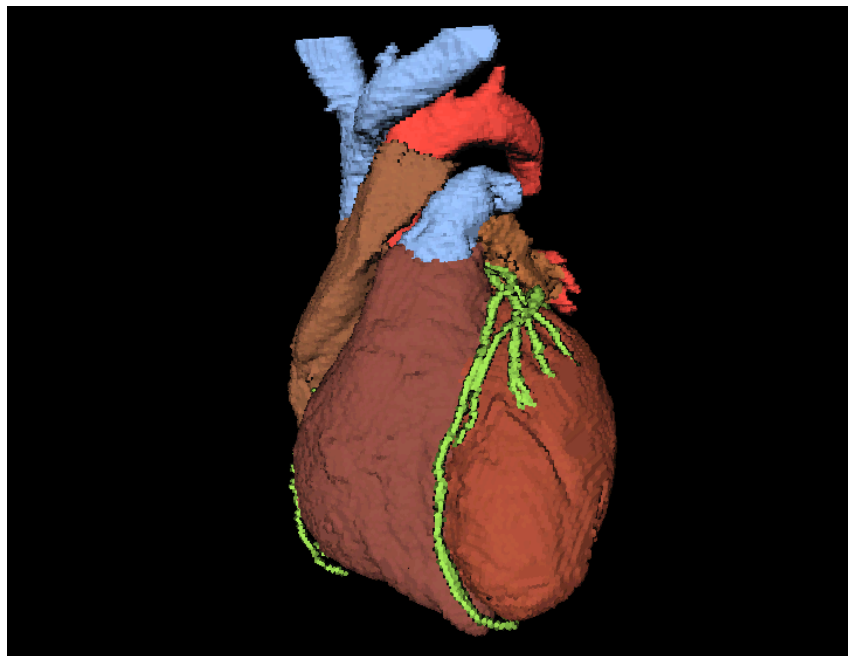
Figure 2.17. The heart with cavities, vessels and coronary arteries reconstructed from the Visible Man Dataset. The colors describe different classified tissues of the heart.

2.5.4 Fiber Orientation

The fiber orientation cannot yet be extracted directly from images acquired by medical imaging systems. However the diffusion tensor imaging (DTI) technique (a special MRT technique) provides means to examine fibrous structures such as e. g. brain, heart [27, 28, 29]. DTI is used to acquire the anisotropic diffusion properties of water in a tissue at a spatial position within the probe. The mapping of fiber orientation is based on the presumption that diffusion of water along the cells is larger than transversal to it. The fibers can be reconstructed by examining the sum of the linear and planar tensor anisotropies of the diffusion tensor and then trace the fibers along the principal eigenvector direction [30, 27]. Zhukov et al. [27] extracted the fiber orientation of an extra corporal canine heart, which rested in a contracted state (fig. 2.18).

Furthermore, manual assignment of fiber orientation of myocytes can be performed using e. g. pointwise definition of restrictions with manual and rule-based methods, interpolation of orientation and lamination by iterative averaging, assignment and validation by human experts [31].
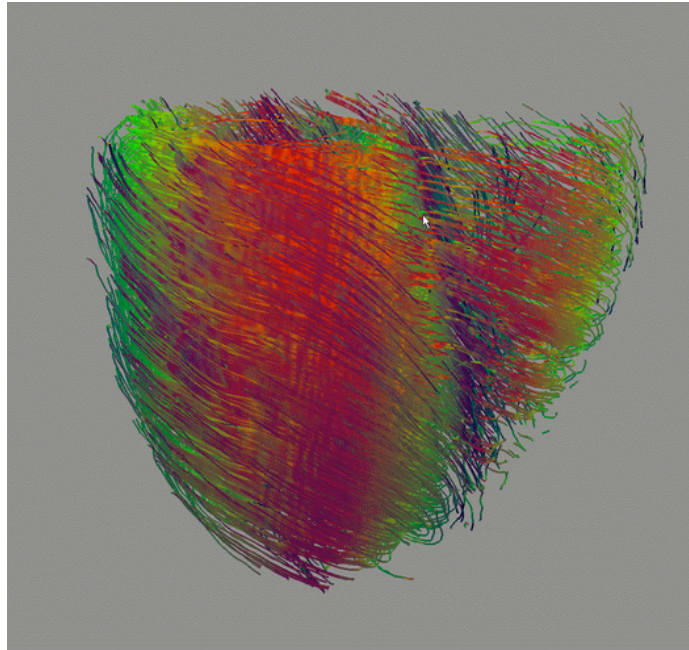
(a)
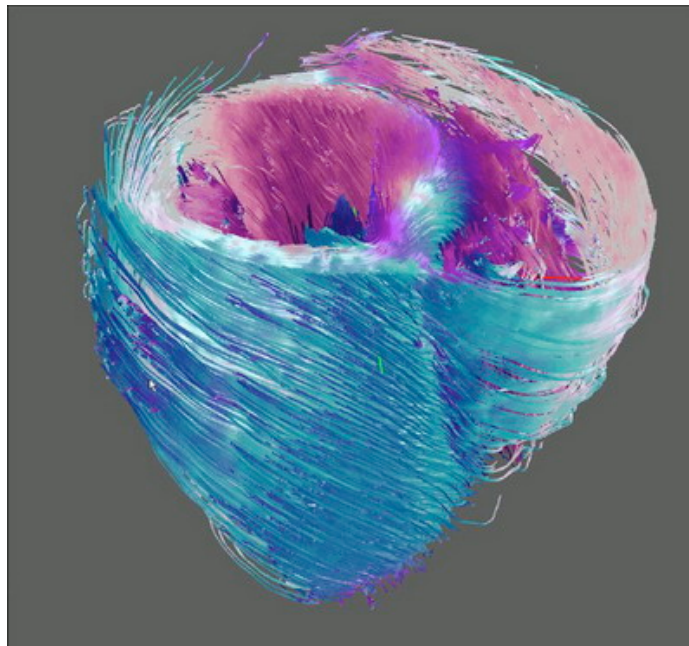
(b)

Figure 2.18. Reconstructed fiber orientation of a canine heart from MRI data (fig. from [27]).

2.6 Analytical Model

2.6.1 Model of the Left Ventricle

An analytical description of a left ventricle is achieved by cropping of two con-focal truncated ellipsoids (fig. 2.19). The length d of the ellipsoid's focus is defined as $d = \sqrt{a^2 - b^2}$ with the ellipsoid's minor radius b and major radius a [32]. The truncation factor f_b specifies the truncation of an ellipsoid. It is defined by $f_b = \frac{l_{be}}{l_{ea}}$ with the basal to equator plane distance l_{be} and from equator plane to apex l_{ea}. A truncation factor of 0.5 is commonly chosen. Sachse applied this analytical approach to create a model of the left ventricle in a voxel based data environment [31]. Furthermore, a corresponding data set was provided, where fiber orientation and lamination for each voxel are stored. The direction of fibers were adapted from anatomical studies [10, 12, 33, 34, 35, 36], however only pursuing a macroscopic averaged perspective (fig. 2.20).
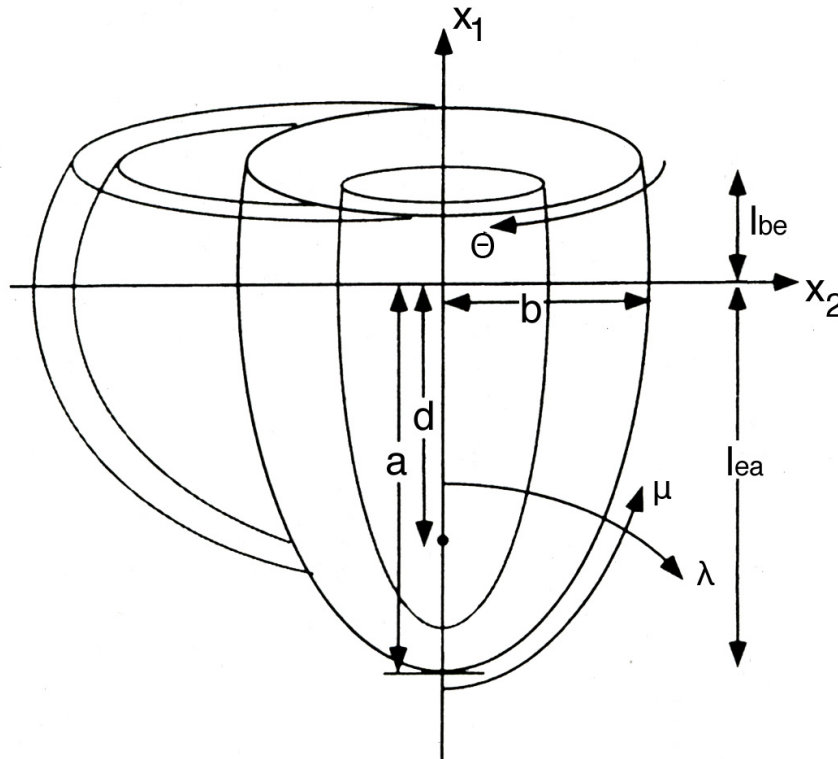
Figure 2.19. Schematic of truncated ellipsoid representation of ventricular geometry, showing major left ventricular radius a, minor radius b focal length d, and spherical coordinates (λ, μ, Θ) (fig. adapted from [32]).
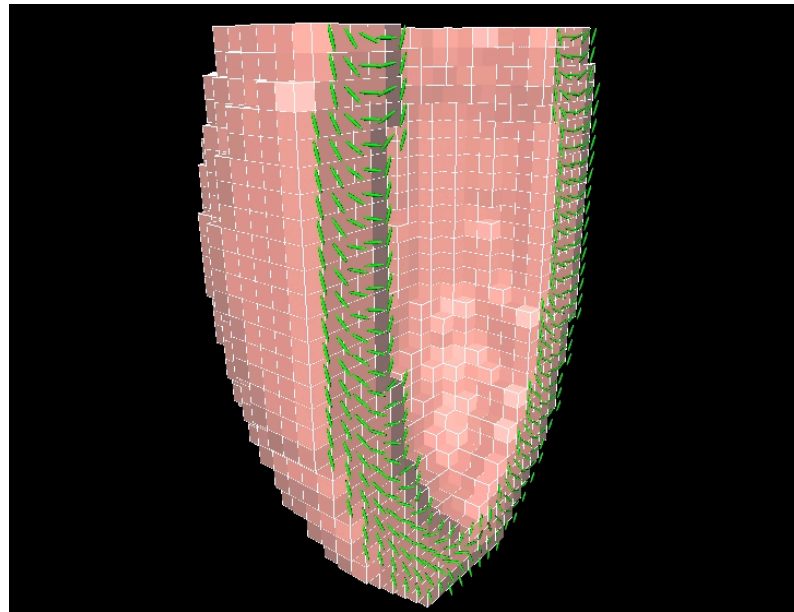
(a)
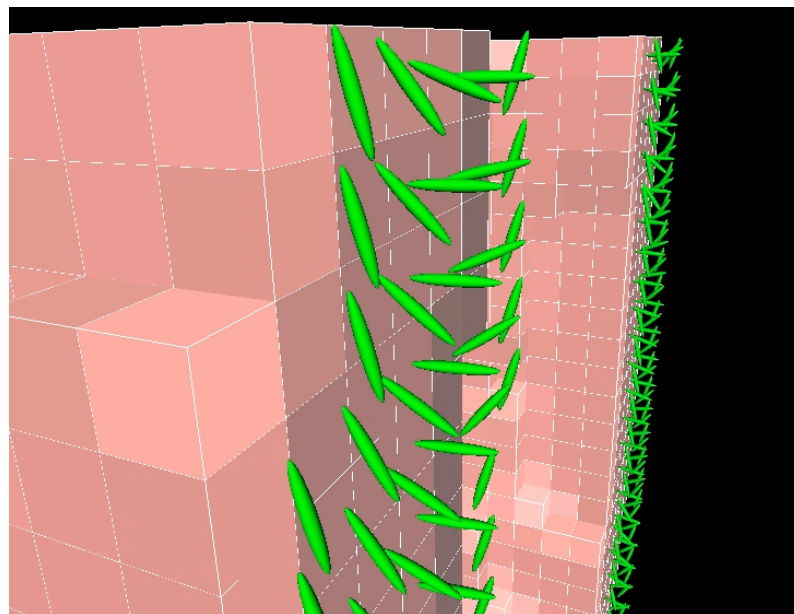
(b)

Figure 2.20. Analytical model of a ventricle represented by truncated half ellipsoids including rule based fiber orientation. (a) lateral cut of truncated half ellipsoid with fiber orientation. (b) close up of fiber orientation, displays fiber twist from epi- to endocardium.

2.6.2 Model of an Analytical Biventricle by Sachse

The biventricular model of Sachse was created by attaching a part of smaller half ellipsoids to the side of the single ventricular model to represent the right ventricle (fig. 2.21).
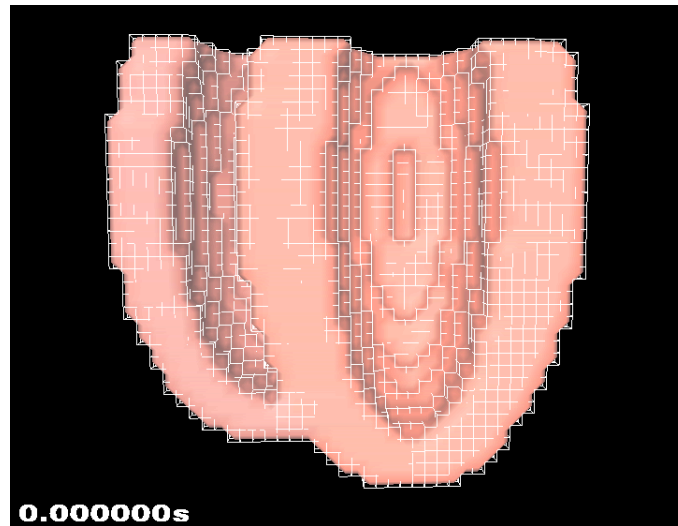
(a)
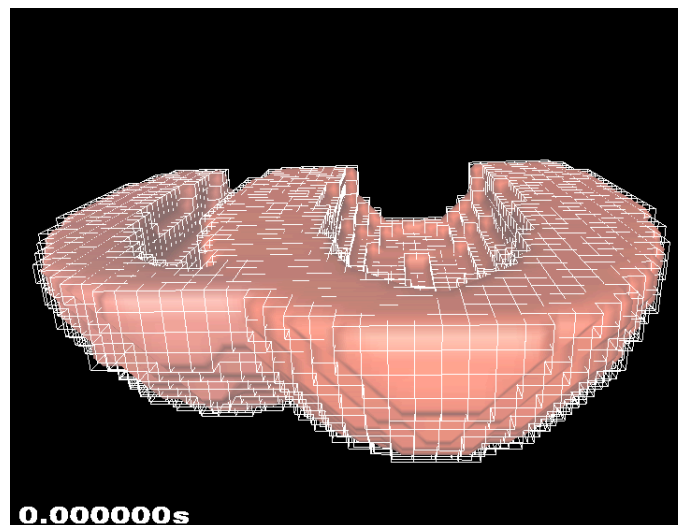
(b)

Figure 2.21. Analytical biventricular model of Sachse. (a) lateral cut of biventricular model. (b) view from apex to valve plane.

2.6.3 Biventricular Model of a Dog Heart by Nielsen

The ventricular anatomy model bases on a regular grid of rectangular Cartesian vector fields representing local myofiber orientations. The vectors were interpolated at a resolution of $0.25 \times 0.25 \times 0.25$ mm from finite elements using the *Continuity* software to detailed anatomic measurements from dogs left and right ventricle [37]. The data set was created from finite element models [38, 39] and is publicly available from [37]. 24 bicubic elements were applied to fit the model to the geometry of a dog heart.

(a)   (b)

(c)   (d)
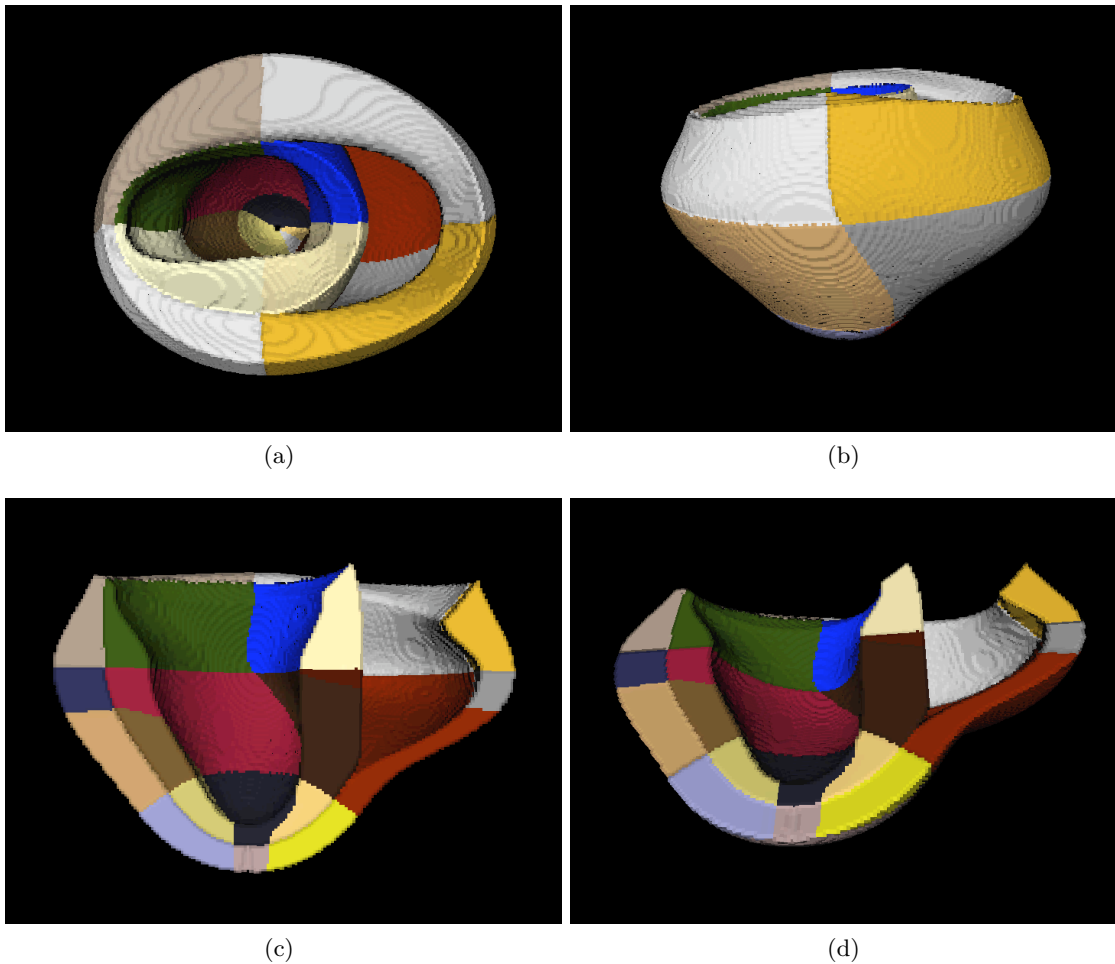
Figure 2.22. Biventricular model of a dog heart by Nielsen. The ventricular geometry consists of a cubic grid structure. In addition, fiber orientation is provided. 24 bicubic elements were applied to fit the model to the geometry of a dog heart.

3

Physiology of the Heart

The physiological functionality of the described anatomy of the heart is relevant for modeling the contraction of the heart. The initiation of contraction, starting out from an electrical stimulus, the propagation along specialized cell structures, and the contraction itself must be examined in the biological field prior to creating mathematical models. In addition the effect of contraction of the heart on the blood pressure is physiologically relevant and has to be incorporated in the modeling process.

The following sections provide an introduction into the physiological relevance of the basic anatomical structures, to explain the electrical stimulation and propagation on the heart, and to show the contraction cycle of the heart. A microscopic view is given onto the cellular electrophysiology, from stimulus to contraction. Furthermore, the functional modeling of the heart is described by mathematical models of electrophysiology, excitation propagation, force development, and blood pressure characteristics.

3.1 Introduction

The heart is the organ which pumps blood through the body. It functions as a rhythmic working pump, whose frequency alters, depending on innervation by the nervous system, on hormones, and the automacy of the sinoatrial node. It supplies oxygen and nutrients to the body via the blood.

The pumping function of the heart relies on the rhythmic alternation of atony (diastole) and contraction (systole) of the ventricles. During the diastole the ventricles fill with blood, whereas during systole the blood is ejected into the aorta and pulmonary artery. The back flow of blood is rejected by the pulmonary and aortic valves. Two atria collect the blood from the veins before passing into the ventricles. The systole of the atria occur prior to the ventricle systoles and support the filling of the ventricles.

The varying activity of the body and hence the demand of the circulatory system forces the heart to be extremely flexible. The cardiac output of an human adult ranges from 6.5 l/min during rest up to 20 l/min and more during strong muscular activity. The optimal adaptation can only

be reached, when all functional parts of the heart interact properly e. g. excitation propagation, contractility of the myocardium, valve activity and blood circulation.

3.1.1 Structural and Functional Differentiation

The heart and connecting organs can be differentiated in two ways. One is the differentiation in body and lung circuit, where the body circuit can be furthermore subdivided into upper and lower body circuit (fig. 3.1) and the other in high and low pressure system.

Body circuit

The body circuit starts at the left ventricle, which pumps oxygenated blood into the aorta. Its function is to transport oxygen and nutrients to the body organs and tissues and return deoxygenated blood back to the heart. From the aorta, the blood follows the artery pathways: from arteries to arterioles to capillaries, where the main exchange of nutrients and oxygen with surrounding tissue takes place. The blood follows the capillaries into the venules, veins into vena cava superior coming from the lower part of the body and vena cava inferior coming from the upper part of the body and finally flow into the right atrium.

Lung circuit

The lung circuit commences at the right ventricle, which pumps the blood into the pulmonal arteries towards the lung. The lung is responsible for oxygenating blood and exhalation of carbon dioxide. The oxygenated blood then follows the pulmonal vein to the left atrium, where it is collected and passed through the mitral valve into the left ventricle and hence, the body circuit.
Furthermore, a differentiation into high and low pressure system can be performed.

Low pressure system

The low pressure system includes all body veins, the right atrium, the right ventricle, the lung vessels, the left atrium and during diastole also the left ventricle. This is due to the fact that in these parts of the system the mid blood pressure does not exceed 20 $mmHg$ [41].

High pressure system

The high pressure system incorporates the left ventricle during systole as well as all arterial vessels up to the arterioles. Its mid blood pressure ranges between 60 and 100 $mmHg$.
The anatomical structure of left and right ventricle resembles the force generating needs accounted by the pressure difference (section 2.2.1).
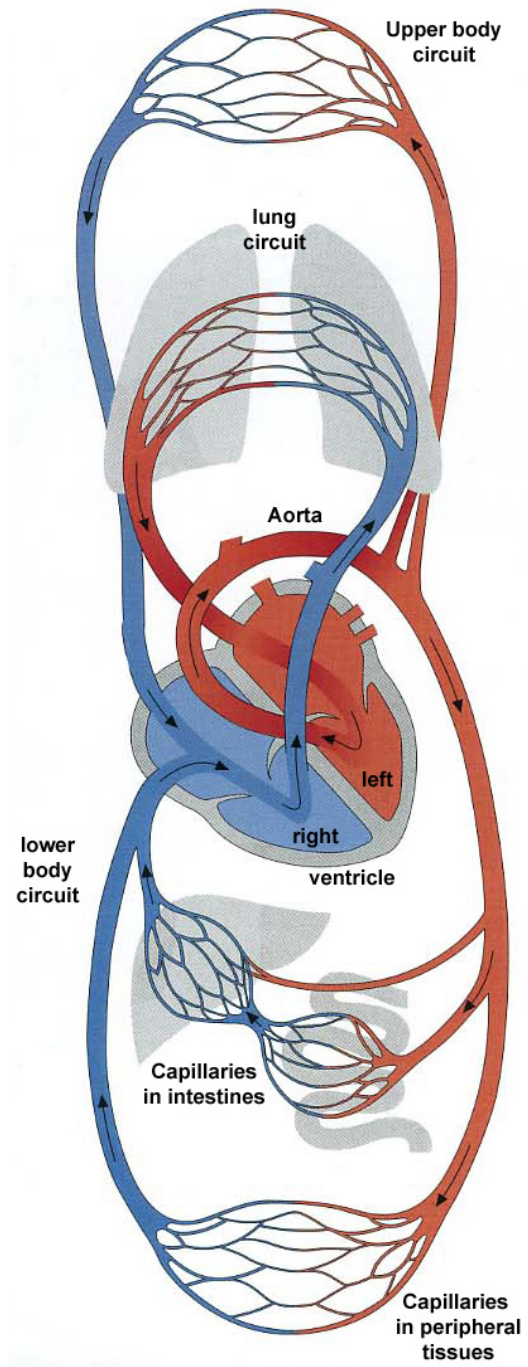
Figure 3.1. Schematic of the heart showing the flow of blood into body and lung circuit (fig. adapted from [40]).
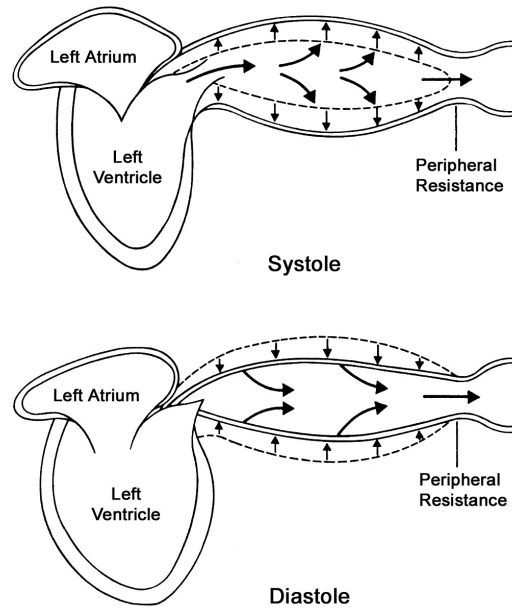
Figure 3.2. Schematic of aortal expansion due to ejection volume (fig. from [42]). During ventricular systole, the stroke volume ejected by the ventricle results in some forward capillary flow, but most of the ejected volume is stored in the elastic arteries. During ventricular diastole, the elastic recoil of the arterial walls maintains capillary flow throughout the remainder of the cardiac cycle.
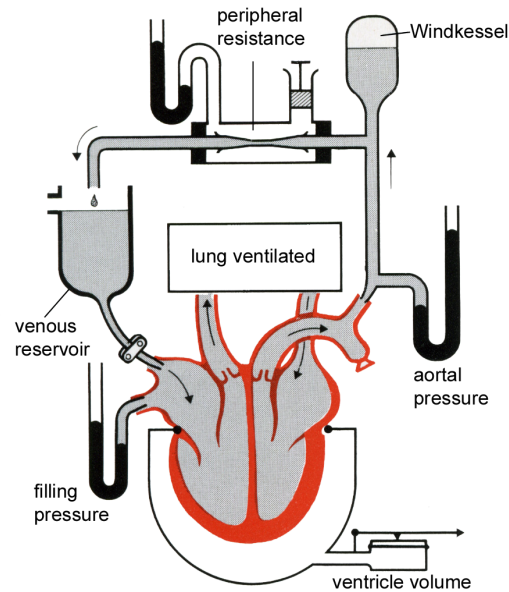
Figure 3.3. Heart lung preparation of Starling (fig. adapted from [43]).

3.2 Macroscopic View of Heart Functions

3.2.1 Valves and Vessels

The valves serve as a regulator for unidirectional blood flow in the cardiac system. The atrioventricular valves (mitral and tricuspid valve) prohibit the backflow of blood from the ventricles into the atria during systole. During diastole the pulmonary and aortic valve prevent the backflow of blood in the ventricles.

The vessels carry the blood to the peripheral tissues. Vessels are distinguished between arteries transporting blood from the heart to tissues and organs and veins transporting blood back to the heart. High flow rates, irregular surfaces, and sudden changes in vessel diameter disturb the smooth flow of blood, creating turbulences. The vessels show a distinct three layer structure, which include e.g. elastic fibers, smooth muscle, and collagen fibers [17]. Therefore, the vessels show an elastic and contractile behavior. The artery vessels feature a thicker muscular layer compared to the veins. The aorta as the connection between the heart and the vessel system possesses a special functionality:

The rhythmic ejection of blood into the aorta is transformed into a pulsating flow. The ejection volume enlarges the aortal vessel and stores temporarily a part of the ejected volume. The valves prevent the blood from flowing back into the ventricle. At the same time the aortal vessels slightly contract towards their regular size and push the blood further into the arterial system (fig. 3.2). This blood storage in the aorta, the delayed contraction and release as well as the resistance of the peripheral system result in a regular blood flow. This functionality is named Windkessel in conjunction with the technical term for a Windkessel, which buffers the pressure stroke of a pump. Following a heart-lung preparation of Starling [44, 45], the ventricular volume and the aortal pressure can be measured. The body circuit is replaced by a mechanical system. The main part is accomplished by the Windkessel, which simulates the elasticity of vessels. The windkessel absorbs the ejected volume. A modal resistance element replaces the total peripheral resistance. This results in a slow blood current. In the Starling preparation the lung circuit remains intact (fig. 3.3).

3.2.2 Excitation

The contraction of a myocyte is initiated by an external electrical stimulus. This excitation stimulus is generated by specialized myocytes. The myocardium consists of different types of myocytes. The main part of myocytes can be designated to the working myocardium, whose main functionality lies in contraction and tension development. However, all myocytes are capable of propagating electrical stimuli (section 2.3.2.2). Specialized myocytes are responsible for the generation of electrical stimuli as well as fast electrical excitation propagation. These specialized myocytes are assigned to the conduction system (section 2.2.3). The conduction system is responsible for initializing and conduction of an electrical stimulus throughout the heart. This results in a temporal and spatial

differentiated activation of myocyte contraction leading to the characteristic contraction of the heart.

3.2.2.1 Excitation Initialization and Conduction

The components of the conduction system are explained in more detail: The initial electrical stimulus in a normal heart is generated inside the sinoatrial node (SAN), the so called primary pacemaker cells. The cells have the ability to automatically depolarize and generate an action potential, which then propagates along the crista terminalis, pectinate muscles and to surrounding right atrial myocytes. Moreover, the Bachmann bundle transmits the activation to the left atria. The electrical stimulus reaches the atrioventricular node, whose slow conductive tissue delays the excitation to the ventricles to account for temporal synchronization of contraction. In a healthy heart, this tissue structure is the only electrical connection between atria and ventricles, due to the insulation of the cardiac skeleton. The pursuing structures are the atrioventricular bundle or bundle of His followed by the Tawara bundle, which splits into three branches. Two of the tree branches conduct the excitation to the left, the third to the right ventricle. They split into a subendocardial network of Purkinje fibers, which connects to myocytes and activates muscle contraction. The ventricles are excited from endo- to epicardium and apex to base.

Furthermore, the atrioventricular node acts as the secondary pacemaker. It also has the ability to self depolarize, but with a lower frequency than the sinoatrial node. In the normal conduction rhythm the excitation from the sinus node overrides the secondary pacemaker. However, this back up system is vitally important should the propagation of the SAN not exceed the atria. The pumping function of the heart would still be triggered.
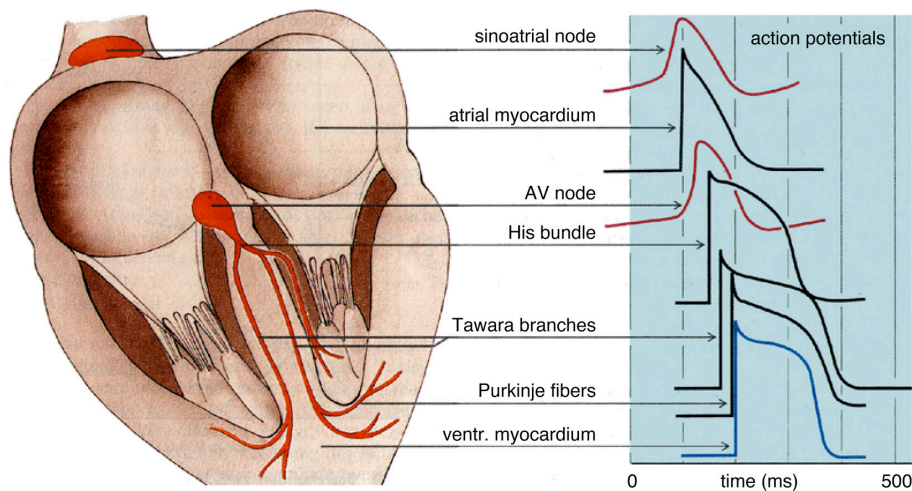
Figure 3.4. The heart with specialized excitation propagation tissues and the corresponding action potential curves in their temporal progression are displayed (fig. adapted from [46]).

The action potential curve for each tissue type following the conduction system to the myocardium varies in length and shape (fig. 3.4). This is due to the cell structure, i.e. amount of channels, pumps, exchangers. The variation of conduction velocities results in a temporal and spatial excitation pattern and hence, the most effective spatial and temporal contraction of myocytes for an optimal pumping functionality.

3.2.3 Contraction

The excited myocytes contract upon excitation. Due to the spatial and temporal activation, the properties of blood, valve functionality, and pressure gradient the typical pumping functionality of the myocardium is achieved.

For a cardiac cycle the walls pass through a series of changes in tension and length. The mechanical state changes and can be best described by a skeletal muscle and a load. Four phases can be differentiated (fig. 3.5):

At rest the muscle is attached to a load, which is supported by a surface. During phase one the muscle builds up tension but not enough to lift the load of the surface, hence the muscle does not shorten, substantially. This is called the isometric contraction (A). The second phase, the so called isotonic contraction, starts, when the developed tension is big enough to lift the load from the surface. A substantial shortening of the muscle takes place (B).

During isotonic relaxation, the third phase, the length of the muscle increases, still bearing the load (C).

After the load is returned to the surface the muscle dissipates the tension without considerable further lengthening. This is called isometric relaxation (D).

These phases can be adopted to the heart walls muscle tissue, where the load resembles the blood volume and intraventricular pressure.
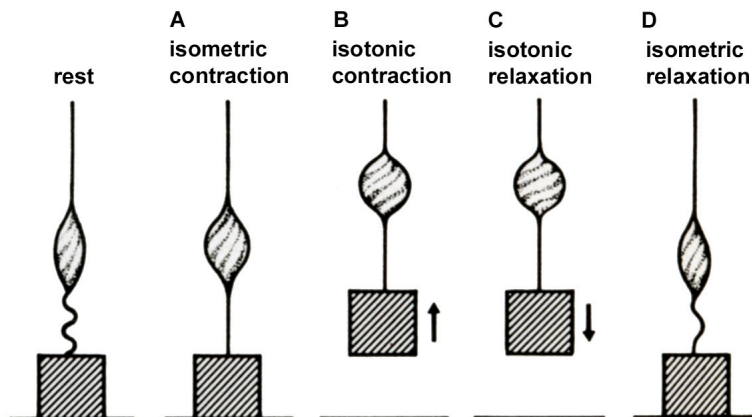
Figure 3.5. Phases of skeletal muscle contraction (fig. from [5]).
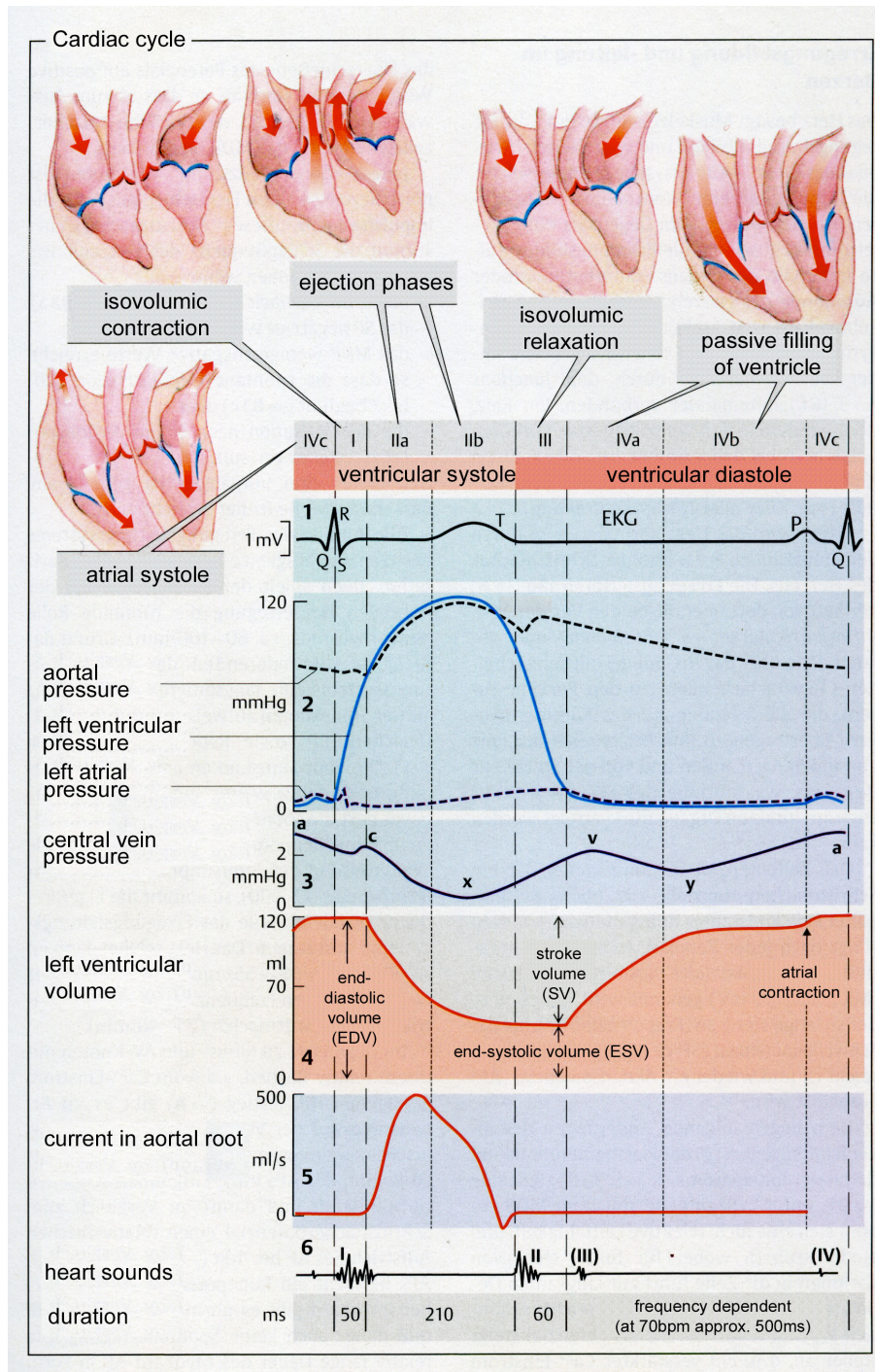
Figure 3.6. Schematic of cardiac cycle (fig. adapted from [47]).

3.2.4 Cardiac Cycle

The opening and closing of valves is dominated by the pressure change in the adjacent cavities and vessels. Therefore, the systole and diastole may be further subdivided into contraction and relaxation phases. These phases can be differentiated according to pressure and volume change. The phases are:

- during systole: isovolumic and isotonic contraction
- during diastole: isometric and isovolumic relaxation.

These phases are marked by the opening and closing of valves (fig. 3.6) and are furthermore explained for the left ventricle.

Isovolumic contraction

Starting with the development of tension in the systole the rising of intraventricular pressure leads to a closure of the mitral valve. At this time the aortic valve is still closed (Fig. 3.6, I). The ventricle performs an isometric contraction surrounding the incompressible fluid blood and adapts towards a spherical shape. The spherical geometry is adapted since a sphere has a smaller surface surrounding a constant volume. Furthermore, the valve plane of the heart consisting of cytoskeleton and valves is pulled towards the apex.
This isovolumic contraction results in a steep pressure increase without volume change. During a regular heart cycle this phase takes approx. 60 ms.

Isotonic contraction

The aortic valve opens as soon as the intraventricular pressure rises above the aortal diastolic pressure and blood is ejected into the arteries (Fig. 3.6, IIa). The intraventricular pressure rises until it reaches a peak and decreases with the end of the systolic phase (Fig. 3.6, IIb). From the blood volume of approx. 140 ml for a normal heart beat only 90 ml are ejected, which is the so called stroke volume. A blood volume of 50 ml remains in the ventricle as end-systolic volume. The fraction of stroke volume to filling volume (end-diastolic) is called ejection fraction, here 0.64.
The closure of the aortic valve marks the end of the systole. However, compared to the pressure curve it is slightly delayed. This is due to the kinetic energy of the blood flowing against the pressure gradient inside the aortic system for a short period of time.

Isometric relaxation

The isometric relaxation commences after the end of the ejection, where the aortic valve closes (Fig. 3.6, III). The cavity relaxes to its regular shape and the pressure drops. As soon as the intraventricular pressure drops below the atrial pressure, the mitral valve opens and the filling phase starts.

Isotonic relaxation

During the passive filling phase a quick (Fig. 3.6, IVa) and a slow filling phase (Fig. 3.6, IVb) can be differentiated. The blood from the atria generates the preload for the next contraction. During a normal heart cycle, the filling of the ventricle is mostly complete, when the atria systole commences (Fig. 3.6, IVc). The additional volume increase is only about 10%. During higher heart frequencies however, the atrial fraction of the filling volume increases since the diastolic phase decreases more than the systolic phase.

The outline of a pressure volume curve can also be detected in the right ventricle. However, the lower resistance of the lung circuit results in a lower systolic pressure. In addition, the contraction phase of the right ventricle is slightly delayed, its duration is shorter following in an earlier ejection phase. The end of systole however is about $10 - 30 \ ms$ delayed compared to the left ventricle.

3.2.5 Ventricular Pressure

The pressure characteristics of a ventricle depends on the contraction of the cavity and the opening and closing of valves. For the left ventricle a pressure cycle conducts as follows:

At the start of the left ventricular systole all valves are closed. The ventricle is pre-loaded with blood. The contraction commences and a steep rise in pressure can be measured (Fig. 3.6, I).
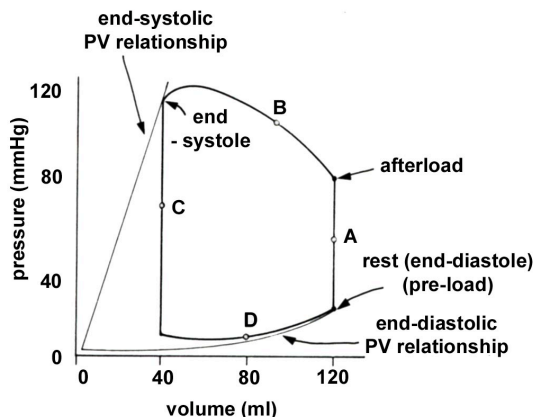
Figure 3.7. Work diagram of the left ventricle. A small preload of the resting heart determines the point along the end-diastolic pressure-volume (PV). This is where the systole begins. After the mitral valve closes the isovolumic contraction (A) proceeds until the ventricle encounters its afterload, the aortic pressure. After the aortic valve opens pressure first rises and then drops during ejection (B). When the systole ends, the ventricular pressure and volume come to lie on the end-systolic pressure-volume (PV) relationship. After the aortic valve closure removes the load (aortic pressure) from the ventricle, relaxation begins under isovolumic conditions (C) because blood can neither enter nor leave the ventricle. When the left ventricular pressure drops below that in the left atrium, the mitral valve opens and the atrium empties into the ventricle during the phase of filling (D). The cycle is completed when ventricular relaxation is completed and ventricular pressure and volume again lie on the end-diastolic PV relationship (from [5]).

When the intraventricular pressure reaches the aortal pressure at approx. 80 $mmHg$, the aortic valve opens and the blood is ejected into the aorta (Fig. 3.6, II). The pressure keeps on rising to a maximum of approx. 120 $mmHg$ (person at rest). The following relaxation phases result in a gradual reduction of pressure. As soon as the pressure drops below 80 $mmHg$ the aortal valve closes (Fig. 3.6, III). During the relaxation and filling phase the pressure returns to its end-diastolic state with a pre-load of approx. $5 - 10$ $mmHg$.

In fig. 3.7 the pressure-volume relationship of the left ventricle during a cardiac cycle is shown.

3.3 Microscopic View of Heart Function

3.3.1 Excitation

The sinoatrial node initiates the heart beat by slowly depolarizing above a certain threshold, where an action potential is created. This action potential is propagated from cell to cell and results in a stereotype reaction of the cell, depending on its excitation history. Ions are interchanged with the extracellular space, and the myocyte contracts. The microscopy description below represents the basic cellular activities without going into detail, as it is beyond the scope of this work.

3.3.1.1 Resting Potential of a Cell

The membrane of the cell with its ion channels, exchangers, ion pumps and gap junctions presents a barrier between intra- and extracellular space. In the resting state specific ion concentrations form at the inside as well as at the outside of the membrane, due to a chemical and electrical gradient as well as open ion channels and ion pumps.

The potential difference between intracellular Φ_i and extracellular Φ_e potential across the membrane is called transmembrane voltage V_m with

$$V_m = \Phi_i - \Phi_e.$$

The equilibrium voltage over a membrane can be described using the Nernst equation for single ions [48].

$$V_{ion} = \frac{R\,T}{z\,F} \ln \frac{[Ion]_e}{[Ion]_i}. \tag{3.1}$$

It describes the membrane voltage V_{ion} of the ion due to the intra $[Ion]_i$ and extracellular $[Ion]_e$ ion concentration, the gas constant R, the absolute temperature T, the ion valence z and the Faraday's constant $F = 9.65 \cdot 10^4 \frac{As}{mol}$. The Goldman-Hodgkin-Katz equation resembles an extension of the Nernst equation and allows the consideration of several ions at the same time [49, 50].

The resting potential across the cell membrane forms due to concentration and permeability differences of intra- and extracellular space. The permeability P describes the ability of ions to diffuse

through the membrane

$$P = \frac{D\beta}{x}.$$

with the diffusion coefficient D and the water-membrane partition coefficient β for the ion, and the thickness of the membrane x.

The resting potential voltage of approx. $-90\ mV$ is almost identical with the Nernst voltage of K^+ [51]. This is due to the fact that K^+ permeability of the membrane is relatively high during rest state.

If the transmembrane voltage is disturbed by an electrical stimulus or a drain of ions an action potential can be initiated.

3.3.1.2 Action Potential

In excitable cells a resting potential is established across the membrane. An arriving electrical stimulus may change the permeability of the cell membrane and the transmembrane voltage varies. If the transmembrane voltage exceeds a threshold an action potential is created (fig. 3.8). Once an action potential is initiated it cannot be stopped (all or nothing principle) [53].

The start of the action potential is characterized by the avalanche-like opening of Na^+ channels. The positive ion current flowing into the cell creates an even higher depolarization, exceeding $0\ mV$ towards positive values of approx. $30\ mV$. The depolarization is called upstroke and the positive transmembrane voltage the overshoot. After approx. $3\ ms$ the Na^+ channels close [54] and Ca^{2+} and early K^+ channels open. However, the time constants of Ca^{2+} and K^+ gates are much slower compared to Na^+ (fig. 3.8). Therefore, the action potential shows a long plateau. The opening of delayed K^+ channels and the outflow of K^+ marks the beginning of the repolarization phase.
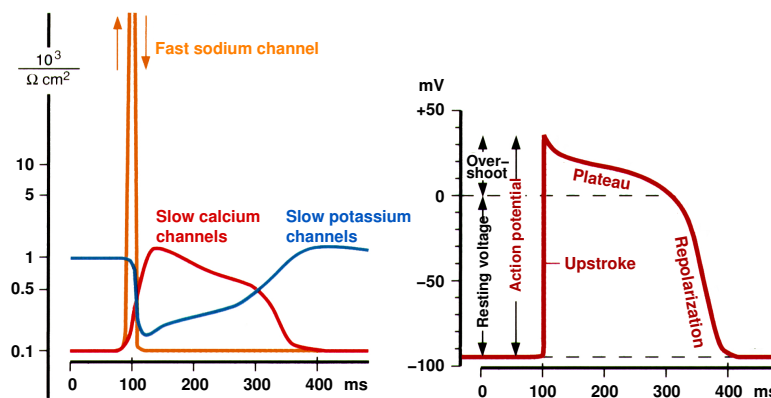
Figure 3.8. Schematic of action potential and underlying ionic currents. The left figure shows the basic ionic currents in their temporal behavior as result of crossing of the transmembrane voltage threshold. The left figure describes the resulting action potential that can be measured (fig. adapted from [52]).

During the course of an action potential, the cell is not excitable until V_m drops below $-50\ mV$ [55]. This is due to the inactivation state of Na^+ channels. During this absolute refractory period, no avalanche-like opening of Na^+ channels can occur and thus the cell is not subject to re-excitation. The relative refractory phase marks the interval, where the cell is not yet fully repolarized but a strong stimulus is able to create another action potential. However, action potentials started in the relative refractory phase show a different shape due to the missing equilibrium of ion concentrations (fig. 3.9).
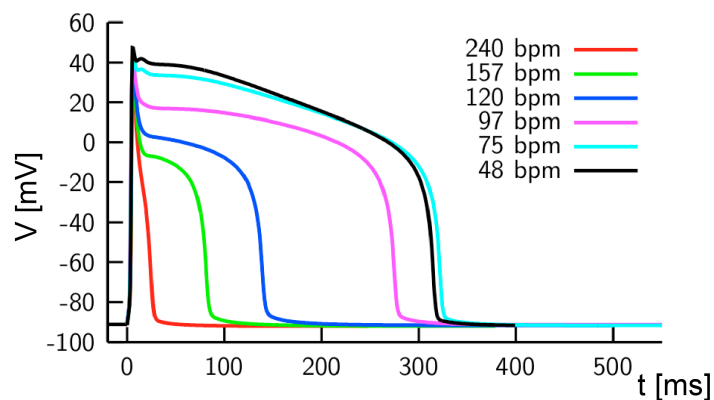
(a)
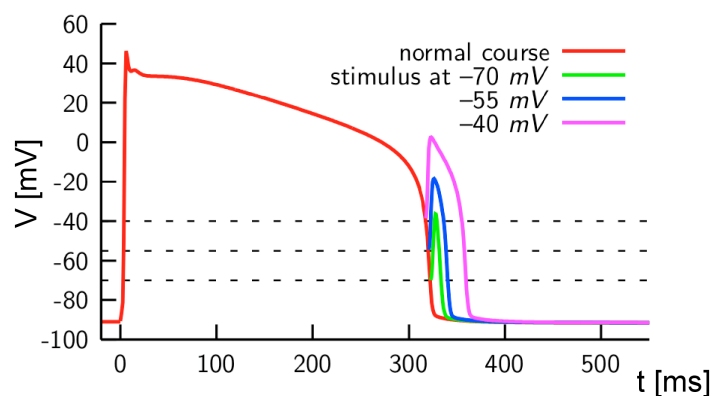
(b)

Figure 3.9. The course of transmembrane voltage in normal ventricular myocardium for different frequencies of excitation (a). The course of transmembrane voltage changes if stimulus is applied in the relative refractory period (b) (fig. adapted from [56]).

3.3.1.3 Propagation of Action Potential

The myocardium is constructed of bundles of myocytes. The myocytes share a common extracellular space and adjacent myocytes are coupled via gap junctions (section 2.3.2.2). The cell structure influences the continuous and discontinuous propagation [57, 58]. An action potential happening at a myocardial cell influences the extracellular ion concentrations and hence the electric field, influencing neighboring cells. This causes an ion as well as an electrical gradient in the extracellular space. Furthermore, ions flow directly through the connective gap junctions into neighboring myocardial cells. This causes an action potential in the neighboring resting cell. Gap junctions link the intracellular space of myocytes and allow for passive passage of ions, anions, and molecules. The conductivity depends on the trans-junctional voltage [59, 60] and on intracellular H^+ concentration [61]. Furthermore, the density of gap junctions influences the electrical conductivity.
The intercellular coupling resembles a functional electrical syncytium. The effect of intercellular currents dominates the characteristics of the spread of activation.

3.3.1.4 Excitation Contraction Coupling - Ca^{2+}

The excitation contraction coupling describes the process of an electrical stimulus igniting a mechanical contraction. It is conducted by the delayed inward Ca^{2+} current during the plateau phase of the action potential. The amount of calcium that enters the cell from the extracellular space however is not sufficient to activate a myocardial contraction. It serves as trigger for the release of much larger amounts of Ca^{2+} from stores in the sarcoplasmic reticulum(SR). This effect is called the Ca^{2+} induced Ca^{2+} release. The t-tubules provide the close proximity of extracellular activator Ca^{2+} to the SR. The intracellular Ca^{2+} released from the SR binds to the filament proteins and enables the contraction of sarcomeres. Calcium is considered the most important ion involved in the cardiac excitation contraction coupling [62].

3.3.2 Contraction

Sliding filament theory

Examination of sarcomeres during contraction showed that H-bands and I-bands get smaller, whereas the A-band retains a constant width. As a result the Z-discs move closer together. The contraction stops when the I-band vanishes. These observations led to the sliding filament theory which constitutes, that the thin filaments slide towards the center of the sarcomere alongside the thick filaments (fig. 3.10). The contraction cycle depends on the intracellular Ca^{2+} released by the SR and the presence of adenosine triphosphate (ATP). It consists of five phases: active-site exposure at the thin filaments, cross-bridge binding, pivoting of the myosin head, cross-bridge detachment and myosin reactivation.
The details of molecular events during the contraction cycle are outlined in fig. (fig. 3.11) and described below: During the resting state of a sarcomere thin and thick filaments are not attached.
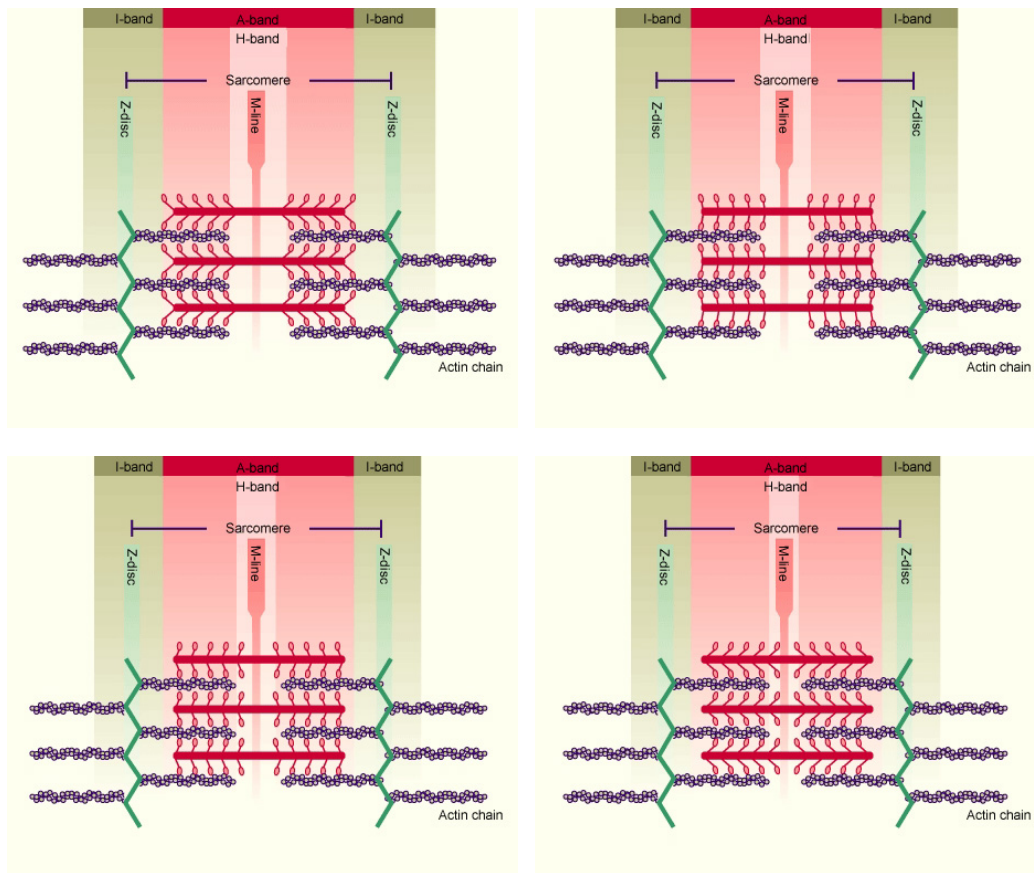
Figure 3.10. Schematic of sliding filament theory. The pivoting myosin heads pull the actin filaments towards the M-line (fig. adapted from [14]).

Each cross-bridge (myosin head) is energized - charged with energy needed to power contraction. It functions as an ATPase, which breaks down ATP into adenosine diphosphate (ADP) and phosphate (P) and stores the released energy. Both breakdown products remain attached to the cross-bridge. The contraction cycle commences with the following steps:

Active-site exposure: The intracellular Ca^{2+} ions bind to troponin. This causes a weakening of the troponin complex and actin. Therefore, the troponin molecule changes position pulling the tropomyosin molecule. This exposes the active-sites and allows for cross-bridge binding.

Cross-bridge attachment: As soon as the active-sites are exposed, the myosin cross-bridge binds to it.

Pivoting: The cross-bridge points away from the M-line during resting state. The myosin head is cocked, which required the energy from the prior splitting of ATP. After the cross-bridge attachment the head pivots towards the M-line releasing ADP and P. This is called the power stroke.
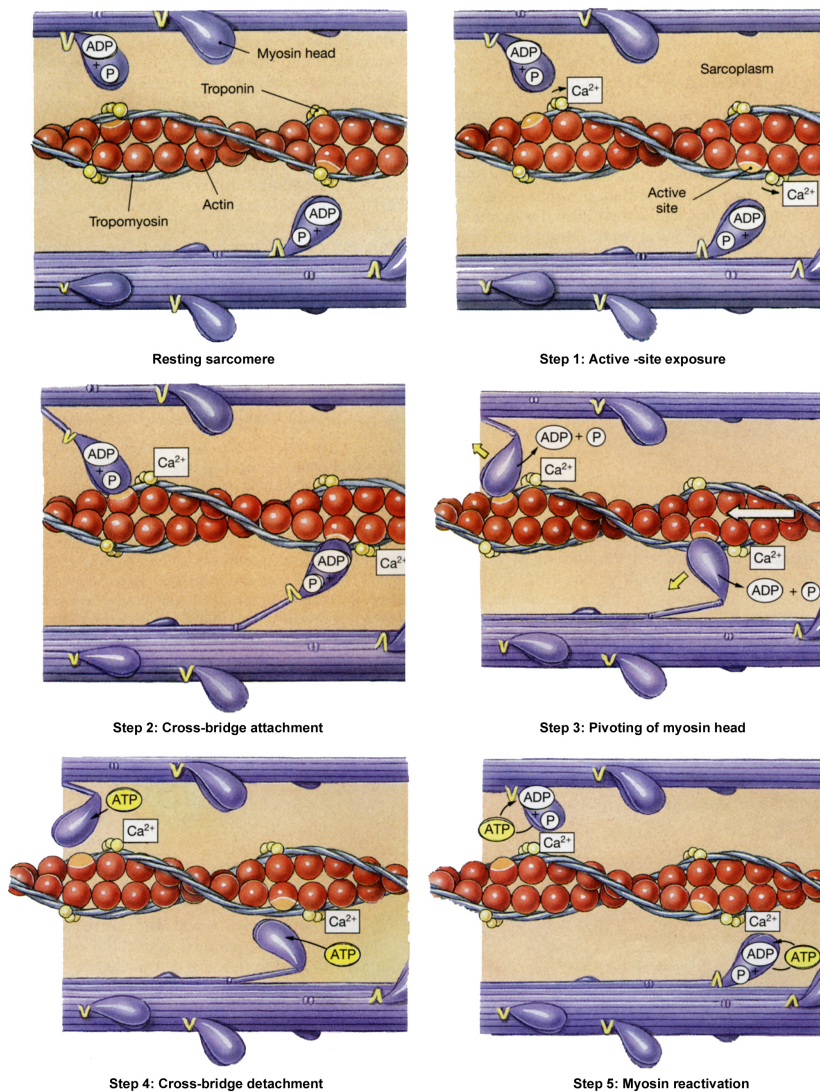
Figure 3.11. Schematic of sliding filament theory on molecular level. The sliding filament theory is described in five steps. The resting myofibril is constructed of the thin filament consisting of an actin chain and attached troponin and tropomyosin. The thick filament is build up from myosin molecules and specialized myosin heads. The myosin heads are loaded and adenosine diphosphate (ADP) and phosphate (P) are attached. In step 1 Ca^{2+} binds to troponin and exposes the active binding site for myosin. Step 2 displays the binding of myosin to the exposed binding sites the so called cross-bridge attachment. In step 3 the energy stored in the myosin head is applied for the pivoting of the head and the actin chain is pulled alongside. During this power stroke the ADP and P are released. Step 4 shows the cross-bridge detachment, where an adenosine triphosphate (ATP) binds to the myosin head and results in a detachment from the binding site. The myosin head is reactivated in step 5 by the splitting of ATP into ADP and P. The released energy is used to recock the myosin head. The entire cycle can now be repeated (fig. adapted from [17]).

Cross-bridge detachment: The ATP binding site at the myosin head is again available. A rebind of ATP to the myosin head breaks the link to the active-site of actin. The cross-bridge detaches and the active-site is capable to interact with another cross-bridge.

Myosin reactivation: The myosin reactivation occurs, when the bound ATP is split into ADP and P. The released energy is used to recock the head. The head may now form another cross-bridge provided that the Ca^{2+} concentration remains elevated and the ATP reserves are sufficient.

3.3.2.1 Mechanical Properties of Myocardium

For the mechanical modeling the mechanical properties of myocardial cells are of significant importance. These properties can only be extracted by experimental studies. Most studies to acquire mechanical properties of myocardium were performed with trabecular and papillary muscles of animals [63], as well as tissue from atrial and ventricular wall [64, 65]. Single and small groups of myocytes were used to quantify cellular mechanical properties [66]. Due to the size of the examined tissue, specialized measurement setups were created. The measurement device described by Dokos et al. [67, 68] allows a triaxial-measurement shear-test of soft tissue. Tab. 3.1 shows publications of researchers with examined tissue types and species.
The myocardial tissue proved to be nonlinear, anisotropic and viscoelastic [69], which is common for most biological tissues. The change in volume due to deformation is small and therefore an approximate incompressibility can be postulated. Furthermore, significant residual stresses are present inside the tissue [70]. The dependence of material properties on intracellular calcium concentration and the state of active contraction have also been reported [71, 66].
The properties based on experimental results are used to parameterize mathematical models to describe mechanical behavior of myocardial tissue.

Year	Author	Tissue	Species
1964	Sonnenblick [72]	papillary muscle	cat
1973	Pinto, Fung [73, 63]	papillary muscle	rabbit
1973/74	Janz, Kubert, Moriarty, Grimm [74, 75]	papillary muscle	rat
1974	Alpert, Hamrell, Halpern [76]	ventricular muscle	rabbit
1975	Kane, McMahon, Wagner, Abelmann [77]	ventricular muscle	hamster
1976	Rankin, Arentzen, McHale, Ling, Anderson [69]	ventricular muscle	canine
1988	Hunter, Smaill [78, 79]	ventricular muscle	canine
1991	Guccione, McCulloch, Waldman [80]	ventricular muscle	canine, rat
1994	Novak, Yin, Humphrey [81]	ventricular muscle	canine
1995	Hunter, Nash, Sands [82, 83]	ventricular muscle	canine
1995	Moulton, Creswell, Actis, Myers, Vannier, Szabó, Pasque [84]	ventricular muscle	canine
1997	Miller, Vanni, Keller [85]	ventricular muscle	chicken
1998	Omens, Vaplon, Fazeli, McCulloch [86]	ventricular muscle	rat
1998	Zile, Cowles, Buckley, Richardson, Cowles, Baicu, Cooper, Gharpuray [66]	ventricular myocytes	cat
2000	Dokos, LeGrice, Smaill, Kar, Young [67]	septal muscle	rat
2000	Okamoto, Moulton, Pasque, Peterson, Li, Guccione [65]	ventricular muscle	canine
2003	Dokos, Smaill, Young, LeGrice [68]	ventricular muscle	pig

Table 3.1. Measurements of mechanical properties of myocardium(Tab. from [31]).

3.4 Functional Modeling of the Heart

The modeling of cells requires knowledge about anatomical and physiological properties. Furthermore, the action, reaction, and interaction of cells need to be investigated. In recent years mathematical models have been created with increasing detail, which represent the corresponding behavior and properties of cells.

3.4.1 Electrophysiological Modeling of Cell Properties

The modeling of the electrophysiology of a cell commences by describing the cell and its proximity in a steady state. The lipid layer forms a barrier between intra- and extracellular space. Gap junctions, channels, exchangers, and pumps allow ions to cross this barrier. In a resting cell a resting potential of approx. -80 mV is established between the inside and the outside of the cell. The reason for this behavior are the varying ion concentrations in combination with different conductances for the ions. The factors driving this behavior are the electrical field created by the ion concentration, the concentration gradient itself and the permeability of the membrane. Furthermore, the cell length is a factor in the electrophysiological behavior.

The modeling of transmembrane voltage, the transmembrane currents, membrane conductivity as well as intra- and extracellular ion concentration is accomplished by coupled differential equations. The cell membrane without its conducting proteins can be modeled as a capacitor. Furthermore, the ion conductivity can be modeled as time and voltage dependent resistors, and the Nernst voltages by voltage sources (fig. 3.12).

A large amount of electrophysiological cell models base upon the equations of Hodgkin and Huxley, who described the electrophysiological behavior of a giant squid axon [88]. Modern cell models are derived from those equations but have become more complex and more detailed. Experiments are
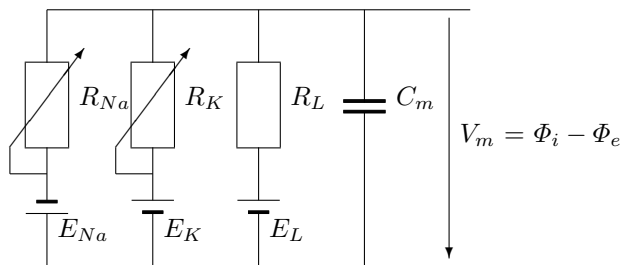

Figure 3.12. Electrical equivalent circuit of the cell membrane of the Hodgkin-Huxley model describing the electrophysiology of a giant squid axon. The resistors R_X describe the conductivity of the channels of type X and V_X are the voltage sources given by E_X (fig. from [87]).

Year	Author	Specimen	Species
1962	Noble [89]	Purkinje fiber	-
1975	McAllister, Noble, Tsien [90]	Purkinje fiber	-
1977	Beeler, Reuter [91]	Ventricular myocardium	Mammalian
1985	DiFrancesco, Noble [92]	Purkinje fiber	Mammalian
1987	Hilgemann, Noble [93]	Atrial working myocardium	Rabbit
1990	Earm, Noble [94]	Atrial working myocardium	Rabbit
1991	Luo, Rudy [95]	Ventricular myocardium	Mammalian
1994	Luo, Rudy [96] [97]	Ventricular myocardium	Guinea-pig
1994	Demir, Clark, Murphey, Giles [98]	Sinoatrial node	Mammalian
1996	Dokos, Celler, Lovell [99]	Sinoatrial node	Mammalian
1996	Demir, O'Rourke, Tomaselli, Marban, Winslow [100]	Ventricular myocardium	Dog
1998	Courtemanche, Ramirez, Nattel [101]	Atrial working myocardium	Human
1998	Jafri, Rice, Winslow [102]	Ventricular myocardium	Guinea-pig
1998	Noble, Varghese, Kohl, Noble [103]	Ventricular myocardium	Guinea-pig
1998	Nygren, Fiset, Firek, Clark, Lindblad [104]	Atrial working myocardium	Human
1998	Priebe, Beuckelmann [105]	Ventricular myocardium	Human
1999	Winslow, Rice, Jafri, Marban, O'Rourke [106] [107]	Ventricular myocardium	Dog
2000	Zhang, Holden, Kodama, Honjo, Lei, Varghese, Boyett [108]	Sinoatrial node	Rabbit
2001	Pandit,Clark, Giles, Demir [109]	Ventricular myocardium	Rat
2001	Puglisi, Bers [110]	Ventricular myocardium	Rabbit
2002	Bernus, Wilders, Zemlin, Verschelde, Panfilov [111]	Ventricular myocardium	Human
2004	Ten Tusscher, Noble, Noble, Panfilov [112]	Ventricular myocardium	Human
2004	Iyer, Mazhari, Winslow [113]	Ventricular myocardium	Human

Table 3.2. Electrophysiological models of cardiac cells.

conducted to determine parameters for the models. In tab. 3.2 some electrophysiological models of myocardial cells are listed in chronological order.

3.4.1.1 Mathematical Description of Cell Models

The mathematical description of a cell model is based on nonlinear coupled differential equations, which have been parameterized by experimental data. The main components are transmembrane voltage, transmembrane currents, gating variables, ion concentration, intracellular components, and mechanoelectrical feedback.

Transmembrane voltage

The cell membrane acts as a capacitor. The electrical description results in

$$Q = C_m V_m$$

with Q the electrical charge accumulated at the membrane, the capacity of the membrane C_m, and the transmembrane voltage V_m.

The ion passage and transport through the membrane results in ion currents. The sum of transmembrane currents can be described as I_{sum}. Furthermore, a stimulus current I_{stim} can be defined, which may evoke an action potential. Therefore, the time derivative of the transmembrane voltage V_m of an isolated cell can be described by :

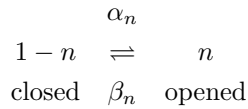$$\frac{dV_m}{dt} = -\frac{1}{C_m}(I_{sum} + I_{stim})$$

Transmembrane currents

The transmembrane current of an ion I_{ion} passing the membrane depends on the transmembrane voltage V_m, the equilibrium voltage V_{ion} (eq. 3.1), the intra- and extracellular ion concentrations $[Ion]_i, [Ion]_e$, and one or more gating variables n.

$$I_{ion} = f(V_m, V_{ion}, [Ion]_i, [Ion]_e, n)$$

Gating variables

Hodgkin and Huxley first introduced the use of gating variables [88]. The cell membrane consists of many channel proteins for one type of ion. Each of these channel proteins can be either opened or closed. The accumulation of opened or closed channels for one type of ion can be described by a gating variable. It ranges between 0 and 1. In case of one gate the fraction of channels in opened state is n and in closed state is $1 - n$. The transition from opened to closed state is described by the voltage dependent rate constants α_n, whereas the opposite direction is described by β_n.

$$
\begin{array}{ccc}
 & \alpha_n & \\
1 - n & \rightleftharpoons & n \\
\text{closed} & \beta_n & \text{opened}
\end{array}
$$

In case of the Hodgkin and Huxley model and the exemplary Na^+ ion channel, two gating variables are defined. One describes the activation (gating variable m) and the other the inactivation (gating variable h). The voltage dependent rate constants α_m, β_m, α_h, and β_h control the activation and inactivation process:

$$\frac{dm}{dt} = \alpha_m(1 - m) - \beta_m m$$
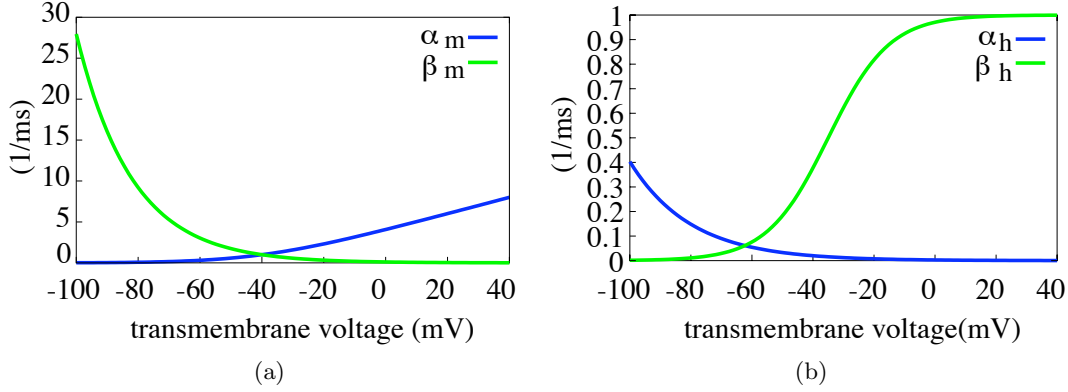
and

$$\frac{dh}{dt} = \alpha_h(1 - h) - \beta_h h$$

(a)   (b)

Figure 3.13. Voltage dependent rate constants in the Hodgkin-Huxley model for sodium channels. (a) The rate constant α_m and β_m for the activation variable m. (b) The rate constant α_h and β_h for the inactivation variable h.

Fig. 3.13 shows the rate constants dependance on V_m. The sodium conductivity g_{Na} can then be computed by:

$$g_{Na} = m^3 h \bar{g}_{Na} \tag{3.2}$$

with the maximal conductance for sodium ions $\bar{g}_{Na}$. The sodium current I_{Na} results to:

$$I_{Na} = g_{Na}(V_m - E_{Na}) \tag{3.3}$$

with V_m the transmembrane voltage and E_{Na} the equilibrium voltage for Na^+ .

Ion concentration

Varying ion concentrations exist in the intra- and extracellular space. These ion concentrations are controlled by opening and closing of passive channels, active exchangers, and pumps. The transport of ions through the membrane results in specific ion currents I_{ion}. Therefore, the temporal variation of the ion concentration depends on the ion currents and the ion concentration $[Ion]$ itself:

$$\frac{d[Ion]}{dt} = f(I_{ion}, [Ion])$$

Mechano-electrical feedback

The mechano-electrical feedback describes the dependence of stretch of a cell to its electrophysiology. The deformation influences the conductivity of ion channels. Therefore, a stretch dependent current can be defined as $I_{stretch}$. This current is dependent on the sarcomere length SL, the conductivity of the ion channel g_{Ion}, the transmembrane voltage V_m, and the equilibrium voltage
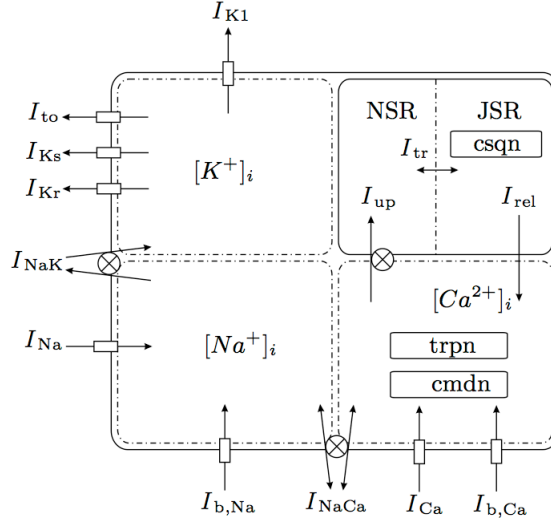
Figure 3.14. Schematic description of ionic model of Priebe Beuckelmann [105], with currents, pumps, exchangers and other components. It contains detailed description of ion currents, intracellular ion dynamics ($[Ion]_i$), sarcoplasmic reticulum (SR) with network SR (NSR) and junctional SR (JSR), and calcium buffers like troponin (trpn), calmodulin (cmdn), and calsequestrin (csqn) (fig. from [87]).

U_{ion}. Thus:

$$I_{stretch} = f(SL, V_m, g_{Ion}, U_{ion})$$

The total current induced by the stretch of a sarcomere depends on the used electrophysiological model and it's applied ion channels.

Several of these basic equations are used in the cell models listed in tab. 3.2. Furthermore, the models are extended by coupled differential equations for a more explicit and precise description.

3.4.1.2 Electrophysiological Cell Modeling

Various models exist to describe electrophysiological behavior (tab. 3.2, [31], [87]). The electrophysiological model used in this work is the Priebe and Beuckelmann model (PBM), which describes the electrophysiology of a human ventricular myocyte [105] (fig. 3.14). It is derived from the phase-2 model of Luo-Rudy, which was parameterized by measurement data from a human myocyte [96, 97]. The enhancement of the PBM was achieved by considering more recent measurements of ventricular myocytes and two sets of parameters, one for a normal and one for a failing myocyte. The sum of the transmembrane currents I_{mem} of the Priebe Beuckelmann model is given by:

$$I_{mem} = I_{Na} + I_{K1} + I_{to} + I_{Kr} + I_{Ks} + I_{Ca} + I_{NaK} + I_{NaCa} + I_{b,Na} + I_{b,Ca} \tag{3.4}$$

with

$$
\begin{array}{ll}
I_{Na} & \text{fast sodium current} \\
I_{K1} & \text{outward rectifier potassium current} \\
I_{to} & \text{transient outward potassium current} \\
I_{Kr} & \text{rapid delayed potassium current} \\
I_{Ks} & \text{slow delayed potassium current} \\
I_{Ca} & \text{L-type calcium current} \\
I_{NaK} & Na^+/K^+ \text{ pump current} \\
I_{NaCa} & Na^+/Ca^{2+} \text{ exchanger current} \\
I_{b,Na} & \text{background sodium current} \\
I_{b,Ca} & \text{background calcium current}
\end{array}
$$

The model was furthermore adapted allowing integration with tension development models, implementing the binding of Ca^{2+} to Troponin (trpn in fig. 3.14). However, its functionality was substituted by applying the model of Glänzel, Sachse, Seemann (section 3.4.3).

3.4.2 Excitation Propagation

The excitation propagation in myocardial tissue can be differentiated into microscopic and macroscopic modeling.

Microscopic models include ion currents, intra- and extracellular ion concentration, and base upon the intercellular currents through gap-junctions. This discrete modeling results in a high degree of mathematical abstraction, and hence complex models. Simulations with such models result in the need of large computational power but allow to reconstruct experimental studies with a very high degree of precision.

Macroscopic models combine several cells and describe the averaged behavior. The complexity of the model and the computational power is reduced at the cost of an averaged result. However, depending on the application, the reduced computational expense is preferred over the precision of the results.

For the excitation propagation two main approaches are used:

- cellular automata
- reaction diffusion system

Cellular automata apply rule-based techniques and allow for efficient simulation of electrical excitation propagation [114, 115, 116, 117]. A reaction diffusion system allows to describe the electrical properties of tissue, using a special type of diffusion equation. The reaction equation reconstructs the ion current across the cell membrane. For further details on modeling with reaction diffusion systems see [118, 119, 120].
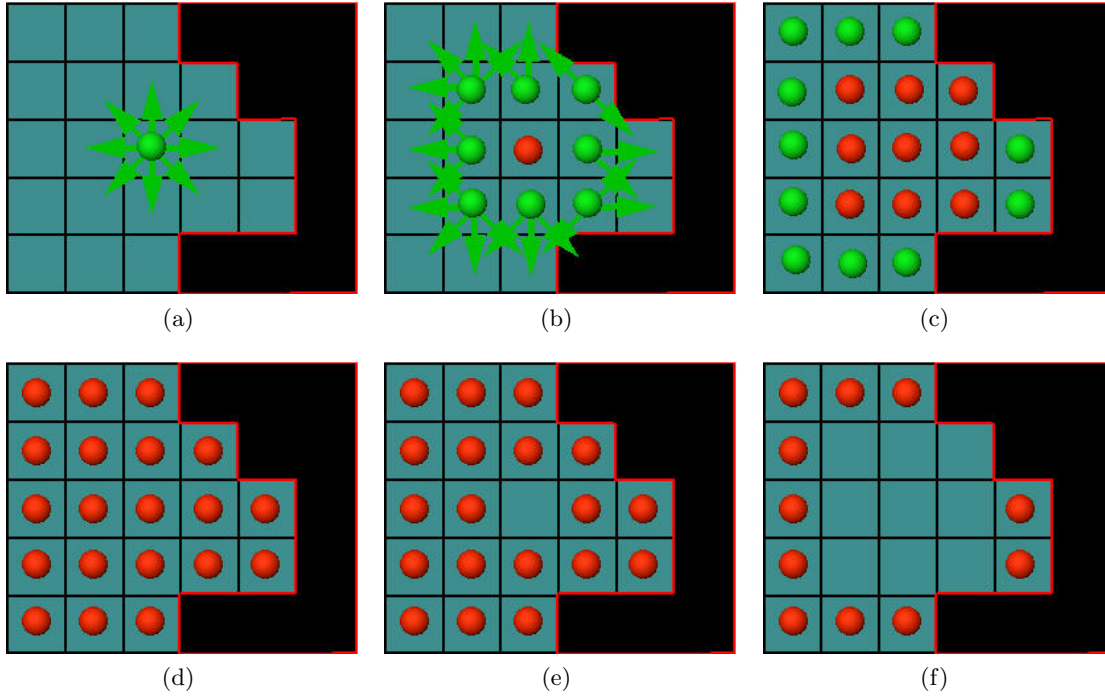
Figure 3.15. Neighbor propagation of a cellular automaton on a surface. Empty squares represent resting cells. Each excited cell (green), communicates the excitation to its eight neighbors (green arrow)(a,b). After an explicit time interval the cell switches to an unexcitable state (red)(c,d). Finally, the cell returns back to an excitable cell (e,f). This process proceeds along the given geometry.

3.4.2.1 Cellular Automata

Cellular automata are applied to model various natural processes, where a domino like effect can be applied. A cellular automaton can be discretized into two components [121, 122]. First, a regular, discrete, infinite network, which represents the underlying structure of the automaton. Second, a finite automaton, which will run at each individual cell (so-called node) during simulation. Furthermore, each cell is connected and can communicate to a finite number of neighbor cells depending on the geometric outline. This communication allows a global evolution of the system during discrete time steps (fig. 3.15).

In this work the cellular automaton of Werner, Sachse and Dössel [123, 124] was used. The automaton works on a geometrical structure including fiber orientation, the excitation initiation, and an excitation conduction system. Physiological parameters for electrical properties of myocytes e.g. refractory periods, up to 9×4 curves to model $V_m(t)$, three excitation velocities in fiber, sheet and sheet normal, and an auto rhythmic mechanism can be implemented for any kind of tissue. Upon a given geometry the automaton provides a spatial and temporal distribution of V_m.

Year	Author	Specimen	Species
1938	Hill [125]	skeletal muscle	frog
1957	Huxley [126]	skeletal muscle	–
1980	Panerai [127]	papillary muscle	mammalian
1991	Peterson, Hunter, Berman [128]	papillary muscle	New Zealand white rabbit
1994	Landesberg, Sideman [129]	skinned cardiomyocyte	–
1994	Landesberg, Sideman [130, 131]	cardiac muscle	–
1997	Hunter, Nash, Sands [83]	cardiac muscle	mammalian
1998	Hunter, McCulloch, ter Keurs [132]	cardiac myocyte	–
1998	Guccione, Motabar-Zadeh, Zahalak [133]	cardiac myocyte	–
1999	Rice, Winslow, Hunter [134]	papillary muscle	New Zealand white rabbit
2000	Rice, Jafri, Winslow [135]	cardiac muscle	ferret
2001	Mlcek, Neumann, Kittnar, Novak [136]	cardiac myocyte	–
2001	Nickerson, Smith, Hunter [137]	cardiac myocyte	–
2002	Glänzel, Sachse, Seemann [138, 139]	cardiac myocyte	–

Table 3.3. Mathematical models of tension development.

However, due to its parameter set, the cellular automaton is not restricted to the computation of transmembrane voltages, only. Depending on the application, the automaton can provide a spatial and temporal distribution of V_m, Ca^{2+} or $force$, depending on the parameterization. The parameter curves can be acquired with microscopic cell models using a cluster of cells. Exemplary curves for V_m, Ca^{2+} and $force$ are displayed in (fig. 3.16).

In this work, the parameterization of the automaton was set to force curves yielding a spatial and temporal distribution of forces for the given geometries (section 6.1).

3.4.3 Force Development Models

The first description of a mathematical tension development model was published by Hill [125]. He described the tension-velocity relationship of a tetanized skeletal muscle of a frog. Tab. 3.3 shows various models describing tension development in the cardiac myocyte. Some apply continuous-time Markov chains [140, 141], which can describe a stochastic process in probability theory. In these processes the knowledge of the present state is used to predict the future state, without the need of past information. Each process can take a state of a discrete set of elements connected by transition probabilities. In case of tension development in the myocyte the discrete states are the bonds of myosin, actin, tropomyosin, and troponin during contraction.

In this work the hybrid tension development model (HTD) of Glänzel, Sachse, Seemann et al. was used [138, 139]. It consists of 14 state variables, which are coupled in three Markov chains (fig. 3.17). The first Markov chain resembles the binding of Ca^{2+} to troponin T (fig. 3.17(a)). Two states are used, which are T for free troponin and TCa for Calcium bound to troponin. The sum of the state variables equals one:
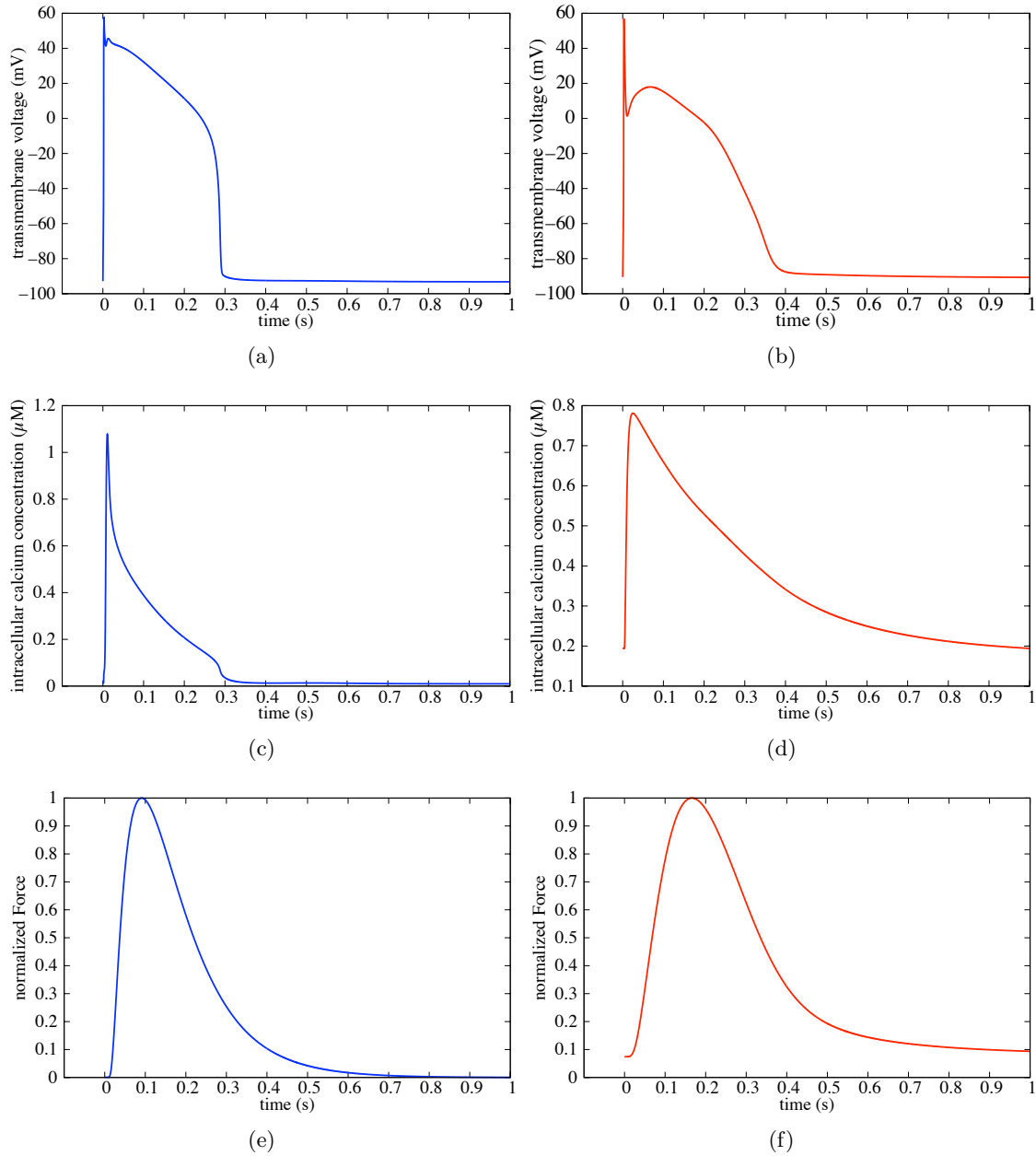
Figure 3.16. Parameterization curves of the cellular automaton. Figures show the parameter curves created with a microscopic cell model of Noble et al. [89] and Rice et al. [134] (a),(c), and (e), and microscopic cell models of Priebe et al. [105] and Glänzle et al. [138, 142] (b),(d), and (f). (a/b) show the transmembrane voltage of an action potential, (c/d) the calcium concentration, and (e/f) the normalized force slope. In this work the curves (b) and (d) were applied for microscopic simulation, whereas (f) was applied for parameterization of the cellular automaton.

$$T + TCa = 1 \tag{3.5}$$

The transition probability from one state to the other is described by k_{on} and k_{off}. The transition rate k_{on} depends on intracellular calcium concentration, the amount of cross-bridges (XB), and of the sarcomere length λ. A coupled differential equation can be applied to model the variation of the binding process:

$$\frac{\mathrm{d}}{\mathrm{d}t} \begin{pmatrix} T \\ TCa \end{pmatrix} = \begin{pmatrix} -k_{on} & k_{off} \\ k_{on} & -k_{off} \end{pmatrix} \begin{pmatrix} T \\ TCa \end{pmatrix} \tag{3.6}$$

The second Markov chain models the configuration of tropomyosin TM (fig. 3.17(b)). The binding of Ca^{2+} to troponin shifts the TM, so that the binding site for myosin on the actin filament is available. This is modeled by the TM_{on} state the so-called permissive state. TM_{off} resembles the state, where the binding site for myosin is unavailable. The states are described by:

$$TM_{on} + TM_{off} = 1 \tag{3.7}$$

The change of states can also be described by a differential equation with the transition rates tm_{on} and tm_{off}:

$$\frac{\mathrm{d}}{\mathrm{d}t} \begin{pmatrix} TM_{on} \\ TM_{off} \end{pmatrix} = \begin{pmatrix} -tm_{on} & tm_{off} \\ tm_{on} & -tm_{off} \end{pmatrix} \begin{pmatrix} TM_{on} \\ TM_{off} \end{pmatrix} \tag{3.8}$$

tm_{on} depends on the fraction of bound TCa and on the sarcomere length λ.
The third Markov chain consists of 10 states, which model the interaction of myosin and actin (fig. 3.17(c)). The process describing the cross-bridge cycle is given by:

$$M + A \sim M \bullet ATP + M \bullet ATP + M \bullet ADP \bullet P_i + A \sim M \bullet ADP \bullet P_i+ \tag{3.9}$$

$$A \bullet M \bullet ADP \bullet P_i + A \bullet M^* \bullet ADP + A \bullet M \bullet ADP + A \bullet M + M \bullet ADP = 1 \tag{3.10}$$

with actin A, myosin M, strong bonds $\bullet$, and weak bonds $\sim$. Furthermore, the system includes the hydrolysis of ATP into ADP and phosphate P_i. The coupled differential equation describing the system is given by:
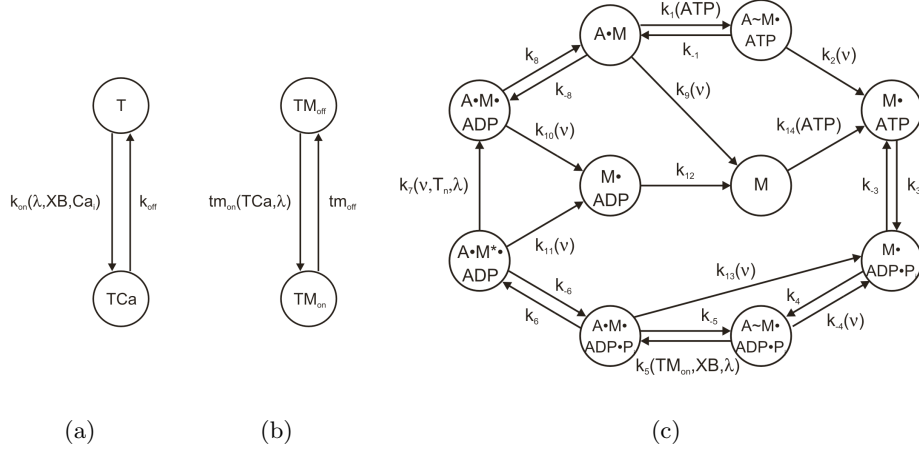
Figure 3.17. Markov chains of the Glänzel, Sachse, Seemann model. The first Markov chain resembles the binding of Ca^{2+} to troponin T and the dependent transition rates k_{on}, k_{off}. The second Markov chain models the configuration of tropomyosin TM, representing permissive and non permissive states for binding of myosin to actin. The third Markov chain represents the interaction of myosin M and actin A, which is also known as cross-bridge cycle. Furthermore, the hydrolysis of ATP in ADP and P_i is included. The symbol $\bullet$ marks strong, whereas $\sim$ marks weak bonds. Transition rates depend on the sarcomere length λ, the stretch velocity ν, the amount of ATP, the amount of cross-bridges XB, the fraction of shifted tropomyosin TM_{on}, the amount of calcium bound to troponin TCa, the intracellular Ca^{2+} concentration Ca_i, and the normalized tension T_n itself (fig. from [87]).

$$\frac{\mathrm{d}}{\mathrm{d}t}\begin{pmatrix} A \sim M \bullet ATP \\ M \bullet ATP \\ M \bullet ADP \bullet P_i \\ A \sim M \bullet ADP \bullet P_i \\ A \bullet M \bullet ADP \bullet P_i \\ A \bullet M^* \bullet ADP \\ A \bullet M \bullet ADP \\ A \bullet M \\ M \bullet ADP \\ M \end{pmatrix} = \boldsymbol{M} \begin{pmatrix} A \sim M \bullet ATP \\ M \bullet ATP \\ M \bullet ADP \bullet P_i \\ A \sim M \bullet ADP \bullet P_i \\ A \bullet M \bullet ADP \bullet P_i \\ A \bullet M^* \bullet ADP \\ A \bullet M \bullet ADP \\ A \bullet M \\ M \bullet ADP \\ M \end{pmatrix} \qquad (3.11)$$

with the matrix $\boldsymbol{M}$ formed by the transition coefficients, depending on sarcomere length λ, the stretch velocity ν, the amount of ATP, the amount of cross-bridges XB, and the fraction of shifted tropomyosin TM_{on} [87]. The tension is developed only in three of the states above, summarized to T_{AM}:

$$T_{AM} = A \bullet M^* \bullet ADP + A \bullet M \bullet ADP + A \bullet M \qquad (3.12)$$

The resulting normalized tension T_n is given by

$$T_n = \frac{\alpha T_{AM}}{T_{max}} \tag{3.13}$$

with the sarcomere overlap function of the Peterson, Hunter, and Berman model [128]

$$\alpha = \begin{cases} 1 - 0.7333(2 - \lambda) & \lambda \leq 2 \\ 1 & 2 < \lambda \leq 2.2 \\ 1 - 0.7333(\lambda - 2.2) & 2.2 < \lambda \end{cases} \tag{3.14}$$

and the maximum tension T_{max} during resting stretch.

Further details of this model are given in [87, 138, 143, 139, 144].

3.4.4 Elasto-mechanical Models

Elasto-mechanical models are used to model tissue or muscle behavior under deformation, stress and strain. During this work a hybrid deformation model was developed, based on a spring-mass system to model contraction of myocardium and deformation of left ventricular models. Further details on deformable models, elasto-mechanical models and the developed hybrid deformation model are given in chapter 4 and 5.

The data acquired from experimental studies (section 3.3.2.1) were used to create mathematical models describing the relationship between stress and strain. A widely used model is the strain energy density function in conjunction with parameter fitting procedures. Tab. 3.4 shows a selection of models in chronological order.

A survey and summary of models based on strain energy density functions is given in [31].

In this work the model of Guccione et al. [64] is applied (section 5.3.2.1).

3.4.5 Pressure Models

The ventricular contraction in a normal heart cycle follows four phases: isovolumic contraction, isotonic contraction, isometric relaxation, and isotonic relaxation (section 3.2.4). Methods modeling the intraventricular pressure corresponding to contraction phases and opening and closing of valves can be applied to implement pressure characteristics into a mechanical model (section 6.5.2).

The intraventricular pressure during the isometric contraction is closely related to the contraction of the ventricle surrounding an incompressible fluid. Hence, a pressure-volume relation can be measured (fig. 3.7).

The intraventricular pressure during the ventricular ejection of blood into the aorta can be modeled following the proposals of Wang et al. [161].

The pressure during the relaxation phase resembles a decay function, which is modeled in general by an exponential decay.

Year	Author	Tissue	Species
1972	Demiray [145]	papillary muscle	cat
1973/74	Janz, Kubert, Moriarty, Grimm [74, 75]	papillary muscle	rat
1974	Glantz [146]	papillary muscle	cat
1976	Rankin, Arentzen, McHale, Ling, Anderson [69]	ventricular muscle	canine
1983	Needleman, Rabinowitz, Bogen, McMahon [147]	ventricular muscle	canine
1987	Humphrey, Yin [148]	ventricular and papillary muscle	canine
1988	Horowitz, Lanir, Yin, Perl, Sheinman, Strumpf [149, 150]	ventricular muscle	canine
1989	Nevo, Lanir	[151] ventricular muscle	-
1990	Humphrey, Strumpf, Yin [152, 153]	ventricular muscle	canine
1991	Huyghe, van Campen, Arts, Heethaar	divers [154]	divers
1991	Yang, Tabber [155]	papillary muscle	rabbit, frog, turtle
1991	Guccione, McCulloch, Waldman [80, 64]	ventricular muscle	canine, rat
1993	Sacks, Chuong [156]	ventricular muscle	canine
1994	Nevo, Lanir [157]	ventricular muscle	-
1994	Novak, Yin, Humphrey	[81] ventricular muscle	canine
1995	Guccione, Costa, McCulloch [158]	ventricular muscle	canine
1995	Hunter, Nash, Sands [82, 83]	ventricular muscle	canine
1998	May-Newman, McCulloch [159]	ventricular muscle	canine
2000	Okamoto, Moulton, Pasque, Peterson, Li, Guccione [65]	ventricular muscle	canine
2000	Usyk, Mazhari, McCulloch [160]	left ventricle	canine

Table 3.4. Models of mechanical properties of myocardium(from [31]).

3.4.5.1 Windkessel and Wave System of Wang et al.

Wang et al. [161] addressed the problem of the difference in shape between central aortic pressure and flow waveforms. They postulated a time domain representation of the ventricular-arterial coupling as a windkessel and wave system. They measured the aortic pressure P_{A0}, the blood ejected into the aorta Q_{in}, the compliance of the aortal tree C and the effective resistance R of the peripheral systemic circulation of 15 healthy mongrel dogs weighing between 18 and 29 kg. Furthermore, they assumed that the aortal behavior can be expressed as a windkessel, which acts as a hydraulic integrator, where the variation of pressure is directly related to the change in volume and inversely to its compliance. So it was possible to compute the windkessel pressure

P_{Wk}. Lighthill et al. [162] proposed that, when considering wave propagation in a reservoir, the measured pressure must be the sum of the reservoir pressure P_{Wk} and the pressure due to wave motion (excess pressure P_{ex}).

Thus:

$$P_{A0}(t) = P_{Wk}(t) + P_{ex}(t) \tag{3.15}$$

Windkessel pressure P_{Wk}

In the case of Wang et al. [161] the aortic Windkessel pressure P_{Wk} depends on the inflow of ejected blood into the aorta Q_{in}, the outflow into the aortal tree Q_{out} and the compliance C of the aortal tree.

$$\frac{dP_{WK}(t)}{dt} = \frac{Q_{in}(t) - Q_{out}(t)}{C} \tag{3.16}$$

The outflow can be described as a simple resistive relationship

$$Q_{out}(t) = \frac{P_{WK}(t) - P_\infty}{R} \tag{3.17}$$

representing the asymptotic pressure of the diastolic exponential pressure decay P_∞, at which the flow from the arteries to the veins ceases and R, the effective resistance of the peripheral systemic circulation. Substituting eq. 3.17 into eq. 3.16 results in:

$$\frac{dP_{WK}(t)}{dt} + \frac{P_{WK}(t) - P_\infty}{RC} = \frac{Q_{in}(t)}{C} \tag{3.18}$$

with the general solution proposed by Wang et al. of

$$P_{WK}(t) - P_\infty = (P_0 - P_\infty)e^{\frac{-1}{RC}} + e^{\frac{-t}{RC}}\int_{t_0}^{t} \frac{Q_{in}(t')}{C}e^{\frac{t'}{RC}}dt' \tag{3.19}$$

where t_0 and P_0 are the time and pressure at the onset of ejection.

However, a part of eq. 3.19: $(P_0 - P_\infty)e^{\frac{-1}{RC}}$ seems to incorporate a typing error. The units of the exponent of the exponential function do not match. Since the term specifies a constant offset of the Windkessel pressure, eq. 3.19 was modified to:

$$P_{WK}(t) - P_\infty = (P_0 - P_\infty)e^{\frac{-t_0}{RC}} + e^{\frac{-t}{RC}}\int_{t_0}^{t} \frac{Q_{in}(t')}{C}e^{\frac{t'}{RC}}dt' \tag{3.20}$$

and was used further on for modeling the Windkessel pressure.

Pressure due to wave motion P_{ex}

When measuring and applying Lighthills equation (eq. 3.15) Wang et al. found that the excess pressure P_{ex} was directly and quite precisely proportional to the aortic inflow Q_{in}. Therefore, the proximal resistance R_{prox} was embedded, which resembles the characteristic impedance determined

by Westerhof et al. [163].

$$P_{ex}(t) = Q_{in}(t)R_{prox} \tag{3.21}$$

Hence, eq. 3.15 can be written as:

$$P_{A0}(t, Q_{in}(t)) = P_{Wk}(t, Q_{in}(t)) + P_{ex}(Q_{in}(t)) \tag{3.22}$$

Since the pressure of the aorta with opened aortic valves resembles that of the ventricle, eq. 3.22 can be applied during the ejection phase. The only variable is the ejection volume $Q_{in}(t)$, which can be easily obtained during deformation simulation. The constants (P_∞, P_0, R, C) can be acquired prior to simulation by measurement.

3.4.5.2 Pressure of Relaxation Phase

Verdonck et al. [164] describe the passive diastolic pressure-volume relationship by the volume and the material properties of the ventricular wall. An exponential function is used including curve fitting parameters:

$$p = be^{k_c V} \tag{3.23}$$

with p the left ventricular cavity pressure, V the cavity volume, b and k_C curve fitting parameters of Gaasch et al. [165].
Weiss et al. [166] described the left ventricular pressure decay by:

$$p(t) = (p_0 - p_\infty)e^{\frac{-t}{\tau}} + p_\infty \tag{3.24}$$

with p the left ventricular cavity pressure, p_0 pressure at peak negative dp/dt, p_∞ atrial pressure, t the time, and τ the time period needed by the pressure to drop to 37% of its starting value.

4

Mechanical Modeling

Various mechanical models can be found in the literature, describing technical objects and biological systems. In computer graphics and simulation the term deformable model describes the sum of all models related to structural change of virtual objects. In the following sections the mainly applied deformable models are briefly described with a distinction between models based on physical and non-physical principles. In addition, approaches and application of deformable models for tissue and muscle simulations are presented.

4.1 Deformable Models

The application of deformable models has become an indispensable tool in industry, research, and medicine. Models are used for e. g. crash tests of vehicles, to model fabric draping and folding for the textile industry, realistic animation of computer games, modeling tissue and muscle behavior, as well as surgical simulators. The demand of increased realism by users can only partly be met by an increase of computer power. This trend is not only apparent in computer games but also in the medical environment. The need to model sophisticated geometrical shapes and physical objects in a complex environment resulted in various approaches for object modeling.

So called deformable object modeling has its roots in computer drawing applications, where it was used e. g. for fitting of complex curves or to create surfaces and solids. In the field of image analysis deformable models are created with a priory knowledge of the objects shape to fit the model to noisy data. Furthermore, the animation and visualization of facial tissue change due to head surgery can be estimated prior to interventions.

Thus, approaches for modeling deformable objects range from non-physical models to continuum mechanical models based on finite elements or boundary elements techniques.

4.1.1 Non-physical Models

Most deformable models are based upon a physical principle. However, in design, often geometrical principles are applied. The later techniques are computationally efficient, but rely on the skill of the user and have no physical concept.

Splines

In CAD, users required to approximate curves and surfaces with numerical methods. Furthermore, they needed to intuitively modify and refine objects. This resulted in the development of Bezier curves, and many other methods to describe curves with only a small amount of vectors e.g. double quadratic curves, various B-splines, and β-splines. A comprehensive coverage of modeling with splines can be found in the literature [167, 168].

Free-form deformation

The method of free-form deformation provides a more powerful control than editing individual control points. The shape of the object can be altered by deforming the space in which the object resides (fig. 4.1). This method can be applied to many different objects like e. g. point sets, polygons, parametric patches, and implicit surfaces. The geometrical mapping of three dimensional space is described in Barr's early work [169]. For example, consider the map $f : \Re^3 \to \Re^3$ given by:

$$f(\mathbf{p}) = \begin{bmatrix} \cos z_c & -\sin z_c & 0 \\ \sin z_c & \cos z_c & 0 \\ 0 & 0 & 1 \end{bmatrix} \begin{bmatrix} x_c \\ y_c \\ z_c \end{bmatrix} \tag{4.1}$$

with the control point $\mathbf{p}$ and its components x_c, y_c, and z_c twisting the objects about the z-axis. Related maps can be used to model movement or deformation such as rigid motion, tapering, bending. Furthermore, more complex deformations can be obtained by assembling various maps. This technique was extended by Coquillart [170], Hsu et al. [171], MacCracken et al. [172], and many others.

4.1.2 Physical Models

In contrast to non-physical models, where "deformation modeling" is simply based on geometrical priciples, physical models allow for a realistic approach. A physically based system consists of basic physical laws and material properties and mathematical consistency.

Spring-mass models

One widely and effectively applied physically based model is the spring-mass systems. An object is e. g. modeled by mass points interconnected by springs, forming a lattice structure (fig. 4.2).
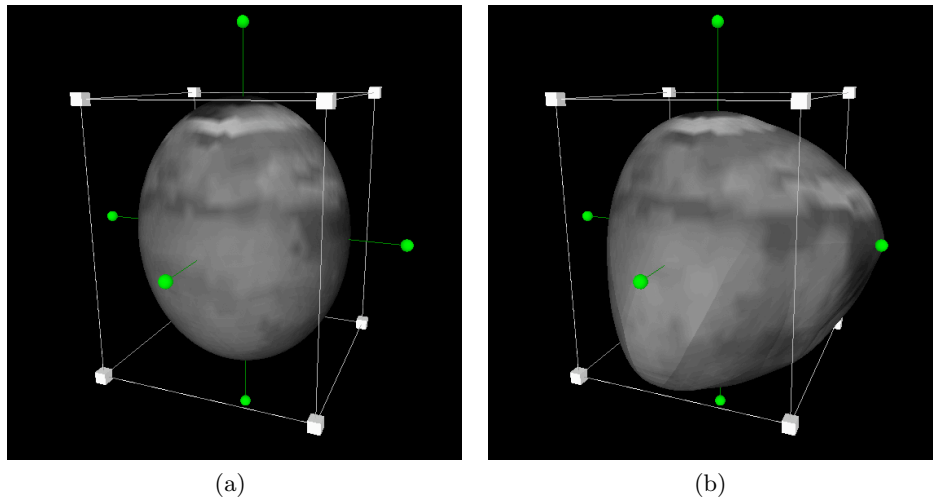
(a)   (b)

Figure 4.1. Example of free form deformation in virtual space. Manipulators can be used to achieve an overall deformation. The figures show an undeformed sphere (a) and the deformed object after manipulation (b).
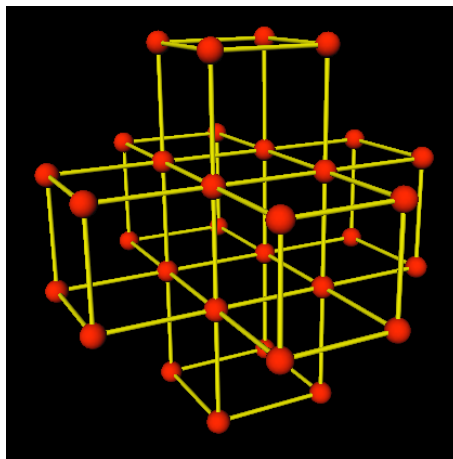

Figure 4.2. Spring mass system in a three dimensional environment. The red spheres indicate masses and the yellow cylinders the connective springs.

The spring properties can be chosen to be linear (Hookean) as e.g. a steel spring, or nonlinear as a simple model for soft tissue and its inelastic behavior. Each mass in the system follows Newton's Law of motion:

$$m_i \ddot{x}_i = -c_i \dot{x}_i + \sum k_{ij} + f_i \tag{4.2}$$

with m_i the mass of point i, $\ddot{x}_i$ its acceleration, c a damping factor, $\dot{x}_i$ its absolute velocity, k_{ij} the in general nonlinear force acting on mass i from linear springs between masses i and j, and f_i the sum of external forces.

The deformation of the whole system can be implicitly described by assembling the motion of each mass into a matrix equation in linear or linearized form:

$$\mathbf{M\ddot{x}} + \mathbf{C\dot{x}} + \mathbf{Kx} = \mathbf{f} \tag{4.3}$$

with $\mathbf{M}$ the mass, $\mathbf{C}$ the damping, $\mathbf{K}$ the stiffness matrix, and $\mathbf{f}$ the sum of forces - in the linear case - acting on the system.

In contrast to the implicit scheme an explicit scheme can be used e. g. explicit Euler or central difference method. In these methods a summation of all forces per mass is performed. The resulting acceleration as well as velocity is computed, and the mass displaced accordingly. The explicit methods are used for the numerical solution in this work (chapter 5.5).

The dynamics of spring-mass systems is based on simple physical laws that are well understood and easily constructed, compared to continuum mechanical methods. Interactive and real time simulations are possible on recent computer hardware in combination with an explicit time integration. The model is suitable for parallel computation, as no matrix triangulation is involved. A spring-mass system model is widely used in medical applications.

The drawbacks of spring-mass systems are the approximation caused by the discretization of a continuous body into mass points. The spring properties and stiffnesses have to be derived from measurement data, which are not always easy to acquire. Furthermore, some constraints are not naturally expressed in the model as e.g. incompressibility of volumetric objects as well as anisotropy needed for muscle modeling. In theses cases additional springs need to be applied, which increase data storage and computational cost.

Continuum models and finite element methods

The spring-mass system approximates a deformable object by a discrete object model usually reducing the real physical connections by a simple model. A more consistent physical description is achieved by treating a deformable body as a continuum. The continuum describes a solid body with mass and energy distributions. A continuum model considers the equilibrium of a body with external and internal forces acting on it. The deformation of the object is a function of the acting forces and the material properties. The object reaches equilibrium when its energy reaches the minimum. The total energy Π can be described by:

$$\Pi = \Omega - W \tag{4.4}$$

with Ω the total strain energy, stored as material deformation and W the work done by external loads. External loads can be distinguished into point loads, body loads such as gravitational loading,

and surface loading such as pressure. Both Ω and W are functions of the material deformation. This leads in general to nonlinear differential equilibrium equations for the continuum, which can be solved for e.g. material displacements [31, 173].

A closed-form analytical solution cannot always be found in particular for general bodies and boundary conditions, therefore numerical methods are used to approximate the deformation behavior. A spring-mass system approximates the object as a finite lattice structure with simplified node-to-node connectivities and equilibrium is computed at the node points. Finite Element Methods (FEM) divide the object into sets of elements and approximate the behavior with functions defined for each element. Equilibrium is found via a weak term or a variational principle e.g. via minimization of the total energy or via weighted residuals or principles of virtual displacements. For the global solution constraints at element borders and node points are needed to allow for continuity between elements and to represent the real geometrical boundary conditions. The element solution is therefore represented by a finite sum of element-specific interpolations, or shape functions. In case of a scalar function $\Phi(x, y, z)$, the value of Φ at the point (x, y, z) is approximated by:

$$\Phi(x, y, z) \approx \sum_i h_i(x, y, z)\Phi_i \tag{4.5}$$

with h_i the interpolation functions for the element containing (x, y, z) and Φ_i the values of $\Phi(x, y, z)$ at the element's nodal points.

Finite elements resemble a more complete physical approach, compared to spring-mass systems. Applied forces are typically interpolated from node-wise specified vectorial forces, which results in numerically integrating forces over the volume and surfaces at each time step and iteration. Mass, stiffness matrices (for implicit schemes) and internal forces have to be computed by numerical integration over the elements, which involves a significant amount of numerical computation. For nonlinear problems, the stiffness matrix and the internal forces have to be re-evaluated in the nonlinear case in each iteration and in each time step. In case of tissue or muscle modeling large deformations of elements are possible.

4.2 Approaches of Modeling Tissue

The geometric representation of an object in a virtual environment may consist of surfaces or volumes. Depending on the application the representation is chosen either for computational efficiency or for physical accuracy. The term "surface model" representing tissue is misleading. A "surface model" can be anything between a real 2D model, where connected elements span a surface, to a 3D model with a specific thickness, modeling e.g. a skin, fat, and muscle layer. These 3D models may also contain holes.

In terms of computation, surface models (or shell/membrane models) are more efficient compared to volume models, due to a smaller amount of vertices surrounding the same geometrical space. However, surface models applied for tissue modeling tend to result in physically invalid deformations, because they are restricted to linear problems.

Both, Finite Element models and spring-mass systems require a mesh structure, which is mostly set up by hexahedral or tetrahedral elements. The amount of vertices in a volume model is much larger and therefore the computational requirements increase. However, this representation allows a fully 3D reaction of the model.

The modeling of muscular tissue differs from regular tissue by the fact that an active change of shape is possible. Muscles have the ability to contract by biochemical reactions. Modeling approaches range from using simple action lines [174, 175] to applying rule based methods to an ellipsoid object [176] to spring-mass systems or finite element models by applying force development models for contraction initiation. Regular tissue only reacts to external forces by changing its shape.

In the following sections current approaches to model tissue and muscle tissue with spring-mass systems are discussed. Many variations of the presented techniques exist. Here, only the most common techniques will be described.

4.2.1 Spring-mass System

4.2.1.1 Surface Models

The main application for spring-mass systems in surface modeling is to model the draping of cloth or facial animation on top of rigid scull.

Desbrun et al. [177] applied a spring-mass system to model a silk scarf being moved interactively in a virtual environment. The behavior of the scarf being subject to gravitation and colliding with objects was modeled. They used nonlinear springs in the plane of surface. The method was designed for real-time interaction and visual realism. However, the model cannot be used for more accurate simulations.

Kang et al. [178, 179] presented a fast animation technique for animating soft objects based on spring-mass models. The main concern was realtime animation of draping of cloth.

Zhang et al. [180] approximated facial skin by a spring-mass system with nonlinear springs. Muscle modeling was performed to deform a facial model to expressions such as sadness, anger, and surprise. They applied an adaptive mesh and refinement method to model facial muscle action.

4.2.1.2 Tissue Models

Spring-mass systems applied for tissue modeling are mainly used in craniofacial surgery planning. Prior to bone surgery, the change in facial expression and facial appearance needs to be examined. Keeve et al. [1, 2] applied a spring-mass system as well as a finite element model (FEM) to model a patient's skin on top of the skull acquired by CT. The pre-operational planing was done on

a virtual system. The spring-mass system consisted of two tissue and one bone layer. The FEM only consisted of a rigid bone layer and one tissue layer. Simulation results compared to the post-operational results showed that both models were suitable for the application. However, the spring-mass system yielded the results faster compared to the FEM.

Spring parameterization of tissue models is a key factor in realistic modeling. Mazzella [181] proposed a method to estimate spring parameters from scanning the outer surface of an object in two different positions. The scan of the resting position is used to create a virtual model at rest. A second scan is carried out under a known acting force. The force is applied to the model and an auto extraction algorithm assigns the elastic constants to the model. However, this model was only applied on homogeneous tissue.

4.2.1.3 Muscle Models

Modeling muscle with action lines is based on a surface model describing the anatomy of a muscle. The action line indicates the direction of muscle contraction. Nedel et al. [174] applied this model to animate human motion. Therefore, a brachialis muscle attached to the humerus and the ulna allowed the flexion of a virtual skeleton forearm model. The muscle was modeled as spring-mass system changing shape according to the shortening along the action line.

Chen et al. [182] and Zhu et al. [183] applied a 3D spring-mass system as well as a 3D FEM to model an anconeus muscle. As template an anconeus muscle from the Visible Man dataset was applied (Visible Human Project [24]). Mechanical and physiological parameters were taken from Stern et al. [184].

Bourguignon et al. [3] proposed an anisotropic 3D spring-mass system modeling muscle tissue, which will be discussed in detail in chapter 5.

Spring-mass systems are commonly applied, when focussing on quick simulation and accepting low quality of the deformation. For more accurate deformation, FEM models based on continuum mechanics are used resulting in more computational effort.

4.2.2 Continuum Mechanics and Finite Element Method

4.2.2.1 Muscle Models

Sachse [31] used a model based on the finite deformations using the strain energy density function of Guccione et al. [64] for passive ventricular myocardium of canine. The analysis of the nonlinear deformation was performed in an incremental total Lagrangian formulation with displacement-based isoparametric finite elements [185].

Hunter et al. [78, 186, 82, 83, 132, 187] established a biventricular model, based on 3D continuum mechanical methods. The theory of finite deformation elasticity is described by continuum mechanical equations. A combination of Galerkin and collocation techniques is used. Further work on this model was performed by McCulloch et al. [188], Costa et al. [189], and Vetter et al. [39].

In both models a realistic deformation depending on the applied boundary conditions and the parameters used was achieved. Sachse provided a deformation data set of a biventricular model including computation of V_m , Ca^{2+} , and $force$.

5

Hybrid Deformation Model

In this chapter, the basics of the hybrid deformation model developed in this work are presented. In addition the merging of continuum mechanical methods and the spring-mass system is explained and occurring numerical problems are discussed.

5.1 Overview

The deformation of myocardium takes a vital part in the pumping function of the heart muscle. Knowledge of myocardium anatomy and physiology makes it possible to create models of cardiac behavior. These models can be used for surgery planning, educational and research purposes. Simulations can be performed, which are beyond the capability of physical experiments. Volume models of myocardium are necessary for realistic simulations.

The target of this work was to create an elastomechanical deformation model based on a spring-mass system to describe myocardial behavior during various states of contraction. The hybrid model created, is based on a spring-mass system enhanced by continuum mechanical methods. In the following sections the basis of the model, the enhancements, and the methods applied are described.

5.2 Spring-mass Model

The basis of the presented spring-mass system was derived from Bourguignon et al. [3]. They presented a deformable model to control isotropy and anisotropy of elastic material.

The modeling of a geometric object with a spring-mass system as with finite element method (FEM) implies a discretization of space. Tetrahedral or hexahedral elements are mainly used in FEM technology to form discrete meshes. The tetrahedral mesh has the advantage to model more easily the geometric object compared to hexahedral elements, when straight lines are used to connect vertices. However, medical data acquired in a clinical environment are stored as voxel data
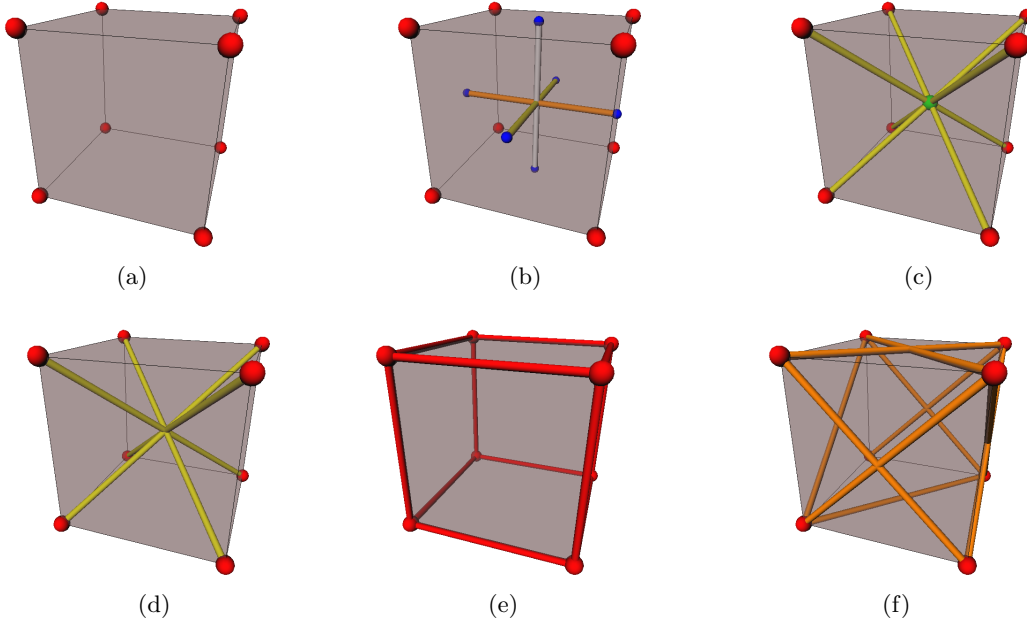
Figure 5.1. A cubic voxel of biological tissue is modeled by masses and springs. Masses are denoted as spheres at the vertices of a voxel (a). Anisotropy is modeled by three springs (displayed as cylinders), which are centered in the voxel. The spring end points (blue spheres) are fixed to the voxel surface planes. They describe fiber (white), sheet (yellow) and sheet normal (yellow) orientation (b). Isovolumetry can be modeled by 8 springs connecting vertices with the barycenter (c), or four cross-element springs running diagonally through the volume connecting opposite vertices (d). The classical structural springs are displayed in (e) and the classical surface springs in (f).

and hence a conversion into hexahedral elements is rather straightforward. Therefore, in this work a hexahedral element based representation was chosen.

A given geometry was represented as a 3D mesh of cubic voxel, which were modeled by masses and springs. For simplicity the conversion of one cubic voxel to a spring-mass system structure is described below (fig. 5.1).

5.2.1 Masses

The mass of a single voxel is evenly split and assigned to the voxel vertices (fig. 5.1(a)). However, adjacent voxel also provide a mass contribution to the vertices. The total mass of a voxel vertex can be computed by applying the Voronoi cell. For a discrete set of vertices S in Euclidean space, the Voronoi cell is defined by all voxel being closer to one vertex than to another, including those being at an equal distance of two vertices. Therefore, the volume of the Voronoi cell V_i for a single vertex i is

$$V_i = \frac{V_{voxel}}{8} N_{voxel,i} \qquad (5.1)$$
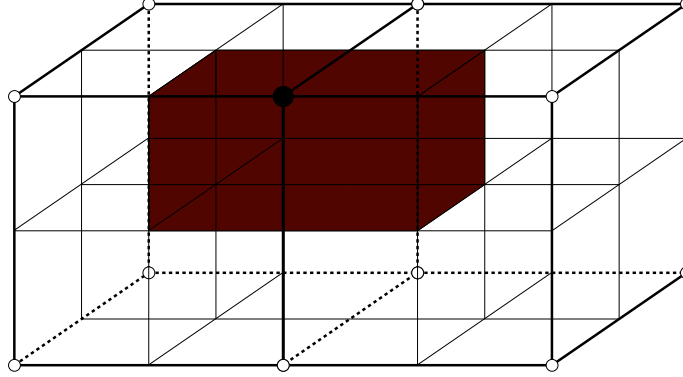
Figure 5.2. Figure displays the vertex i (black circle) and its Voronoi cell (red), which consists of two hexahedral elements (fig. from [190])

with V_{voxel} the volume of a voxel and $N_{voxel,i}$ the number of voxel with vertex i.

An example of a two voxel Voronoi cell is described in fig. 5.2.

In a homogeneous voxel, its density ρ and its volume V_i define the voxel mass m_i to:

$$m_i = \rho V_i \tag{5.2}$$

If V_i is given by eq. 5.1, m_i can be computed using:

$$m_i = \rho \frac{V_{voxel}}{8} N_{voxel,i} \tag{5.3}$$

If the geometry consists of regional differing densities and therefore differing voxel densities, the mass m_i of vertex i can be described by

$$m_i = \frac{V_{voxel}}{8} \sum_{k=0}^{N-1} \rho_k \tag{5.4}$$

with ρ_k the density of voxel k and $k = 0, .., N - 1$. This method is the so-called mass lumping method in FEM literature for regular meshes and eight node elements.

5.2.2 Spring Types

The hybrid deformation model consists of two basic spring types. One type is the active spring, where forces are applied along the spring orientation and the other type is a passive spring reacting solemnly to length change.

The active springs are the anisotropy springs (section 5.2.4) and explicitly the spring along the fiber of the myocardium. The contraction initiation is started by applying a force at the spring ends inward (fig. 5.3). This force is relayed as described in (section 5.2.4) to the corresponding masses.

In case of active volume springs (section 5.2.6.3) all anisotropy springs become active springs, as the volume conservation force is applied.

All other applied springs are categorized passive springs, which react to length change depending on their property. Many properties were implemented e. g. linear, quadratic, uniaxial exponentials (section 5.3.2.2) but mainly linear springs were applied during simulation.

5.2.3 Linear Spring Damper

A spring connected between two vertices $\mathbf{x_1}$ and $\mathbf{x_2}$ exerts the following force on each vertex:

$$\mathbf{f_{1l}} = -\left(k\left(\|\mathbf{l_{21}}\| - r\right) + c\frac{\dot{\mathbf{l}}_{\mathbf{21}} \cdot \mathbf{l_{21}}}{\|\mathbf{l_{21}}\|}\right)\frac{\mathbf{l_{21}}}{\|\mathbf{l_{21}}\|}, \mathbf{f_{2l}} = -\mathbf{f_{1l}}, \tag{5.5}$$

with $\mathbf{l_{21}} = \mathbf{x_1} - \mathbf{x_2}$, r the initial length of the spring, $\dot{\mathbf{l}}_{\mathbf{21}} = \mathbf{v_1} - \mathbf{v_2}$ the relative velocity of end point vertices, k the stiffness, and c the damping constant of the damper (fig. 5.4(a)).

These types of springs were applied to construct a discrete spring-mass-damper system (furthermore addressed as spring-mass system) of a given geometry. Furthermore, these classical springs retain the continuity of a voxel (fig. 5.1(e) and 5.1(f)) and constitute with the masses the discretization of the geometry of the object to model.

5.2.4 Anisotropic Springs

The integration of anisotropy is not built into a spring-mass system by default. Therefore, the approach of Bourguignon et al. [3] was followed.
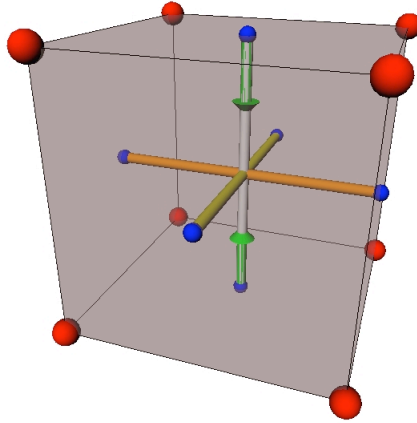
Figure 5.3. Contraction force (green) implementation into one cubic element represented by masses and springs.
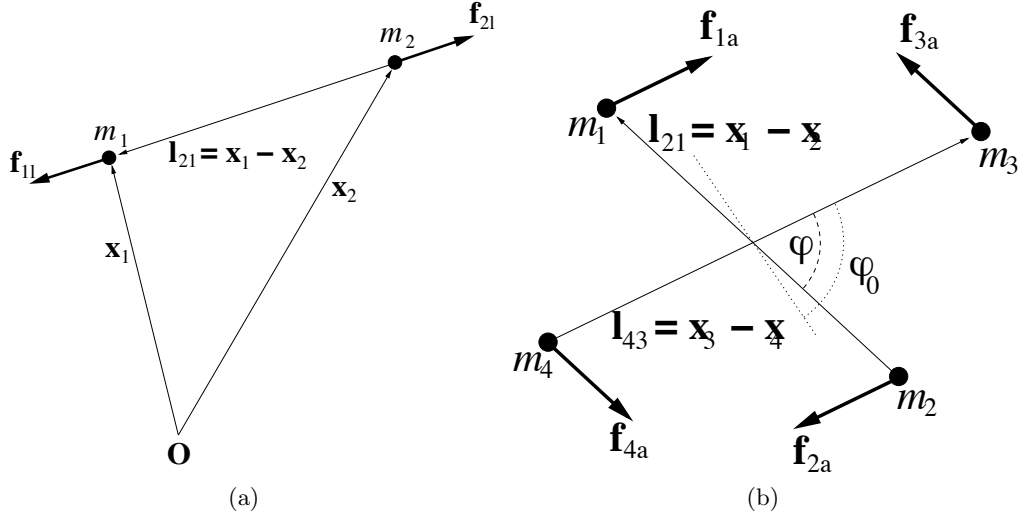
Figure 5.4. Force orientation of compressed spring damper with masses m_i, offset vectors x_i from the origin O, and the acting forces f_i (a). Illustration of force integration for angular springs with an angle changed from φ_0 to φ between $\mathbf{l_{21}}$ and $\mathbf{l_{43}}$ (b). The offset vectors are not displayed (fig. from [190]).
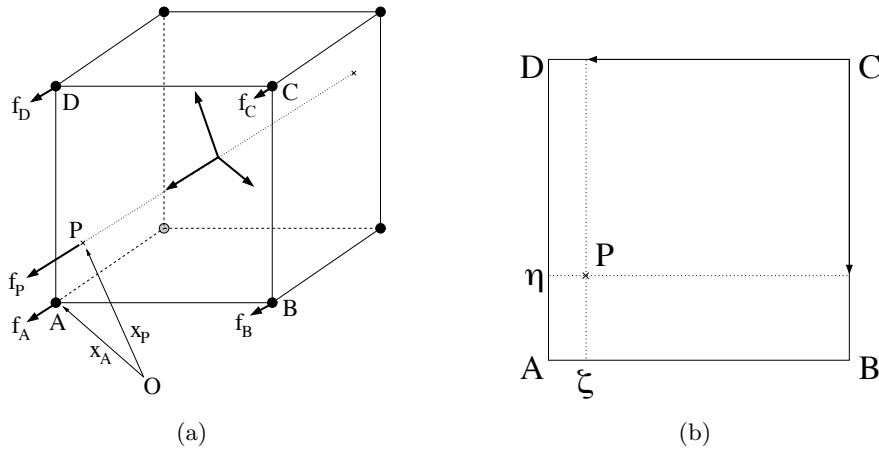
Figure 5.5. Cubic myocardium element with 8 vertices. The directions of fiber, sheet and sheet normal are centered inside the voxel and intersect the voxel planes (a). The position of one exemplary intersection P is described by the bilinear form factors ζ and η (b).

An additional set of three springs denote fiber, sheet and sheet normal direction (fig. 5.1(b)). The fiber springs are oriented parallel to the anatomical fiber direction. Their intersection points with the voxel planes $\mathbf{x_P}$ (Fig. 5.5) are computed with the bilinear form function:

$$\mathbf{x_P} = \zeta\eta\,\mathbf{x_A} + (1 - \zeta)\,\eta\,\mathbf{x_B} + (1 - \zeta)\,(1 - \eta)\,\mathbf{x_C} + \zeta\,(1 - \eta)\,\mathbf{x_D}$$

Here, $\mathbf{x_A}$, $\mathbf{x_B}$, $\mathbf{x_C}$ and $\mathbf{x_D}$ denote the vectors describing the position of the vertices of a given voxel and ζ and η the form factors. The force $\mathbf{f_P}$ acting on an intersection point consists of the contraction initiation force implemented by the system and the reaction of the fiber spring to elongation. This force is distributed to the neighboring masses by the following equations:

$$\mathbf{f_A} = \zeta \eta \, \mathbf{f_P} \tag{5.6}$$

$$\mathbf{f_B} = (1 - \zeta) \, \eta \, \mathbf{f_P} \tag{5.7}$$

$$\mathbf{f_C} = (1 - \zeta) \, (1 - \eta) \, \mathbf{f_P} \tag{5.8}$$

$$\mathbf{f_D} = \zeta \, (1 - \eta) \, \mathbf{f_P}. \tag{5.9}$$

The forces $\mathbf{f_A}$, $\mathbf{f_B}$, $\mathbf{f_C}$ and $\mathbf{f_D}$ are forces distributed to the vertices A, B, C, and D, respectively (fig. 5.5).

The anisotropic spring behavior can be modeled by linear springs (section 5.2.3) as well as by uniaxial stress strain relations as described by Hunter et al. (section 5.3.2.2).

5.2.5 Angular Springs

The springs for fiber, sheet and sheet normal are directed in three perpendicular directions. The angles between these springs must be kept constant during simulation, to prevent misalignment. Therefore, angular springs are implemented [3].

Two springs attached to the vertices $(\mathbf{x_1}, \mathbf{x_2})$ and $(\mathbf{x_3}, \mathbf{x_4})$ representing fiber and sheet orientation form an angle of $90°$ (fig. 5.4(b)). The pair of forces needed to counteract a small relative rotation of an angle φ_0 can be modeled by:

$$\mathbf{f_{1a}} = -k_s \left[\frac{\mathbf{l_{21}} \cdot \mathbf{l_{43}}}{\|\mathbf{l_{21}}\| \, \|\mathbf{l_{43}}\|} - \cos(\varphi_0) \right] \frac{\mathbf{l_{43}}}{\|\mathbf{l_{43}}\|}, \qquad \mathbf{f_{2a}} = -\mathbf{f_{1a}},$$

$$\mathbf{f_{3a}} = -k_s \left[\frac{\mathbf{l_{21}} \cdot \mathbf{l_{43}}}{\|\mathbf{l_{21}}\| \, \|\mathbf{l_{43}}\|} - \cos(\varphi_0) \right] \frac{\mathbf{l_{21}}}{\|\mathbf{l_{21}}\|}, \qquad \mathbf{f_{4a}} = -\mathbf{f_{3a}},$$

with vectors $\mathbf{l_{21}} = \mathbf{x_1} - \mathbf{x_2}$, $\mathbf{l_{43}} = \mathbf{x_3} - \mathbf{x_4}$, and k_s the spring stiffness. Angular springs have no parallel damper.

This method can be applied assuming, that only small relative rotations occur. Therefore, the variation of angle can be replaced by the cosine function of the angle. Furthermore, for the integration of the counteracting force, the unit vector of the interacting direction was applied. This is an approximation to the correct direction of the vector normal.

5.2.6 Incompressibility

In classical spring-mass systems, the option of incompressibility of a modeled element is not directly included. Forces are applied along springs, which are mostly located at edges or across the

elements surfaces. Various methods however, have been proposed to model isovolumetry of tissue. All methods described below have been implemented into the developed hybrid deformation model and can be exclusively chosen for mechanical simulations.

5.2.6.1 Barycenter Spring

Maintaining a constant volume can be basically achieved by radial force as proposed by Promayon et al. [191]. Bourguignon et al. [3] adapted a soft volume-preservation constraint of Lee et al. [192]. The barycenter of an element is computed by

$$\mathbf{x_B} = \frac{1}{8} \sum_{i=0}^{7} \mathbf{x_i}, \tag{5.10}$$

with $\mathbf{x_B}$ the barycenter position, and $\mathbf{x_i}$ the positions of the eight vertices belonging to the element. Between the barycenter and each vertices linear springs are established (fig. 5.1(c)), exerting the following force on the vertices

$$\mathbf{f_i} = - \left(k_s \left(\|\mathbf{l_i}\| - r \right) + k_d \frac{\dot{\mathbf{l_i}} \cdot \mathbf{l_i}}{\|\mathbf{l_i}\|} \right) \frac{\mathbf{l_i}}{\|\mathbf{l_i}\|}, \tag{5.11}$$

with $\mathbf{l_i} = \mathbf{x_i} - \mathbf{x_B}$, $\dot{\mathbf{l_i}} = \mathbf{v_i} - \mathbf{v_B}$, the springs rest length r, the velocity $\mathbf{v_i}$ of vertex i, the velocity of the barycenter $\mathbf{v_B}$, the stiffness k_s and the damping factor k_d of the spring. This method applies only passive springs without taking the effective volume change into account. Furthermore, the update of barycenter velocity and position has to be computed at each time step.

5.2.6.2 Cross-Element Springs

A simplified model of the barycenter spring model is the cross-element spring model. The conservation of volume is also achieved by passive springs being spanned from opposite vertices across the element volume (fig. 5.1(d)). The calculation of barycenter velocity and position is omitted and a reduction of springs is achieved. The volume conservation does not differ to a great extent from the method above.

5.2.6.3 Active Volume Springs

An active spring model was created in the course of this work [193]. The active spring is modeled using continuum mechanical methods. The volume of the deformed voxel is computed by establishing the deformation gradient tensor $\mathbf{F}$.

$$\mathbf{F} = \frac{\partial \mathbf{x}}{\partial \mathbf{X}}$$

It describes the transformation of a line element $\partial\mathbf{X}$ from the reference $\mathbf{X}(t)$ to a line element $\partial\mathbf{x}$ in the current configuration $\mathbf{x}(t)$ [173][1]. The tensor $\mathbf{F}$ can be set up by knowing the initial and the current displacement of the eight vertices of a voxel. The current volume V and the initial volume V_0 is computed.

$$V = V_0 \det \mathbf{F}, \qquad \Delta V = V - V_0 = V_0 \left(\det \mathbf{F} - 1\right).$$

The change in volume ΔV is scaled with the active spring factor k_a and issued as additional volume preserving forces $\mathbf{f_i}$ to the vertices $\mathbf{x_i}$.

$$\mathbf{f_i} = -k_a \Delta V \frac{\mathbf{l_i}}{\|\mathbf{l_i}\|}, \qquad \frac{\mathbf{l_i}}{\|\mathbf{l_i}\|} = \frac{\mathbf{x_i} - \mathbf{x_B}}{\|\mathbf{x_i} - \mathbf{x_B}\|}$$

The vector $\mathbf{x_B}$ describes the position of the barycenter. A positive change in volume results in a scaled volume force $\mathbf{f_i}$ towards the barycenter. A negative change in volume results in forces radial from the barycenter. The scaling factor k_a was estimated by numerical experiments.

5.3 Continuum Mechanical Enhancements

Many mathematical models of myocardial tissue use continuum mechanical methods to describe mechanical properties. Three procedures were implemented in this work. One to model the incompressibility or isovolumetry of hyperelastic material, and two to model passive mechanical properties of myocardial tissue.

5.3.1 Mooney-Rivlin Incompressibility

The methods of incompressibility or isovolumetry described above yield an acceptable volume preservation ratio for small and thin models. However, modeling ventricular tissue requires a more accurate conservation of volume. Ventricular tissue is described to be a hyperelastic material, which refers to the property, that finite elastic deformations are completely recoverable [194]. These materials are mainly described by continuum mechanical methods applying an energy density function $\mathbf{W}$.

The isovolumetric springs can be replaced by isovolumetric constraints adopted from a Mooney-Rivlin model. Therefore, only the isovolumetric component of the Mooney-Rivlin strain energy density function $\mathbf{W_M}$ is applied:

$$\mathbf{W_M} = \kappa \left(det\mathbf{F} - \frac{1}{det\mathbf{F}} \right)^2$$

The factor κ was chosen by numerical experiments.

This energy density function $\mathbf{W}$ was used to compute stresses resulting from a change in volume.

---

[1] For an introduction into continuum mechanics see appendix A.

5.3.2 Passive Material Properties

The spring-mass system, applying linear springs, is not capable to model the passive mechanical properties of the myocardium to a great extent. Models based on continuum mechanical foundations were derived from experimental studies. Most models are based on a strain energy density function to model the behavior of myocardial tissue (section 3.4.4).

In this work, the models of Guccione et al. [80] and Hunter et al. [83] were implemented.

5.3.2.1 Energy Density Function of Guccione et al.

An exponential strain energy density function $\mathbf{W}$ describes the passive mechanical properties by

$$\mathbf{W} = \frac{C}{2}\left(e^Q - 1\right)$$

with a constant C chosen as described by Sachse [195] and the function Q, depending on the Green-Lagrange strain tensor $\mathbf{E}$. This strain energy function is based upon the constitutive laws for arteries assuming orthotropic material properties [196]. The function Q is the representation of the three-dimensional transverse isotropy with respect to fiber orientation dependent on the Green-Lagrange strain tensor $\mathbf{E}$ and can be described by

$$\begin{aligned}
Q = {} & 2b_1\left(\mathbf{E}_{RR} + \mathbf{E}_{FF} + \mathbf{E}_{CC}\right) \\
& + b_2\mathbf{E}_{\mathbf{FF}}^{\mathbf{2}} + b_3\left(\mathbf{E}_{CC}^2 + \mathbf{E}_{RR}^2 + \mathbf{E}_{CR}^2 + \mathbf{E}_{RC}^2\right) \\
& + b_4\left(\mathbf{E}_{RF}^2 + \mathbf{E}_{FR}^2 + \mathbf{E}_{FC}^2 + \mathbf{E}_{CF}^2\right)
\end{aligned}$$

with constants b_i chosen as described by Sachse [195]. The indices F, C and R describe the components of the Green-Lagrange strain tensor $\mathbf{E}$ and indicate fiber axis, cross-fiber in plane axis and radial axis, respectively.

5.3.2.2 Energy Density Function of Hunter et al.

Hunter et al. [83] proposed the following energy density function:

$$\begin{aligned}
\mathbf{W} = {} & k_1\frac{\mathbf{E}_{11}^2}{(a_1-|\mathbf{E}_{11}|)^{\beta_1}} + k_2\frac{\mathbf{E}_{22}^2}{(a_2-|\mathbf{E}_{22}|)^{\beta_2}} + k_3\frac{\mathbf{E}_{33}^2}{(a_3-|\mathbf{E}_{33}|)^{\beta_3}} \\
& + k_4\frac{\mathbf{E}_{12}^2}{(a_4-|\mathbf{E}_{12}|)^{\beta_4}} + k_5\frac{\mathbf{E}_{23}^2}{(a_5-|\mathbf{E}_{23}|)^{\beta_5}} + k_6\frac{\mathbf{E}_{31}^2}{(a_6-|\mathbf{E}_{31}|)^{\beta_6}},
\end{aligned} \tag{5.12}$$

to describe the anisotropy and inhomogeneity of the myocardium, with k_i the relative contribution of each strain energy term, a_i the limiting strain for a particular type of deformation, β_i expressing the curvature of the uniaxial stress-strain curves, and $\mathbf{E}_{ij}$ the components of the Green-Lagrange finite strain tensor.

The extraction of only diagonal elements of eq. 5.12 - neglecting all shear terms - results in uniaxial stress strain relationships (fig. 5.6):

$$\mathbf{W} = k_1 \frac{\mathbf{E}_{11}^2}{(a_1 - |\mathbf{E}_{11}|)^{\beta_1}} + k_2 \frac{\mathbf{E}_{22}^2}{(a_2 - |\mathbf{E}_{22}|)^{\beta_2}} + k_3 \frac{\mathbf{E}_{33}^2}{(a_3 - |\mathbf{E}_{33}|)^{\beta_3}} \qquad (5.13)$$
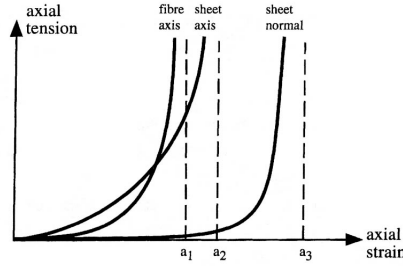
Figure 5.6. Uniaxial stress strain relationship of Hunter et al. [83]. This figure shows the stress strain relationship in fiber, sheet, and sheet normal direction. The limiting strains for axial deformation are marked by a_i.

5.4 Application of Continuum Mechanics in a Spring-mass System

Various models describe mechanical properties of the heart by energy density functions $\mathbf{W}$, depending on the Green-Lagrange finite strain tensor $\mathbf{E}$.

The following mathematical method describes the application of the energy density function $\mathbf{W}$ in the hybrid deformation model.

The hybrid deformation model results in a step wise deformation of cubic elements. The displacement of the cubic vertices is used to compute the deformation gradient tensor $\mathbf{F}$ (appendix A, eq. A.10). The Green-Lagrange finite strain tensor $\mathbf{E}$ can be computed by:

$$\mathbf{E} = \frac{1}{2} \left(\mathbf{F}^T \mathbf{F} - \mathbf{I} \right) \qquad (5.14)$$

with $\mathbf{F}^T$ the transpose of the deformation gradient tensor $\mathbf{F}$ and $\mathbf{I}$ the identity tensor.

The differentiation of the energy density function $\mathbf{W}$ by $\mathbf{E}$

$$\mathbf{S} = \frac{\partial \mathbf{W}}{\partial \mathbf{E}} \qquad (5.15)$$

results in the second Piola-Kirchoff stress tensor $\mathbf{S}$.

The second Piola-Kirchoff stress tensor $\mathbf{S}$ can also be derived from the first Piola-Kirchoff stress tensor $\mathbf{T}$ and the inverse $\mathbf{F}^T$ of the deformation gradient tensor $\mathbf{F}$.

$$\mathbf{S} = \mathbf{T}(\mathbf{F}^{-1})^T \qquad (5.16)$$

The tensor $\mathbf{T}$ can be described by :

$$\mathbf{T} = J\mathbf{F}^{-1}\boldsymbol{\sigma} \tag{5.17}$$

with J the Jacobian of $\mathbf{F}$ and $\boldsymbol{\sigma}$ the Cauchy stress tensor. Substituting eq. 5.17 in eq. 5.16 results in

$$\mathbf{S} = J\mathbf{F}^{-1}\boldsymbol{\sigma}(\mathbf{F}^{-1})^T \tag{5.18}$$

For the extraction of $\boldsymbol{\sigma}$ from eq. 5.18 the following steps need to be applied:

$$\mathbf{S} = J\mathbf{F}^{-1}\boldsymbol{\sigma}(\mathbf{F}^{-1})^T \tag{5.19}$$

$$\frac{1}{J}\mathbf{S} = \mathbf{F}^{-1}\boldsymbol{\sigma}(\mathbf{F}^{-1})^T \tag{5.20}$$

with

$$\mathbf{F}\mathbf{F}^{-1} = \mathbf{I} \tag{5.21}$$

follows

$$\mathbf{F}\frac{1}{J}\mathbf{S} = \mathbf{F}\mathbf{F}^{-1}\boldsymbol{\sigma}(\mathbf{F}^{-1})^T \tag{5.22}$$

$$\mathbf{F}\frac{1}{J}\mathbf{S} = \boldsymbol{\sigma}(\mathbf{F}^{-1})^T \tag{5.23}$$

and multiplying eq. 5.23 by $\mathbf{F}^T$ results in

$$\mathbf{F}\frac{1}{J}\mathbf{S}\mathbf{F}^T = \boldsymbol{\sigma}(\mathbf{F}^{-1})^T\mathbf{F}^T \tag{5.24}$$

Furthermore, applying

$$(\mathbf{F}^{-1})^T(\mathbf{F})^T = \mathbf{I} \tag{5.25}$$

to eq. 5.24 results in

$$\mathbf{F}\frac{1}{J}\mathbf{S}\mathbf{F}^T = \boldsymbol{\sigma} \tag{5.26}$$

Rearranging eq. 5.26 to:

$$\boldsymbol{\sigma} = \frac{1}{J}\mathbf{F}\mathbf{S}\mathbf{F}^T \tag{5.27}$$

results in the Cauchy stress tensor $\boldsymbol{\sigma}$.

The deformation gradient tensor $\mathbf{F}$ can be understood as material gradient of deformation. Since any deformation can always be reversed, the Jacobian determinant J must be $J \neq 0$. Therefore, the inverse gradient tensor $\mathbf{F}^{-1}$ exists (eq. 5.21)(see section A.5).

The transpose $\mathbf{F}^T$ of the deformation gradient tensor is constructed by interchanging rows and columns of the deformation gradient tensor $\mathbf{F}$ following the condition eq. 5.25 (appendix A.5).

The components of the Cauchy stress tensor $\boldsymbol{\sigma}_{ij}$ can be used to compile a stress vector for each plane (fig. 5.7) e. g. :

$$\boldsymbol{\sigma}_{W1} = \begin{pmatrix} \sigma_{11} \\ \sigma_{12} \\ \sigma_{13} \end{pmatrix}, \boldsymbol{\sigma}_{W2} = \begin{pmatrix} \sigma_{21} \\ \sigma_{22} \\ \sigma_{23} \end{pmatrix}, \boldsymbol{\sigma}_{W3} = \begin{pmatrix} \sigma_{31} \\ \sigma_{32} \\ \sigma_{33} \end{pmatrix} \tag{5.28}$$

Stresses are defined as a force $\mathbf{f}$ divided by a surface area A:

$$\boldsymbol{\sigma}_{Wi} = \frac{\mathbf{f}_i}{A} \tag{5.29}$$

Thus, the forces can be described by

$$\mathbf{f}_i = A\boldsymbol{\sigma}_{Wi} \tag{5.30}$$
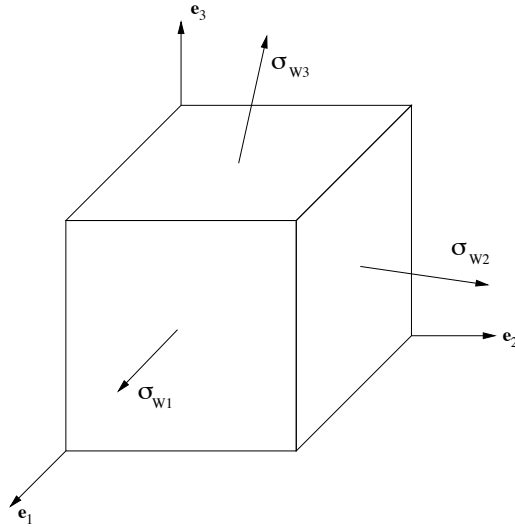
Figure 5.7. Schematic of stress vectors on voxel surfaces. Vectors indicate the acting stresses upon the voxel surface derived from the Cauchy stress tensor.

Thus, a force vector for each voxel plane derived from the energy density function **W** can be obtained. This force vector can be applied to the spring-mass system to model stresses depending on the material deformation.

5.5 Numerical Solution

Various ways of handling deformable models are presented in the literature. The numerical procedures for spring-mass systems can be categorized into two main branches. One is the setting up of mass, damping and stiffness matrices (section 4.1.2) and applying a solver for differential equations the so-called implicit methods. The other are explicit methods e.g. Euler forward or difference integration method where all occurring forces are collected per mass, the acceleration as well as the velocity computed, and the masses displaced.

In this work an explicit Euler integration scheme as well as an explicit difference method was applied, which is explained in the following sections.

5.5.1 Internal Forces

The anisotropic springs of the hybrid deformation model are loaded with a set of forces describing the force generated by myocytes (fig. 5.3). This force distribution resembles the connective element between tension and elasto-mechanical modeling (section 3.4.3). Even though this force is fed from external sources, it is considered as internal force generated by the active spring representing the behavior of myocardial cells.

The deformation gradient tensor is computed on the given displacements of the voxel and the continuum mechanical methods for passive tissue are evaluated (section 5.3).

The resulting stress is converted in a surface force and applied at the intersection points of fiber, sheet, and sheet normal springs with the surfaces (section 5.4) (fig. 5.8).

The force is distributed to the corresponding masses (section 5.2.4).

5.5.2 External Forces

In contrast to internal forces, which are generated by the active properties of the muscle, external forces can be loaded upon the system, modeling a variety of external manipulations of the system. Manipulations can be e.g. intraventricular pressure, boundary conditions, and instrument interaction. Since the system relies on forces for manipulation, this section is called external forces. However, manipulations can also be realized by changing properties or mass of a vertex during the explicit integration scheme. Two examples of applying forces and manipulating mass properties are described below.
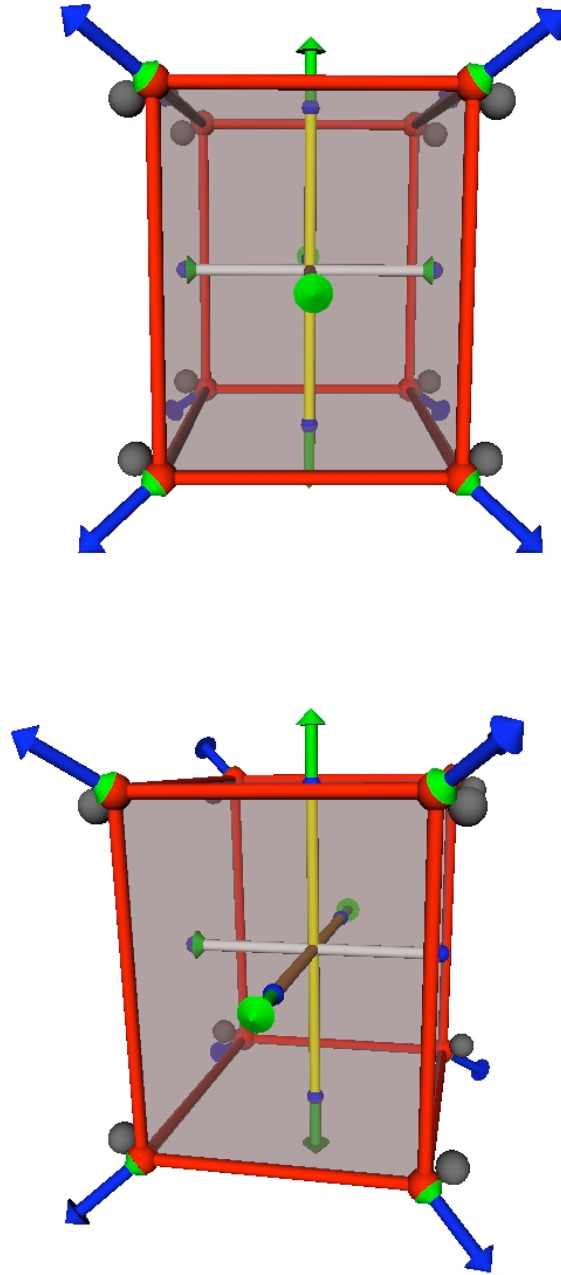
Figure 5.8. Deformed voxel from different perspectives with force vectors (green) at the intersection points and velocity vectors (blue) at vertices. The gray spheres denote masses at rest position.

5.5.2.1 Boundary Conditions

Boundary conditions are position, velocity (Dirichlet boundary condition), and force (Neumann bounary condition) acting on a mass. Furthermore, additional boundary conditions can be established. A simple implementation of a boundary condition is the possibility to fix a mass to its current position completely by applying $\mathbf{x} = const$ and $\mathbf{v} = 0$. Other boundary conditions allow the motion in only one or two specified directions. With such conditions the ventricular apex can be strongly bonded to the pericardial sac (section 6.5).

5.5.2.2 Pressure Forces

A specific boundary condition are forces acting directly on the masses. In the case of pressure, a force vector can be computed for each mass and the modeling of intraventricular pressure can be achieved. Therefore, the masses of the inner wall of a ventricle are loaded by force vectors pointing from the inside to the outside (section 6.5.2.1).

5.5.3 Dynamics Governing Equations

5.5.3.1 Basics

The motion of each vertex with mass m in time is governed by Newton's law of motion:

$$\mathbf{a}(t) = \frac{1}{m} \sum_{k=0}^{N} \mathbf{f}_k(t) \tag{5.31}$$

with k the number of linear and nonlinear forces $\mathbf{f}_k$ acting on the mass, including spring and continuum effects as well as pressure and other boundary conditions. For the solution the continuous motion is discretized in time by so-called time integration schemes.

The proposed scheme is as follows: the internal time step is defined by $\Delta t_i = t_i - t_{i-1}$. Then a constant acceleration during the time step is assumed:

$$\mathbf{a}(t) = \mathbf{a}_{t_i} = \text{const for } t \in (t_{i-1}, t_i]. \tag{5.32}$$

computed by

$$\mathbf{a}_{t_i} = \frac{1}{m} \left(\mathbf{f}_{ci} + \mathbf{f}_{sp} + \mathbf{f}_W + \mathbf{f}_v + \mathbf{f}_p + \mathbf{f}_{bc} \right) \tag{5.33}$$

with m the mass, the internal forces (section 5.5.1) acting on the mass including e. g. contraction initiation forces $\mathbf{f}_{ci}$, spring forces $\mathbf{f}_{sp}$, forces derived from energy density functions $\mathbf{f}_W$, viscosity forces $\mathbf{f}_v$ and the external forces (section 5.5.2) acting on the mass including e. g. pressure forces $\mathbf{f}_p$ and boundary conditions $\mathbf{f}_{bc}$.

The velocity becomes then:

$$\mathbf{v}_{t_i} = \mathbf{v}_{t_{i-1}} + \mathbf{a}_{t_i} \Delta t \tag{5.34}$$

which is constructed of the velocity of the prior time sub-step $\mathbf{v}_{ti-1}$ in addition with the constant acceleration $\mathbf{a}_{t_i}$ and the internal time step Δt. This velocity $\mathbf{v}_{t_i}$ is used to compute the viscosity force for each mass for the next time step.

The new position of a mass $\mathbf{x}_{t_i}$ is computed by

$$\mathbf{x}_{t_i} = \mathbf{x}_{t_{i-1}} + \mathbf{v}_{t_i} \Delta t. \tag{5.35}$$

This results in a new configuration of the nodal positions, nodal velocities, and spring elongations, which must be updated prior to a new time step. This is the so-called classical Euler forward marching scheme.

5.5.3.2 Addressing Numerical Problems

This method of displacement update yields some computational problems. Depending on the time step as well as on generated forces of springs and continuum mechanical methods, an increase of velocity of masses at the end points of springs can occur, which might lead to the exchange of place of masses and therefore to the destruction of the lattice structure. Another reason for divergence can be the delay in propagation of force within a body. Forces applied to a surface are delayed in a spring-mass system, whereas it is instantaneous in the real world. The divergence grows with lattice size and simulation time step Δt. This is widely known for the Euler forward marching scheme.

Miyazaki fusion model

Miyazaki et al. [197] proposed a constraint to take care of nodal velocities creating numerical instabilities. In addition, the propagation of momentum from mass to mass is increased. They applied a ratio of rigidity to each spring, disallowing relative velocity of end masses to grow beyond a threshold.

The difference between rigid and elastic models is, that the force acting on a certain point of the rigid body is instantaneously distributed to all connected elements, whereas in an elastic continuum, the force is propagated with some delay. Therefore, when excessive forces act on a point of the spring-mass model, springs can be extended or contracted, beyond the physical principles (fig. 5.9(a)). In case of springs, rigidity can be modeled by applying the force acting on one end point with the same magnitude to the other end point connected by the spring (fig. 5.9(b)).

The fusion model of Miyazaki et al. is based on the sum of kinetic and potential energy, which may not exceed the maximum possible potential energy generated by the spring:

$$\frac{1}{2}m\left|\mathbf{v}_2 - \mathbf{v}_1\right|^2 + \frac{1}{2}k\left|l - L\right|^2 < \frac{1}{2}kL^2 \tag{5.36}$$

with $\mathbf{v}_2$ and $\mathbf{v}_1$ the velocities of the connected masses, the mass m, the spring constant k, the actual length of the spring l, and the rest length of the spring L. The relative velocity $|\mathbf{v}_2 - \mathbf{v}_1|$ must be below a threshold Θ which depends on the actual spring length. Miyazaki proposes that eq. 5.36 simplifies to:

$$|\mathbf{v}_2 - \mathbf{v}_1| < \Theta \left(= \tfrac{k}{m}\sqrt{l(2L - l)}\right) \tag{5.37}$$

However, the units do not match for eq. 5.37, therefore, in this work the implementation was carried out as follows:

$$|\mathbf{v}_2 - \mathbf{v}_1|^2 < \Theta \quad \left(= \tfrac{k}{m}l(2L - l)\right) \tag{5.38}$$

$$|\mathbf{v}_2 - \mathbf{v}_1| < \Theta \left(= \sqrt{\tfrac{k}{m}l(2L - l)}\right) \tag{5.39}$$

The fusion model applies an elastic model. In addition an external force acting on one of the endpoints is partly propagated directly to the other end, modeling rigidity of the object (fig. 5.9(c)). It is realized by reducing or increasing the velocity of the end points by $\Delta\mathbf{v}$:

$$\Delta\mathbf{v} = \frac{1}{2}\left(|\mathbf{v}_2 - \mathbf{v}_1| - \Theta\right) \tag{5.40}$$

Therefore, the relative velocity of end points can be regulated to an acceptable value.
The implementation includes:

- computation of velocities with eq. 5.34 with completely elastic springs
- velocities are increased or decreased by eq. 5.40 to reduce the relative velocity if eq. 5.39 is not satisfied.

These steps are repeated until the inequality equation (eq. 5.39) is satisfied.
This method increases stability and decreases the sensitivity for large external forces. However, the computational cost increases due to the additional computational complexity.

Jakobsen model

Another method for fast and stable physically based simulation was proposed by Jakobsen [198]. Jakobsen applies for his modeling the Verlet integration for particle systems [199]. The Verlet method for particle systems was adapted to the hybrid deformation system. The method uses a "velocity-less" representation to compute the displacement. The implementation of mass dynamics (section 5.5.3) applies the acceleration computed by Newton's law and stores the current position $\mathbf{x}_i$ and the corresponding velocity $\mathbf{v}_i$ for each mass. In the time-stepping loop, the new velocity $\mathbf{v}_{t_{i+1}}$ (eq. 5.34) and position $\mathbf{x}_{t_{i+1}}$ (eq. 5.35) is computed.
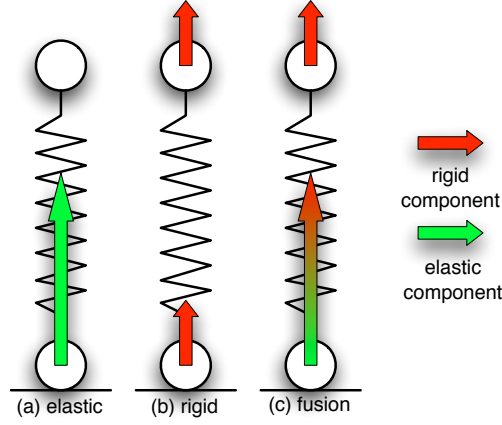
Figure 5.9. Elasticity, rigidity, and fusion model for a spring by Miyazaki et al. [197]. (a) shows the elasticity component acting on only one of the elements. (b) shows the instantaneous propagation of rigid components. (c) shows the fusion model where the elasticity component is split partly in an rigid component, which is propagated to the other element. The adaptation is realized with a rigidity ratio (fig. adapted from [197]).

The "velocity-less" representation depends only on the storage of the previous nodal position $\mathbf{x}_{i-1}$ and current position $\mathbf{x}_i$. The integration step becomes then:

$$\mathbf{x}_{i+1} = 2\mathbf{x}_i - \mathbf{x}_{i-1} + \mathbf{a}_i \Delta t^2 \tag{5.41}$$

$$\mathbf{x}_{i-1} = \mathbf{x}_i \tag{5.42}$$

which is widely used in simulating molecular dynamics. The implicitly given velocity results in a more stable system.

The implicit velocity derives from applying a difference scheme:

$$\mathbf{v}_{i-\frac{1}{2}} = \frac{\mathbf{x}_i - \mathbf{x}_{i-1}}{\Delta t} \tag{5.43}$$

and

$$\mathbf{x}_{i+1} = \mathbf{x}_i + \mathbf{v}_{i-\frac{1}{2}} \Delta t + \mathbf{a}_i \Delta t^2 \tag{5.44}$$

and results in the Verlet integration method eq. 5.41.

Therefore, the real physical velocity is approximated by the distance travelled in the last internal time step, divided by the internal time step. This method is also known as the central difference scheme.

5.5.4 Times of the forward marching scheme

Various times and time intervals are used during simulations (fig. 5.10). The times are:

- *simulation time*: the time during which a simulation is performed. In case of mechanical simulation an interval of $1s$ is assumed during which a complete cardiac cycle (section 3.2.4) is simulated.
- *simulation time step*: the time interval that the *simulation time* is divided into. In case of the hybrid deformation model the *simulation time* is divided into 100 steps of $0.01s$ length.
- *internal time sub-step* Δt: the time step used for a position update of masses in the basic loop (section 5.5.5).
- *computation time*: the total real time a computer needs to perform all calculations needed for the *simulation time* of $1s$.

5.5.5 Basic Loop

The basic loop starts with the collection of internal (section 5.5.1) and external forces (section 5.5.2), then the displacement of masses (section 5.5.3) is updated followed by the update of spring geometries (fig. 5.11).
The basic loop is performed with several sub-steps during a *simulation time step*. The amount of sub-steps per *simulation time step* can be varied by a constant parameter or by the definition of a loop terminating condition e. g. a velocity limit. The constant parameter must be big enough to allow for the system to get close to an energetic minimum. The loop terminating condition can be defined by setting a velocity threshold. The loop is continued until all mass velocities drop below this threshold. Therefore, a small kinetic energy of the system results in the loop termination.
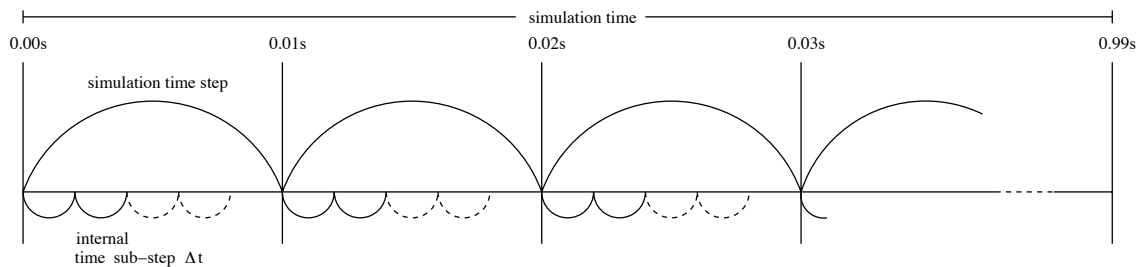
Figure 5.10. Schematic of forward marching times applied during simulation.
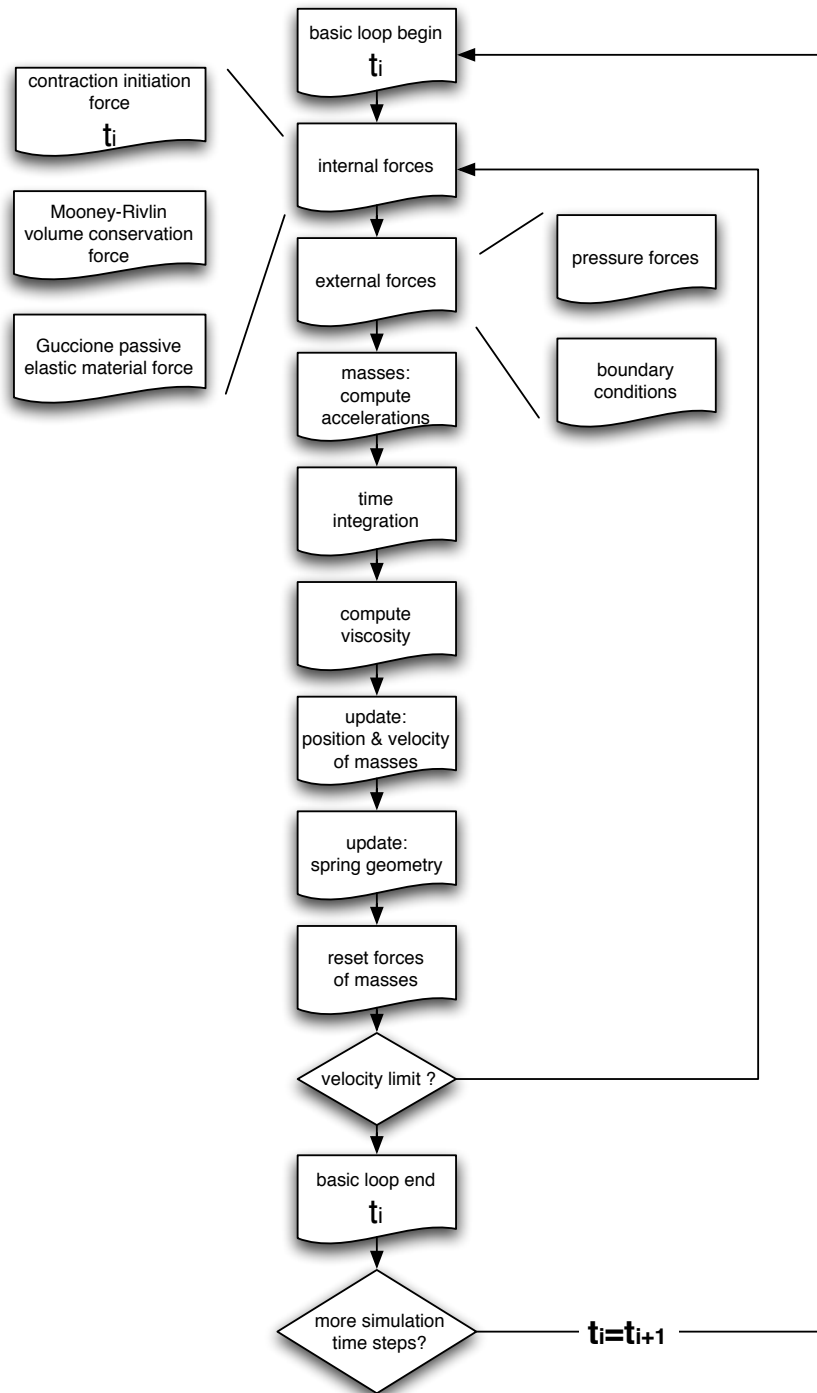
Figure 5.11. Schematic of basic loop of the spring-mass system.

6

Methodology of Simulation

In this section, the methodology of the performed simulations is explained. Two differing analysis of contraction initiation force are described. The setup of the hybrid deformation model with the confocal truncated ellipsoids is presented from the spring-mass system to the implementation of pressure.

The various steps in the simulation of a complete heart cycle can be distinguished into:

- modeling electrophysiology (section 3.4.1),
- excitation propagation (section 3.4.2),
- force development (section 3.4.3),
- pressure characteristics (section 3.4.5), and
- deformation via elastomechanical models (chapter 4).

Therefore, a coupling of models is required. Various models exist known as either microscopic or macroscopic models. Microscopic models allow for direct comparison with measurements on the cellular level, but are computationally more expensive. Macroscopic models approximate reality in a more coarse manner and lead mostly to an averaged result, but with less computational effort. The individual selection of models depends on the desired results.

A contraction is initiated by an action potential stimulating a myocardial cell, which generates tension and deforms along the fiber orientation. In the modeling process this reaction was represented by a force acting along the given fiber orientation. Two methods of calculating force initiation were performed. One is based on coupled microscopic cell models (fig. 6.1). This computationally fairly expensive technique was applied for spring parameter estimation and basic deformation modeling but was later dropped for more complex geometries like truncated ellipsoids. The second method applied a cellular automaton parameterized by microscopic cell models (fig. 6.2). This method is computationally more efficient and yielded sufficient temporal and spatial force distribution for mechanical modeling.

In the following section the methodology of elasto-mechanical modeling in this work is presented. The modeling of contraction initiation force is described as well as the creation of the hybrid de-

formation model based on a geometrical ventricle model (section 6.1). The deformation simulation
started with the creation of the spring-mass system (section 6.3) and the implementation of bound-
ary conditions (section 6.5). In each simulation time step, a new force vector field (section 6.4) was
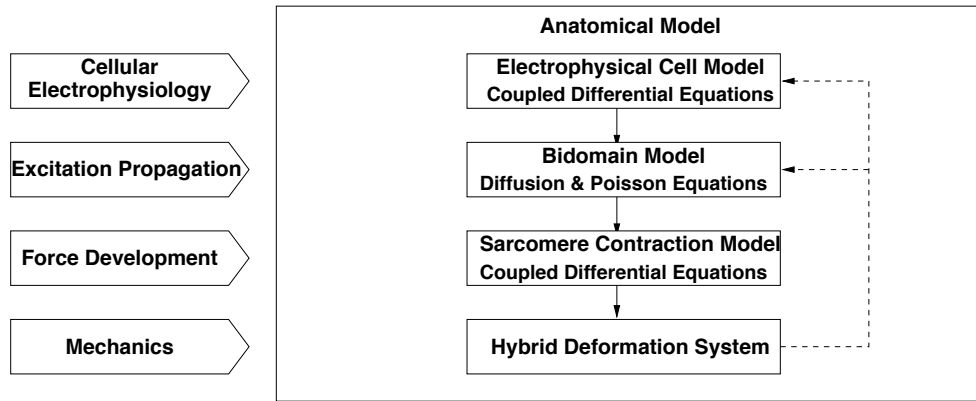
Figure 6.1. The figure shows the interconnection of cellular electrophysiology, excitation propagation,
force development, and mechanics. Solid arrows show the coupling of models, dashed arrows show the
possibility of deformation feedback. In addition, the basic underlying mathematical equations are named.
The bidomain model describes the behavior of excitation propagation for intra- and extracellular compo-
nents [200].
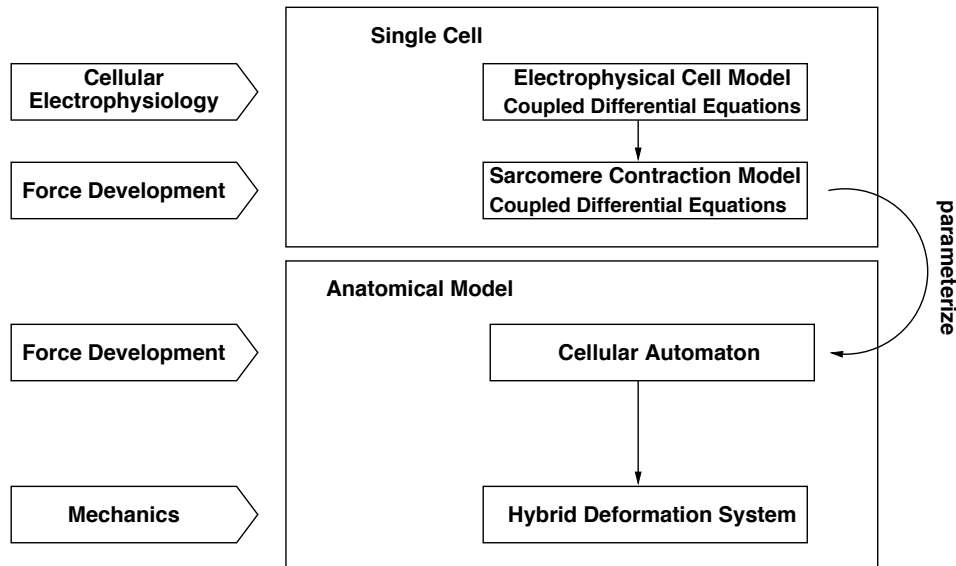
Figure 6.2. The figure shows the coupling of cellular electrophysiology, excitation propagation, and force
development for a myocardial patch. The resulting curves are used to parameterize the cellular automa-
ton (fig. 6.3), which provides the mechanical model with temporal and spatial force vector fields.

introduced into the system and the pressure was added to the inner wall (section 6.5.2). Then, the basic loop (section 5.5.5) was performed deforming the geometry until the velocities of all masses fell below a limit representing an approximation of an energetic minimum. If the velocities did not decline below the limit, parameters were adapted. The deformation was saved and the simulation proceeded with the next simulation time step.

6.1 Contraction Initiation Force

The focus of this work is set on the creation, implementation, and application of a deformation model. Therefore, the coupling of models was used to acquire spring parameters at the creation state of this work (section 7.1), only. The deformation simulations presented in Chapter 7 have been gained by creating the contraction initiating forces as follows:

A microscopic electrophysiological model of Priebe et al. [105] (section 3.4.1.2) was coupled with the hybrid tension model of Glänzel et al. [138, 142] (section 3.4.3) and applied on a single cell model. In a steady state, the models produce three curves: transmembrane potential V_m, intracellular calcium concentration Ca^{2+}, and $force$ (fig. 6.3).

The resulting force curve was used to parameterize a cellular automaton (section 3.4.2.1). A computation of spatial and temporal force distribution throughout the geometrical model was achieved with the cellular automaton. The simulation of one cardiac cycle of $1\ s$ was divided into 100 steps of $10\ ms$, resulting in 100 pre-calculated force vector fields (fig. 6.4).

6.2 Spring-mass Parameters

The spring-mass parameters are stored in an additional file, where stiffness, damping and spring property values can be chosen for each type of spring e. g. anisotropic, angular, barycenter-mass, and cross-element springs. The spring property value allows to switch between different spring behavior e. g. linear, quadratic, or uniaxial exponentials (section 5.3.2.2). Spring parameters for four different tissue classes can be set, allowing the modeling of left and right ventricle as well as left and right atrium. However, mainly left ventricular experiments with and without pathologies were conducted.

Further values define e. g. mass density, continuum mechanical constants and their integration into the computation, forward marching time sub-step, maximum of forward marching time sup-steps, and velocity threshold.

6.3 Creation of Spring-mass Damper

The spring-mass system bases upon a geometry rendered in a cubic lattice (fig. 6.5). Each voxel

that is marked as myocardial tissue is split into eight corner masses and integrated into the system (fig. 5.1(a)). The fiber orientation stored in corresponding lattices is used to create springs in fiber, sheet, and sheet normal direction (section 5.2.4) (fig. 6.6). Any set of structural springs and volume springs are created, set up and integrated into the system resulting in a spring-mass system (fig. 6.7). During the setup of the spring-mass system only non existing masses are created, while an additional mass contribution is added to existing masses (section 5.2.1). As neighboring voxel share springs, only non existing springs between masses are created.

6.4 Introduction of Internal Forces

Once the model creation is complete, the contraction driving forces need to be introduced. Therefore, in each simulation time step, a force vector field (section 6.1) is loaded upon the fiber springs of the hybrid deformation model (fig. 5.3).
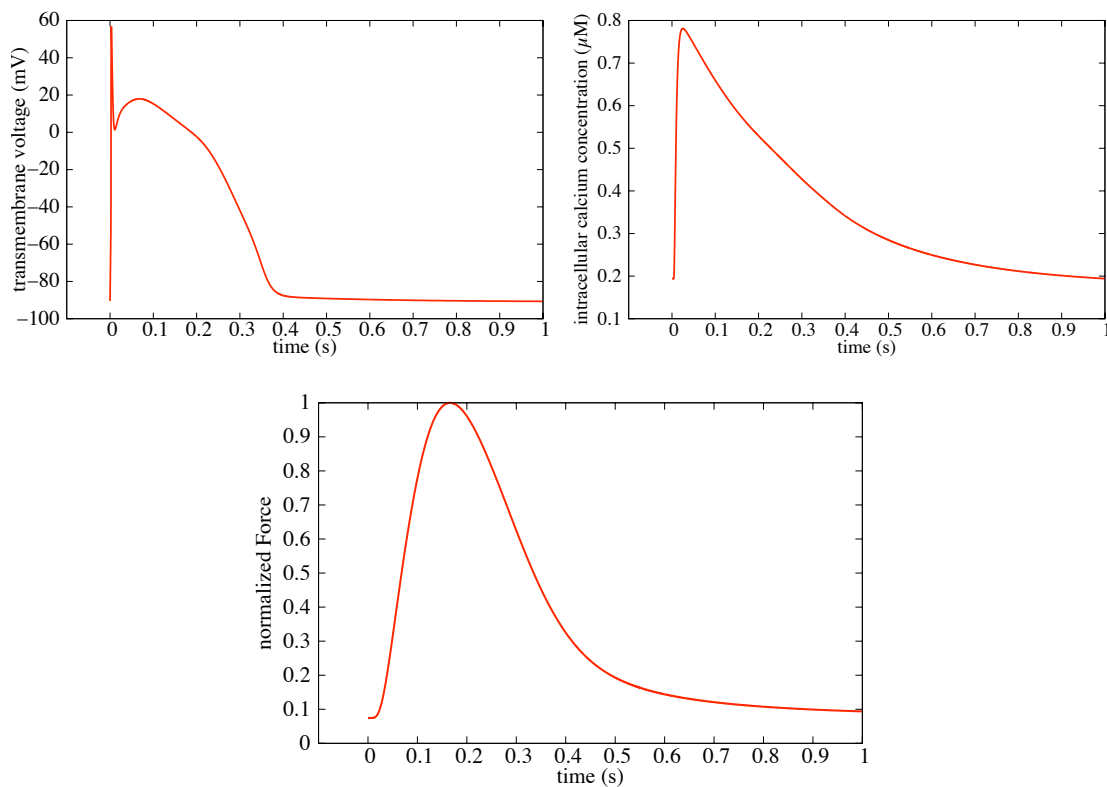
Figure 6.3. Transmembrane voltage, intracellular calcium concentration, and force curve for simulation.
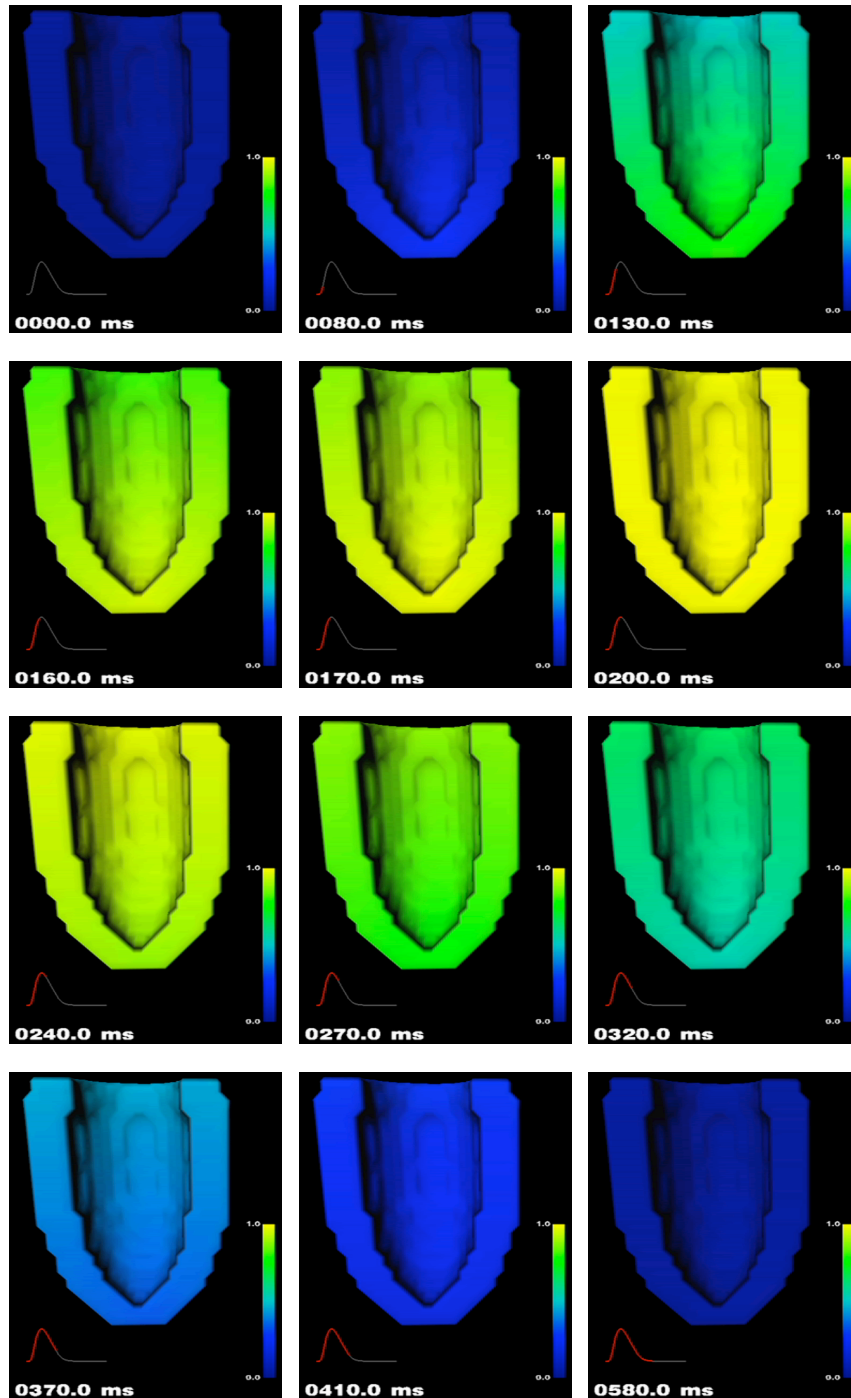
Figure 6.4. Pre-calculated normalized force distribution. Colors denote no force (blue) and maximum force (yellow). The force curve in the lower left hand corner shows the force in a voxel at the apex of the model.
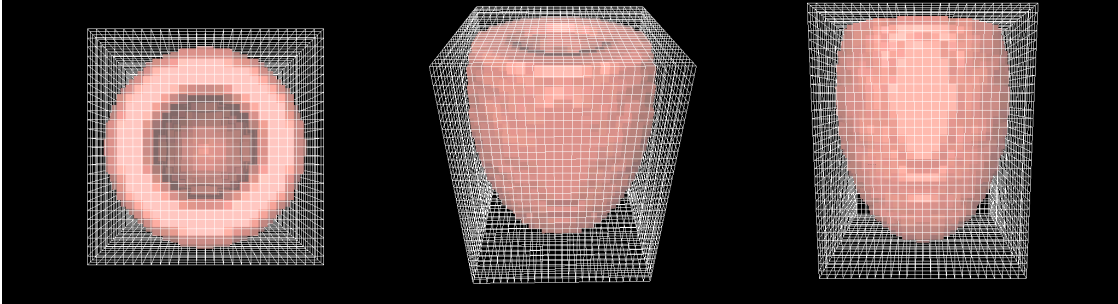
Figure 6.5. Ventricle geometry from different angles. Wireframe denotes the lattice boundaries.
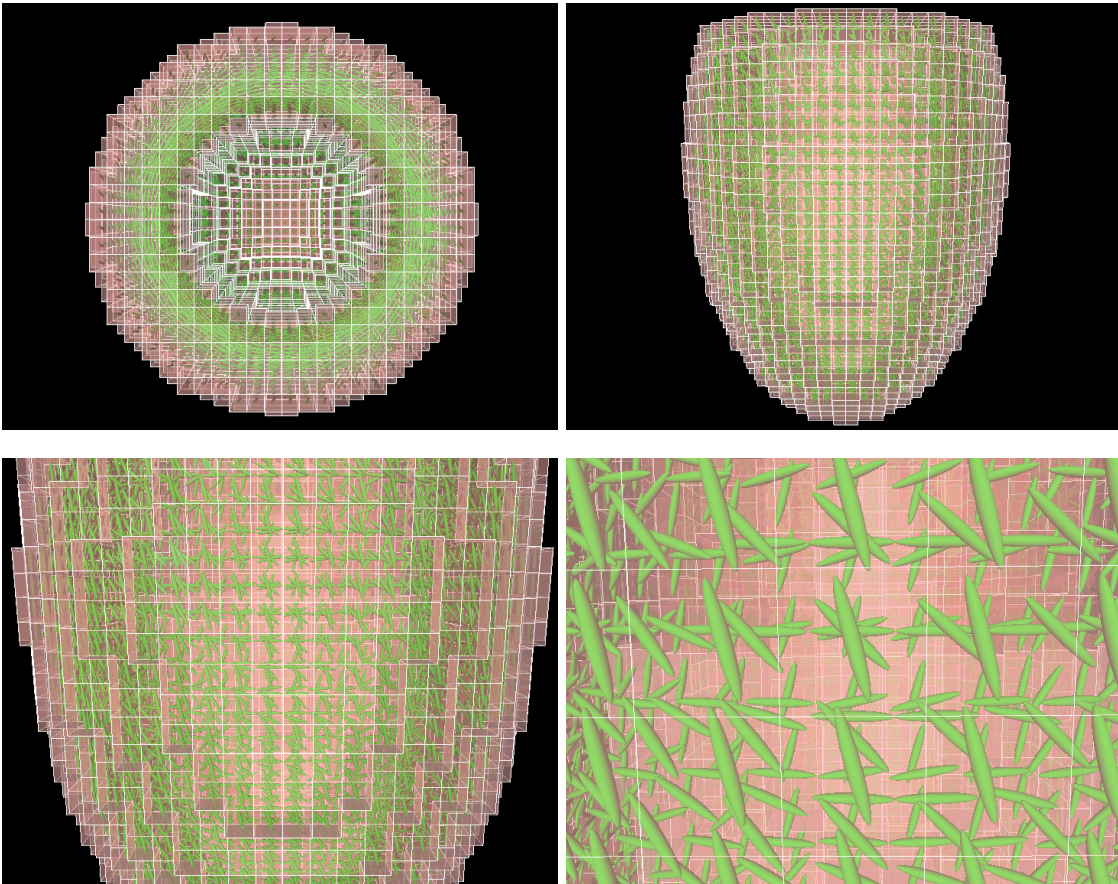
Figure 6.6. Fiber orientation inside the ventricle model. Fiber orientation was linearly interpolated from epicardium $-70°$ to endocardium $70°$ with an angle of $0°$ in the mid-wall.
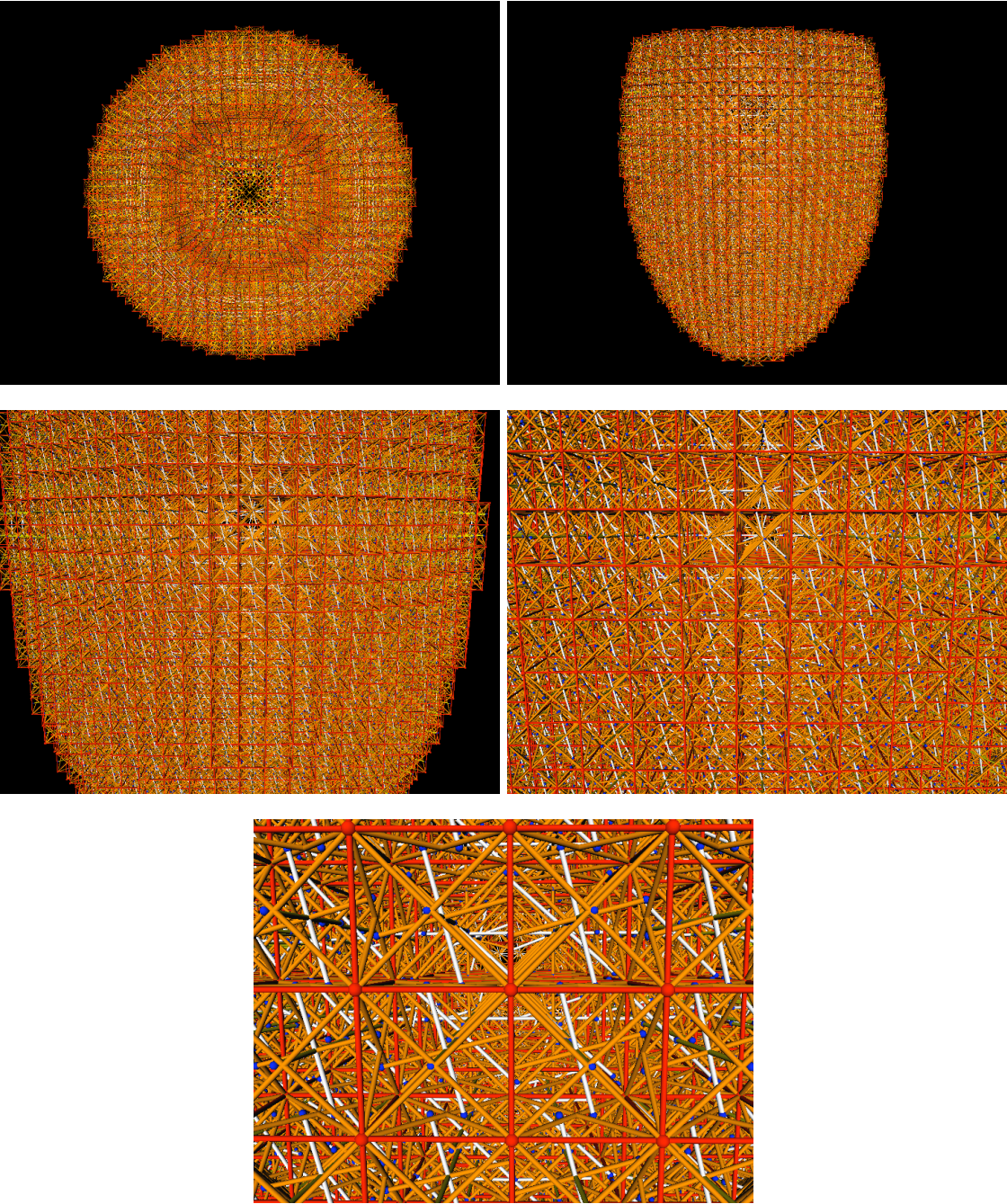
Figure 6.7. Ventricle geometry discretized with spring-mass system. Red spheres denote masses, blue spheres intersection points of anisotropy springs with voxel surface. White springs indicate springs oriented in fiber direction. Red and orange cylinders form the structural spring network.

6.5 Application of Boundary Conditions

6.5.1 Apex Fixation

The deformation simulations in virtual space need a reference point. In case of simulating a ventricle deformation, the apex was chosen to be fixed horizontally. This behavior is consistent with reality, as the heart apex is fixed to the pericardial sac, whereas the heart base with cytoskeleton and valves is pulled towards the apex.

Thus, the nodal masses of the spring-mass system forming the apex of the model were restricted concerning the vertical motion. Motion in the horizontal plane were allowed. This resulted in the apex ability to rotate and deform (fig. 6.8).
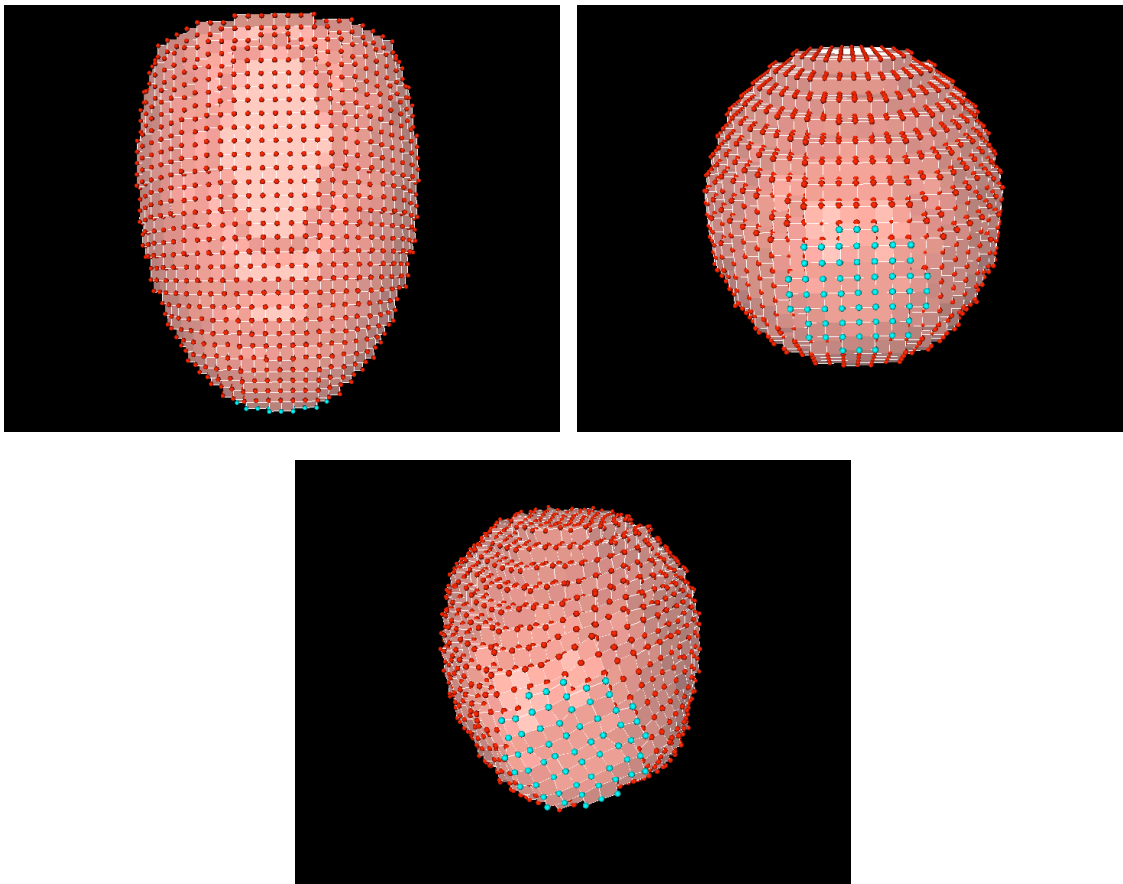
Figure 6.8. Figure shows the simulation model with masses (red spheres) at voxel vertices. The apex was fixed in one plane, allowing tangential but not normal motion (bottom). Fixed masses are denoted by turquoise color.

6.5.2 Pressure Forces

6.5.2.1 Introduction of Pressure

The intraventricular pressure was modeled as a force vector field acting on the masses forming the inner wall of the ventricle. The pressure $\mathbf{p}$ was split into a vector of normals $\mathbf{n}$ and a scalar s describing the force on a voxel surface (fig. 6.9 and 6.10).

$$\mathbf{p} = s\mathbf{n} \tag{6.1}$$

The higher density of force vectors at the apex result in the choice of cubic voxel elements. An interpolation of the surface was not applied as the effect for the deformation simulation are expected to be neglectable. Both, normalized vector field and scalar value can be manipulated at any time of the discrete internal simulation but were changed only at simulation time steps.

The vector field was set up by a virtual vertical line coinciding with the main axis of the ellipsoid and ending at a focus point. Vectors were directed perpendicular from the vertical line to each mass point at the inside surface and furthermore from the focus of the ellipsoid to the masses at the apex (fig. 6.9). Various stages of pressure modeling are applied during simulation of a cardiac cycle.
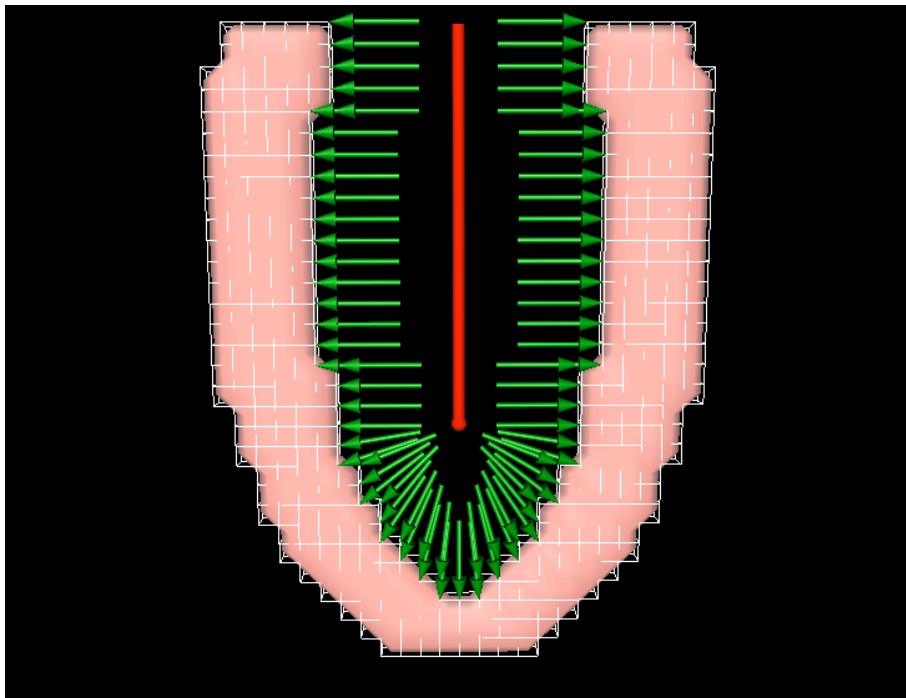
Figure 6.9. Slice of ventricular model with virtual axis (center) and normalized pressure vectors onto endocardial wall.
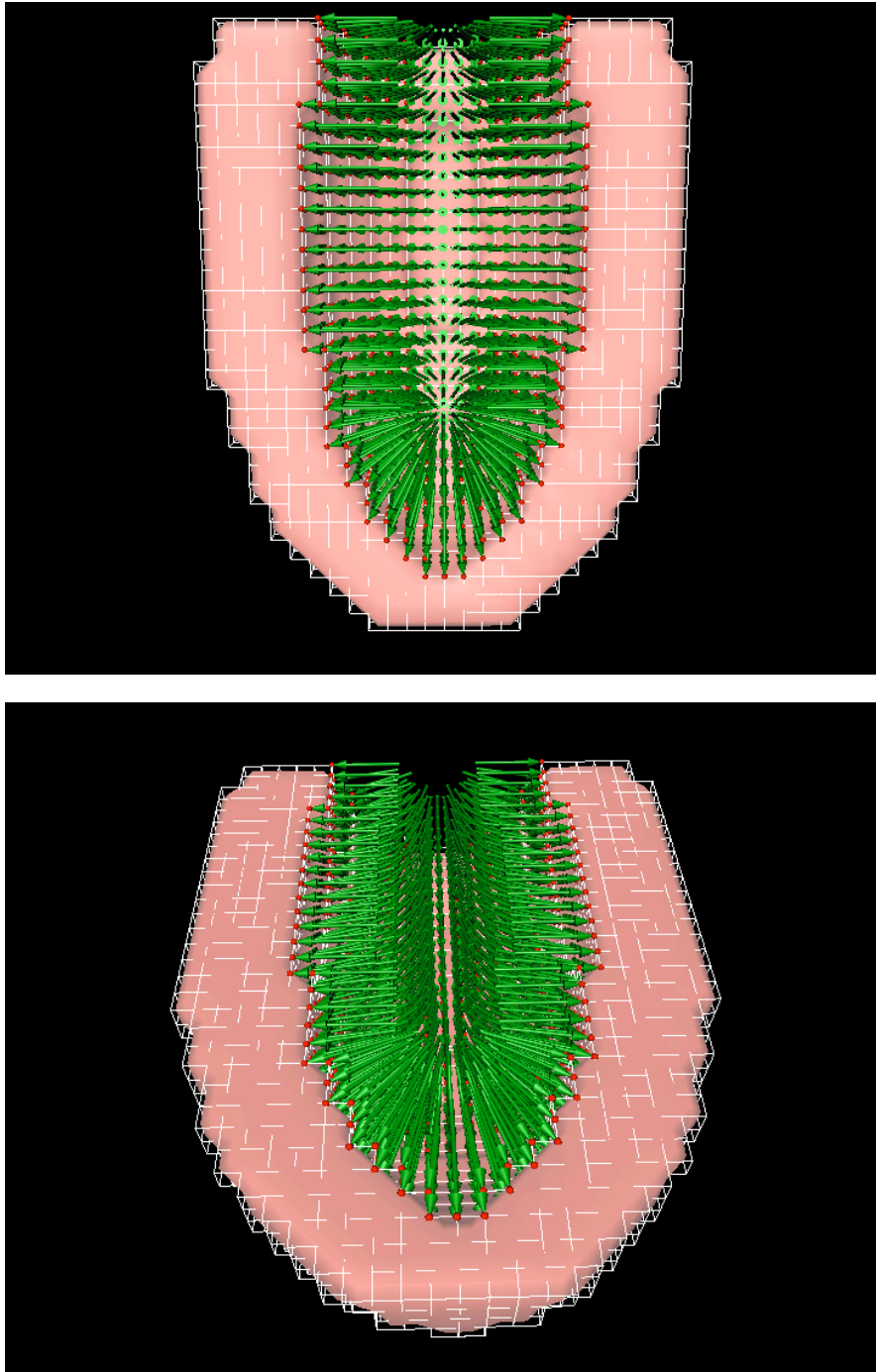
Figure 6.10. Normalized pressure vector field of ventricular model (Ventricular model was cut for visualization).

6.5.2.2 Pressure Modeling

In the scope of this work, models of the left ventricle were used to model the mechanical behavior. Therefore, a main focus was on pressure models describing intraventricular pressure.

The contraction cycle is divided into four major phases, the isovolumic contraction, the ejection phase, isovolumic relaxation and the filling phase (section 3.2.4).

The first three phases mentioned above were modeled using different approaches. The filling phase was not modeled since only a minimal change of pressure occurs.

Isovolumic phase

During the isovolumic phase, the myocardium tightens around the incompressible fluid, pushing it towards the aortic valve. The valve is closed resulting in a rise of the pressure value inside the ventricle until the level of the aortal pressure is reached. Then the valve opens.

This phase was modeled by applying as much pressure to the inside of the ventricular walls as was needed to retain a constant volume. In the modeling process a change of volume was accepted during an internal time sub-step. Then the pressure needed to keep a constant volume was computed. The model was set back to the deformation of the previous time step and the new pressure was applied.

A scheme was developed to increase or decrease the pressure depending on the relative change of volume and the pressure from the previous simulation step [201]. The following mathematical description was applied:

$$p_i = p_{i-1} + (1 - \frac{V_i}{V_0})k f_{max} \qquad (6.2)$$

with f_{max} the maximum introduced force used for contraction initiation, k a scaling factor, V_i the intraventricular volume at sub-step i, V_0 the initial intraventricular volume, p_{i-1} the pressure at the preceding time step, and p_i the resulting pressure.

In case of

- $V_i < 1$, the intraventricular volume decreased and the pressure needs to be increased.
- $V_i > 1$ the intraventricular volume increased and the pressure needs to be decreased.

The application of f_{max} allows to create a dependency of the pressure to the introduced force. The factor k is used to scale f_{max} and allows for force to pressure transfer with unit $\frac{1}{m^2}$.

The pressure oscillates depending on the volume change. A volume oscillation during the isovolumic phase remains below 5%. An optimization of pressure values can be accomplished by successively repeating the method above, applying the values achieved from the previous cycle. Four optimization cycles were applied and showed, that the oscillation can be reduced from 5% to 2% (fig. 6.11). Further optimization can be accomplished by decreasing the sub-time step.
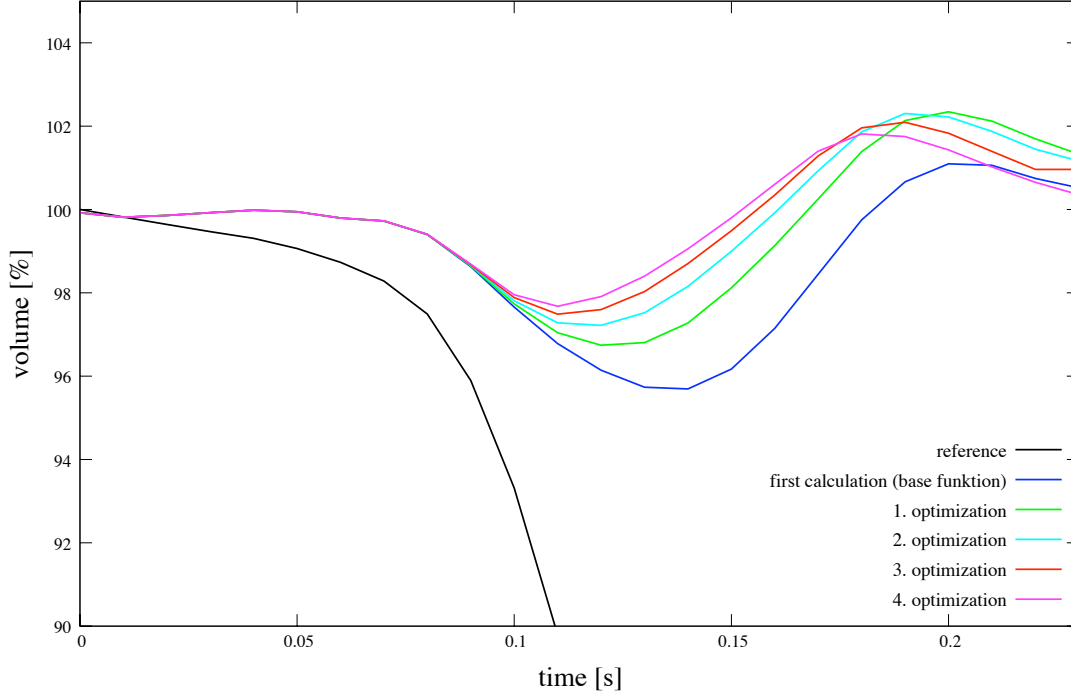
Figure 6.11. The volume during the isovolumic phase was restricted by applying intraventricular pressure. The pressure correction yielded a 5% volume variation in the first cycle and a 2% volume variation in the fourth cycle.

The step over to the ejection phase modeling was performed when a pre-defined pressure value was reached. In the physiological case valves open and the ejection phase begins, when the intraventricular pressure reaches the aortal pressure.

Ejection phase

The displaced volume of the cavity can be computed during the ejection phase. The proposals of Wang et al. [161] were applied (section 3.4.5.1), however in the opposite direction.

Wang et al. measured the aortic pressure P_{A0}, the blood ejected into the aorta Q_{in}, the compliance of the aortal tree, and the resistance R_{prox} of the peripheral systemic circulation and created an equation to describe the interdependence of static and dynamic pressure and ejected volume (eq. 3.15):

$$P_{A0}(t) = P_{Wk}(t) + P_{ex}(t) \tag{6.3}$$

with eq. 3.20

$$P_{WK}(t) = P_\infty + (P_0 - P_\infty)e^{\frac{-t_0}{RC}} + e^{\frac{-t}{RC}} \int_{t_0}^t \frac{Q_{in}(t')}{C} e^{\frac{t'}{RC}} \, dt' \tag{6.4}$$

and eq. 3.21

$$P_{ex}(t) = Q_{in}(t)R_{prox} \tag{6.5}$$

In the course of this work, a scheme was implemented to model eq. 6.3 [201]. The hybrid deformation model provides the ejected volume Q_{in} into the aorta given by the change of intraventricular volume. Parameters P_∞, P_0, R, C, and R_{prox} (section 3.4.5.1) were adapted from the measurements of Wang et al. [161] and Westerhof et al. [163]. Thus, the aortic pressure could be computed from the given Q_{in} of the deformation. Since the pressure inside the aorta and the ventricle is almost identical during the ejection phase (Fig. 3.6 IIa, IIb), the computed pressure was taken as intraventricular pressure during the simulation.

During the simulation of the ejection phase the ejected volume Q_{in} decreases after the maximal contraction of the ventricle occurred. When the intraventricular volume reaches the minimum and hence $Q_{in} = 0$ the isovolumic relaxation phase begins.

Isovolumic relaxation

The aortic and bicuspid valve are closed and the myocardium relaxes during the isovolumic relaxation phase. The pressure decays to the left atrial pressure within approx. 60 ms. In the literature, the pressure decay is described by an exponential decay (section 3.4.5.2). At first an approximation of the pressure decay in Fig. 3.6 was applied. Thus, the diastolic pressure $P_D(t)$ was introduced into the system by:

$$P_D(t) = (P_{A0}(t_D) - P_a)\left(\frac{t_D}{t}\right)^n + P_a \quad t \geq t_D \tag{6.6}$$

with t_D the point in time where the relaxation begins, $P_{A0}(t_D)$ the pressure computed by eq. 6.3 at time t_D, and P_a the atrial pressure to which $P_D(t)$ decreases. The exponent was chosen to $n = 8$ to achieve a close approximation of Fig. 3.6 [201].

Furthermore, studies with exponential functions were conducted. The alternatively applied function derived from eq. 3.23 resulted in:

$$P_D(t) = (P_{A0}(t_D) - P_a)\,e^{\frac{V(t_D)-V(t)}{C}} + P_a \quad t \geq t_D \tag{6.7}$$

with $V(t)$ the intraventricular volume at time t, $V(t_D)$ the intraventricular volume at the beginning of relaxation, and C the compliance of the aortal tree.

Application in the model

The application of the presented phases in the model was achieved as follows:
The simulation was started with the isovolumic phase. For each sub-time step deformations were accepted and the change of volume computed. Applying eq. 6.2 the resulting pressure was computed, introduced into the system, and the deformation reverted. Then another forward marching step was initiated. This procedure was repeated until the computed pressure reached the pre-defined

pressure value for the opening of the valves.

With the opening of the valves, the ejection phase began and the pressure value was computed by eq. 6.3 and the ejected volume Q_{in}. Then the value was introduced into the simulation at the sub-time step and a forward marching step was performed. The ejection phase ended when the computed ejected volume Q_{in} decreased to zero.

The pressure value computed at $Q_{in} = 0$ was used as starting value for the isovolumic relaxation phase. In this phase the pressure was modeled by eq. 6.6 and later by eq. 6.7 and introduced into the system.

7

Results

In the following chapter the chronological development and the performance on varying geometrical models of the hybrid deformation model is described. It started out as a simple spring-mass system, where spring parameters were adapted to a continuum mechanical deformation model by Sachse [31]. Simulations were conducted, testing the systems stability with anisotropic fiber orientation. The modeled geometries evolved from a patch of myocardium to hollow tube like structures and further to ventricular models, represented by confocal truncated ellipsoids. Moreover, pathologic regions were introduced into the ventricular model and the effects on the deformations were examined.

The switch to different computer hardware decreased calculation time. Methods for stable numerical integration were implemented into the hybrid deformation model and allowed for broader parameter range. The introduction of pressure into the model advanced the possibility to reproduce close-to-reality deformations. Especially, simulations with pathologies revealed that tissue behavior was achieved as reported in literature. Deformation simulations were conducted with biventricular geometrical models. A 4D data set of a ventricle acquired from MRI measurements was used to estimate the realistic behavior of the hybrid deformation model.

The following sections describe which methods were applied for simulation and visualization of the deformation results. The methodology of simulation is explained in chapter 6 and will only briefly be mentioned.

The deformation model created first is addressed as pure *spring-mass system*. With the implementation of continuum mechanical methods, the term *hybrid deformation model* is used. The hybrid deformation model is therefore a spring-mass system enhanced by continuum mechanical methods.
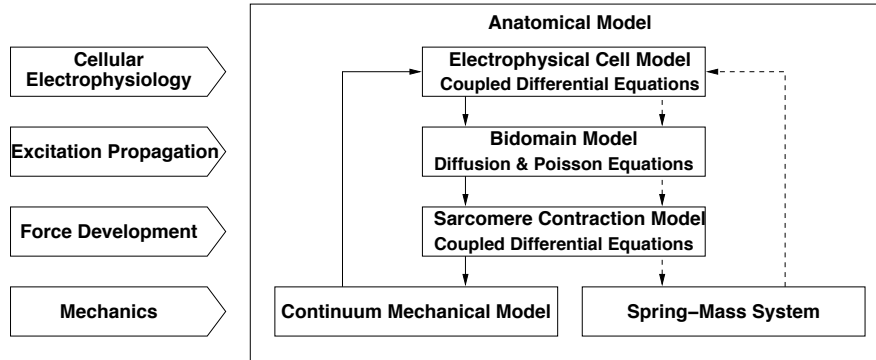
Figure 7.1. The figure shows the coupling of cellular electrophysiology, excitation propagation, force development, and mechanics. Solid arrows show coupling of models, dashed arrows show the possibility of deformation feedback. In addition the basic underlying mathematical equations are named. In this setup the models of Noble et al. [103] and Rice et al. [134] were applied. The bidomain model describes the behavior of excitation propagation for intra and extra cellular components [200]. The left side shows the modeling with a continuum mechanical model by Sachse, and the right side shows the modeling with the spring-mass system.

7.1 Spring Parameter Estimation

The estimation of spring parameters was first accomplished by the author [202] in collaboration with L.G. Blümcke [190] prior to this work. A cube of $4 \times 4 \times 4$ voxel with voxel edge length of 0.1 mm was used to study the interaction of microscopic electrophysiology and mechanics. Fiber orientation was implemented by alignment of all fibers into one direction for all elements.

Models of cellular electrophysiology and excitation propagation were coupled with a force development model (fig. 7.1). Electrophysiological simulations were carried out using a model by Noble et al. [103]. The excitation propagation was carried out by taking the bidomain model into account [200]. Electromechanical coupling was implemented via the exchange of intracellular calcium concentration [126]. The resulting force distribution was applied to a continuum mechanical model by Sachse [31] as well as to a simple spring-mass model. For the deformation simulation, one outer plane of the cube was fixed in virtual space. Gravity was not implemented. The deformation results were compared and spring parameters were adapted. At this stage, the spring-mass system consisted of only linear springs as described by Bourguignon et al. [3] and of active volume springs (section 5.2.6.3). Deformation results of surface based rendering including color coded force distribution of the continuum model (fig. 7.2) and the deformation of the spring-mass system (fig. 7.3) are displayed.   Spring parameters of the spring-mass system were adapted to achieve a deformation that was only differing by a few percent from the continuum mechanical model.
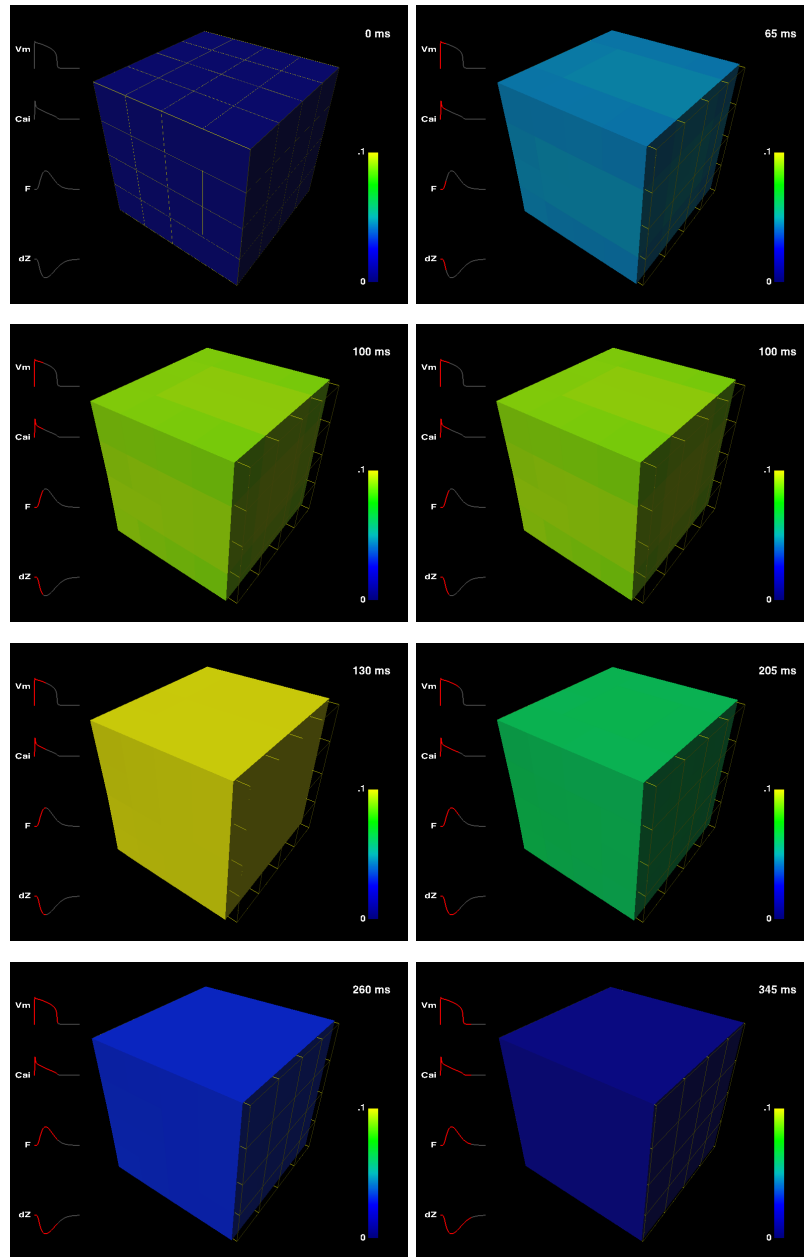
Figure 7.2. Development of deformation of cubic geometry determined with the continuum mechanical model of Sachse [31] at specific point in time. Curves at the left side of each figure show in gray the outline of the estimation of transmembrane voltage V_m, calcium concentration Ca^{2+}, force development **f**, and displacement dZ in Z-direction throughout simulation time. The red coloring of these curves indicate the progression of the curve until the given time instance. The color coding of the voxel resemble the acting force in each voxel, with the scale on the right indicating force intensity (blue, no force and yellow maximum force). The wireframe denotes the undeformed model.
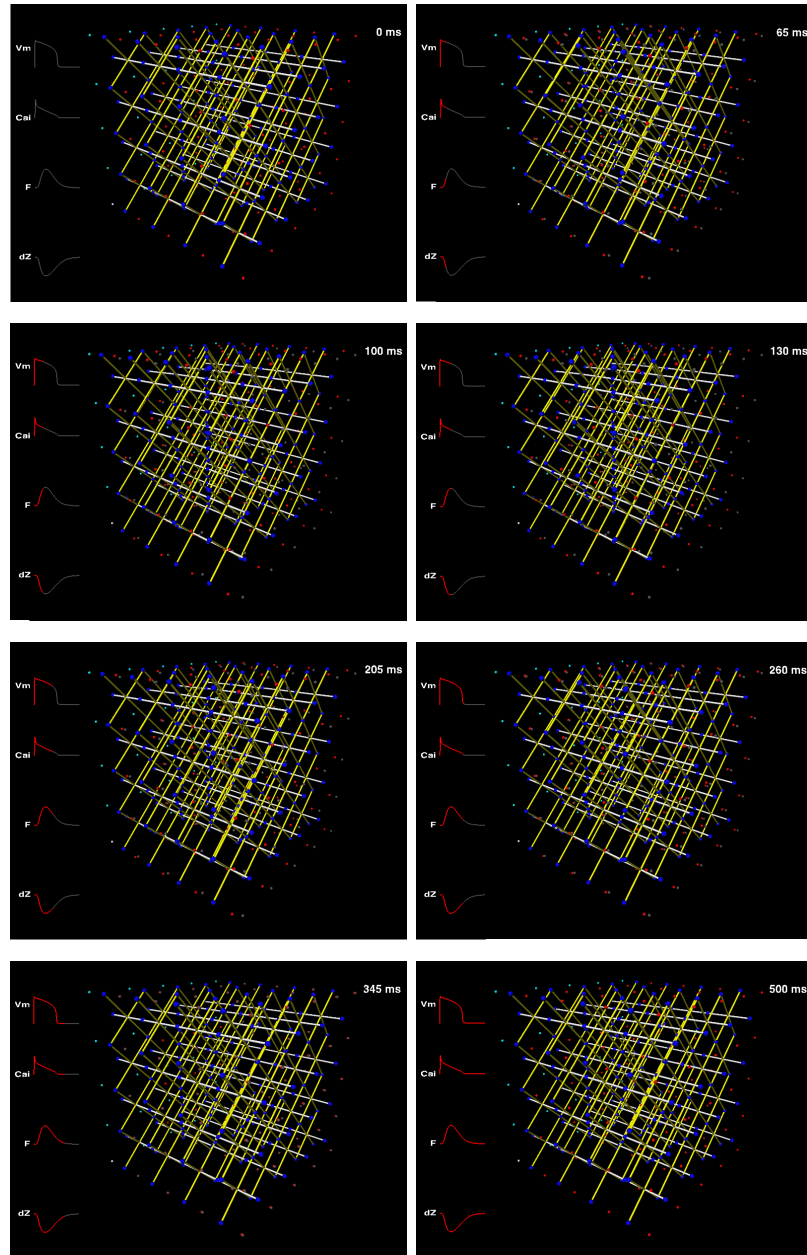
Figure 7.3. Development of deformation of the cubic geometry at specific points in time computed with an early state spring-mass system [202]. The red spheres indicate masses at the actual position and gray spheres the masses at the initial position. The turquoise spheres indicate masses fixed to their position. The white and yellow cylinders represent the fiber, sheet and sheet normal springs. Structural springs were applied but not visualized. The blue spheres mark the intersection of anisotropy springs with the voxel surfaces. Curves at the left side of each figure are equivalent to fig. 7.2.

7.2 Anisotropic Fiber Orientation

In the work of Blümcke [190] performed in close cooperation with Mohr [202] an anisotropic fiber orientation was applied to the simple model. The anisotropy was assumed to represent a ventricular wall patch by defining a fiber twist from inside (top) to outside (bottom of Fig. 7.4) from $-50°$ to $50°$. The simulation set up was equivalent to the one in the previous section. By then, no anisotropic deformation simulation was possible with the continuum model. The focus was set on testing the ability of the spring-mass system to simulate stable deformations with anisotropic tissue. Deformation simulations resulted in a twist of the cubic model following the applied fiber orientation (fig. 7.4).

Following the successful anisotropic deformation, another study model was created [203]. The effects of a circular fiber orientation on a tissue block were examined. Therefore, a $5 \times 5 \times 5$ cubic volume was created and the fiber orientation was arranged to resemble concentric circles (fig. 7.5(a)). The same fiber orientation was applied to all layers of the cube. The top plane of the cube was fixed in virtual space for the deformation simulation. Gravity was not applied.

Deformation simulations showed an in-plane contraction and an elongation perpendicular to the circular plane (fig. 7.5(c)). An elongation was obtained due to the incompressibility model of the volume by barycenter-mass springs. While the fiber springs shortened, the sheet and sheet normal springs were allowed to expand to compensate the reduced volume.
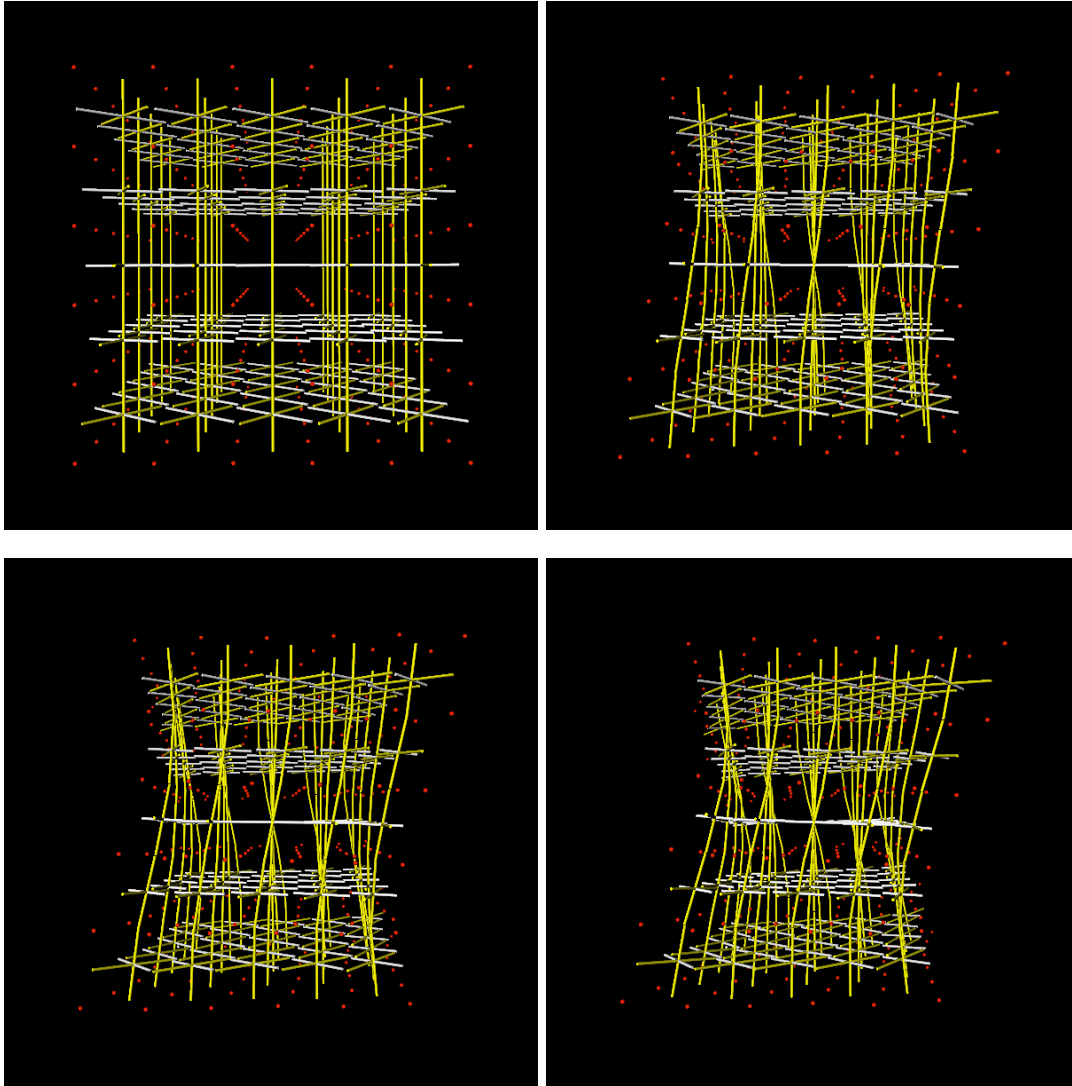
Figure 7.4. Development of the deformation of a cubic geometry with anisotropic fiber orientation computed with an early state spring-mass system [190]. The red spheres indicate masses at the actual position. The white and yellow cylinders represent the fiber, sheet and sheet normal springs. Structural springs were applied but not visualized (fig. from [190]). Figures show the deformation at 0, 1600, 2000, and 2400 forward steps with a constant time step.
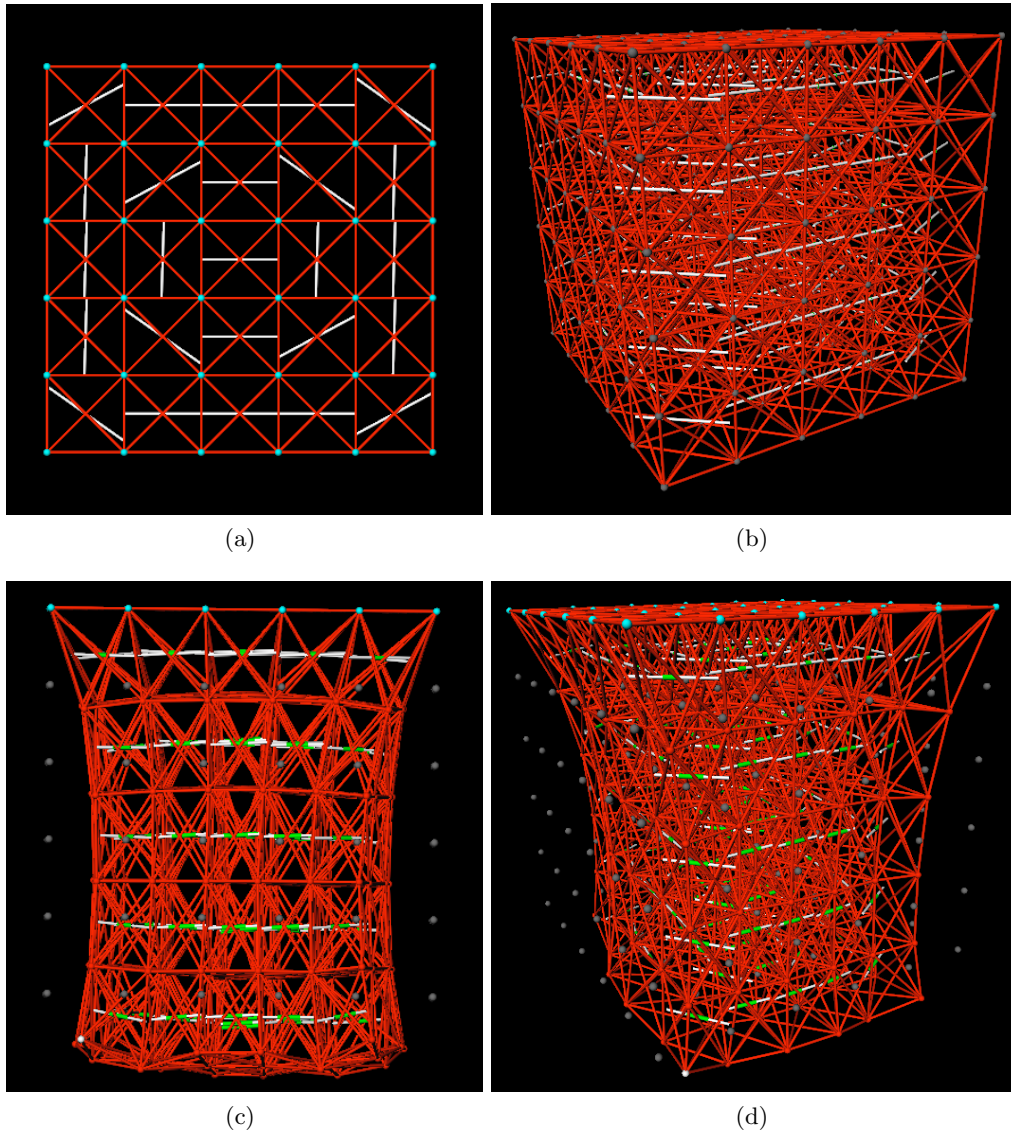
Figure 7.5. Development of the deformation of a cubic geometry with circular fiber orientation computed with an early state spring-mass system [202]. The red spheres indicate masses at the actual position and gray spheres the masses at the initial position. The turquoise spheres are masses fixed to their position. The white cylinders represent the fiber orientation springs and green indicates the amount of compression. The red springs resemble structural springs. (a) shows a view from the top where the in-plane fiber orientation is indicated by the white lines. (b) shows the study model in the initial position. (c) and (d) display the model at maximum contraction from different perspectives. No gravity force is applied to the system.

7.3 Modeling Objects with Holes

As the ventricle is a hollow organ with a specific wall thickness, further study models were created to examine performance of the spring-mass system with more sophisticated models

7.3.1 Cubic Tube Structure with Circular Fiber Orientation

A myocardial structure of $15{\times}15{\times}15$ cubic voxel with a voxel edge length of 1 mm was created [193]. A free space of $5{\times}5{\times}5$ voxel was introduced in the center to examine deformation effects with a tube like structure (fig. 7.6). The fibers show a circular orientation in each z plane (fig. 7.6(a)). The top plane was fixed. A linear ramp function from 0 to 370 kPa was used for the contraction initiating force and all voxel were subject to this force at the same time. Hereby, models of electrophysiology were not applied. The spring-mass system was created with all springs (section 5.2). Energy density functions were not implemented.
Simulations were conducted with this setup and deformation results are displayed (fig. 7.6). A volume preservation was achieved with an average of 75% by applying the active volume springs (section 5.2.6.3) .
The deformation shows a uniform inward motion of the walls (fig. 7.6(c) and 7.6(d)). The decrease of volume inside the tube is visible. Thus, a virtual blood volume inside the tube would be displaced, as happens e. g. in vessels and cavities. Due to the steep descent of the ramp function the spring-mass system returned to the initial position by swaying (fig. 7.6(e) and 7.6(f)).
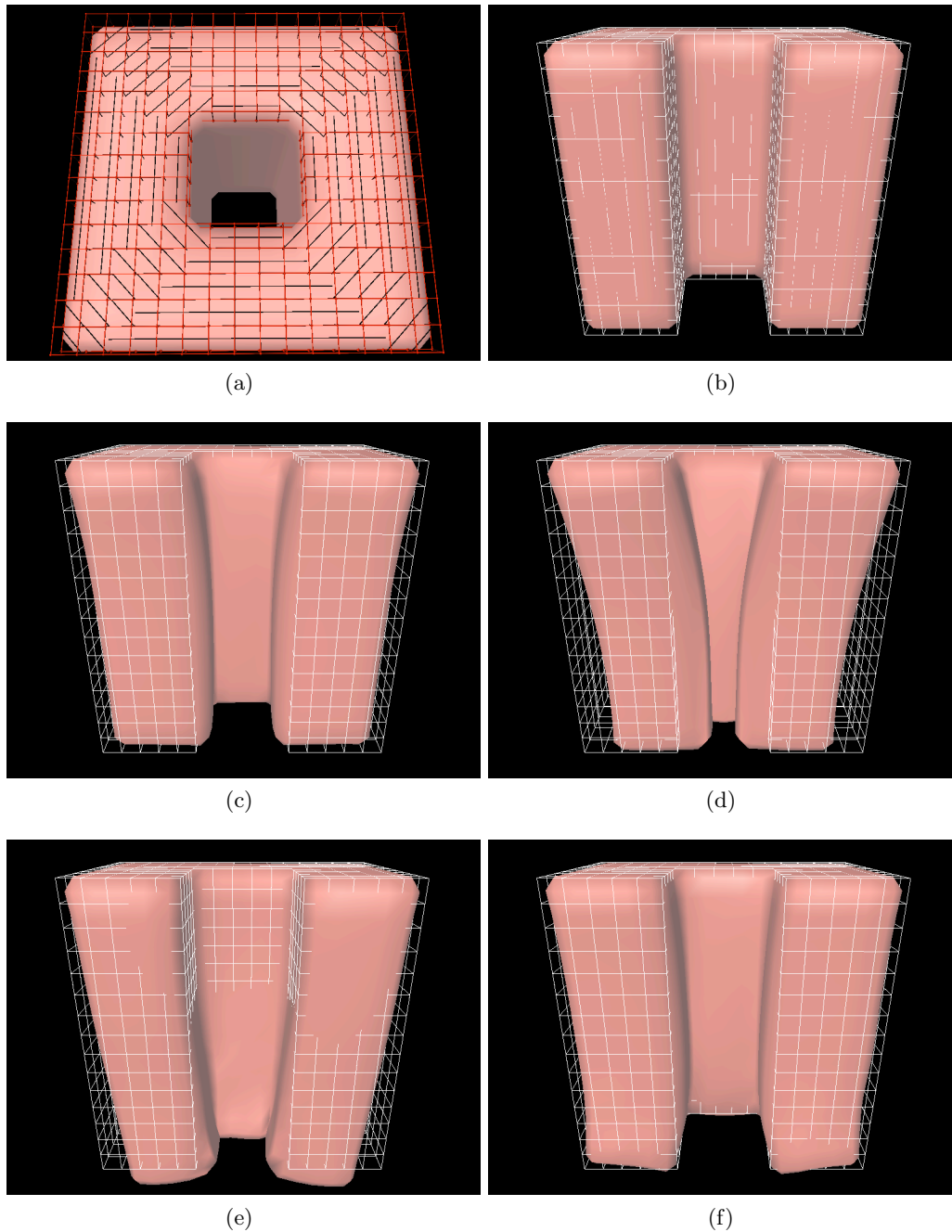
Figure 7.6. Simulations with a tube like structure. A circular fiber orientation was introduced into each plane to test anisotropic behavior. The black lines indicate fiber orientation (a). A lateral cut of the model is shown in a relaxed state with no force acting on the tissue (b). The following figures display the deformation for an increasing force (c), at maximum force peak (d), (e) and (f) for a fading force. Figures were taken at time (b) 0, (c) 40, (d) 70, (e) 110, and (f) 140 ms.

7.3.2 Cylinder Model with Realistic Fiber Orientation

The geometrical model with hole was extended towards a simplified ventricular model [193]. A cylinder was rendered in a lattice of $21 \times 21 \times 21$ voxel with a wall thickness of 3 voxel (fig. 7.8). The fiber orientation was set according to anatomical studies at the subepicardium to $-75°$, at mid-myocardium to $0°$, and at endocardium to $75°$. The cylinder was fixed at the upper rim and an excitation was initiated at the lower rim. This behavior can be found in the left ventricle, as the excitation of myocardial tissue commences from apex to base and from the inside to the outside wall (section 3.2.2.1).

In contrast to section 7.3.1, the force was generated by coupling of the microscopic electrophysiological, the excitation, and the force generating models (fig. 7.7). The resulting force was used as input for the spring-mass model to determine the deformation (fig. 7.9 and 7.10).

The simulation shows, that the contraction follows the excitation propagation allowing for spatially differentiated contraction (fig. 7.9). Thus, an upward transport of intraventricular volume can be recorded. Furthermore, a torsion of the cylinder can be recognized, while the force already decreases (fig. 7.10). The right side of the cylinder advances to the front, which can be determined by the surface rendering exceeding the wireframe. At the same time, the left side is drawn back behind the wireframe mesh. This indicates a clockwise torsion, which is solemnly induced by the fiber orientation. The change in fiber orientation compared to the cubic tube model (section 7.3.1) results in a torsion, but a smaller inward deformation. Thus, less volume is displaced inside. This indicates that the wall thickness should be increased.

The spring-mass system slowly vibrates towards its initial position while the acting force decreases. The examination of tissue isovolumetry showed that only an accuracy of approx. 75% was achieved. When real myocardial tissue contracts and deforms, however, the tissue volume should be close to 99%. The ability of the spring-mass system to maintain the voxel volume showed to be limited depending on geometry and fiber orientation of the used model.
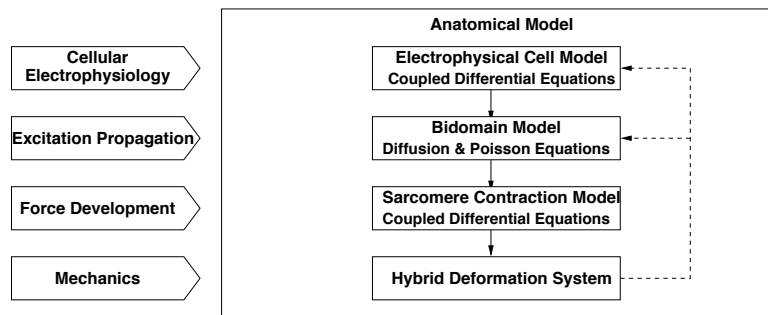
Figure 7.7. The figure shows the coupling of cellular electrophysiology, excitation propagation, force development, and mechanics. Solid arrows show the coupling of models; dashed arrows show the possibility of deformation feedback.

(a)

(b)

(c)
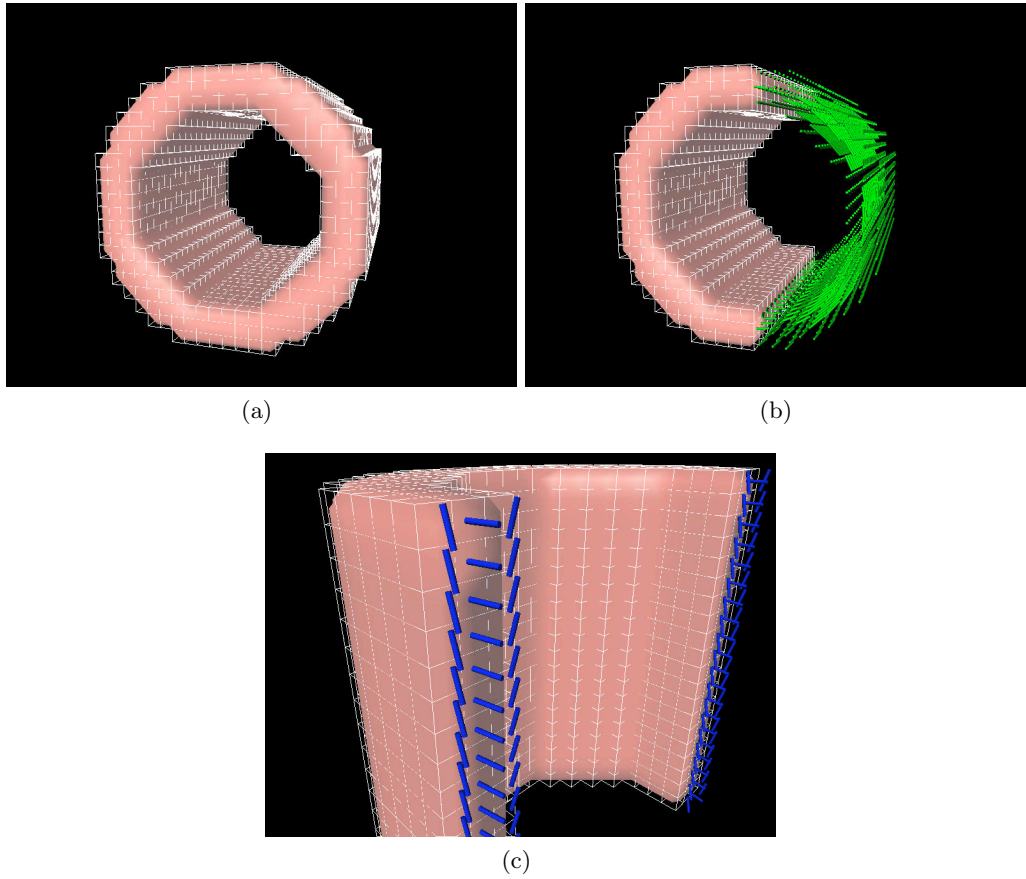
Figure 7.8. A cylinder used as a simple ventricle model (a). The white wireframe denotes the undeformed cylinder. A cut through the cylinder is displayed to visualize the fiber orientation (b). A close up of the cylinder wall shows the fiber orientation varying from endocardium ($75°$) to mid-myocardium ($0°$) and subepicardium ($-75°$) denoted by blue cylinders.
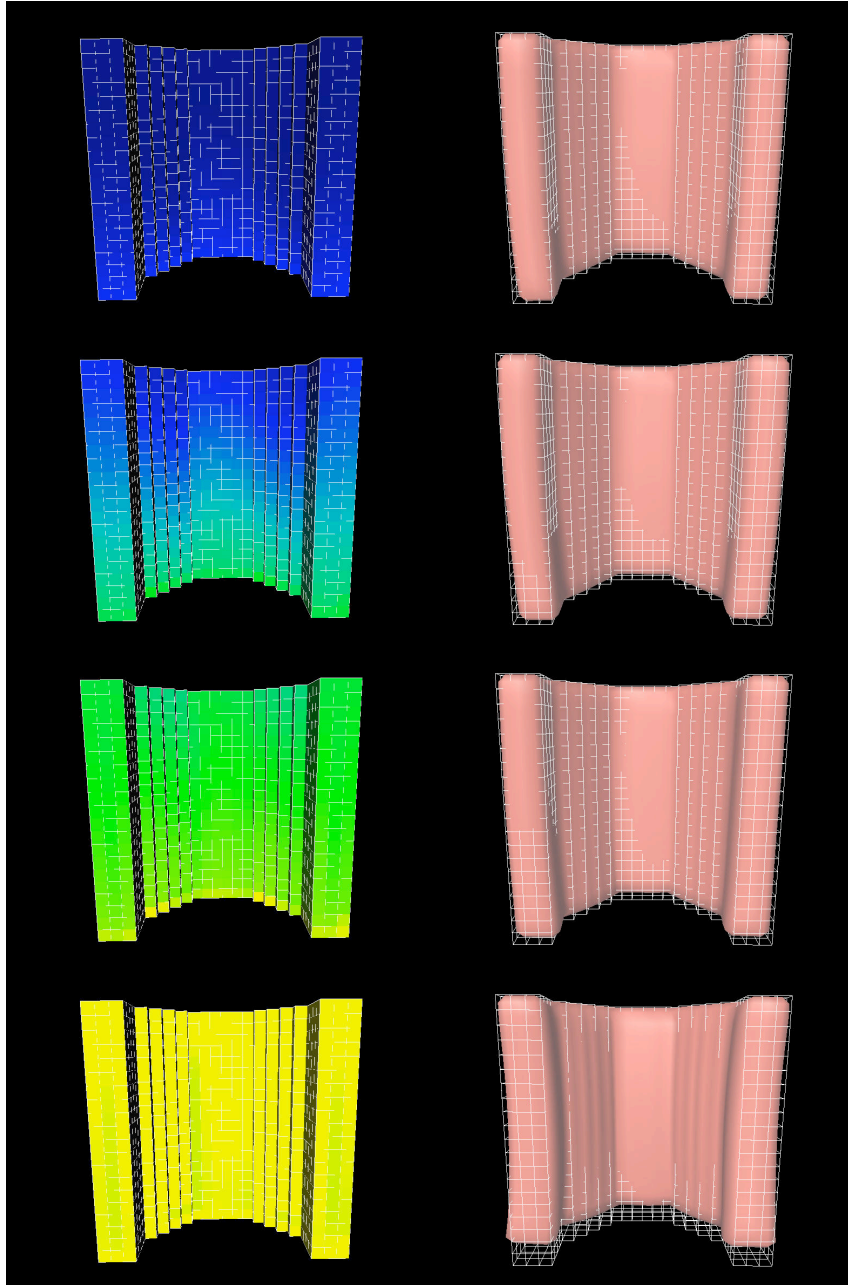
Figure 7.9. Deformation simulation with a cylindrical model. The left side shows the force propagation over the cylinder. The color scale ranges from no force (dark blue) to maximum force (yellow). The right side shows the corresponding deformation with the spring-mass system. Figures from top to bottom are captured at 20, 30, 40, and 60 ms. The white wireframe shows the relaxed model.(for continuation see fig. 7.10)
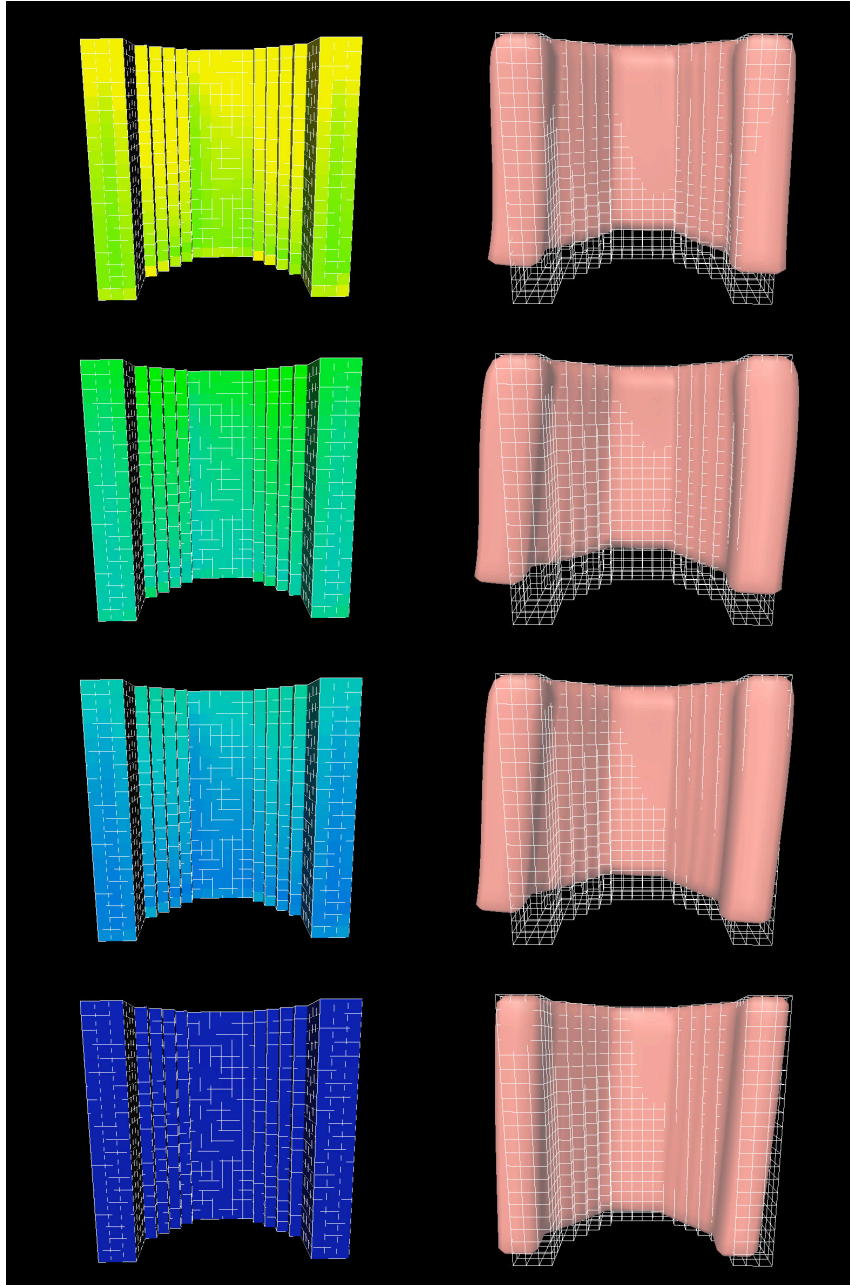
Figure 7.10. Deformation simulation with a cylindrical model (continued from fig. 7.9). The left side shows the force propagation over the cylinder. The color scale ranges from no force (dark blue) to maximum force (yellow). The right side shows the corresponding deformation with the spring-mass system. Figures from top to bottom are captured at 80, 115, 135, and 230 ms.

7.3.3 Cylinder Model Including the Energy Density Function of Guccione

The non-linear behavior of myocardial tissue was first modeled by linear springs. The parameterization of spring constants depending on length was implemented by applying the proposals of Hunter et al. (section 5.3.2.2). However, the poles limiting the uniaxial stress strain relationship resulted in numerical difficulties due to stepping beyond the limit. Therefore, the model was extended using continuum mechanical methods to model the non-linearity of the myocardium [204]. The strain energy density function of Guccione et al. [80] was adopted (section 5.3.2.1). This energy density function $\mathbf{W}$ was used to compute material stress initiated by material strain. For each voxel the deformation gradient tensor $\mathbf{F}$ and the Green-Lagrange strain tensor $\mathbf{E}$ were determined at each time step. The second Piola-Kirchhoff stress tensor $\mathbf{S}$ was derived and the Cauchy stress tensor $\boldsymbol{\sigma}$ computed.

The tensor $\boldsymbol{\sigma}$ was applied to the voxel surfaces, which led to a force acting on the voxel vertices. The masses were displaced and a new strain setup was achieved (section 5.4).

The contraction initiation force was determined as described in the previous section.

Simulating 500 ms took approximately 6 hours on a SGI Octane Mips R12000 400 MHz using the deformation model. The deformation results did not vary visibly from the results given in fig. 7.9 and fig. 7.10. However, isovolumetry per voxel was sustained by approx. 90%.

The implementation of the strain energy function resulted in a more accurate deformation in the vector space spanned by fiber, sheet and sheet normal. However, implementing continuum mechanical methods increased the number of computations considerably and the according simulation time by more than 20%.

7.4 Ventricular Model

The cylindrical model with realistic fiber orientation did not sufficiently represent a ventricle. There-
fore, an analytical ventricular model was created in the form of an half ellipsoid (fig. 7.11) [205].
The half ellipsoid was rendered in a $20 \times 20 \times 20$ voxel lattice with edge length of $0.2\ mm$. The
wall thickness was set to 5 voxel due to the results of previous sections. The force development was
computed by coupled microscopic models (fig. 7.7).
In addition, isovolumetric springs were replaced by isovolumic constraints adopted from a Mooney-
Rivlin model (section 5.3.1). This newly implemented method resulted in additional computational
effort.
The computer power to perform simulations was limited to a single processor SGI Mips R12000
$400\ MHz$. Therefore, only a patch of $6 \times 5 \times 4$ voxel of the ventricular wall was used for deformation
simulations (fig. 7.12, 7.13, and 7.14). The simulation time of $600\ ms$ was divided into steps
of $20\ ms$. For each $20\ ms$ time step the deformation was computed with $10,000$ sub-steps to
ensure relaxation towards an energetic minimum. The patch was fixed at the top layer and no
further boundary conditions were considered for the sides. The following table shows the relative
simulation times and the average voxel volume during deformation by the spring-mass system with
linear springs, and by the hybrid deformation model with energy density functions, respectively.

model type	time in %	average vol %
spring model	100	91
hybrid model	120	98

The increase in average tissue volume showed that the applied isovolumic constraints were able
to sustain the volume to a greater extent compared to linear springs. An increase of computation
time of 20% was required for the additional numerical effort.   The deformation of the tissue
patch compared to the spring-mass system showed that the contraction as well as the torsion was
reduced. This can be accounted to the fact, that the patch was small compared to the fixed area
as well as the stricter enforcement of the constraints forced by the Mooney-Rivlin model. As an
concluding remark it must be noted that including sophisticated mathematical models into the
hybrid deformation model resulted in more realistic deformation, however the computation time
increased.
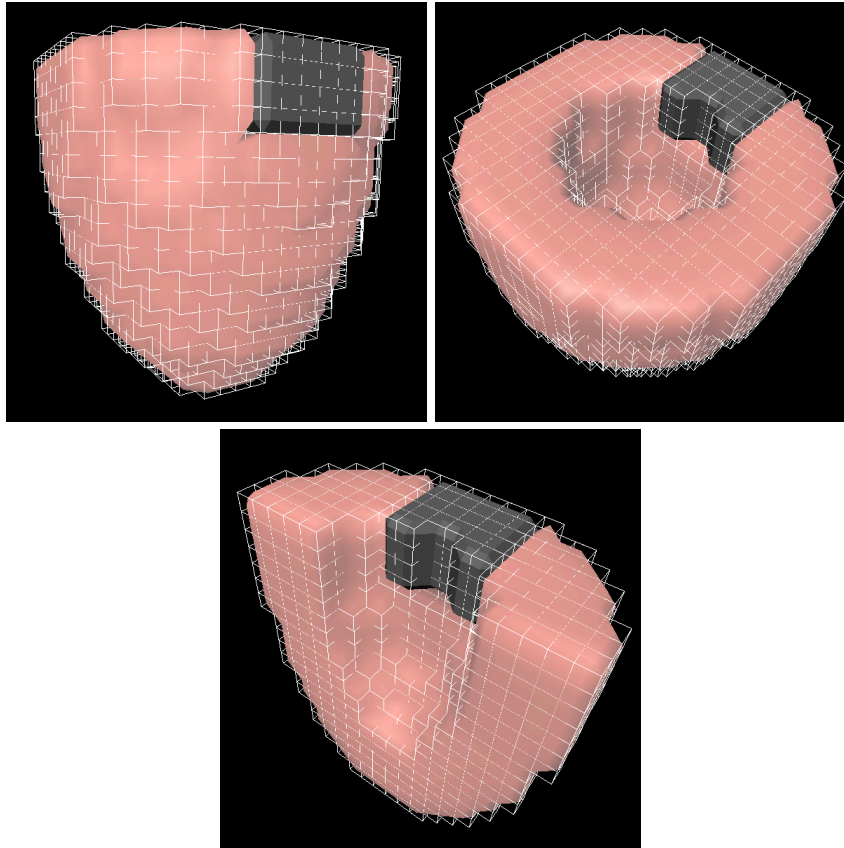
Figure 7.11. A half ellipsoid was discretized into a $20 \times 20 \times 20$ voxel lattice with edge length of 0.2 mm. A patch of $6 \times 5 \times 4$ voxel was extracted (shown in dark gray), to conduct deformation simulations.

(a)   (b)
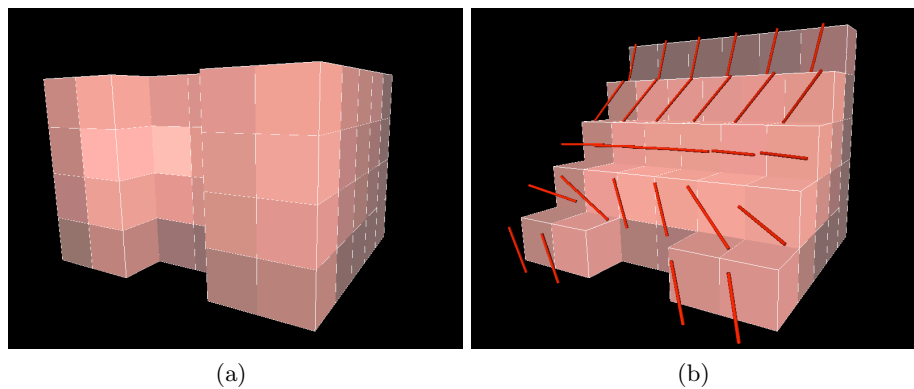
Figure 7.12. Myocardial patch built of $6 \times 5 \times 4$ voxel. The wireframe denotes voxel edges (a). The patch is displayed as a stairway to show fiber twist from endo- to epicardium ($+75°$ to $-75°$) in red cylinders (b).
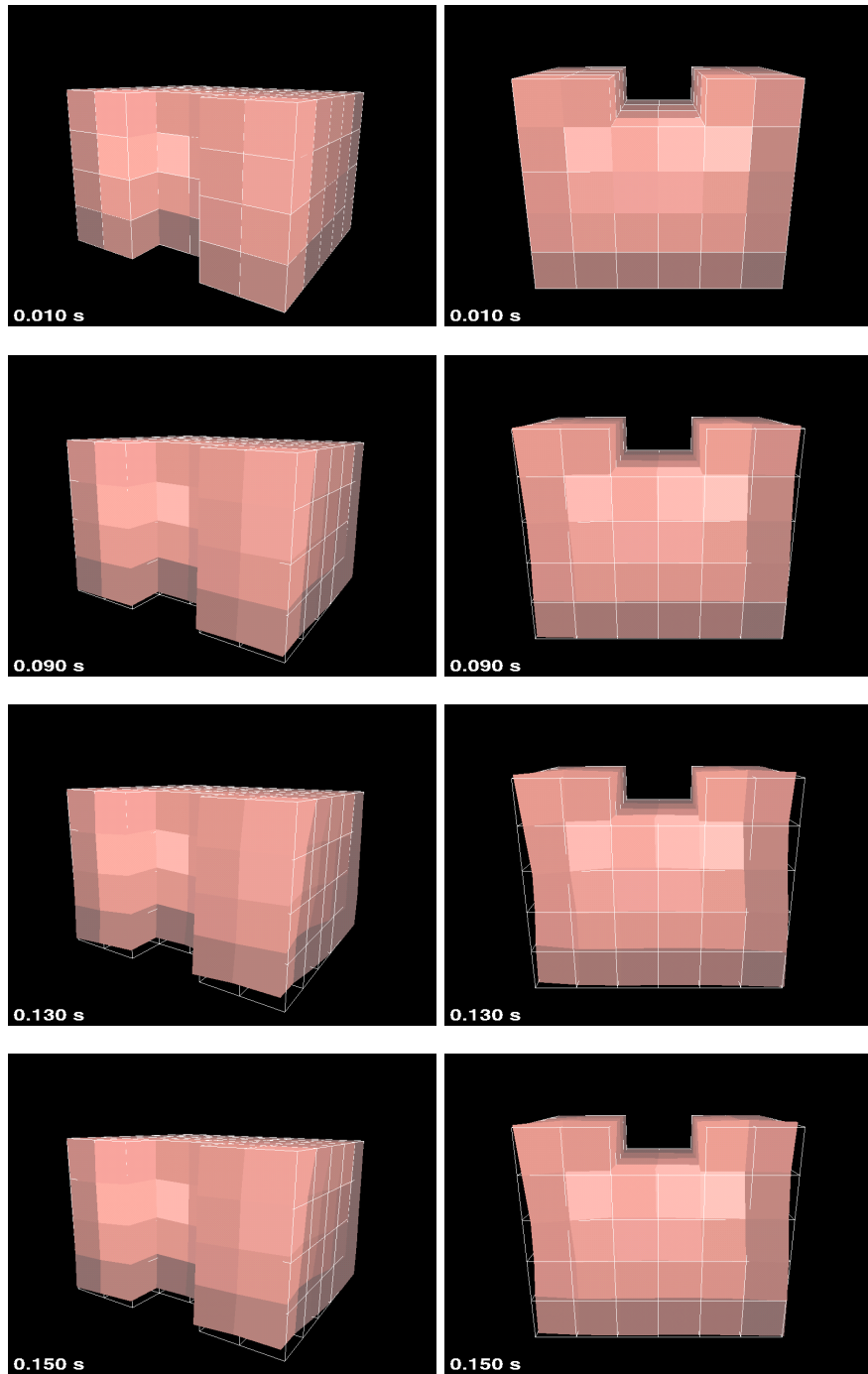
Figure 7.13. Deformation simulation with the $6 \times 5 \times 4$ voxel patch. The left column shows a frontal view of the patch. The right column the view from the bottom. The patch was fixed at the top layer. The white wireframe indicates the undeformed state (for continuation see fig. 7.14).
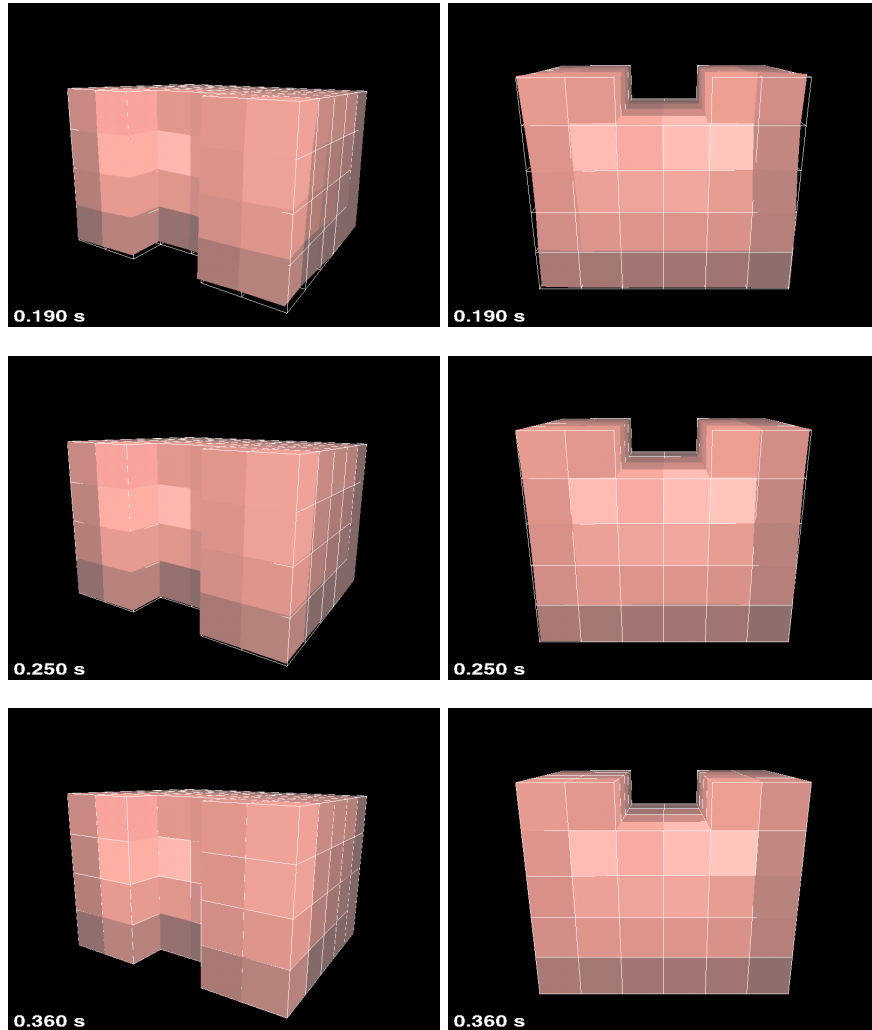
Figure 7.14. Deformation simulation with the $6 \times 5 \times 4$ voxel patch. (fig. 7.13 continued)

7.5 Ventricular Model Including Pathologies

A more sophisticated anatomical model and new simulation strategies allowed the modeling of not only a patch of ventricular wall but the complete left ventricle. The application of the ventricular geometry resulted in the following spring-mass setup:

type	quantity
voxel	8 224
masses	10 748
anisotropic springs	24 672
structural springs (edges)	29 671
structural springs (diagonal surface)	54 312
volume springs (diagonal through voxel)	32 896
sum of all springs	141 551

The application of new computer hardware (namely Apple PowerPC G5 $2GHz$), running with the MacOS X system and the software adaptation to this system resulted in a reduction of computation time. The mechanical deformation was computed in approx. 2 hours (1 s simulation time, 10 ms simulation time step).

This enhancement allowed to investigate the capabilities of the deformation model to represent tissue behavior with varying mechanical properties [206].

Simulations with regional changes of tissue characteristics were performed to model the behavior of healthy, necrotic, and dilated tissue.

The elasto-mechanical ventricular model was enhanced by applying the truncation close to the upper focus of the ellipsoids yielding a more realistic model of a left ventricle (fig. 7.15). The ellipsoid was discretized into a $26 \times 26 \times 33$ cubic voxel lattice with a voxel edge length of 0.2 mm. A rule based fiber orientation varying from epi- to endocardium from $-75°$ to $75°$ was used (fig. 7.15(b)). Propagation of deformation forces inside an elastic model is delayed to surrounding elements, therefore the fusion model of Miyazaki et al. [197] was applied for partial spring rigidity (section 5.5.3.2).

A simulation with the truncated ellipsoids was performed and used as reference deformation, representing non pathologic (healthy) tissue. The tissue was set up with linear springs, Gucciones strain energy density function, and Mooney-Rivlin material with incompressibility. The Green-Lagrange finite strain tensor $\mathbf{E}$ was computed for each sub-step and the Cauchy stress tensors $\boldsymbol{\sigma}_G$ (Guccione energy density function) and $\boldsymbol{\sigma}_{MR}$ (Mooney-Rivlin energy density function) were computed (section 5.4). The resulting forces were applied to the voxel surfaces.

A region of the wall with the size of $8 \times 9 \times 10$ voxel was set to either necrotic or dilated tissue for the pathologic set ups (fig. 7.16). Due to missing comparable data, all parameters described below were found empirically. Pathologic tissue was assumed to be unexcitable and not complying

(a)   (b)
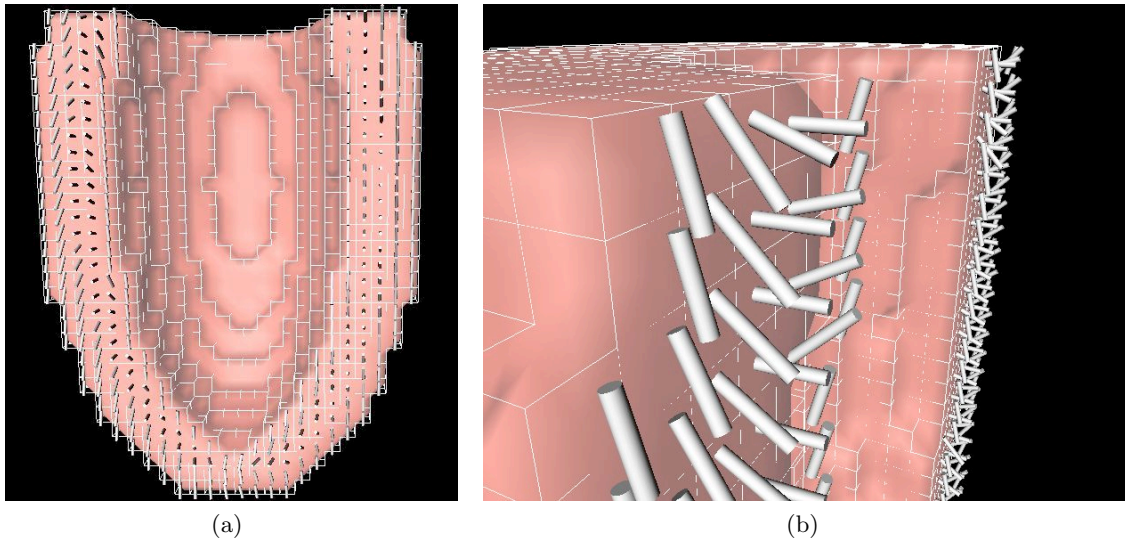
Figure 7.15. A truncated ellipsoid was discretized into a $26 \times 26 \times 33$ cubic voxel lattice with edge length of 0.2 mm. The left figure shows a lateral cut with fiber orientation for each voxel. The right figure displays the upper left corner, where the twist of fiber orientation from endo- to epicardium is visualized by white cylinders.
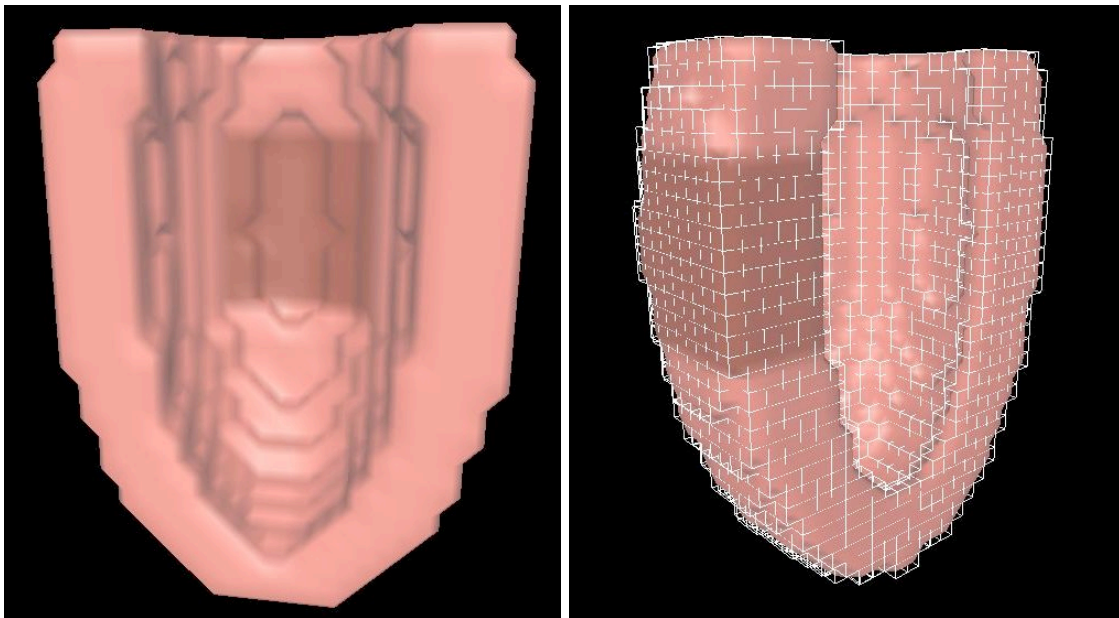
Figure 7.16. Lateral view of open truncated half ellipsoid. The darker region displays the $8 \times 9 \times 10$ voxel patch with pathologic tissue properties. The wireframe denotes undeformed position.

to so-called passive properties of healthy tissue. Necrotic tissue was assumed to be rigid. Dilated tissue was assumed to be viscose.

Necrotic Region

The necrotic region was simulated by setting the parameters for the $8 \times 9 \times 10$ voxel region as follows:
The strain energy density function of Guccione et al. and Mooney-Rivlin was deactivated. Spring parameters for stiffness and damping were increased by approximately 10% and 40%, respectively as demonstration values. The tissue density was slightly raised to simulate increased inertia. The parameter for the implemented fusion model of Miyazaki was increased to enhance the rigidity of springs.

Dilated Region

The dilated region was simulated by setting the parameters for the $8 \times 9 \times 10$ voxel region as follows:
The exponential strain energy density function of Guccione et al. and Mooney-Rivlin was deactivated. Spring stiffness parameters were reduced to approx. 5% and damping was turned off, which did not result in oscillations. The tissue density was held constant. The rigidity of the fusion model was turned off.

Deformation Simulations

Deformation simulations with the described scenarios were conducted. The deformation results are displayed (fig. 7.17, 7.18, and 7.19). The movement of the apex of the half ellipsoid is similar for all three systems (fig. 7.17). The simulation with necrotic tissue shows less contraction in the lower half of the ventricle compared to simulations performed with healthy tissue (fig. 7.17(c)).
For healthy tissue, the wall at the patch shows a slight curvature towards the inside of the ventricle, whereas the necrotic patch forms a straight line, and the dilated wall bends slightly towards the outside of the ventricle.
The view from apex to base allows a better observation of the torsion for each simulation. Both simulations of pathological conditions show a reduced torsion (fig. 7.18). A comparison between maximum deformation of healthy and pathologic tissue is visualized in fig. 7.19. The figures in the left column depict necrotic tissue and the figures in the right column represent dilated tissue. Simulations of necrotic tissue revealed a reduced torsion within the healthy tissue below the pathologic area compared to simulations of healthy tissue as the surface exceeds the wireframe (fig. 7.19(a)). The symmetry of deformation of the necrotic model is sustained. This is visualized by fig. 7.19(c) and fig. 7.19(e), where the left side of the apex exceeds the wireframe and the right side remains behind it.
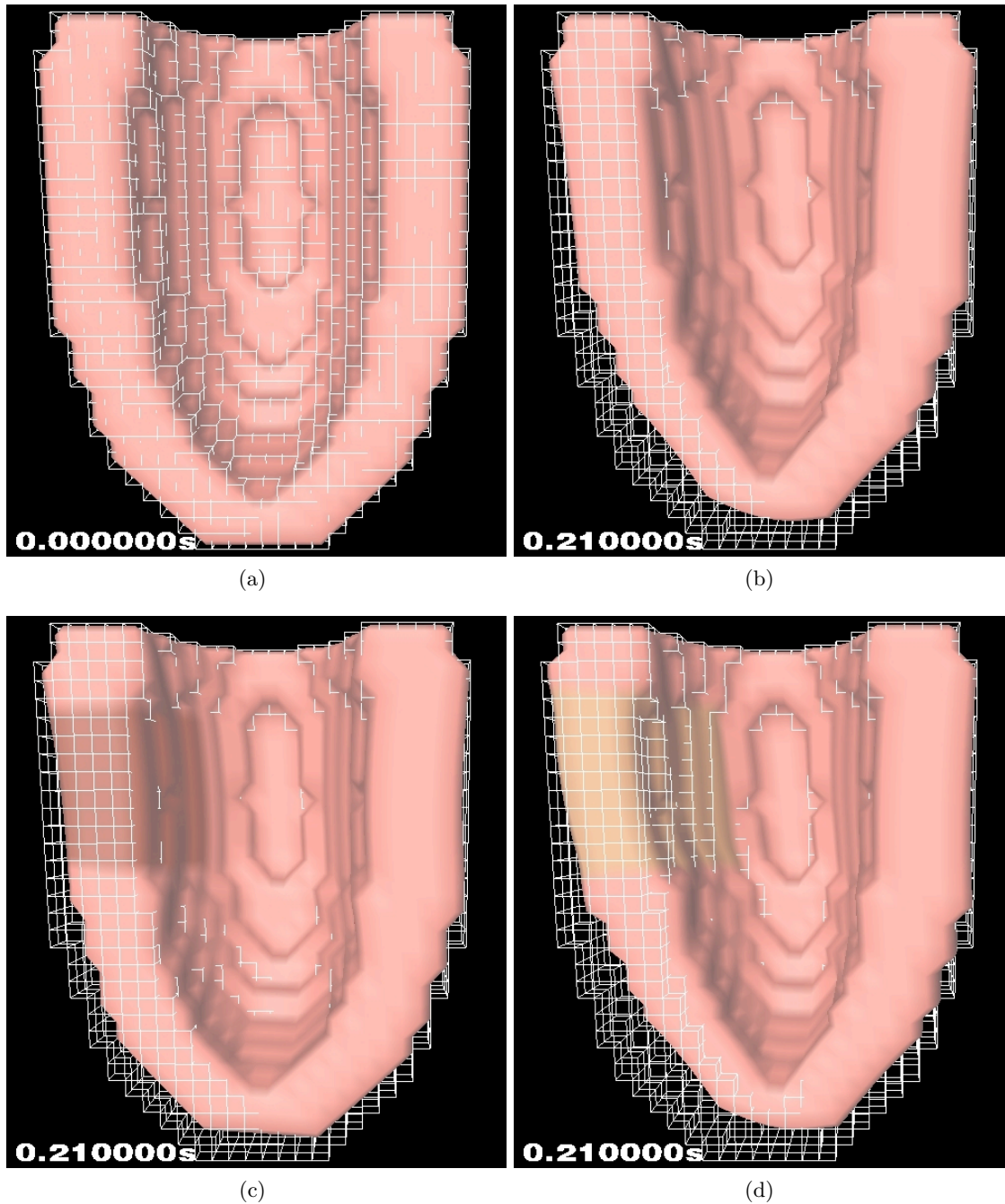
Figure 7.17. Lateral view of truncated half ellipsoid. The top row shows healthy tissue (a) at the initial position and (b) at maximum deformation. The lower row depicts pathologic tissue simulations at maximum deformation after $0.210\ s$. The patch of necrotic tissue is displayed in dark shade (c) and the patch of dilated tissue in light shade (d). The white wireframe denotes the half ellipsoid without deformation.
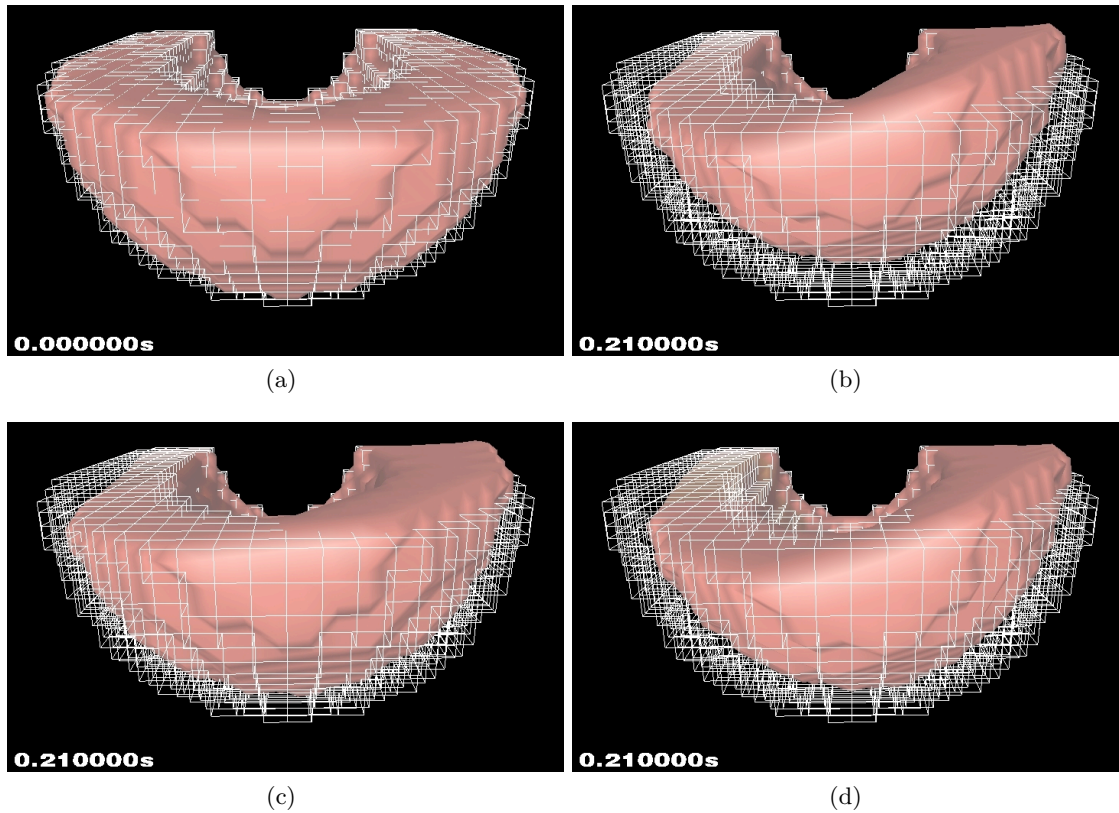
Figure 7.18. Apex view of truncated half ellipsoid. The top row figures show the healthy tissue a) at initial position and b) at full deformation. The lower row figures depict pathologic tissue simulation at maximum deformation (c) necrotic, d) dilated).

In contrast, fig. 7.19(d) and fig. 7.19(f) show that the symmetry is lost with the dilated model, as the deformed apex remains behind the wireframe at both sides. The necrotic patch keeps its width compared to a thickened wall of the healthy tissue, which is found looking at the wireframe (fig. 7.19(a) and 7.19(e)). The apex upward movement is reduced (fig. 7.19(c)). The torsion of the dilated model is stronger on the side of the pathologic area compared to healthy tissue. However, symmetry is lost as the opposite side of the patch does not exceed the healthy tissue (wireframe in front of surface rendering) (fig. 7.19(b) and 7.19(f)). Again, the apex upward movement is reduced (fig. 7.19(d)). The tissue at the patch is deformed in outward direction (fig. 7.19(f)).

(a)   (b)

(c)   (d)

(e)   (f)
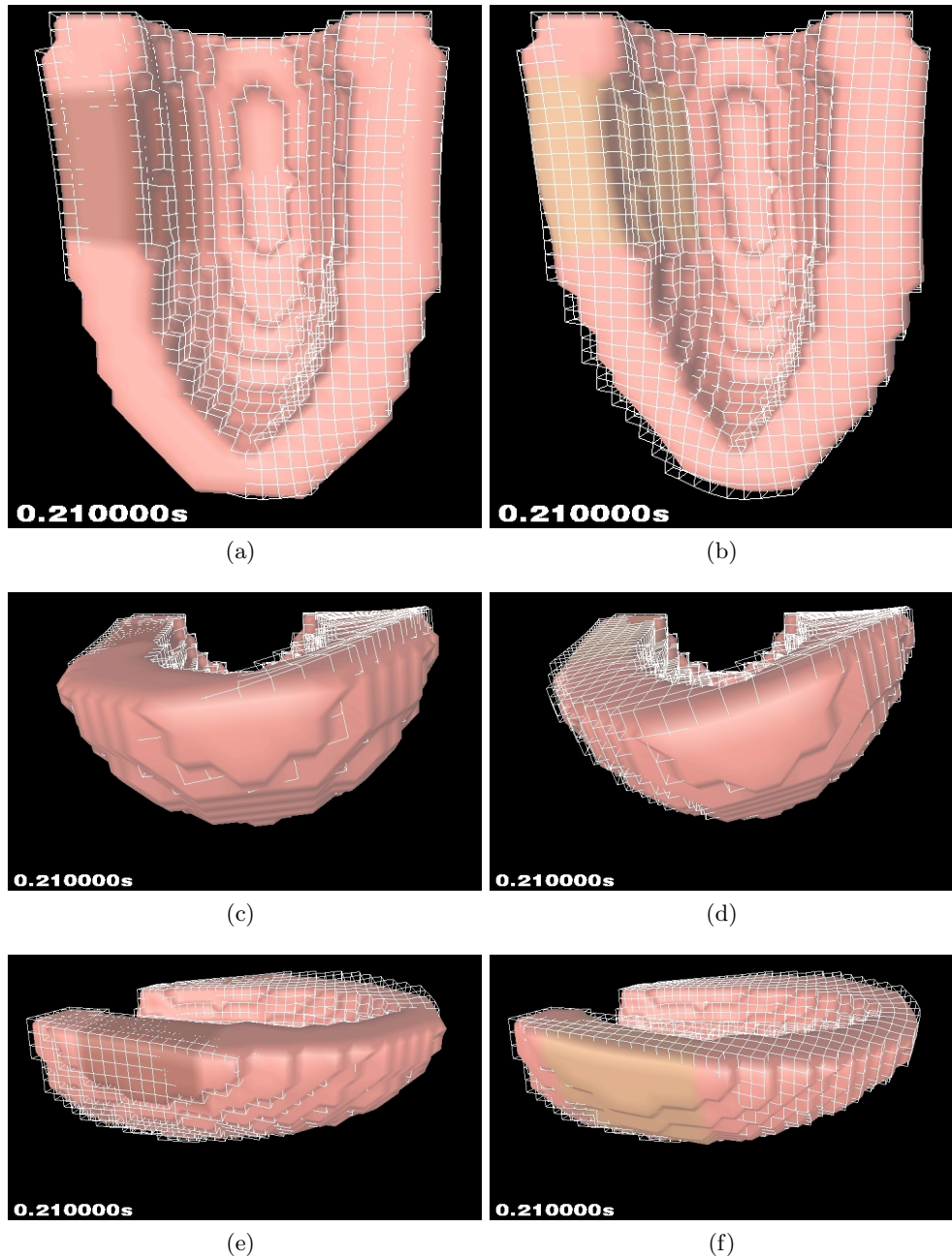
Figure 7.19. Lateral and apical view of truncated half ellipsoid at maximum deformation for pathologic scenarios. The wireframe in all pictures denotes the deformation with healthy tissue, whereas the colored surface shows pathologic simulations at 0.210 s. The left and right column display the deformation with a necrotic patch (a,c,e) and a dilated patch (b,d,f), respectively.
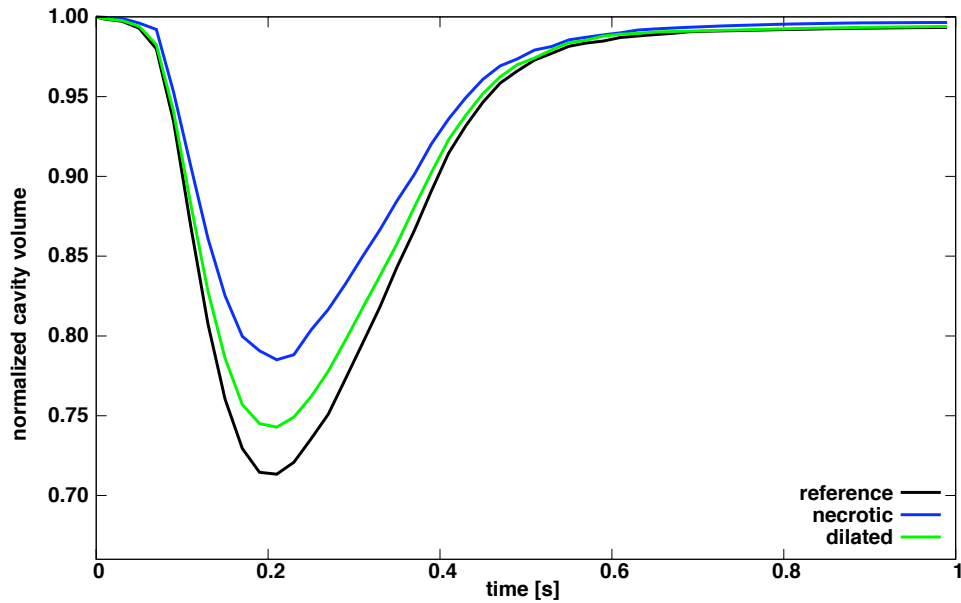
Figure 7.20. Variation of intraventricular volume change depending on the assumed all healthy, or partially necrotic, or dilated tissue.

For each simulation the cavity volume and tissue volume was computed and plotted at each time step (fig. 7.20). The graph of the normalized cavity volume shows the normalized filling volume of the ventricle model throughout the progression of a simulation sequence (fig. 7.20). The simulations of pathological conditions showed a reduced volume displacement by 7% for necrotic tissue and by 3% for dilated tissue compared to healthy conditions. The overall tissue volume decreased for healthy tissue to 91% at maximum contraction.

Conclusions

Simulations with the hybrid deformation model were conducted to evaluate the capabilities for pathologic tissue simulation. Three scenarios were investigated. The parameters were empirically chosen, as the applied ventricular geometry only approximates a real ventricle. The use of tissue properties found in literature was postponed until a measured geometry of a ventricle will be applied.

The results for the deformation show, that especially for dilated tissue, only a minor bend towards the outside is recorded. In a real pathologic case, a dilation causes a bleb (small bubble), into which blood is pressed, reducing the ejection fraction considerably. Thus, the focus is set upon adding intraventricular pressure to extend the realistic behavior of the hybrid deformation model.

7.6 Enhancing Numerical Stability

The hybrid deformation model created, proved to be stable in only a parameter range of a few percent. The range of applicable maximum force for contraction initiation was also limited to a small range. A standard sub time step included the computation of the velocity and the displacement of each mass by solving Newtons law of motion with the applied force vector field (section 5.5.3). Depending on the choice of parameters the accumulated velocities grew sometimes beyond values, which could not be compensated by reactional forces of springs, isovolumic or material constraints. This leads to an unstable system. Such a behavior is well know for conditionally stable time integration.

The system was enhanced by applying the central difference scheme, known in molecular dynamics as Verlet method, originally proposed for particle systems [199]. Jakobson [198] (section 5.5.3.2) proposed this method to improve stability of numerical integration. The method uses a velocity-less representation to compute the displacement:

$$\mathbf{x}_{i+1} = 2\mathbf{x}_i - \mathbf{x}_{i-1} + \mathbf{a}_i \Delta t^2 \tag{7.1}$$

The new position $\mathbf{x}_{i+1}$ is computed from the current position $\mathbf{x}_i$, the previous position $\mathbf{x}_{i-1}$ and the acceleration $\mathbf{a}_i$, derived from the induced forces divided by the mass. Thus, the real physical velocity is approximated by the intermediate velocity $\mathbf{v}_{i-\frac{1}{2}}$ in the last internal time step Δt assuming:

$$\mathbf{v}_{i-\frac{1}{2}} = \frac{\mathbf{x}_i - \mathbf{x}_{i-1}}{\Delta t} \tag{7.2}$$

The truncated half ellipsoid model representing a ventricle described in the previous section was used as geometrical model. However, in contrast to the previous simulations, the apex was fixed and not the valve plane. This was done due to the fact that the valve plane is pulled towards the apex during contraction (section 3.2.4). The deformation simulation of one virtual ventricular beat of 1 s duration was divided into 100 steps of 10 ms. For each step a pre-calculated force vector field was introduced to the system computed by the cellular automaton (section 6.1). The model was deformed in sub-steps until the velocity threshold was reached. Due to neglecting the preceding velocities the velocity threshold was reached with less sub-steps. This resulted instantly in a simulation time decrease to approx. 40 min, which describes the "Reference" simulation in tab. 7.1.

Numerical stability investigations with the hybrid deformation model applying the central difference scheme were conducted with varied parameters for spring stiffness, internal time sub-step, maximum of time sub-steps, and introduced force [207]. The varied parameters are given in tab. 7.1.

In addition, the approximated total amount of computation time on an Apple PowerPC G5 2GHz is listed.

	Force	Spring k	Time step	Iteration step	Simulation time
Reference	1	1	1	1	40 min
Simulation 1	10	1	1	1	40 min
Simulation 2	1	0.01	1	1	40 min
Simulation 3	1	1	1	0.1	6 min
Simulation 4	20	1	1	0.1	6 min
Simulation 5	1	0.01	1	0.1	6 min
Simulation 6	5	1	2	0.1	6 min
Simulation 7	1	1	1	0.5	26 min
Simulation 8	10	1	1	0.5	26 min
Simulation 9	1	1	2	0.5	26 min

Table 7.1. Varied parameters for stability simulations with the hybrid deformation model applying the central difference scheme. Numbers indicate factors applied to the reference simulation

The deformation of the ventricular model at the maximum induced force with the parameters from tab. 7.1 are shown (fig. 7.21 and 7.22). The fact that an increase of induced force by a factor of up to 20 led to a stable simulation shows the advantage of the method (Simulations 1, 4, 8). The reduction of spring stiffness parameter k (Simulations 2, 5) and even the decreased number of sub steps (Simulations 3 - 9) did not influence the stability of the simulations. Furthermore, the possibility to advance simulations with an internal sub time step of twice the size was tested (Simulations 6, 9). A reduction of total simulation time was achieved by varying the internal time step and the sub-time steps without apparently destabilizing the system.

Conclusions

The central difference scheme allows a greater range for parameters and is stable within limits. It is capable of stabilizing numerical simulation and reducing total simulation time, compared to the previously used Euler forward marching scheme.
The modification of the resulting deformation due to the application of the central difference scheme was not examined.
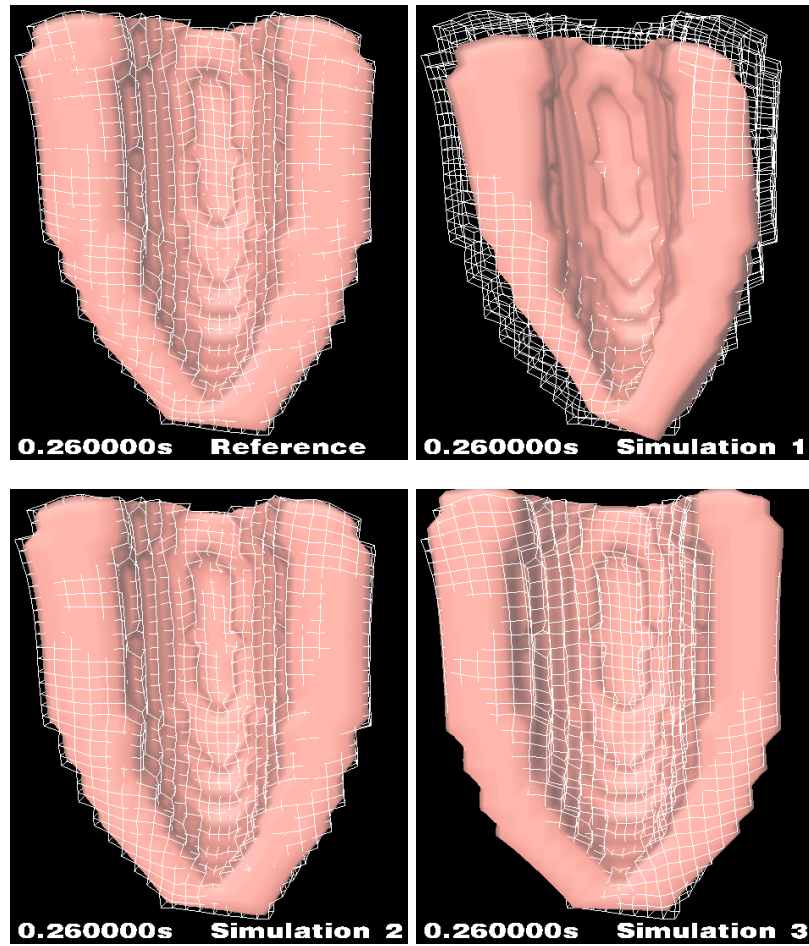
Figure 7.21. Deformation simulation with the central difference scheme. The wireframe denotes reference deformation.
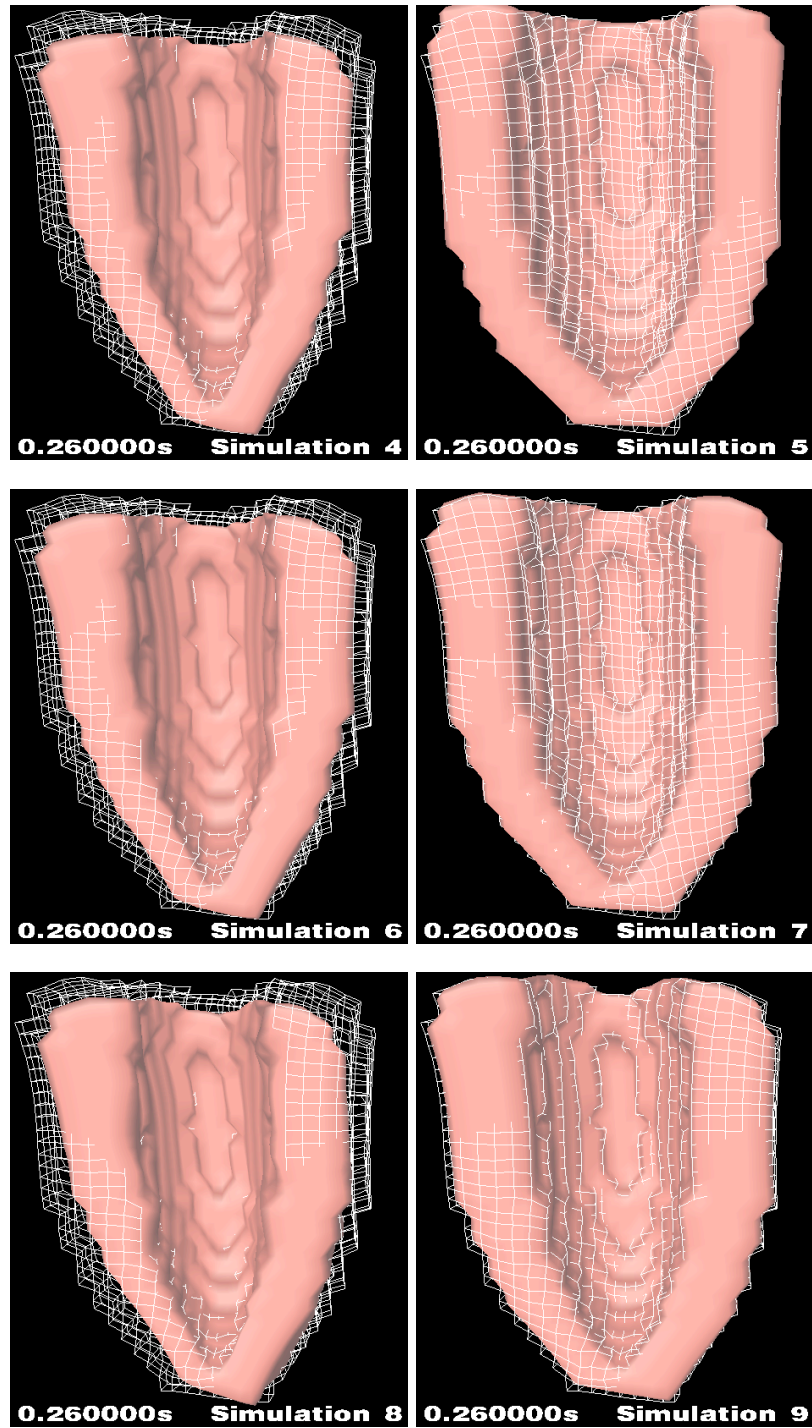
Figure 7.22. Deformation simulation with the central difference scheme. The wireframe denotes reference deformation.

7.7 Introducing Pressure Load

One part in mechanically modeling the heart consists in acquiring information about anatomy and physiology. Furthermore, the microscopic properties and behavior of myocardial tissue needs to be described by mathematical models. The other part consists of modeling blood pressure, valve functionality, and blood flow.

In the course of this work, the incorporation of blood pressure characteristics into the elastomechanical ventricular model was performed [208, 201]. The windkessel and wave pressure model from Wang et al. [161] was adapted and the relationship of pressure and intraventricular volume change was applied (section 3.4.5.1).

Confocal truncated ellipsoids provided the anatomical model of a left ventricle. The temporal and spatial force distribution was provided from simulations with the cellular automaton. A mechanical parameter set as well as a spatial force distribution was used for simulations, which resulted from previous simulations. Settings for parameters and force were not varied during pressure simulations.
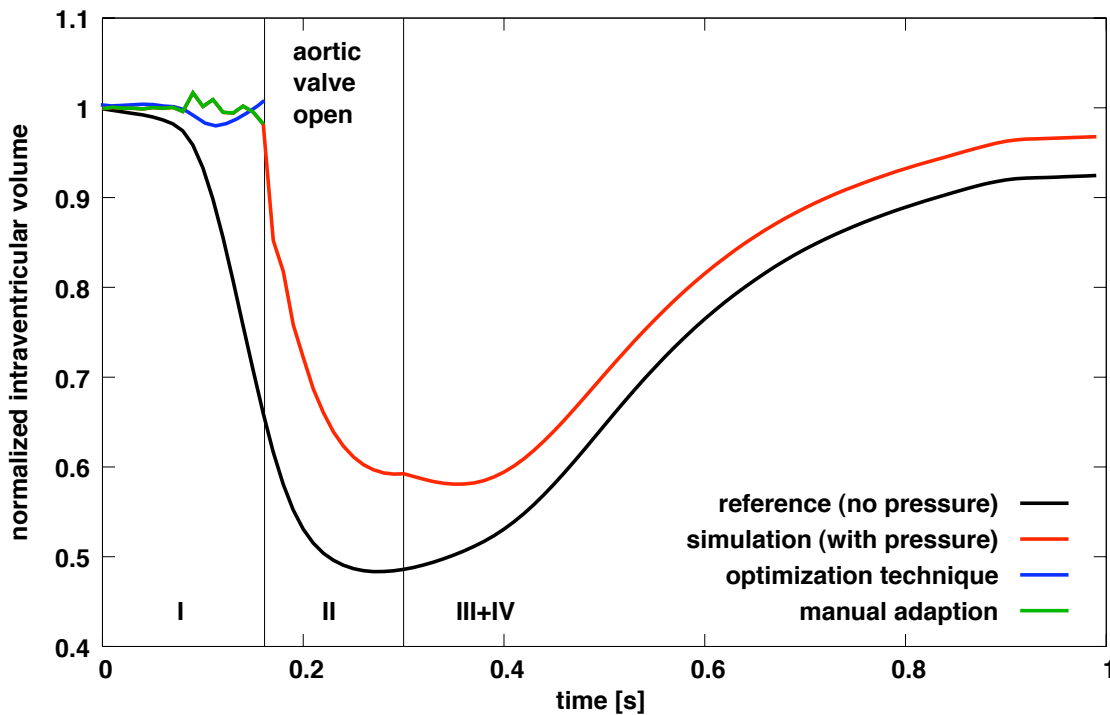
Figure 7.23. Normalized intraventricular volume. The curves describe the change of volume during deformation simulation. Vertical lines indicate the opening at $t = 0.15\ s$ and closing at $t = 0.3\ s$ of the aortic valve. The curve with applied pressure shows an oscillation of volume due to the regularization of the applied pressure depending on the volume change during phase I. A steeper decent during phase II, and a slight drop after closing of the valve, compared to the curve without pressure, is visible.
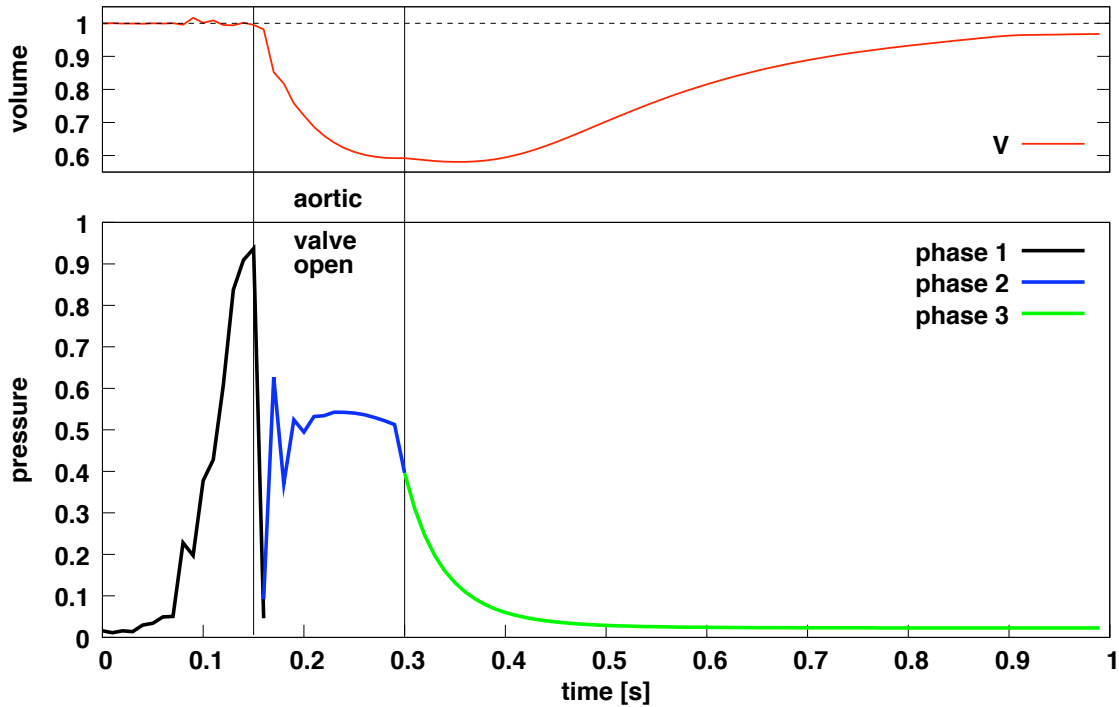
Figure 7.24. Pressure progression and intraventricular volume change. The upper graph displays the changing of intraventricular volume. The lower graph shows the three phases and the corresponding pressure time behavior. Vertical lines indicate the opening at $t = 0.15\ s$ and closing at $t = 0.3\ s$ of the aortic valve.

The pressure inside the ventricle was modeled during three of the four phases of a cardiac cycle (section 6.5.2.2). Deformation simulations were performed with the mechanical model. The difference of the intraventricular volume change in simulations with and without pressure load was recorded (fig. 7.23). The volume change in the simulation without pressure resulted in a smooth curve. The volume decreased from the beginning and fairly rapidly drops between approx. $t = 0.10\ s$ to $t = 0.20\ s$. It reached its minimum at $t = 0.25\ s$ with $\Delta V_{max} \approx 0.5$, then gradually increased again to approx. 91% of the original volume.

In contrast, the intraventricular volume curve computed with pressure load showed a horizontal line with some oscillations until $t = 0.16\ s$ (isovolumic contraction) (fig. 7.23). Furthermore, a steeper descent was visible until $t = 0.3\ s$ reaching $\Delta V_{max} \approx 0.4$. Following was a small descent until $t = 0.35\ s$ then increasing parallel to the curve computed without pressure to approx. 97% of the volume.

The pressure progression during the first three phases and the intraventricular volume are plotted together in fig. 7.24. The pressure curve during phase one was used modeling isovolumic contraction. It depended on the pre-determined displacement due to the contraction force (section 6.5.2.2). In phase two the pressure was reset to zero (see conclusions) and only the pressure due to the ejected volume as described by eq. 3.22 was applied. This resulted in a jump passing from phase one to
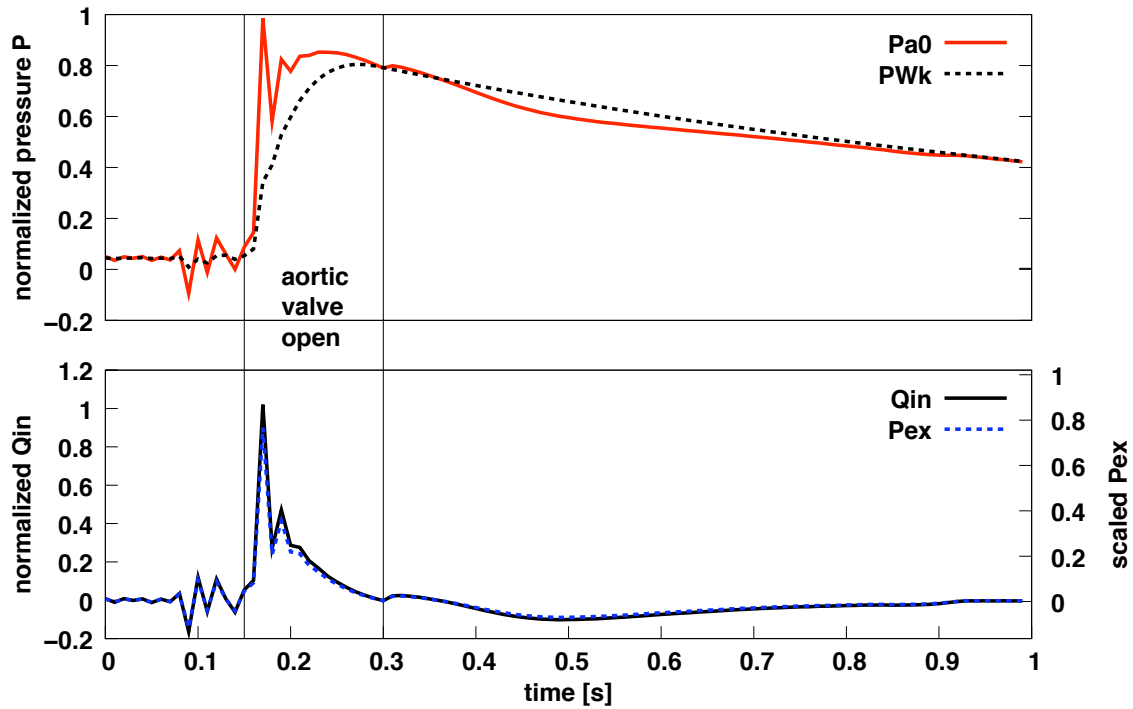
Figure 7.25. Pressure curves determined with the model of Wang and Lighthill. Model was applied during open valves only.

phase two. Starting from the offset of phase two, a rational function (eq. 6.6) described the decay in phase three (relaxation phase).

The adaptation of the model of Wang et al. was used for phase two (fig. 7.25), which marks the opening of valves and the ejection of blood into the aorta (fig. 7.26). This model was only applied during this time period, as a change in volume is needed to derive pressure. The displaced volume Q_{in} was used to compute P_{ex}, P_{Wk}, and P_{A0} (section 6.5.2.2). The displacements during the deformation simulation were recorded and are displayed for a sequence of timesteps (fig. 7.27).
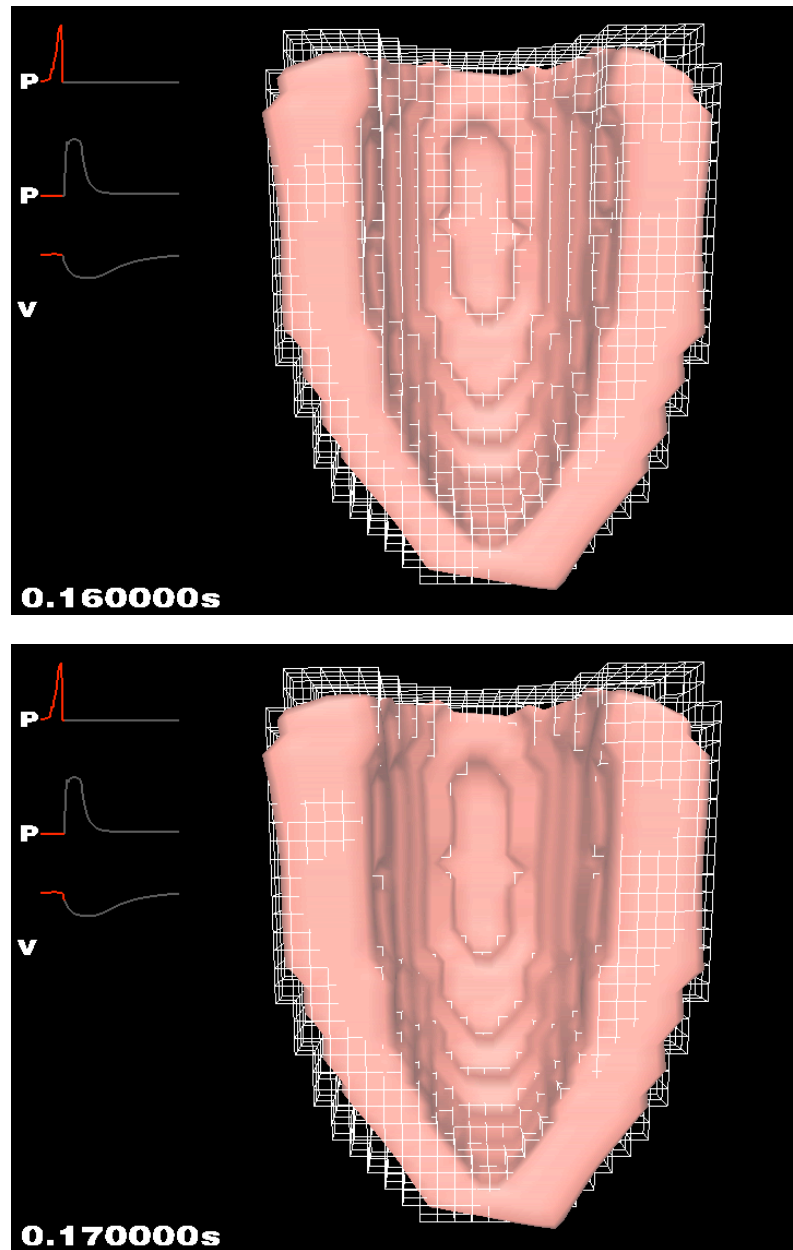
Figure 7.26. Lateral view of deformed truncated half ellipsoids at valve opening. The white wireframe denotes an undeformed ellipsoid. The figures show the deformation before (top) and after the valve opening (bottom). After the valves opened, the wireframe at the inner wall is not visible. This is due to a quick inward motion, resulting from the release of pressure in the ventricular cavity.
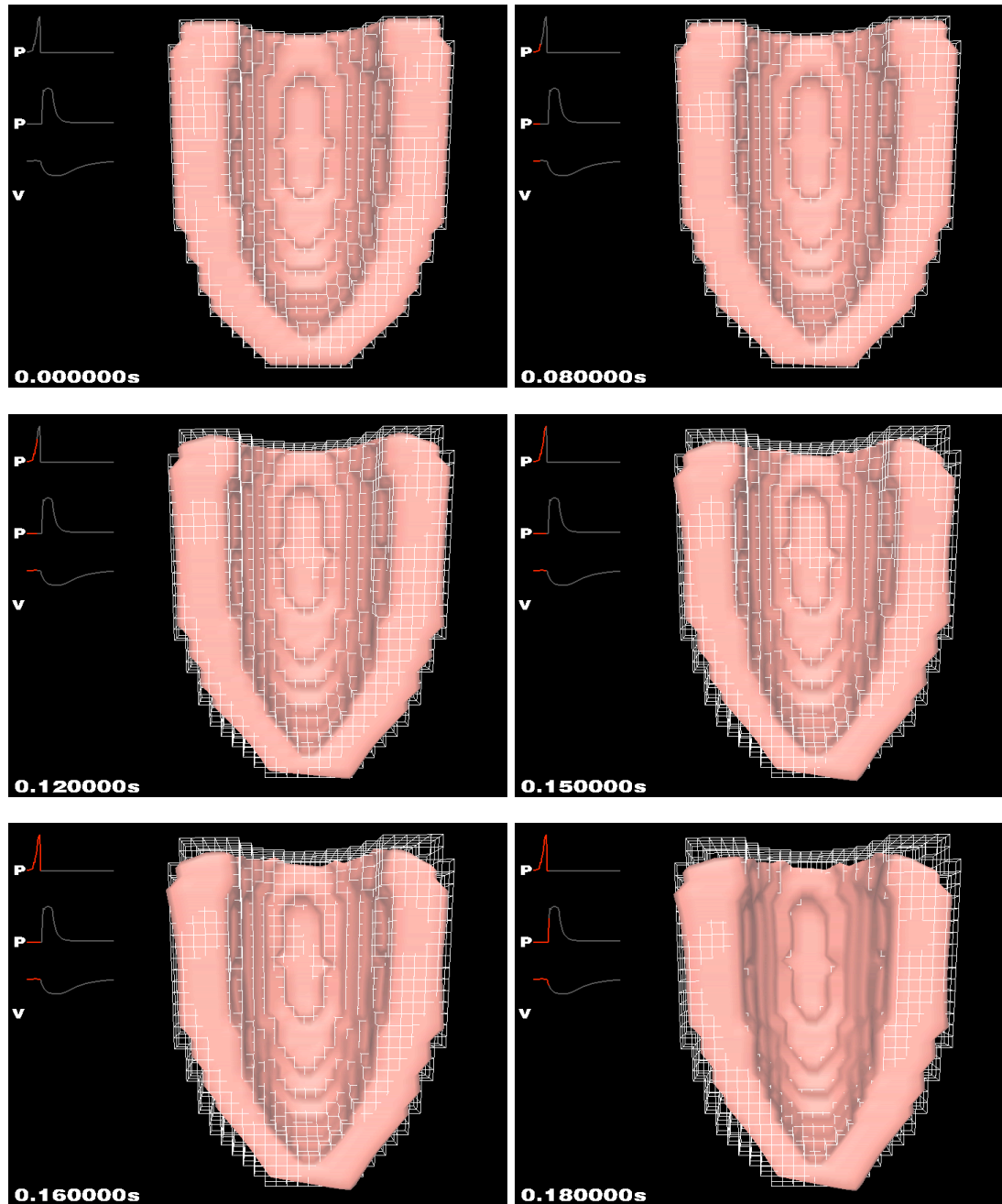
Figure 7.27. Lateral view of a deformed truncated half ellipsoids at successive timesteps. The white wireframe denotes an undeformed ellipsoid. The deformation shows the isovolumic phase, where only small deformations towards the inside occur ($t = 0$ s to 0.16 s), until the valves open. The curves in each figure from top to bottom show the pressure in the isovolumic phase, the pressure during ejection and relaxation phase, and the intraventricular volume (for continuation see fig. 7.28).
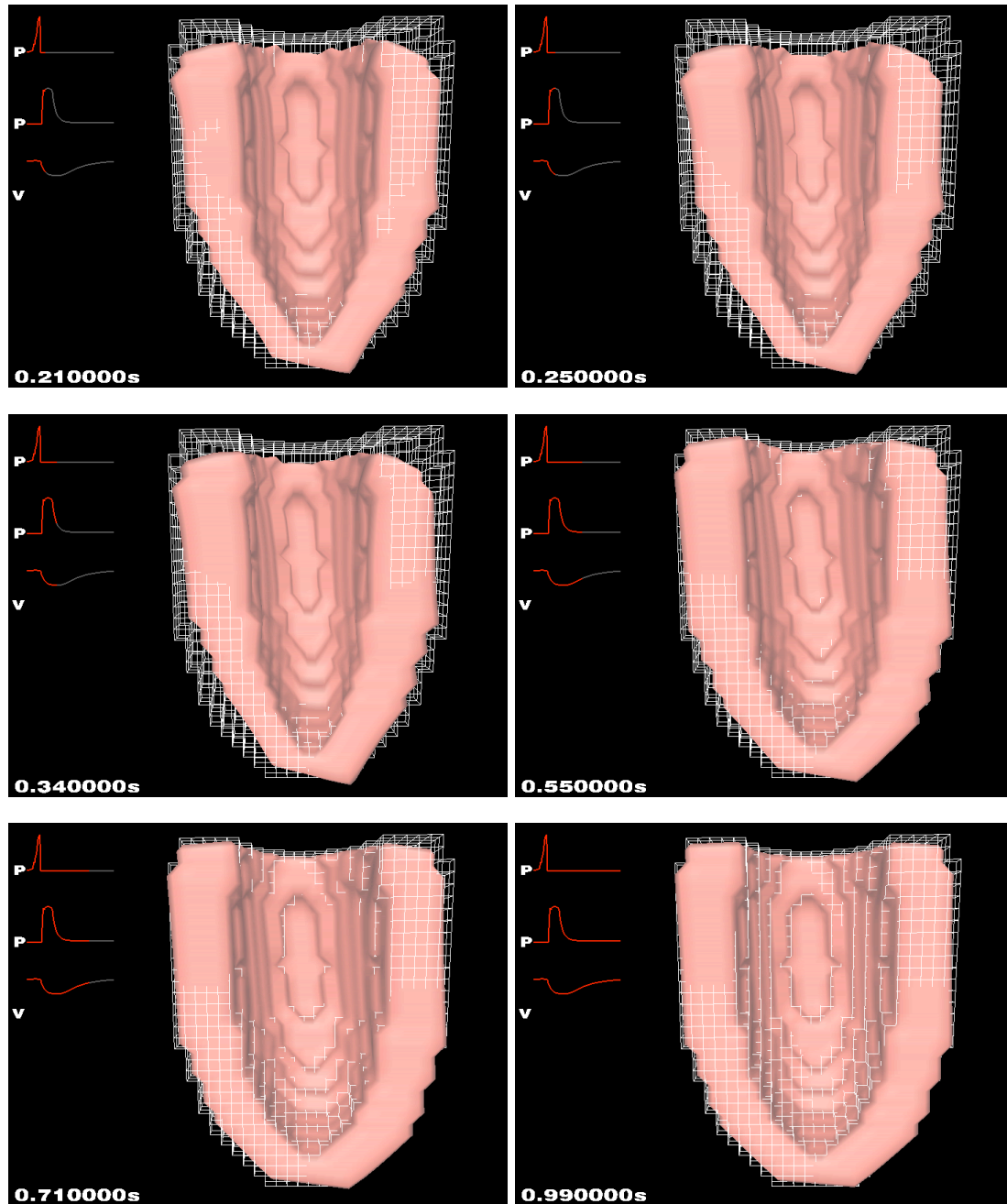
Figure 7.28. Lateral view of deformed truncated half ellipsoids at successive timesteps (continued from fig. 7.27) with ejection phase ($t = 0.18\ s$ to $0.30\ s$) and relaxation phase ($t = 0.30\ s$ to $0.99\ s$).

Conclusions

Phase one (fig. 7.24) shows a steep raise in pressure until $t = 0.15$ s, which resembles recordings in the literature [17]. Oscillations in the pressure and volume curves during this phase are caused by an unprecise approximation of the pressure to volume relationship. This can be enhanced by using smaller timesteps and eventually using more sophisticated mathematical methods to derive adapted pressure values.

During phase two, the proposals of Wang et al. were followed. The ejection volume was acquired and resulted in a pressure curve. The oscillating peaks shortly after valve opening are due to the size of timestep, the passover from phase one, and the fast ejection. This phase describes the atrial pressure curve and should start with the offset pressure of the atrial base pressure. Hence, the pressure curve should commence with the offset pressure given by the peak of phase one. However, the forces driving the contraction in phase two were not able to sustain the pressure offset given by phase one. It is shown that the pressure peak of phase one is almost twice the size of the pressure generated by the model of Wang et al.. Therefore, further investigations need to be conducted, focusing on the crossover from pressure phases. Furthermore, the applied forces need to be reevaluated, since electrophysiological and force development models were used, based on fully relaxed muscle fibers.

Phase three resembles the isovolumic relaxation, where the pressure was modeled by a simple rational function. This decay was chosen to approximate the decay found in fig. 3.6, III. Although modeling of phase four has only a minor impact on the deformation model, it should be taken into account to complete the model for a full cardiac cycle.

The normalized intraventricular volume with and without applied pressure was plotted in fig. 7.23. In the isovolumic contraction phase the curves show an explicit difference between simulations with and without pressure. The curve with pressure shows slight oscillations during $t = 0$ s and $t = 0.15$ s. The steeper decent in the pressure simulations during opened aortic valve indicates a faster ejection of blood into the aorta. At the border from phase two to three, another descent of the volume curve is visible. An investigation revealed that the intraventricular pressure in phase three decays faster than the contraction initiating force. Therefore, another slight contraction takes place in phase three. However, this issue can be addressed by applying force development models with different shape or contraction dependent force generation models instead of static models. Furthermore, phase III resembles the phase of isovolumic relaxation, where all valves are closed and hence the volume does not change. Thus, the delayed start of volume increase resulting from the pressure model appears more realistic than the steep increase of the volume curve of the model without pressure.

7.8 Parameter Improvement of the Pressure Model

The modeling of a measured pressure can be achieved by the means presented in the previous section. The realistic adaptation of the consisting pressure model for the confocal truncated ellipsoids was done by scaling the introduced pressure values during phase one to the corresponding value in $mmHg$, which is a common unit used, when measuring pressure inside the human body [201]. Conversion factors for $mmHg$ are:

$$1.00\,atm = 760.0\,mmHg = 101.325\,kPa = 101\,325\,Pa = 101\,325\,\tfrac{N}{m^2}$$

with atm the unit atmosphere, $mmHg$ millimeters of mercury, Pa Pascal, kPa kilo Pascal, N Newton, and m meter.

Wang et al. [161] also used $mmHg$ as unit for their computations. Thus, a uniform pressure curve was established applying phase dependent models (fig. 7.29). The end-diastolic atrial pressure was applied as lower limit for the simulation. This means that the pressure calculation was started and finished with an offset, set by the end-diastolic atrial pressure.

Deformation simulations with the presented pressure models were conducted and parameters and pressure values were given by Wang et al. (fig. 7.29 and 7.30). The measurements of Wang et al. were conducted upon dog hearts, thus pressure values resemble those of a dog not a human. An adaptation to human pressure values must be carried out, when applying a measured data set of a human left ventricle. In contrast to the previous pressure computations (section 7.7) the pressure in fig. 7.29 resembles in close detail data in the literature (fig. 3.6). The proportion of the isovolumic phase of 50 ms as well as the ejection phase of approx. 200 ms were met. However, the intraventricular volume change shows still the extra descent when passing from phase II to III (fig. 7.30).

Therefore, the $mmHg$ scaling factor was reduced, resulting in an almost doubled intraventricular pressure for the model (fig. 7.31). Due to this reduction, the pressure in the isovolumic phase increased, resulting in a later opening of the valve and a pressure peak at the passover from phase I to II. The sudden pressure peak cannot be damped out by the model of Wang et al. and results in a strong oscillation during phase II. The ejection volume depends on the intraventricular pressure, hence it oscillates in phase II. Only about 25% of the volume is ejected (fig. 7.32) compared to 40% in the previous simulation (fig. 7.30). In addition, the pressure decay during the relaxation phase was reduced to avoid an extra descent of the volume curve. This measure resulted in a smooth curve, but led to an expansion of the ventricle beyond the initial volume.

Conclusions

In summary, intraventricular pressure heavily influences the contraction of the ventricle. An adapted pressure must be used depending on the ventricle geometry and on the amplitude of the contraction initiation force. The hybrid deformation model is capable of interacting with boundary conditions namely intraventricular pressure. Further pressure adaptation to the truncated ellipsoids were postponed for simulations with measured data of human ventricles.
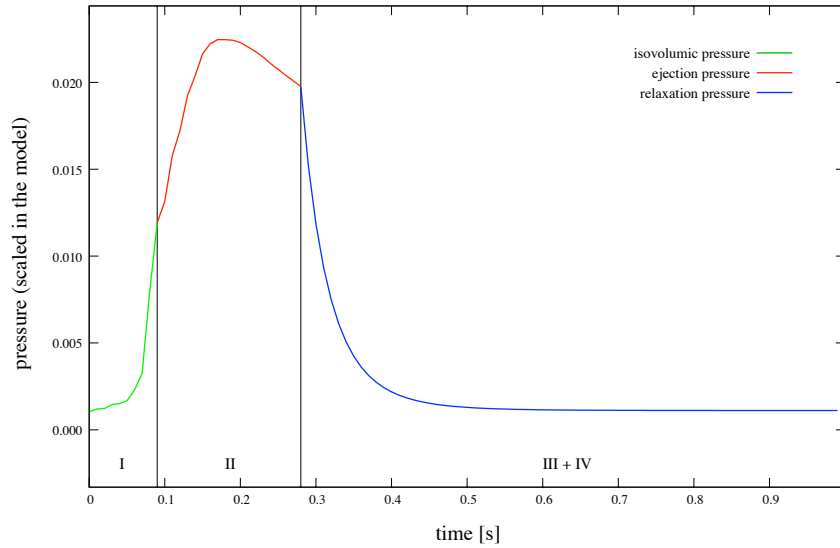
Figure 7.29. Total computed pressure during deformation simulation. The ventricular pressure consists of three curves for the different cardiac phases. Phase I describes the pressure during isovolumic contraction, phase II the pressure during the ejection of blood into the aorta following the model of Wang et al., and phase III and IV the relaxation phases modeled by a rational function.
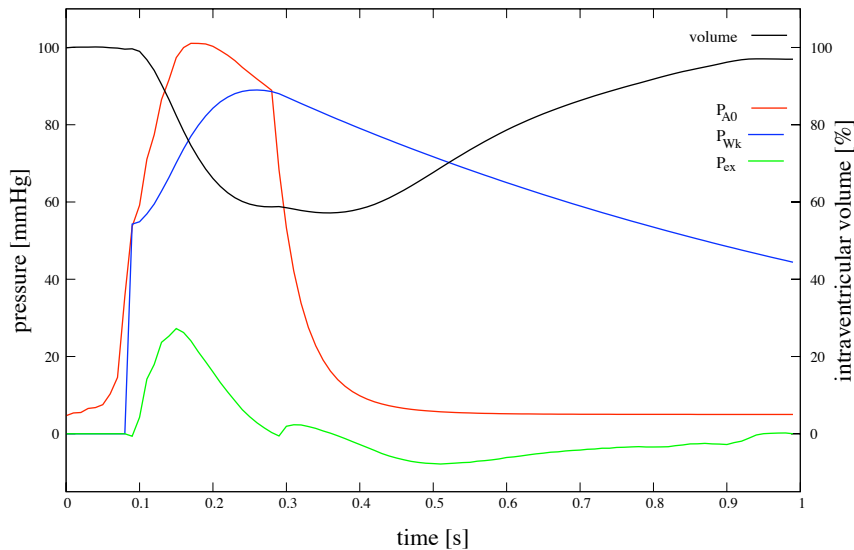
Figure 7.30. Pressure and volume change during deformation simulation. The aortic pressure P_{A0} consists of the Windkessel pressure P_{Wk} and the pressure due to wave motion P_{ex}. The Windkessel pressure as well as the wave motion pressure are displayed for phases II to IV but applied only for phase II. In addition, the change in volume is displayed.
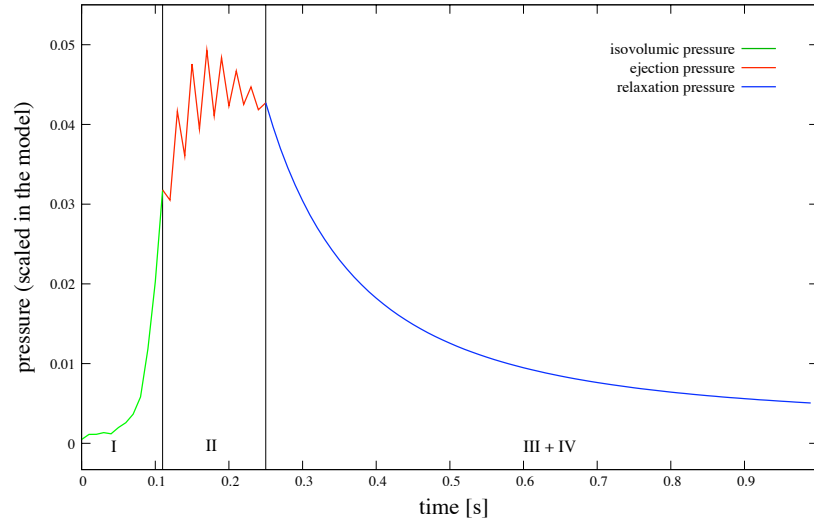
Figure 7.31. Total modeled pressure during deformation simulation with varied parameters. Due to the reduction of the scaling factor, the pressure during the isovolumic phase increases, resulting in a delayed opening of the valve and a pressure peak at the passover from phase I to II. An oscillation occurred during phase II. The reduced decay in the relaxation phase caused the pressure curve to end above the atrial pressure.
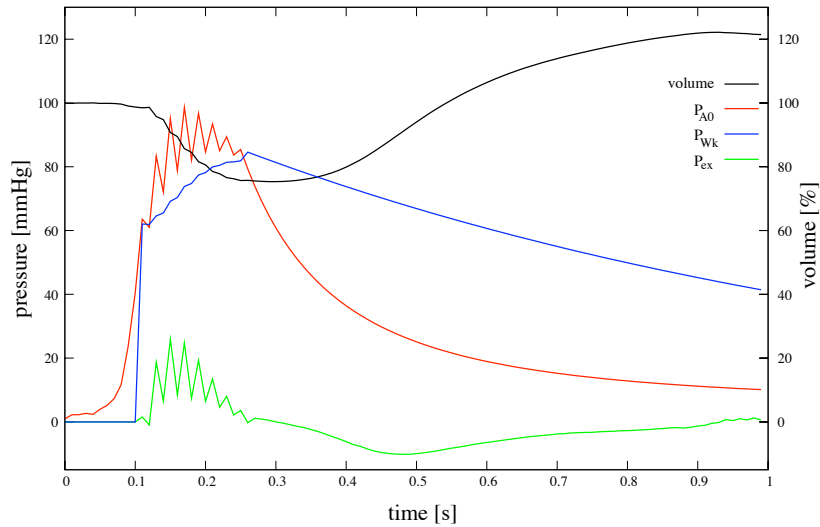
Figure 7.32. Pressure and volume change during deformation simulation. The aortic pressure P_{A0} consists of the Windkessel pressure P_{Wk} and the pressure due to wave motion P_{ex}. The Windkessel pressure as well as the wave motion pressure are displayed for phases II to IV but applied only for phase II. In addition, the change in volume is displayed. An oscillation occurred during phase II. A reduced pressure decay in the relaxation phase caused an unrealistic expansion of the ventricle at $t = 0.5\ s$ to more than 100% volume.

7.9 Pathologic Tissue and Pressure Load

One indication of a malfunctioning heart is the ejected volume. Pathologies of the tissue reduce the hearts ability to eject as much blood into the aorta as needed by the body. As a result the patients physical abilities are reduced.

As an example of heart pathologies, a patch of tissue was altered in its contractility. Deformation simulations showed that pathologic tissue can be modeled with the hybrid deformation model (section 7.5). However, proper tissue behavior can only be examined including intraventricular pressure. Therefore, in the course of this work, simulations of section 7.5 were repeated including the intraventricular pressure found in section 7.8 [201].

The ejected volume of necrotic and dilated tissue is smaller compared to healthy tissue (fig. 7.33). The same effect can be seen conducting simulations with pressure (fig. 7.34). The comparison of ejected volume simulations with and without pressure shows a significant difference of approx. 10%. The pressure generated by the ventricle with pathologic tissue is reduced by approx. 10% - 12% (fig. 7.35). Visualization of the ventricle at maximum contraction force shows, that the pathologic tissue bends to the outside as a result of acting pressure. This causes a so called bleb for a patch of dilated tissue (fig. 7.36(d)). The necrotic tissue also shows an outward bend, but can restrain the acting pressure much better (fig. 7.36(c)).

The different material properties of the pathologic patch result in a smaller torsion of the left upper side of the ventricle (fig. 7.37). The reduced torsion of the pathologic patch and the adjacent tissue can be differentiated by visualization of healthy tissue deformation vs. pathologic deformation (fig. 7.38). In this case the wireframe shows deformation of healthy tissue and the rendered surface the deformation of pathologic tissue. The torsion of the pathological deformation on the left side of the ventricle is smaller when the rendered surface is positioned in front of the wireframe.

Conclusions

The comparison of deformation results acquired with and without pressure load reveals, that the pressure is a key factor in modeling pathologies, besides the elasto-mechanical properties of the tissue itself. Simulations without pressure show a recognizable change in ventricular deformation, however the pathological consequences can only be received by including intraventricular pressure. Further analysis of the change of mechanical properties of pathologic tissue must be examined to parameterize the hybrid deformation model.
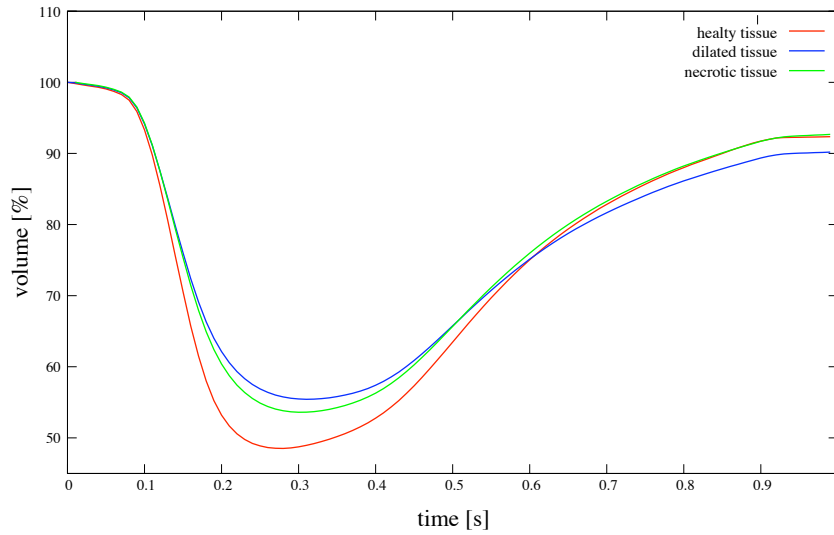
Figure 7.33. Volume change with healthy and pathologic tissue without pressure load during deformation simulation.
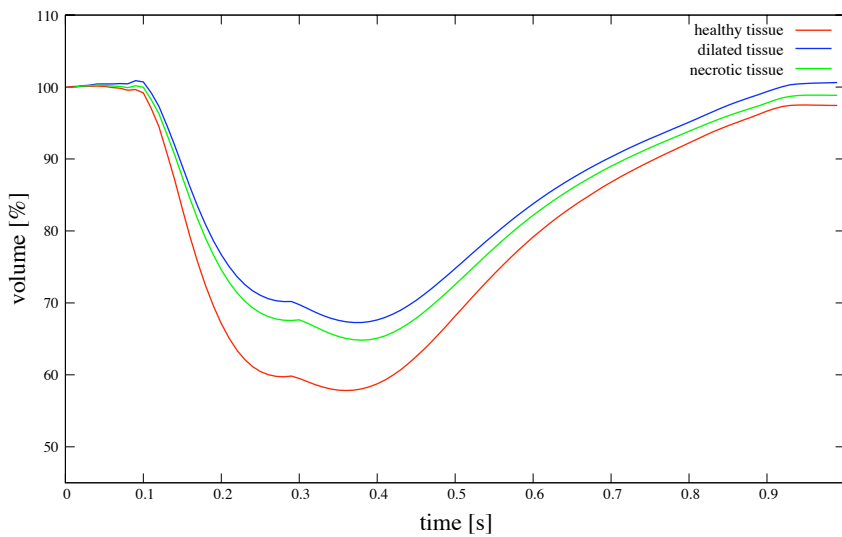
Figure 7.34. Volume change with healthy and pathologic tissue and pressure load during deformation simulation. The extra descent is still visible, which is caused by the faster descent of the pressure curve compared to the contraction initiation force (section 7.7).
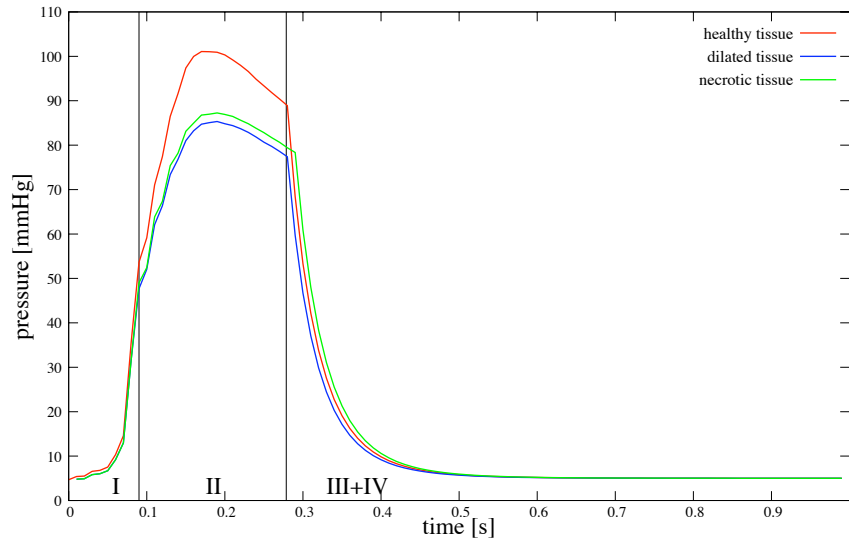
Figure 7.35. Pressure of healthy and pathologic tissue during deformation simulation. During isovolumic contraction (phase I) the same pressure curve for all simulations was applied. During phase II the reduced intraventricular pressure resulted from the reduced ejected volume.
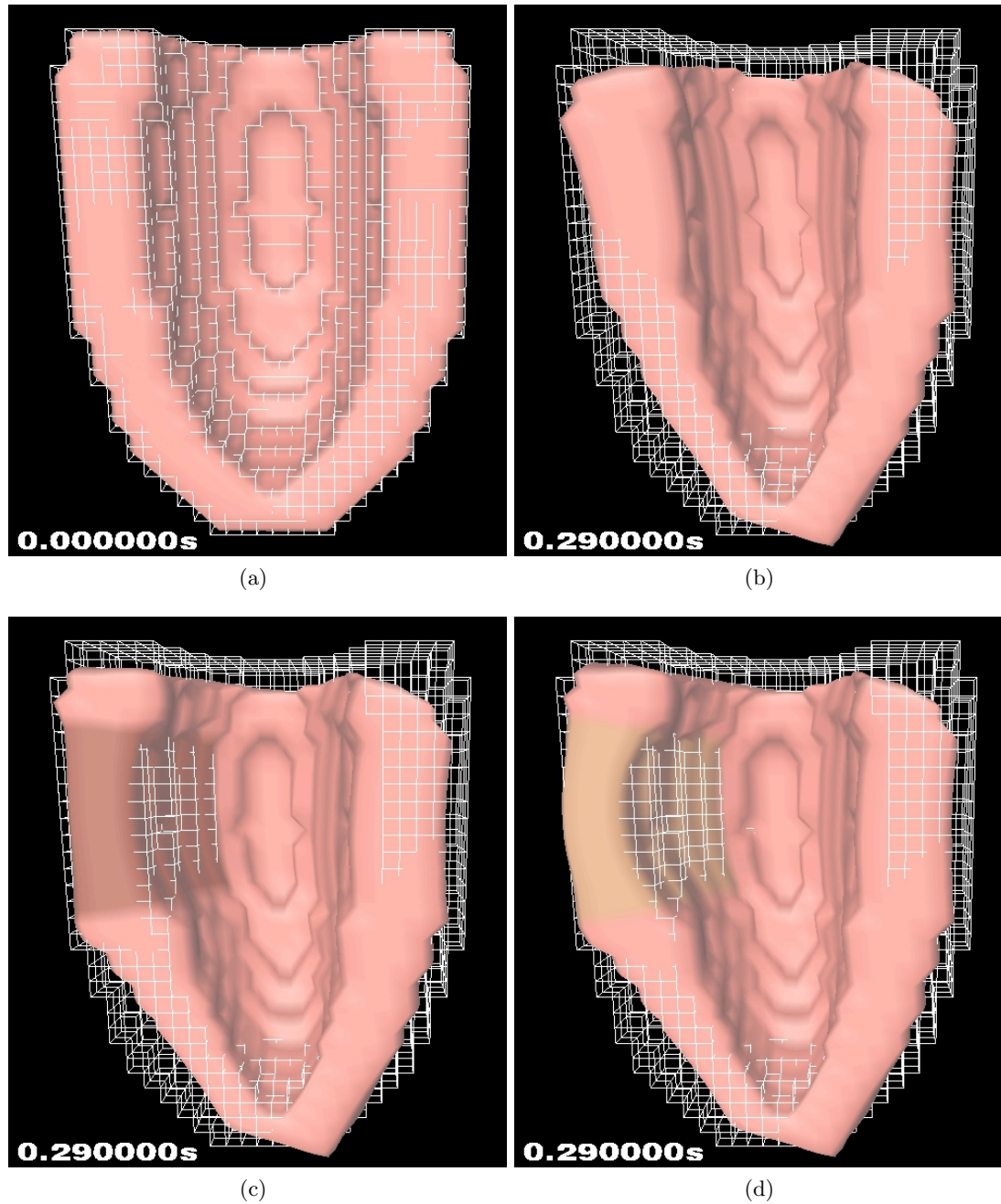
Figure 7.36. Lateral view of truncated half ellipsoid including pressure load. The top row figures show healthy tissue (a) at initial position and (b) at maximum deformation. The lower row figures depict simulation results with pathologic tissue at maximum deformation (0.290 s). The patch of necrotic tissue is displayed in dark shade (c) and the patch of dilated tissue in light shade (d). The white wireframe denotes an half ellipsoid without deformation.

(a)

(b)

(c)

(d)
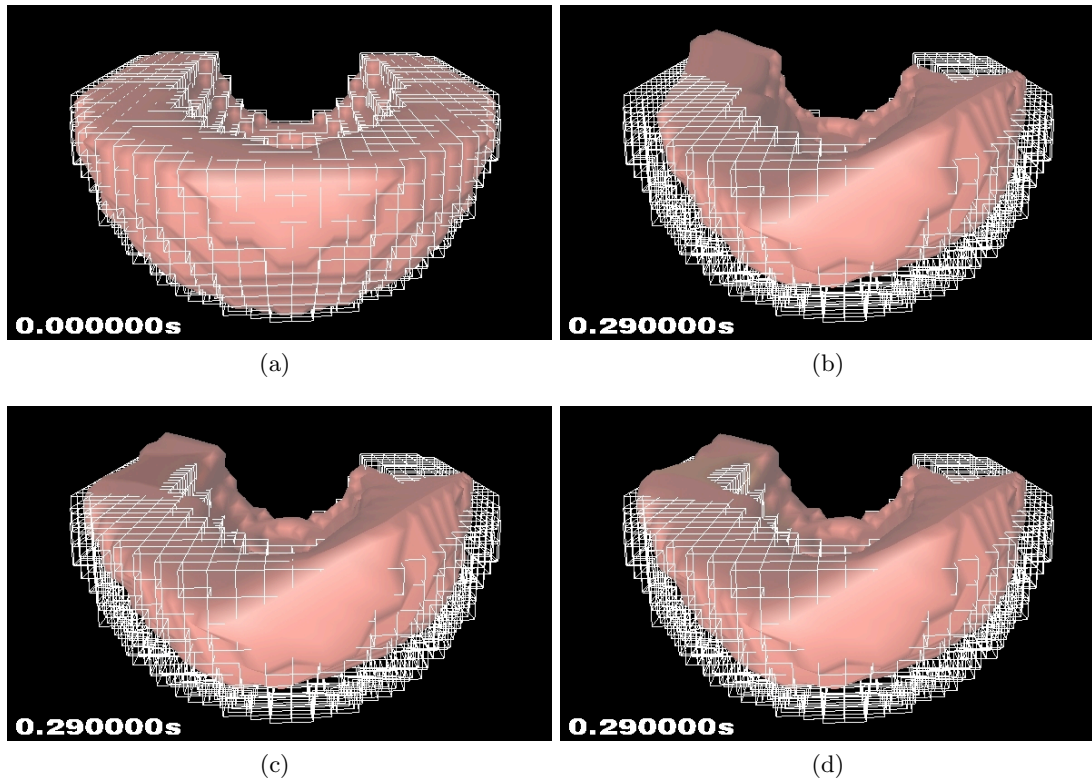
Figure 7.37. Apex view of the truncated half ellipsoid including pressure load. The top row figures show healthy tissue and the lower row figures depict pathologic tissue simulation at maximum deformation (c) necrotic, d) dilated).
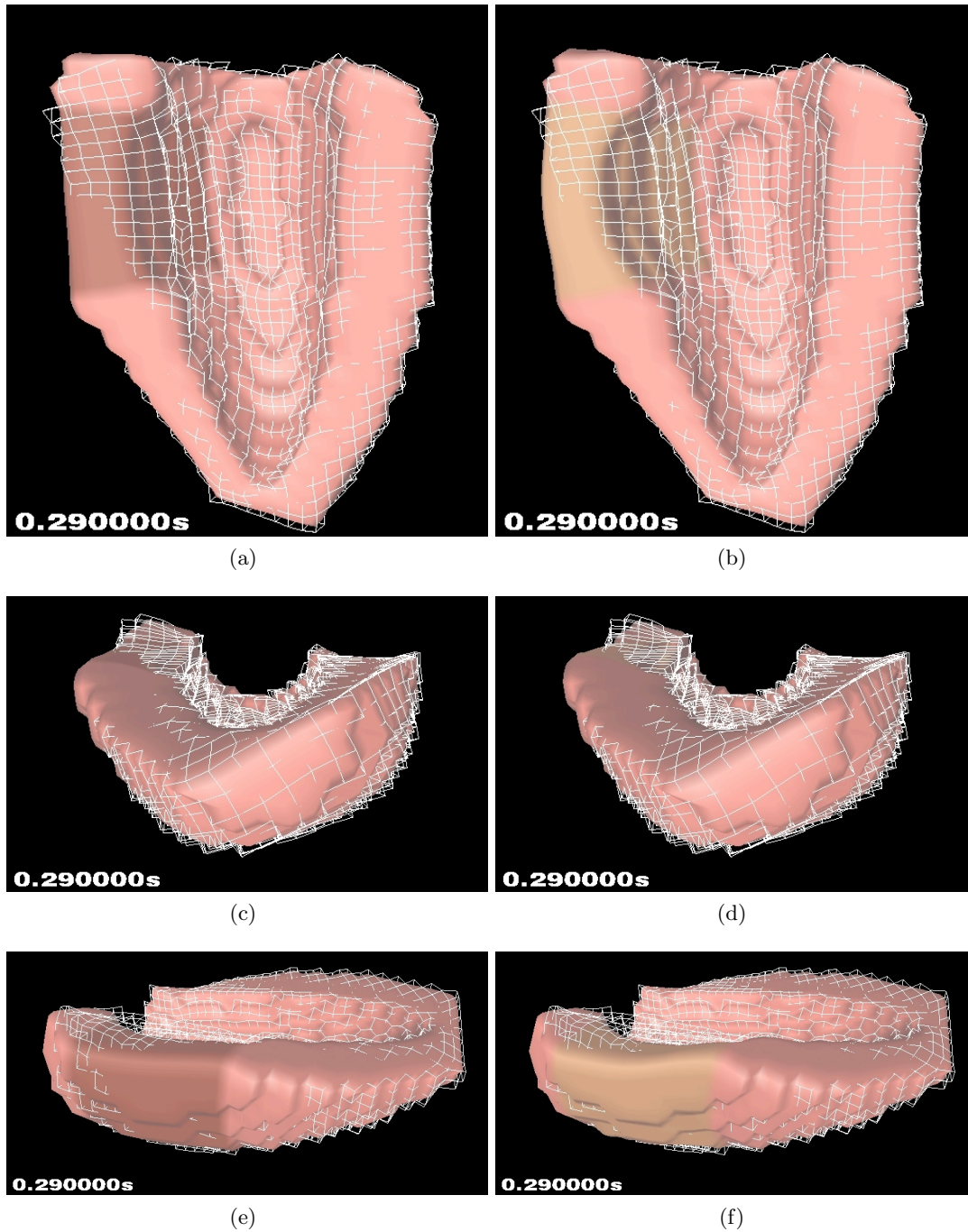
Figure 7.38. Lateral and apex view of truncated half ellipsoids at maximum deformation for pathologic scenarios including pressure load. In all pictures, the wireframe denotes the deformation with healthy tissue, whereas the rendered surface shows pathologic simulations at $0.290\ s$. The left and right column display deformations with a necrotic patch (a,c,e) and a dilated patch (b,d,f).

7.10 Pressure with Different Force Model

The plots of intracellular volume from the previous sections indicate, that the pressure during relaxation decays faster than the contraction force declines. This results in an additional contraction in the relaxation phase.

Thus, simulation series were conducted applying the force development model of Rice et al. [134]. The force curve has a quicker upstroke as well as a steeper descent (fig. 7.39). Deformation simulations were conducted with the same geometry and pressure setup of section 7.9 and healthy tissue. The tissue deformation did not differ visibly, however, the intraventricular volume shows a significant deviation (fig. 7.40). More volume is ejected with the Rice model indicated by the minimum of the volume at approx. 50% compared to the Glänzel model of only 60%. Furthermore, the relaxation phase shows a negligible descent only at the crossover from phase II. The cardiac phases are time shifted due to the fact that the pressure marking the opening of valves is reached earlier by the Rice model. This results in a reduced isovolumic phase, too.

Conclusions

The force model is one factor leading to the extra descent of the intraventricular volume. The notch at the passover from phase II to phase III could be partly compensated by applying a different force model. Another factor influencing the behavior might be found in the application of the decay function during phase III.
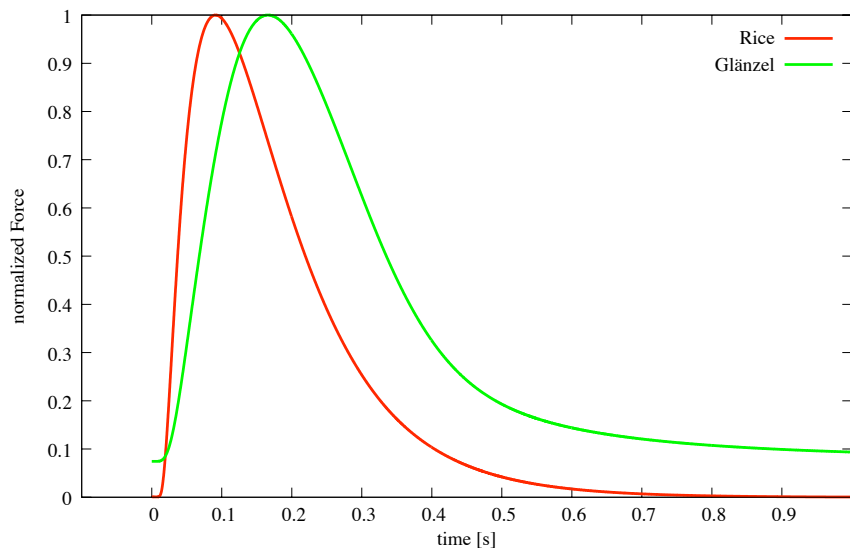
Figure 7.39. Force curve for models of Rice et al. and Glänzel et al.. The force curve of Rice shows a steeper increase and a steeper descent of the force compared to the model of Glänzel. The model of Glänzel starts and declines to an offset of approx. 0.98.
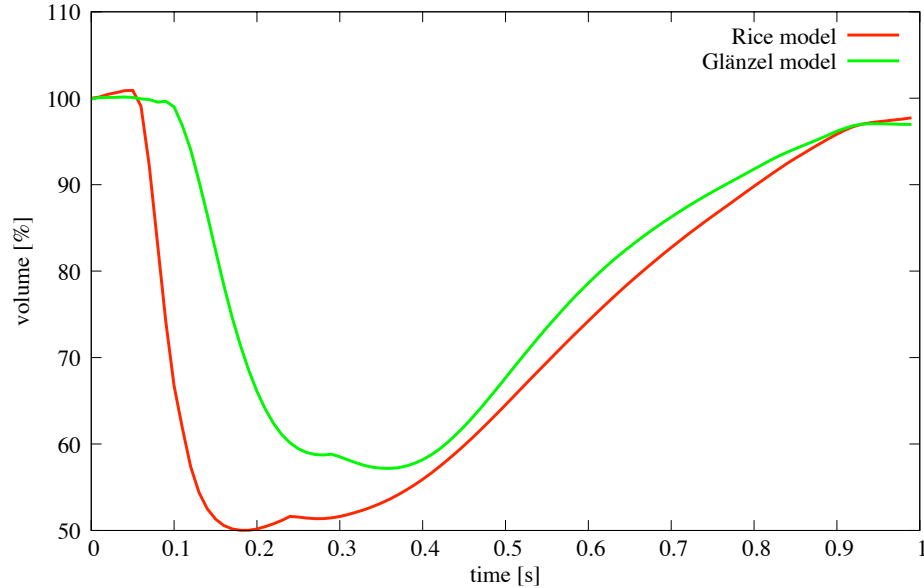
Figure 7.40. Intraventricular volume change for force model of Rice et al. and Glänzel et al.. The curve determined with the Rice model shows a shorter isovolumic phase, a steeper descent, a higher displaced volume, and a smaller extra descent compared to the volume change of the model of Glänzel et al.

7.11 Pressure Adaption for Phase III

The results of the previous section indicate that the contraction initiation force is not the only factor responsible for the edge at the passover.

Therefore, the simulations were repeated applying the model of Glänzel, since pressure components were optimized for this model. However, for modeling phase III+IV the exponential decay (eq. 6.7) was applied (fig. 7.41). This function takes the actual intraventricular volume into account, too. Simulations depicted that the edge at the passover could be smoothed, however slight oscillations were introduced during phase III (fig. 7.42). These oscillations result in the volume factor V given by the exponent in eq. 6.7, where the coupling of the pressure with the volume change is described.

Conclusions

Pressure adaptation with a changed force model (section 7.10) results in a better approximation of volume ejection during simulations. However, the application of the exponential function for modeling the pressure decay during phase III resulted in a realistic volume ejection curve of the heart.
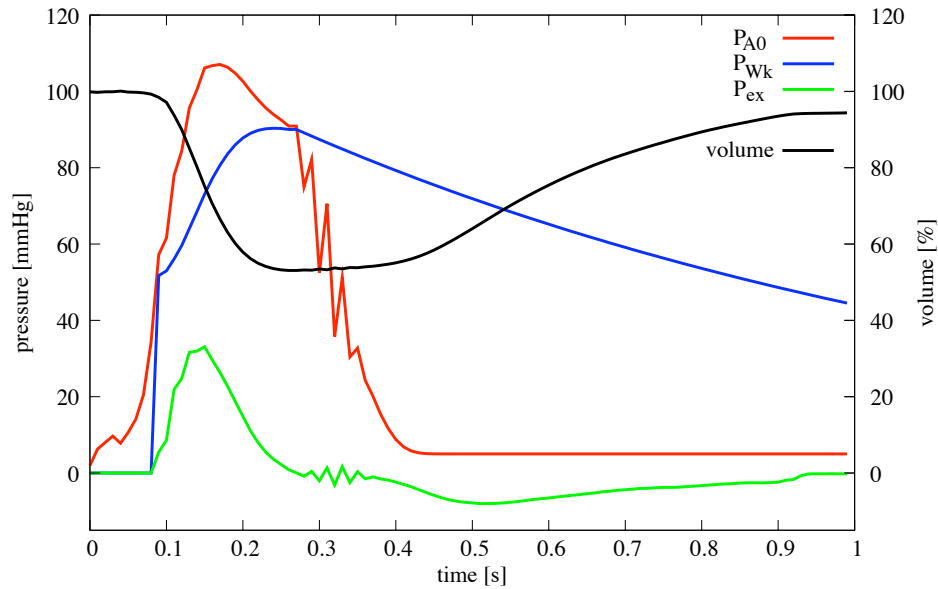
Figure 7.41. Pressure and volume change determined with an exponential pressure decay for phase III. At the beginning of phase III oscillations occur due to the incorporation of volume dependent pressure.
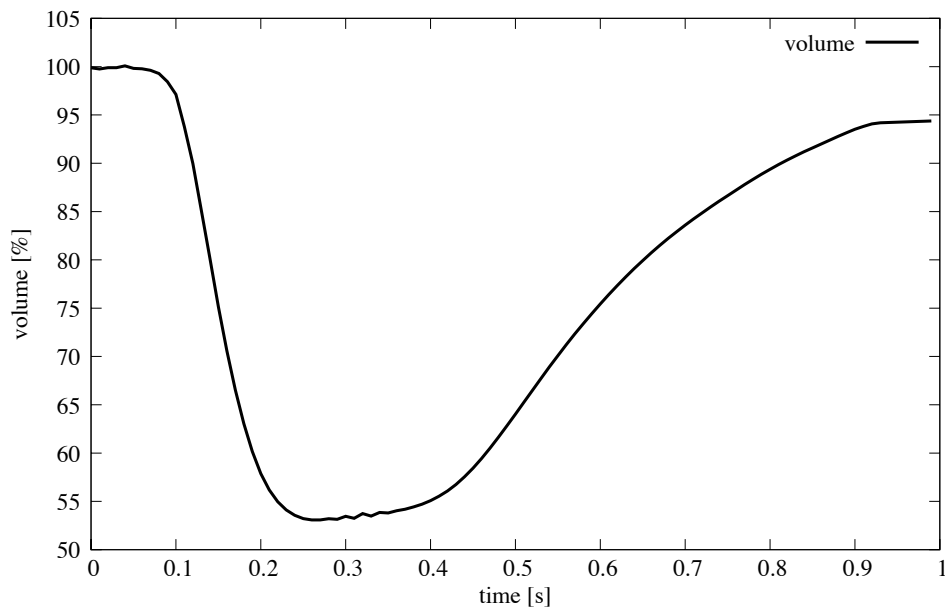
Figure 7.42. Volume computed with an exponential pressure decay function for phase III.

7.12 Importance of Fiber Orientation

The orientation of fibers and, thus the contraction direction, influences the mechanical behavior of a model. This was demonstrated on simple geometries in section 7.2 and section 7.3. The fiber orientation of a human left ventricle is approx. $-75°$ (epi-) to $55°$ (endocardium) (fig. 7.43(a)). In a further experiment, the fiber orientation of the truncated ellipsoids from epi- to endocardium was modified (fig. 7.43(b)). The orientation was inverted starting from $55°$ (epi-) to $-75°$ (endocardium). In addition, a slight rotation around the vertical axis was performed. The anatomical and the model fiber orientation are displayed in fig. 7.44 and fig. 7.45. Deformation simulations with intraventricular pressure and the setup of healthy tissue were performed as in section 7.9. The deformation simulation with correct anatomical fiber orientation was used as reference.

Deformation simulation results given by the model fiber orientation show a significant effect on the pumping function of the ventricle (fig. 7.47(b)). Even though, the ventricle slightly contracted, a shear of geometry can be distinguished, revealing that almost no volume is displaced. The latter is supported by the examination of the ejected volume over time (fig. 7.46). The ejected volume was computed by summation of each element inside the ventricular geometry. Thus, the deformation of the upper wall towards the top produced an extreme elongation of the attached elements, resulting in a volume increase during the first 15 ms. With increasing force the ventricle slightly contracts, which can be seen by the ejected volume of approx. 5%. The simulation with anatomical fiber orientation shows a volume ejection as already presented.

Conclusions

The fiber orientation has significant influence on the contraction of the myocardium. This was already presented in previous sections. However, the effect on the efficiency of the pumping of the heart was revealed by this experiment. A modification of the fiber orientation has an enormous effect on the displacement of intraventricular volume and results in this case in hardly any ejected volume.
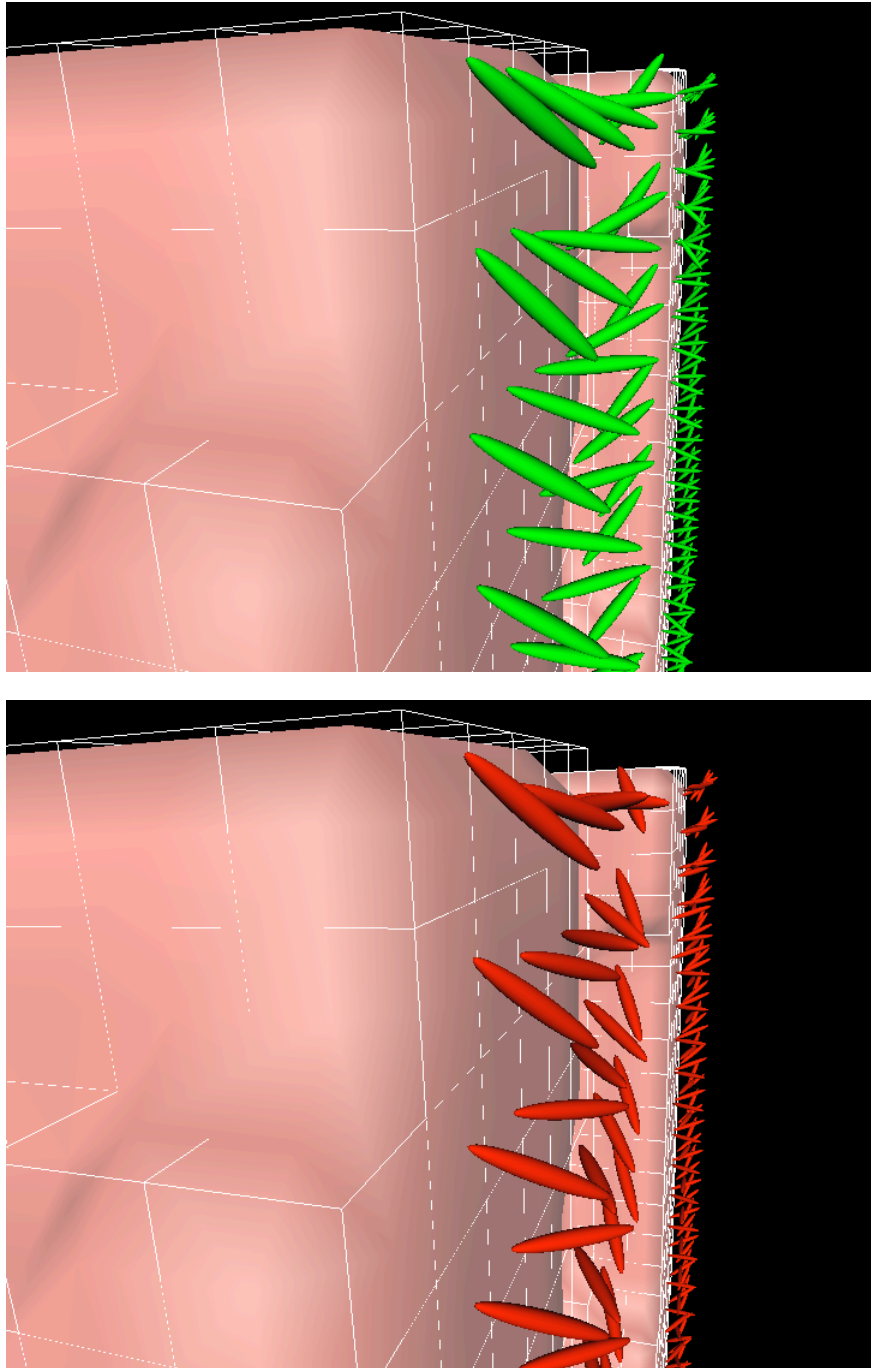
Figure 7.43. Anatomical (green) and model (red) setup of fiber orientation. The upper figure shows the anatomical fiber orientation from epi- ($-75°$) to endocardium ($55°$). The lower figure displays the modified fiber orientation.
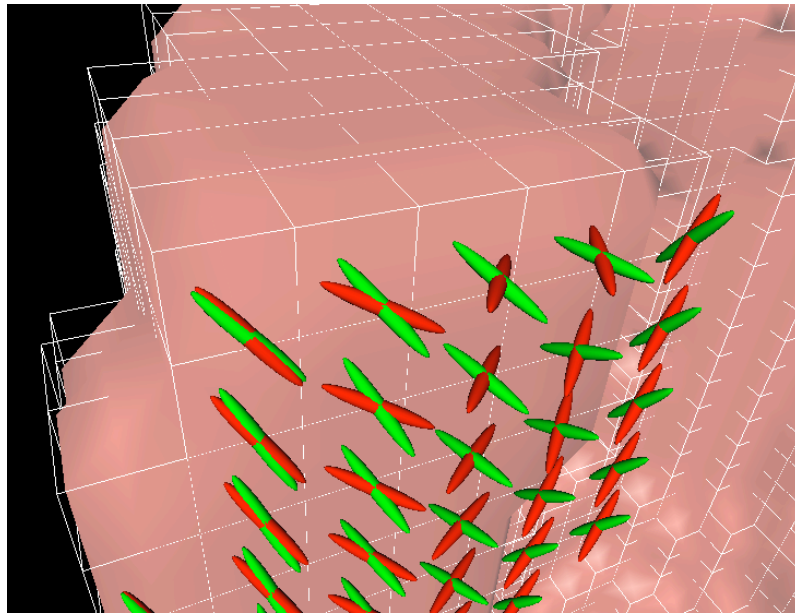
(a)
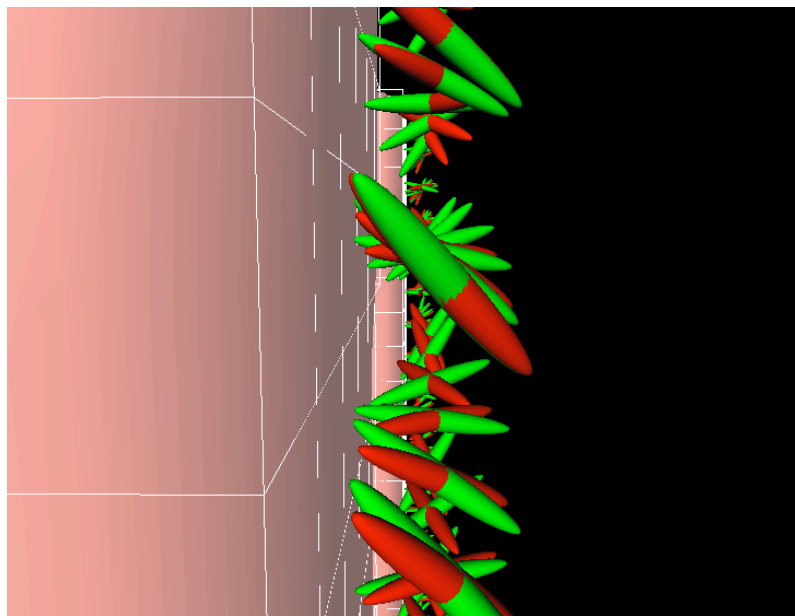
(b)

Figure 7.44. Combined visualization of anatomical (green) and model (red) fiber orientation setup. (a) shows both fiber orientations at the upper rim of the ventricular model. (b) shows the perspective from epi- to endocardium. The linear fiber twist is visible (green).
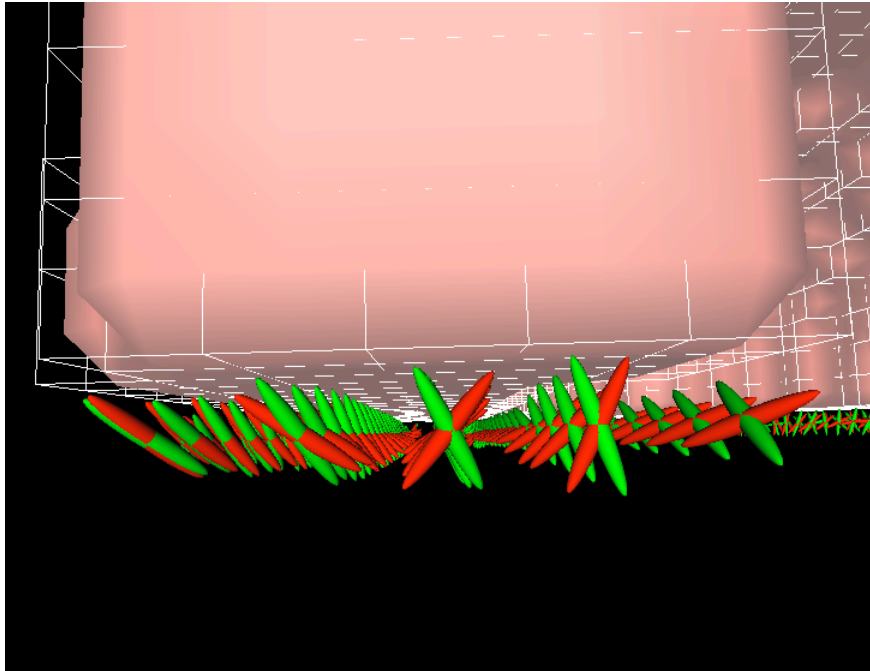
Figure 7.45. Combined visualization of anatomical and model fiber orientation setup. The perspective from valve plane to apex is shown.
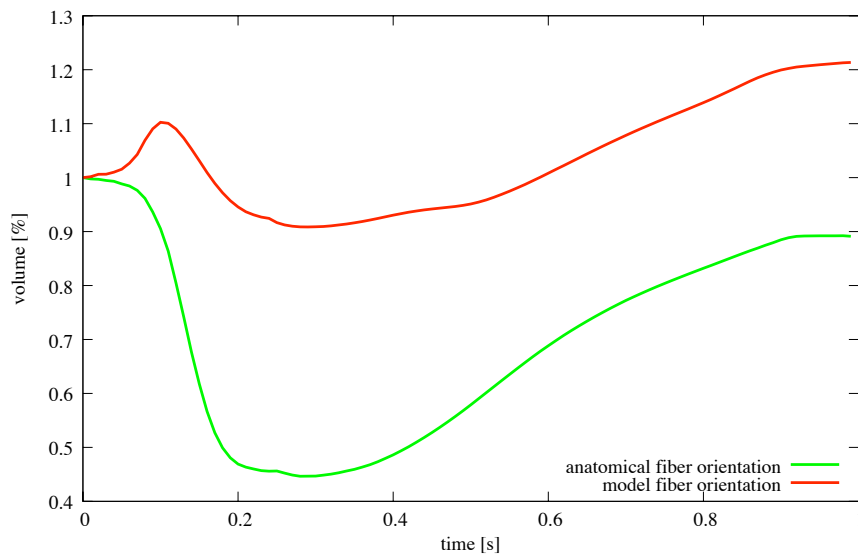
Figure 7.46. Intraventricular volume change with anatomical and model fiber orientation setup. The simulation with anatomical fiber orientation shows the expected volume displacement (green). The simulation with model fiber orientation demonstrates, that almost no volume is ejected (red).
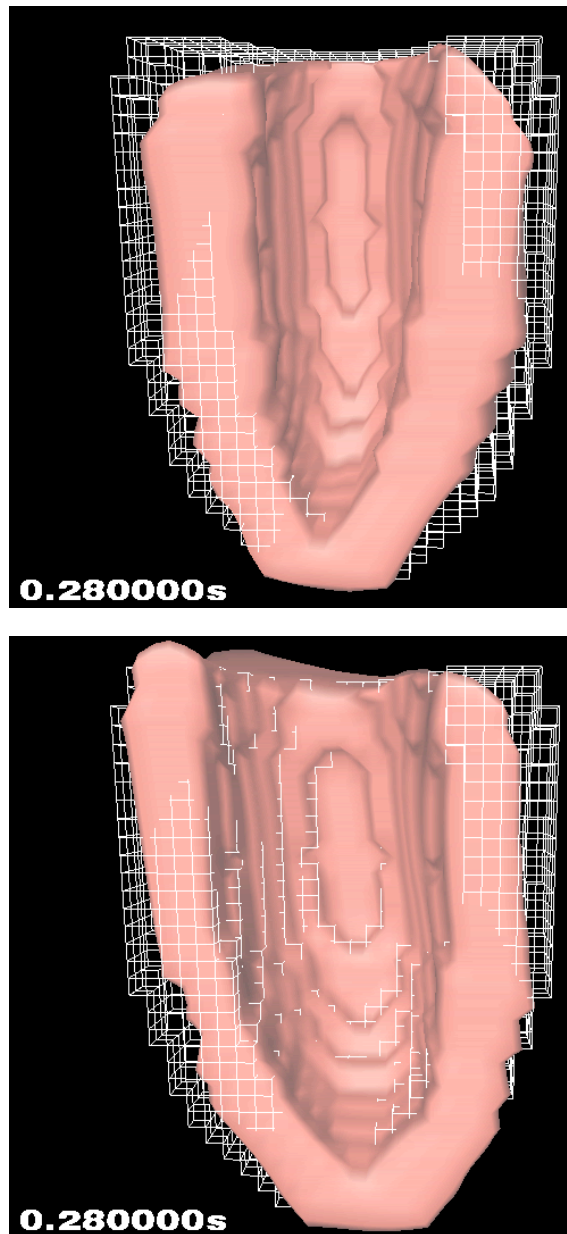
Figure 7.47. Deformation of truncated half ellipsoids with anatomical and model fiber orientation. The anatomical fiber orientation results in a contraction similar to simulations presented in previous sections (top). The model fiber orientation results in a torsion of the ventricular model similar to the anatomical fiber orientation, however no contraction is achieved. The geometry is sheared with only little displacement of intraventricular volume (bottom).

7.13 Deformation of a Biventricular Model

Sachse provided the geometrical data set of a biventricular model including fiber orientation as well as a deformation data set derived by his model [31]. The biventricular model was fixed at the valve plane for vertical movement; the electrophysiology, excitation propagation and force development were computed by microscopic cell models as shown in fig. 7.1 (left side). The result of deformation simulations are displayed in fig. 7.49. The simulation time required for the complete cycle took one week on a SGI Origin 3800 with 32 Mips 14 k 600 MHz processors, upon which 90% was used for deformation simulation. No intraventricular pressure was considered.

The application of the biventricular geometry resulted in the following spring-mass setup:

type	quantity
voxel	18 684
masses	23 062
anisotropic springs	56 052
structural springs (edges)	66 113
structural springs (diagonal surface)	122 394
volume springs (diagonal through voxel)	74 736
sum of all springs	319 295

The deformation simulation with the hybrid deformation model (HDM) and pre-calculated forces required approx. 53 min, on a PowerPC G5 2 GHz, running MacOS X. For the simulation with this model the stiffness of structural springs was increased by 30% and the maximum force by 20%. The adaptations were necessary as the wall thickness in the given geometry increased.

A deformation simulation with the HDM was performed with the forces provided by Sachse. Although physiologically incorrect, the valve plane was fixed in vertical direction to allow comparison (fig. 7.50). Intraventricular pressure was modeled as described in the previous sections for the left ventricle, only.

The deformation with the model by Sachse (SM) shows a homogenous counter-clockwise torsion from apex to valve plane (fig. 7.49, bottom). The right side of the ventricle exceeds the wireframe, whereas the left side stands behind. The upward movement of both ventricles is almost one voxel. The left ventricle contracts inward only about 2 voxel from both sides. This results in an ejected volume of approx. 25%.

The simulation with the HDM was performed with the temporal and spatial force values provided by Sachse. The amplitude was scaled to the maximum value to correlate with the spring parameter setup. In contrast to the deformation by the SM, the HDM does not show a homogenous torsion. The lower half of the left ventricle deforms counter-clockwise, however the upper part shows a clockwise rotation (fig. 7.50, bottom). The inward movement shows a displacement of more than 3 voxel at each side, which results in a larger ejection volume of approx. 50% (fig. 7.48). The upward movement of the apex compared to the SM is larger, too.

Another simulation was performed with the HDM applying a force generated by the cellular automaton. In addition, the apex was fixed vertically yielding a more realistic boundary condition. Deformation simulations show similar behavior of the displacement compared to the previous simulation, however, with a reduced torsion and a reduced inward movement. The lowering of the valve plane is clearly visible. The model of Sachse led to numerical instabilities when the geometry was fixed at the apex. This did not occur using the HDM for simulation.

Conclusions

The hybrid deformation model was applied successfully to a more complex anatomical model without many changes in parameters. The torsion generated by the HDM was smaller and asymmetrical compared to the model by Sachse. The asymmetrical movement is supported measurements of e. g. Jung [209], Nagel et al. [210], and Masood et al. [211], who stated a wringing movement of the ventricle. This fact must be further investigated and compared to ventricle measurements. The ejected volume of the HDM is larger compared to the SM. This might be due to the scaling factor of the contraction initiation forces. However, an ejected volume of 25% is pathologic. In contrast to the model by Sachse, the hybrid deformation model is not numerically influenced by the change in the spatial boundary conditions.
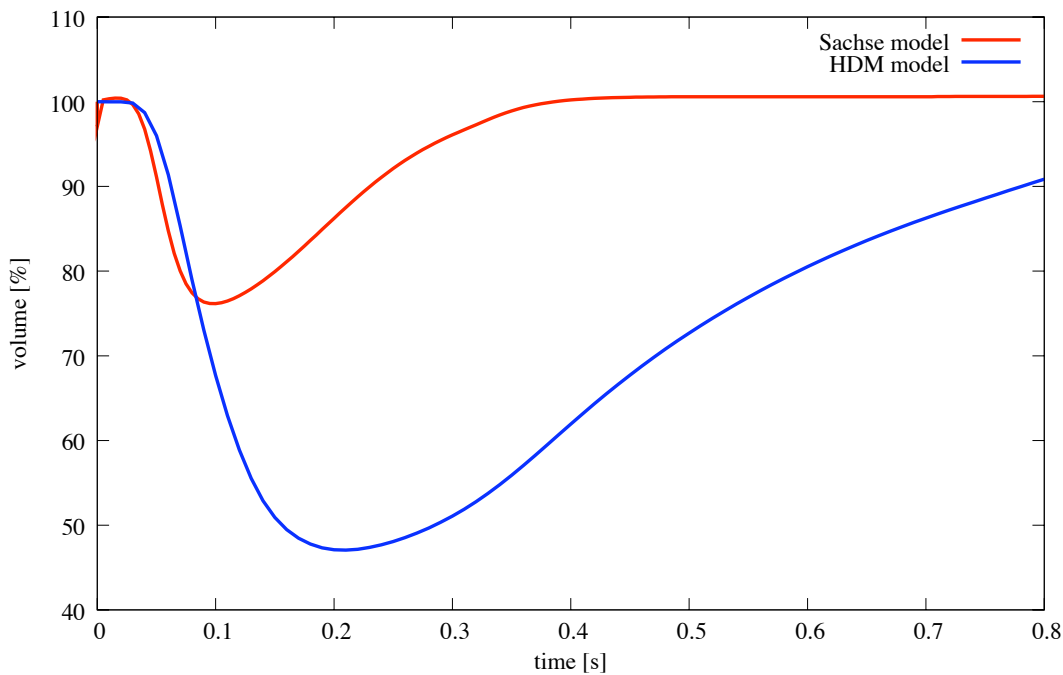
Figure 7.48. Intraventricular volume change of the biventricular model determined by the model of Sachse as well as by the hybrid deformation model (HDM).
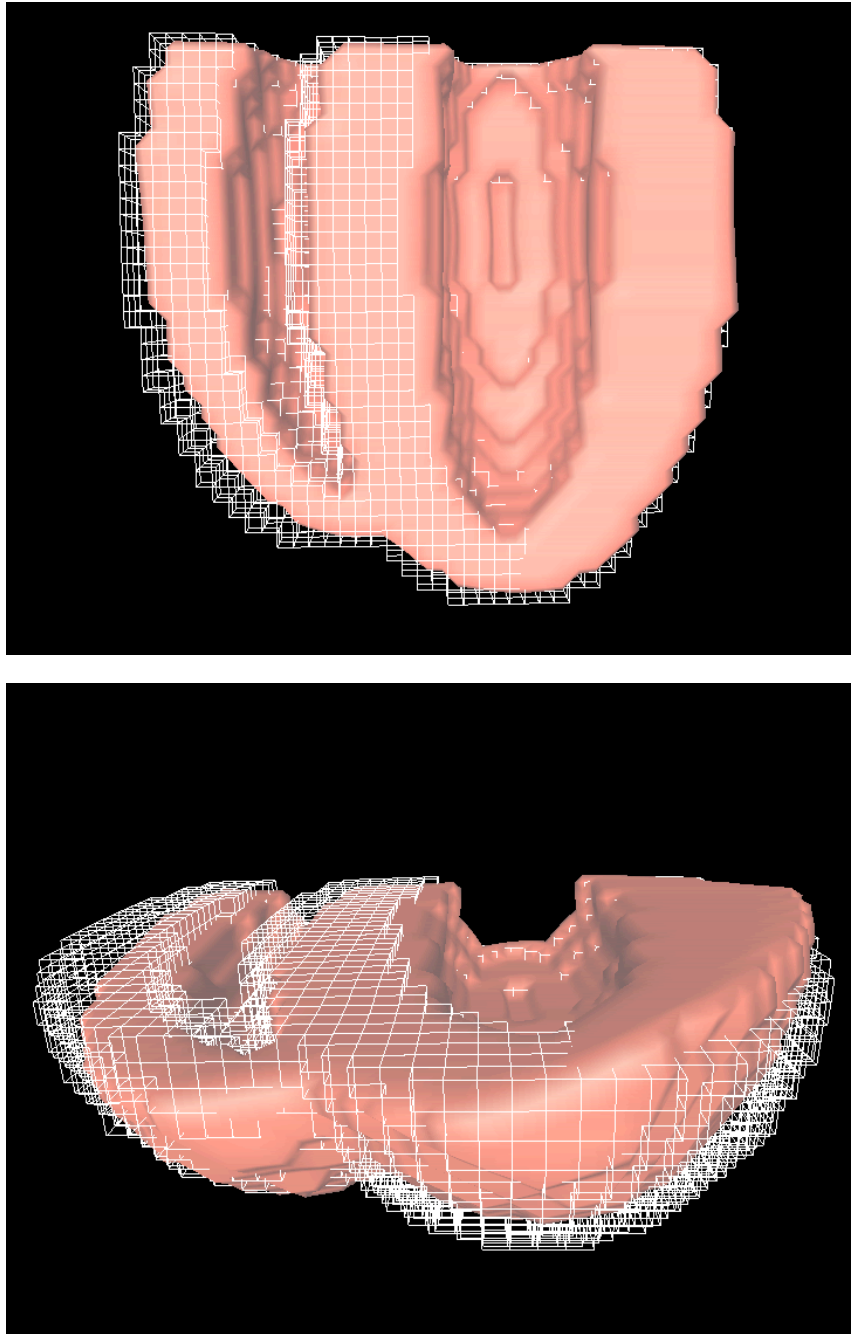
Figure 7.49. Deformation simulation with a biventricular model determined by the model by Sachse. The valve plane was fixed vertically.
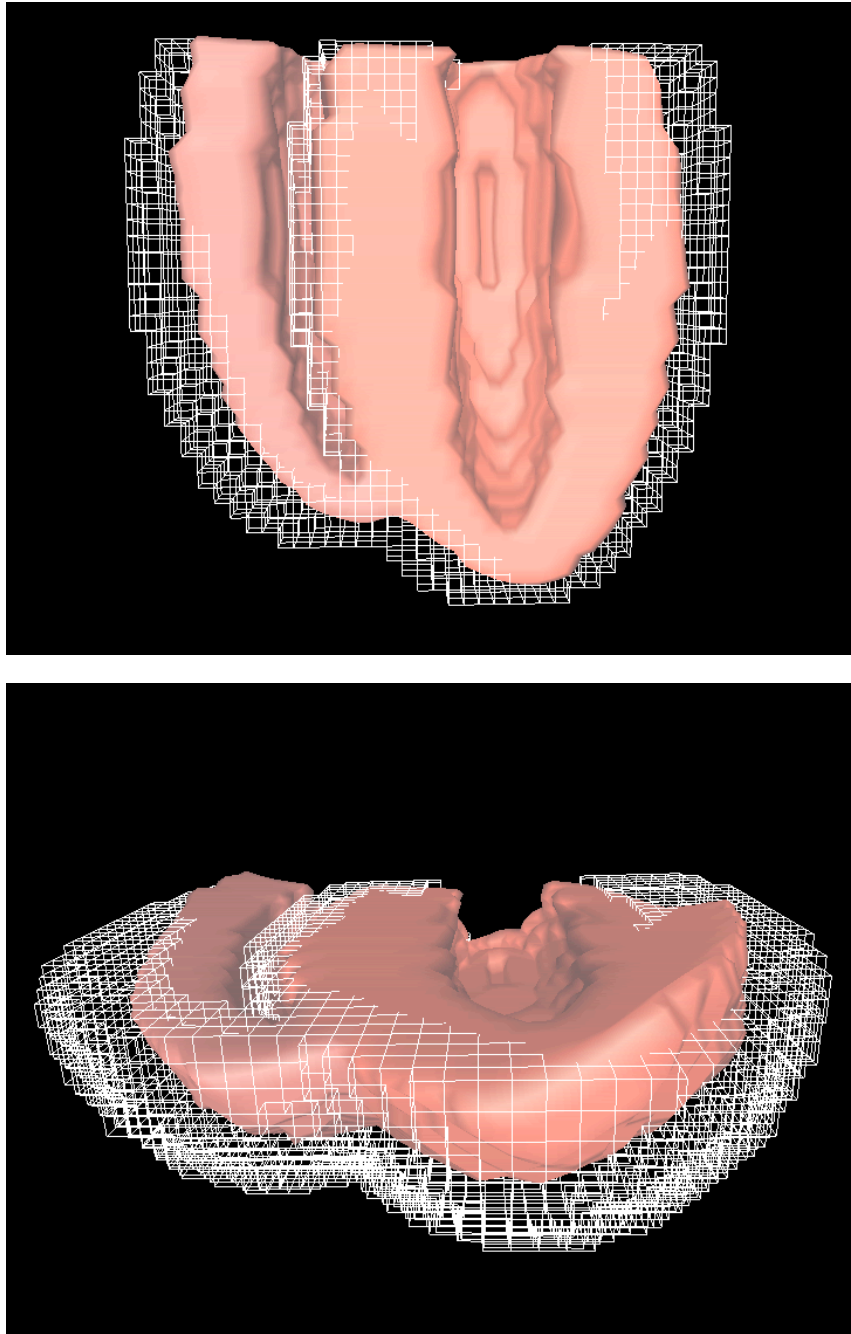
Figure 7.50. Deformation simulation with a biventricular model determined by the hybrid deformation model, the temporal and the spatial forces provided by Sachse. The valve plane was fixed vertically.
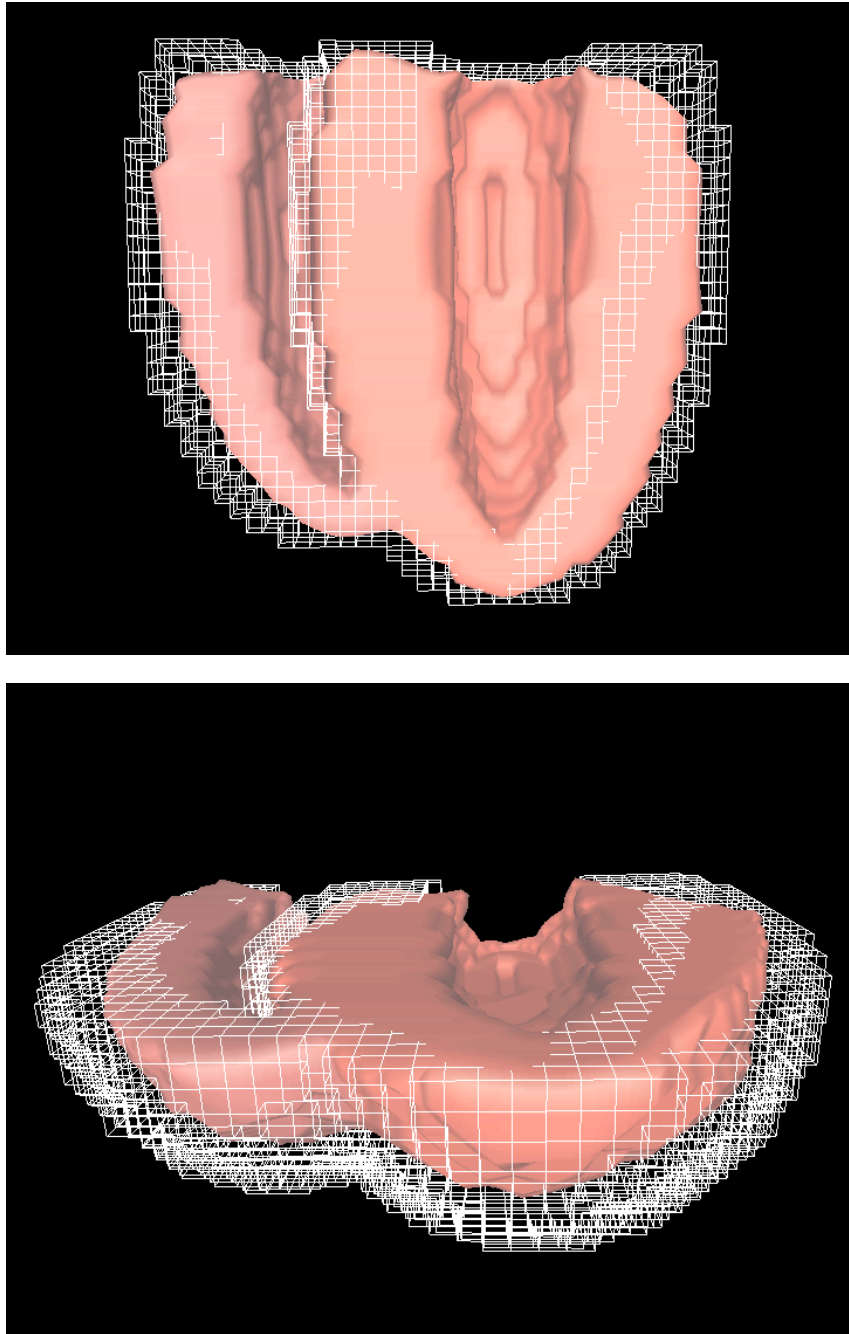
Figure 7.51. Deformation simulation with a biventricular model determined by the hybrid deformation model. Spatial and temporal force distributions were computed with the cellular automaton. In addition, the apex was fixed vertically.

7.14 Deformation Simulation with the Dog Heart Model of Nielsen

The anatomical model of a dog heart created by Nielsen et al. [38] formed the geometrical basis of the following simulation. The data set was created from finite element models [38, 39] and is publicly available from A. McCulloch at the University of California, San Diego, U.S.A.. The model of Nielsen consists of 129 927 cubic elements describing the anatomical geometry. In addition, the fiber orientation for each cubic element is given. The geometry is divided into 24 bicubic elements (fig. 2.22), which were used to fit the geometry to the left and right ventricle of dogs [38]. The model of the dog ventricles shows a hole at the apex, but no further specifications were given upon this fact. However, the experimental setup described by Nielsen et al. [38] indicates that it was the point of fixation for the measurement. The geometry was converted into a spring-mass system by the hybrid deformation model resulting in the following amount of masses and springs:

type	quantity
voxel	129 927
masses	148 930
anisotropic springs	389 781
structural springs (edges)	427 873
structural springs (diagonal surface)	818 504
volume springs (diagonal through voxel)	519 708
sum of all springs	2 155 866

The deformation simulation with the hybrid deformation model and pre-calculated forces required approx. 237 min, on a PowerPC G5 2 GHz, running MacOS X. The contraction initiating force was computed with the cellular automaton, as no such data were otherwise provided. The stiffness of the structural springs was increased by a factor of 10 compared to the single ventricular model (section 7.5), due to the increase in wall diameter. No pressure load was applied. The undeformed dogs biventricle and its deformation at maximum contraction are displayed (fig. 7.52, 7.53, and 7.54). The lateral cut (fig. 7.52) and the view from the apex in upward direction (fig. 7.54) show a small torsion. The left side of the left ventricle deforms in counter-clockwise rotation and the upper right side as well as the right ventricle a rotation in clockwise direction (fig. 7.54). The valve plane moves downward by approx. 3 voxel. The intraventricular volume is displaced by approx. 25%.

Conclusions

A simple parameter adaptation allows to simulate deformation with the geometry created by Nielsen. The wall thickness slows the deformation down, as the propagation of momentum is slower in more complex geometries. One part of the energy is used for oscillation of masses and not for propagation of displacement. The application of rigidity proposed by Miyazaki et al. [197] was adapted for wall thicknesses of up to 10 voxel, only. A deformation comparison to the model of Nielsen was not possible as only the geometrical data were available.
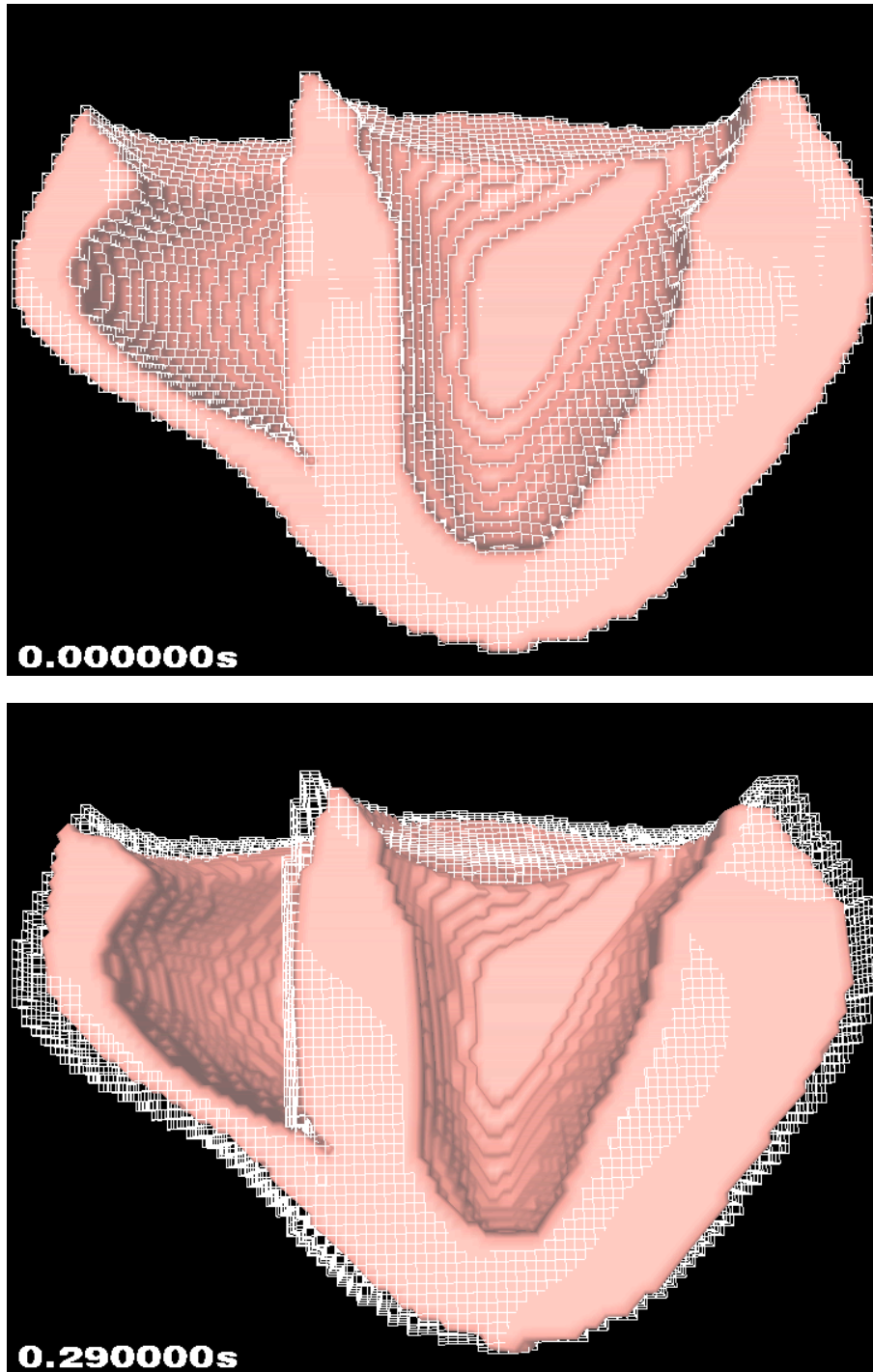
Figure 7.52. Deformation of biventricular model of dog (lateral view)
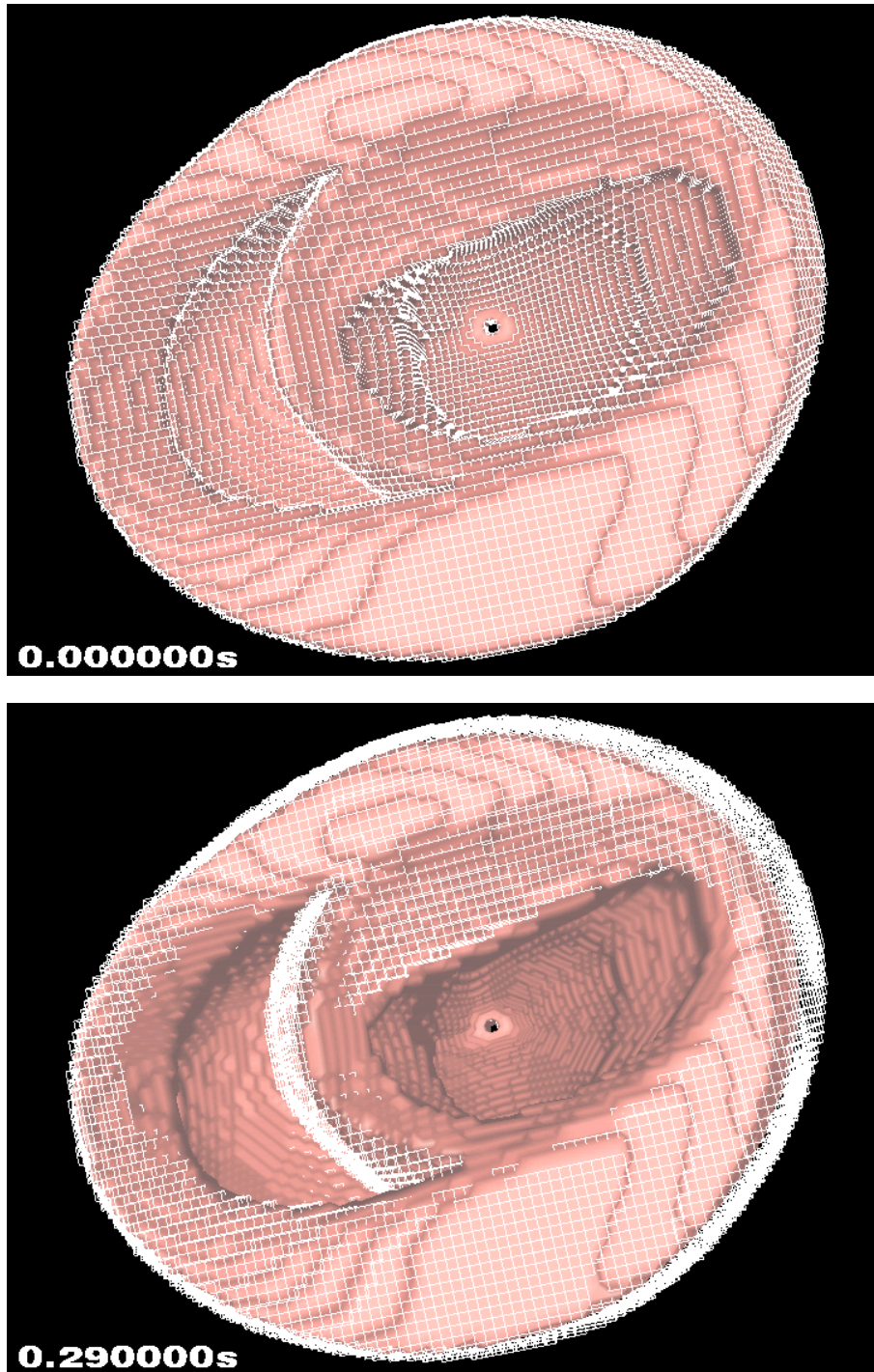
Figure 7.53. Deformation of biventricular model of dog (valve plane view)
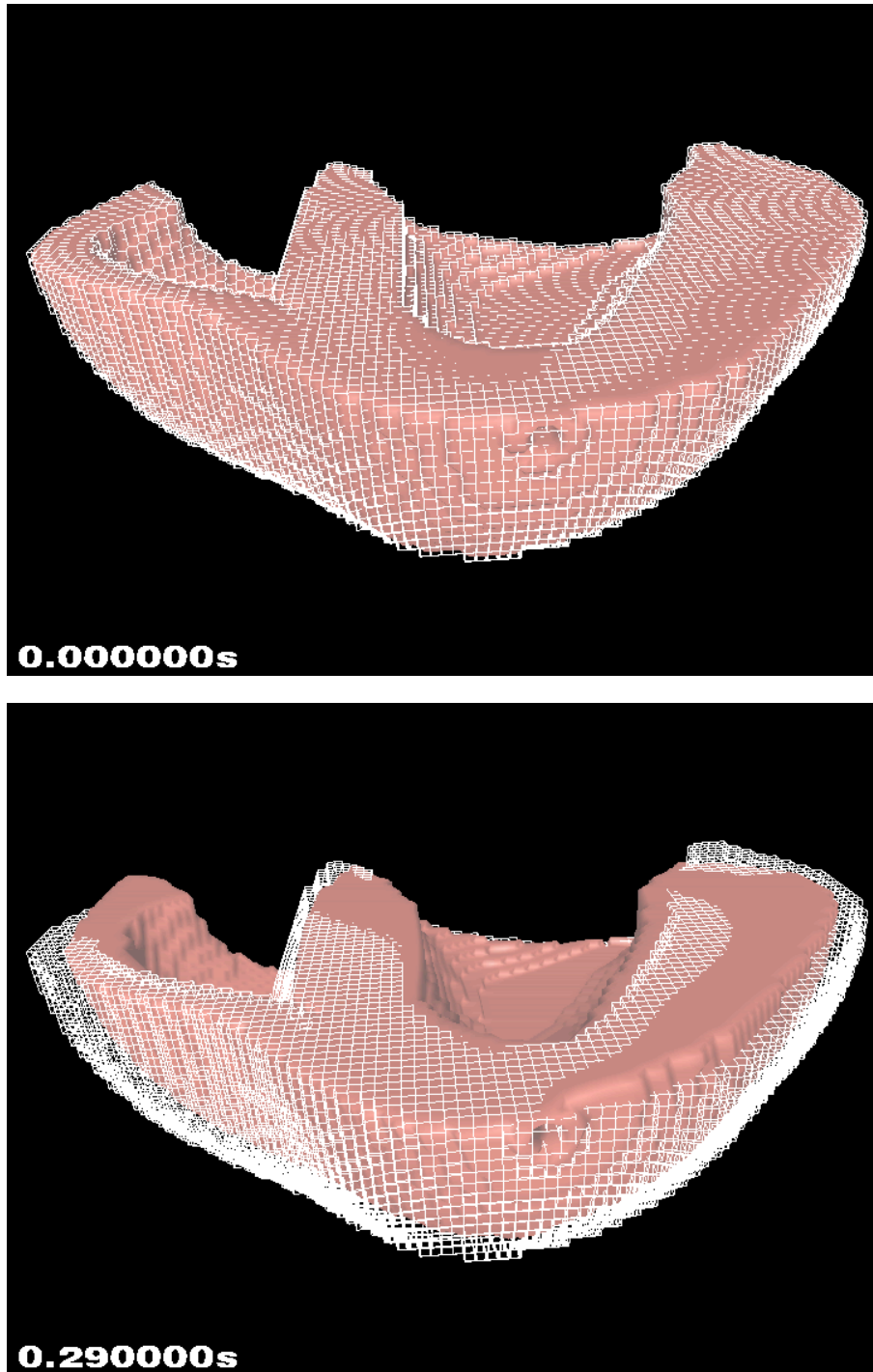
Figure 7.54. Deformation of biventricular model of dog (apex view)

7.15 Comparison of Measured and Simulated Ventricular Deformation

The hybrid deformation model was applied on models representing singular and biventricular geometries. Deformations were achieved which comply with anatomical and physiological findings. Further investigations were performed on a measured left ventricle data set.

Dr. Bernd Jung provided a segmented 4D geometrical data set of a left ventricle acquired of a healthy volunteer by MRI. The data set consisted of 57 3D data sets. The acquisition started at 14 ms after the R peak of the ECG and slices were measured at successive intervals of 14 ms until approx. 800 ms. At each time instant 9 slices were recorded with a resolution of 64×64 voxel with edge length of 1.4 mm. The images were recorded at a vertical distance of 8 mm resulting in the thickness of a slice. Successive images were used to interpolate to a slice thickness of 4 mm.

The slices at each time step were stacked to create a single 3D data set, consisting of a lattice of $64 \times 64 \times 17$ with a cuboid voxel size of $1.4 \times 1.4 \times 4\, mm$. The slices were acquired during a sequence of heart beats. Vertical movement was not tracked. Respiratory movement was suppressed during image acquisition by breath holding.

The phase contrast sequence (a specialized MRI sequence) developed by Jung [209] allowed the reconstruction of velocity vectors of the heart wall. This new method has several advantages compared to tagging methods that are also used to track the motion of landmarks over time.

This clinical data were used to test the hybrid deformation model on a human left ventricular data set. The segmented left ventricle at time 0.014 s was applied to represent the anatomical ventricle at the beginning of the systole. The $1.4 \times 1.4 \times 4\, mm$ data set was transfered to cubic voxel by splitting the z-slice into three 1.4 mm slices. Thus, the geometry was slightly stretched to a $64 \times 64 \times 51$ lattice with cubic elements of 1.4 mm. The transfer was necessary as the hybrid deformation model requires the geometry to consist of isotropic voxel.

The geometry was converted into a spring-mass system by the hybrid deformation model resulting in the following amount of masses and springs:

type	quantity
voxel	39 012
masses	50 208
anisotropic springs	117 036
structural springs (edges)	139 287
structural springs (diagonal surface)	256 182
volume springs (diagonal through voxel)	156 048
sum of all springs	668 553

Extension of Geometrical Model

The medical data set only provided geometrical data of anatomy and velocity vectors for each voxel. Therefore, the fiber orientation was introduced as follows: The epi- and endocardium were automatically extracted and marked as boundary limits. The transmural direction was determined starting from each epicardial voxel pointing towards the center of the slice. The fiber orientation was created along the transmural direction by applying the proposals of Streeter et al. [12] (fig. 7.55). The contraction initiation force was calculated. As the apex is not fully available from the image data set, 4 stimulation points were set in the lowest slice of the model. A cellular automaton was applied to compute spatial and temporal force distributions as described in previous sections.
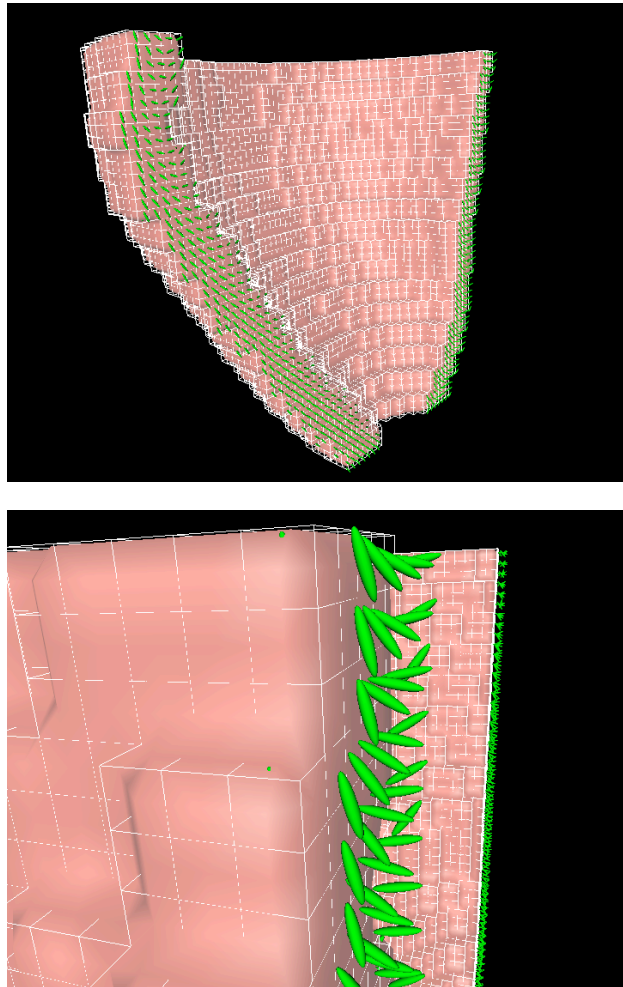
Figure 7.55. Fiber orientation for measured ventricular data set.

Deformation Simulation

The deformation simulations were carried out with the hybrid deformation model. The mechanical parameters resulted from previous simulations with the truncated half ellipsoids were applied. The only adaptation was done by reducing the mass of each voxel by 25% to receive similar circumferential deformation compared to measurement data. In contrast to the acquired slices and the resulting 2D deformation of Jung, not only circumferential but also vertical movement was achieved. The deformation of the model is displayed at specific times steps as a view from valve plane to apex (fig. 7.56 and 7.57) and as lateral cut of the ventricle (fig. 7.58 and 7.59).
Both figures contain the measured deformation in the left column and the simulated deformation in the right column. The comparison of the valve plane to apex view shows a successive contraction for both results, measurement and simulation, in circumferential direction until a maximal contraction at $0.280\ s$ is reached (fig. 7.56). The simulation result shows regular symmetric contraction, in contrast to the measured deformation of the ventricle that is slightly distorted (fig. 7.56, left column). During the relaxation phase, similar results are obtained as the left and right walls of the measured ventricle relax more quickly compared to the top and bottom wall at $0.462\ s$ (fig. 7.57, left column). The simulated deformation shows a slower but symmetric restoration to the initial position in contrast to the measured deformation (fig. 7.57, right column).
The lateral cut of the measured ventricle reveals also a distorted contraction (fig. 7.58, left column). The right wall only moves slightly to the vertical center of the ventricle, whereas the left side deforms in a strong inward bend until $0.280\ s$ (fig. 7.58, left column). In comparison, the simulated deformation shows an almost symmetrical contraction, which is only distorted by the geometry of the model itself (fig. 7.58, right column). The top left side rim slightly tilts towards the outside at maximum contraction $0.28000\ s$ (fig. 7.58, right column). In the simulation, the restoration to the initial position of the geometry is delayed at $0.80000\ s$ (fig. 7.59, right column).
All four pictures at time step $0.2800\ s$ (fig. 7.56 and 7.58) indicate that the thickening of the wall of the simulated model is not as extensive as found from the measured data.
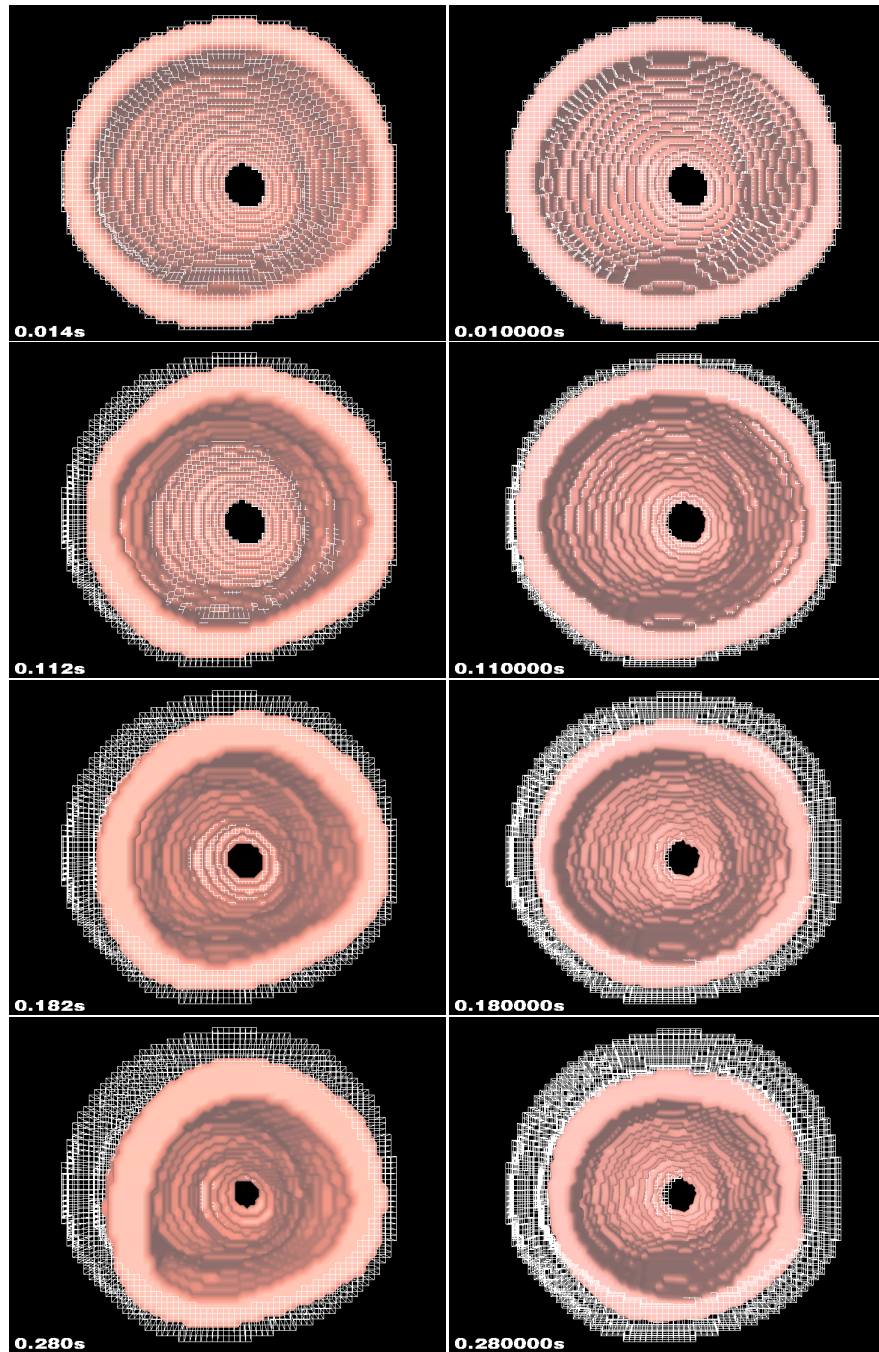
Figure 7.56. Comparison of measured and simulated ventricular deformation. The left column contains figures of the deformation according to measured data and the right column figures of the deformation achieved with the hybrid deformation model (view from valve plane to apex) (for continuation see fig. 7.57).
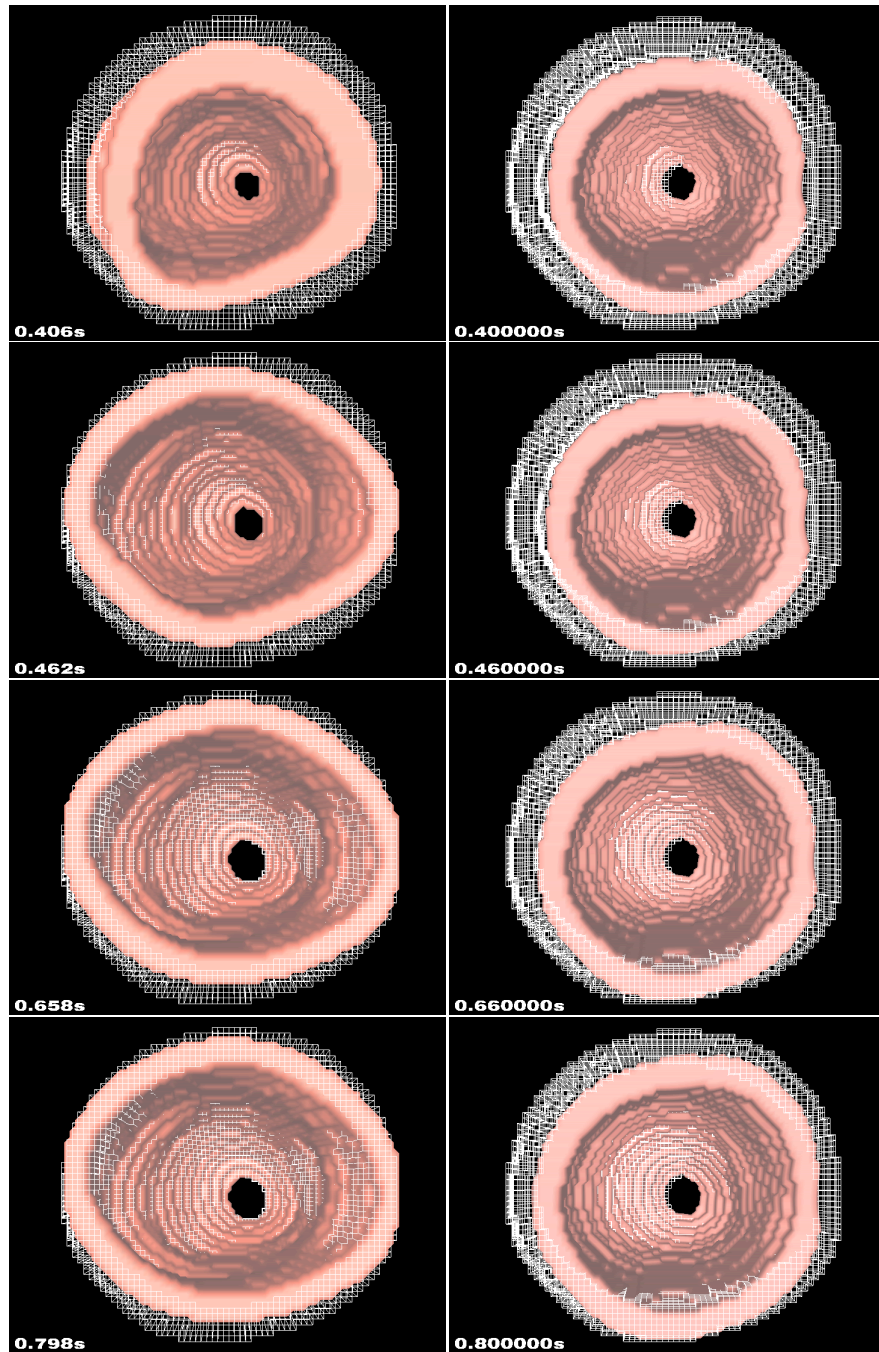
Figure 7.57. Comparison of measured and simulated ventricular deformation. The left column contains figures of the deformation according to measured data and the right column figures of the deformation achieved with the hybrid deformation model (view from valve plane to apex) (continued from fig. 7.56).
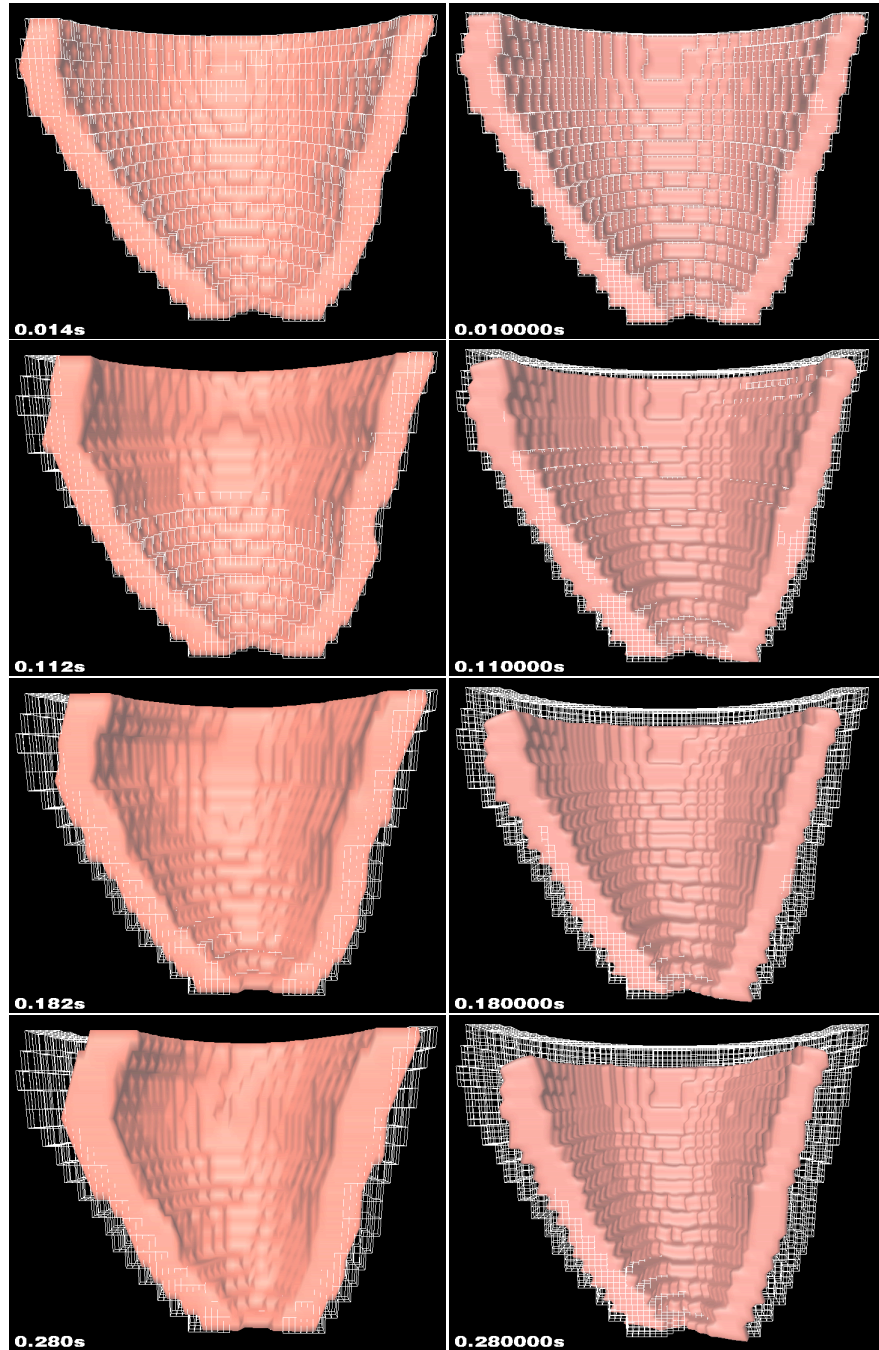
Figure 7.58. Comparison of measured and simulated ventricular deformation. The left column contains figures of the deformation according to measured data and the right column figures of the deformation achieved with the hybrid deformation model (lateral cut) (for continuation see fig. 7.57).
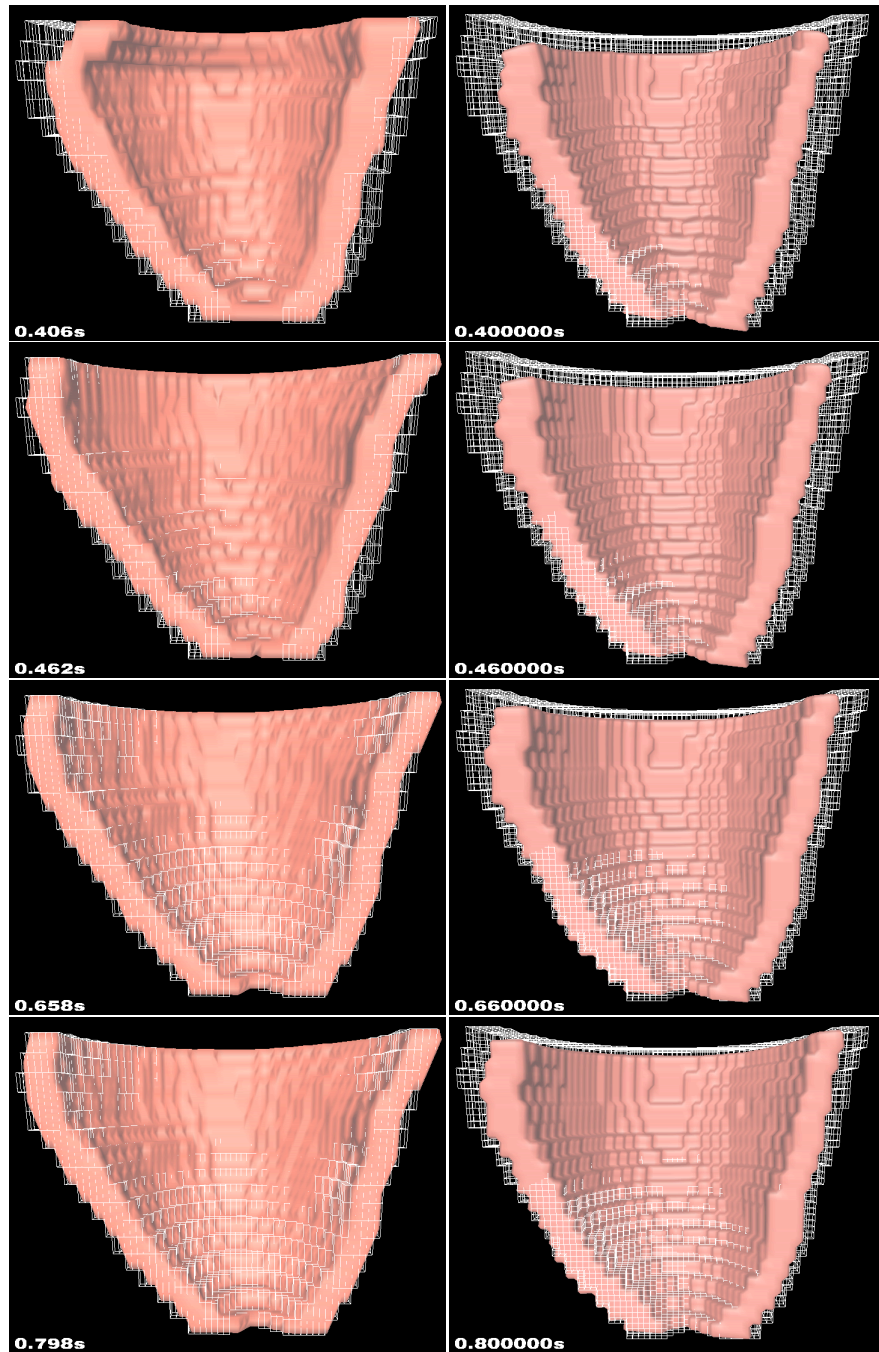
Figure 7.59. Comparison of measured and simulated ventricular deformation. The left column contains figures of the deformation according to measured data and the right column figures of the deformation achieved with the hybrid deformation model (lateral cut) (continued from fig. 7.58).
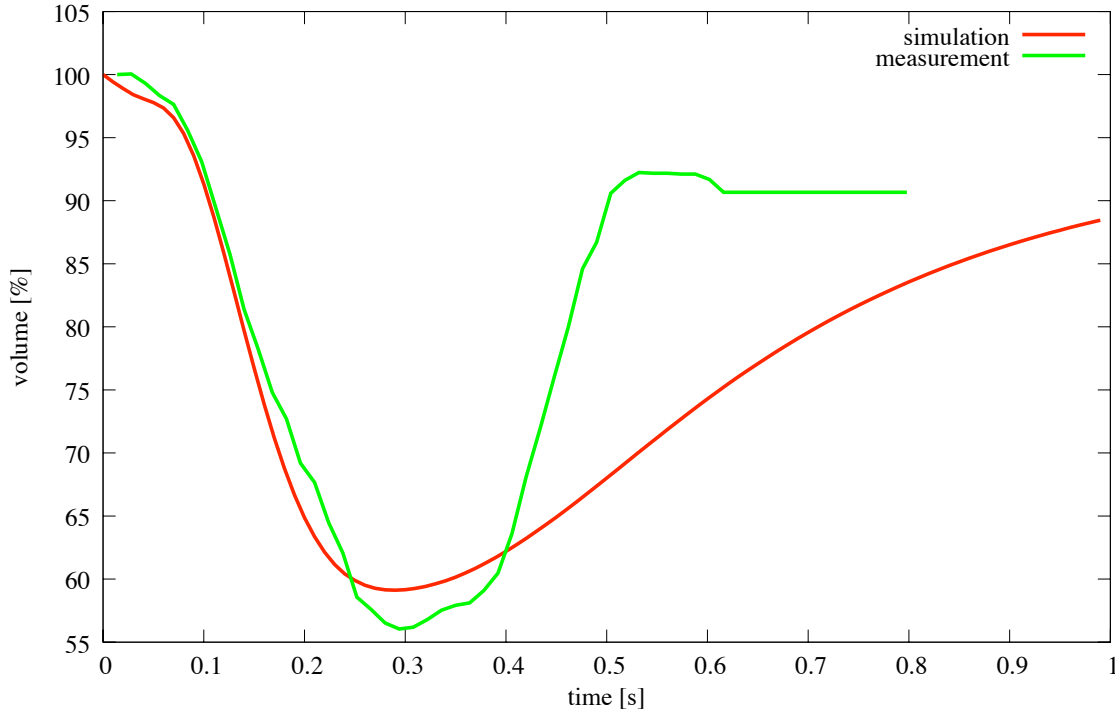
Figure 7.60. Comparison of displaced volume of measured and simulated ventricle contraction.

Change of Intraventricular Volume

The displaced volume is given in fig. 7.60. During the first few milliseconds the volume of the measured data does not decrease as quickly as in the simulation. This can be accounted for by the missing pressure and therefore, the missing isovolumic phase during the simulation. Thereafter, a similar reduction of volume can be obtained, reaching different maximum displaced volumes varying approx. by $4 - 5\%$. The ascent of the intraventricular volume for the measured data is larger compared to the simulation.

Measures Velocity Vectors

The velocity vectors (displayed as green vectors) acquired by Jung show a locally different velocity distribution throughout the contraction cycle (fig. 7.61). The velocity vectors were extracted for the slice at the valve plane and near the apex, normalized, and projected onto the slice plane. The slices are displayed in the same picture for different time steps (fig. 7.62 and 7.63). Velocity vectors vary throughout the progression of time.
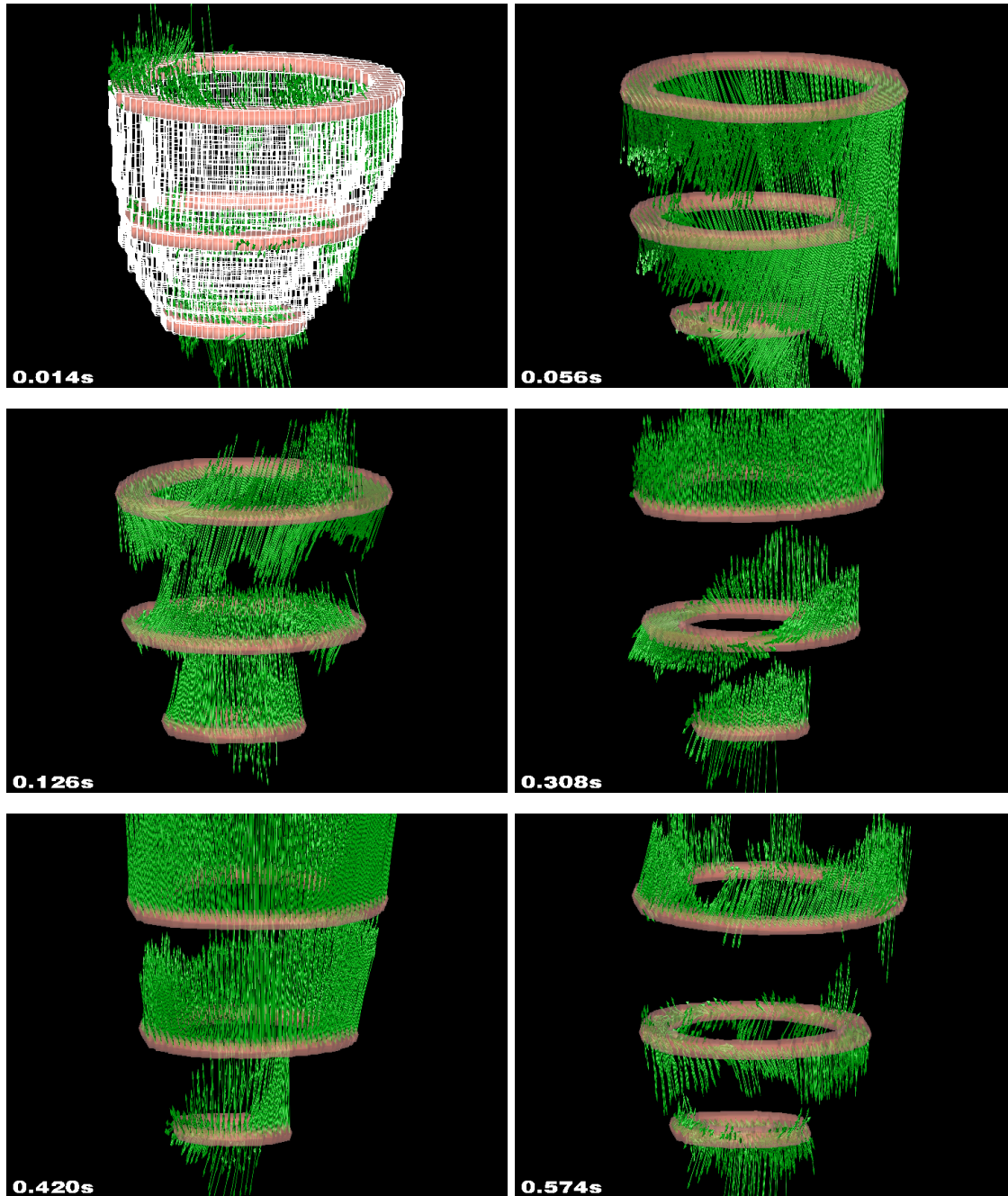
Figure 7.61. Velocity vector distribution at specific time steps for three slices acquired from phase contrast MRI images extracted by Dr. Jung [209]. Green Arrows indicate velocity orientation and amplitude for each voxel. Locally differing orientation and magnitudes can be distinguished.
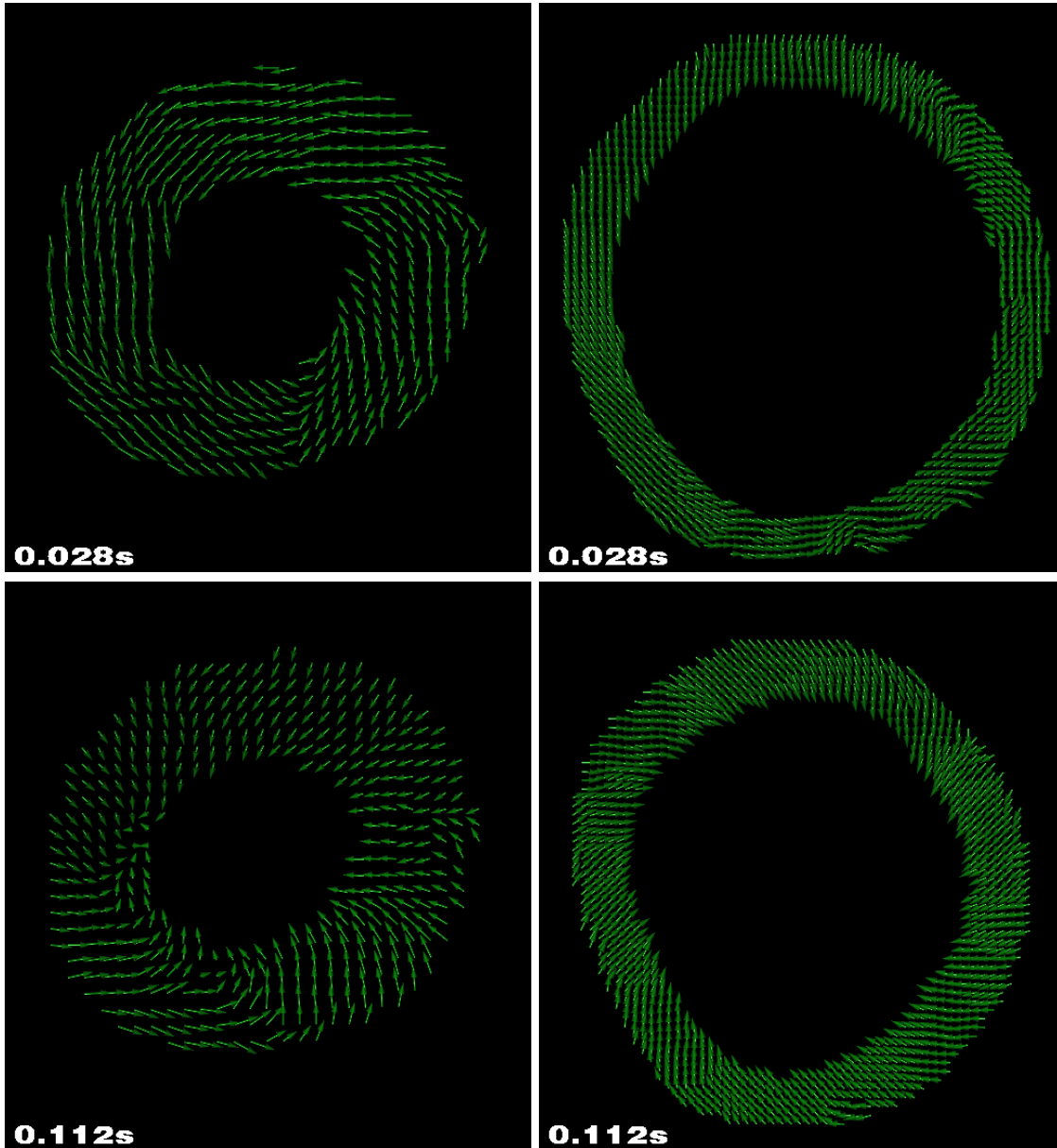
Figure 7.62. Normalized velocity vectors projected into the slice plane. The green arrows indicate the measured velocity vectors provided by Dr. Jung. The figures in the left column show the slice near the apex and the figures in the right column the slice at the valve plane. Figures shows slices seen from apex to valve plane (for continuation see fig. 7.63).
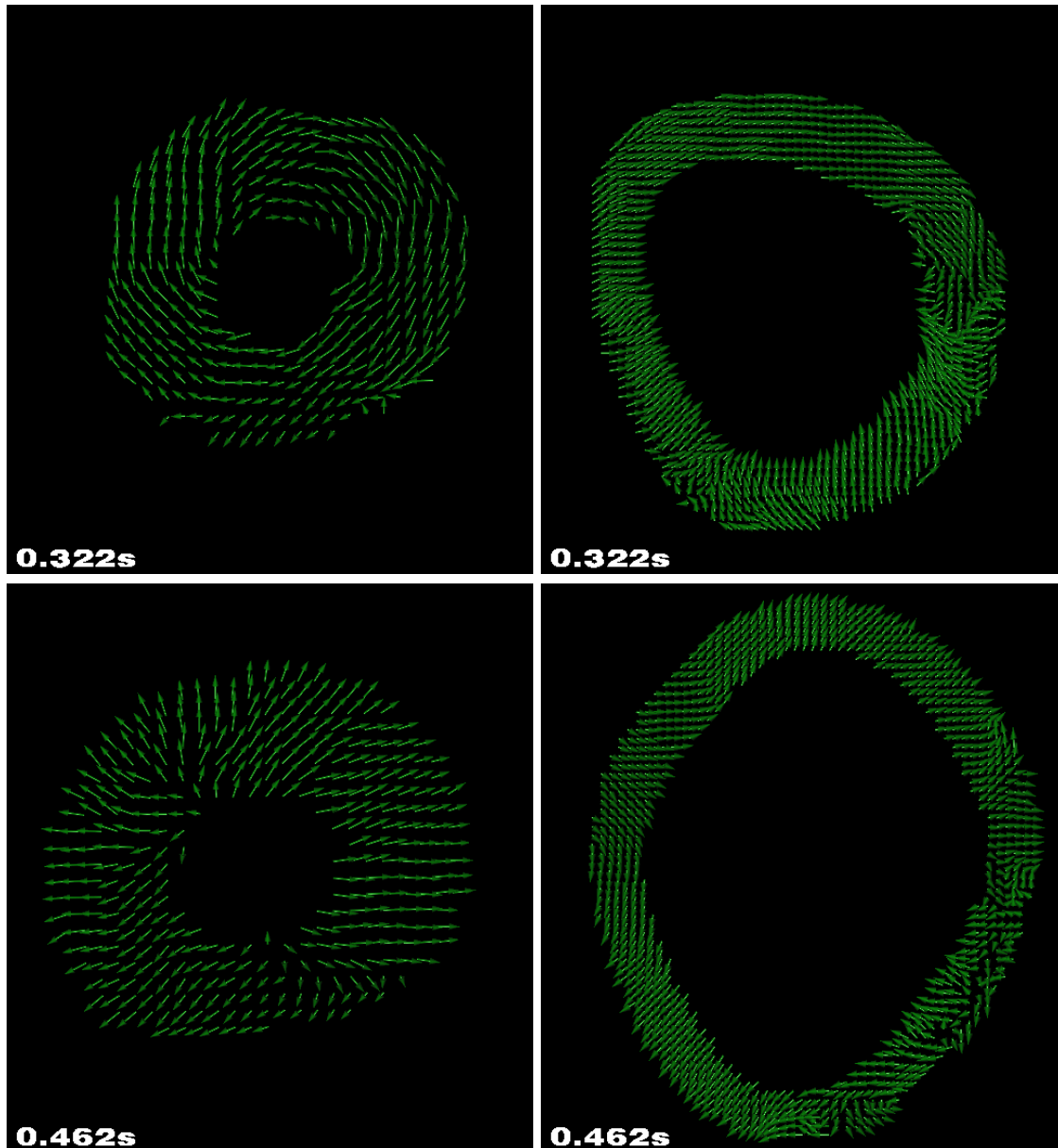
Figure 7.63. Normalized velocity vectors projected into the slice plane. The green arrows indicate the measured velocity vectors provided by Dr. Jung. The figures in the left column show the slice near the apex and the figures in the right column the slice at the valve plane. Figures shows slices seen from apex to valve plane (continued from fig. 7.62).

Conclusions

The comparison of a measured ventricle compared to a deformation simulation with the hybrid deformation model showed the capability of the models simulating the ventricular deformation of a patient even without considering pressure. However, pressure should be modeled to achieve a closer match during the relaxation phase and to allow for more realistic modeling. In addition, a larger range of healthy persons has to be examined to find mechanical parameters for wall thickening. Due to data available from Jung, the comparison of ventricular deformation along the vertical axis of the ventricle was not possible. Therefore, additional clinical data have to be examined to verify and evaluate vertical ventricular movement.

The changing orientation of velocity vectors at the valve plane and at the apex of the measured data supports the clock- and counter-clockwise rotation of the ventricle at valve plane and apex, respectively, which is also reported by Nagel et al. [210] and Masood et al. [211]. The velocities measured show extremely rapid and asymmetric variations of amplitude and direction, which is hard to model applying physical laws, where each mass has its momentum and hence an inertia without further boundary conditions. Nevertheless, the hybrid deformation model reproduced the wringing motion of the ventricle. Further focus has to be set on the measurement of vertical motion of the ventricle to match vertical velocity vectors with tissue movement.

In addition, more intensive studies of the boundaries of the ventricles such as movement of the septum, fixation of the epicardium at the pericardial sac, connection with the right ventricle, as well as apex fixation have to be performed and considered in the model. Furthermore, the blood flow is expected to influence an asymmetrical contraction of the left ventricle.

As the slices were acquired at a size of 8 mm and interpolated twice, a deviation from the real ventricular movement must be assumed. However, this experiment showed that the application of patient specific data is straight forward and proves the capability of the hybrid deformation model for future application in a clinical environment.

8

Discussion and Future Work

In this work an elasto-mechanical model was created representing the mechanical behavior of heart tissue. By combining a spring-mass system with continuum mechanical methods, a hybrid deformation model was developed. A good representation of non-linear, anisotropic, and incompressible characteristics of myocardial tissue was achieved. Deformation simulations were performed with various geometrical models. The importance of fiber orientation for the cardiac output, as well as the significance of intraventricular pressure on mechanical deformation was outlined. The tissue properties of anisotropy, non-linearity, and incompressibility were modeled and maintained to a certain percentage. The intraventricular volume of a ventricle modeled by truncated half ellipsoids was reproduced as found in literature. With slight modifications of parameters, the model was adapted to more complex geometries.

The simulation time of 53 min (PowerPC 2 GHz, single CPU) using the hybrid deformation model on a biventricular model (section 7.13) compared with approx. one week (SGI Origin 3800 with 32 Mips 14k 600 MHz CPUs) using a close to finite element model with dominantly continuum mechanical basis the main advantage of the hybrid deformation model: While the hybrid deformation model might be considered in clinical applications in the near future, the computation time of the continuum mechanical model in the current form is unacceptable for clinical use.

However, the hybrid deformation model has to be categorized as a macroscopic model. This means, the results have to be understood as averaged results. The explicit comparison with microscopic experiments will certainly show differences. This is due to the fact, that even though continuum mechanical methods were applied to model microscopic findings, the time step used for time integration was too large for comparison with microscopic experiments. This is apparent e. g. in the application of pressure. Here, oscillations can occur at pass over stages of cardiac phases (section 7.7). They also appear if volume dependent pressure algorithms are implemented (sections 7.8 and 7.11). A reduction of the time step length is easily possible, but at the cost of increasing overall simulation time.

Measurements revealed a clockwise rotation of the myocardium close to the valve plane and a counter-clockwise rotation at the apex [209, 210, 211]. This behavior was reproduced by simulations with ventricular models using the hybrid deformation model. As the setup of fiber orientation plays a significant role in contraction and hence ventricular rotation, the simulation results indicate a close match of myocardial and modeled fiber orientation.
Further focus must be set on the exact boundary conditions inherent in the heart. Fixation of the ventricle to the pericardial sac, the influence of the cytoskeleton forming the valve plane, the movement of the septum, and the influence of the right ventricle must be examined and considered in the model. In addition, the blood flow and its influence on mechanical deformation must be examined.

The numerical solution of the equation of motion was performed first by an Euler forward marching scheme. In addition, the central difference method was applied resulting in more stable simulations and the possibility to advance in larger time steps. However, as a constant time step was applied, occurring oscillations could not always be fully damped. Therefore, more sophisticated algorithms for time incrementation and time step control should be implemented.

In this thesis a mechanical simulation model is proposed which allows to reproduce macroscopic myocardial deformations. It provides a solid basis for future application in the field of cardiology and cardiac surgery. The comparison of measured and simulated deformation in section 7.15 revealed that patient specific data can be successfully processed by the hybrid deformation model. With additional knowledge of boundary conditions of ventricular connection to peripheral tissue a realistic simulation of ventricular deformation can be achieved. Further studies have to be conducted to compare and to reproduce measured ventricular deformation. The knowledge of pathologic regions of a patients ventricle can be introduced into the model (section 7.5), providing an additional step towards clinical application. Thus, virtual operation planing can be performed and resulting effects on heart contraction can be estimated for patients prior to an intervention.

A

Continuum Mechanics

A.1 Introduction

Continuum mechanics is a branch of mathematics dealing with continuous matter, including solids and fluids and its deformation. Even though matter is in the microscopic limit based on atoms aligned in a heterogeneous microstructure with certain interaction laws, this is simplified to so-called macroscopic or microscopic material laws. Further, energy and momentum conservation can be described in each level of abstraction. Differential equations associated with proper boundary conditions can be developed for the solution of problems in continuum mechanics.

For mechanical modeling of the myocardium a subsection of continuum mechanics is applied. This subregion is called solid mechanics and implies the elasticity and plasticity of the material. This allows for a quantitative description of finite deformations of inhomogeneous, anisotropic tissue due to acting internal and external forces.

The following sections introduce the basic continuum mechanical configurations and tensors needed for stress strain analysis in this thesis.

A.2 Configurations

The continuous medium B can be assumed to be a coherent and compact amount of particles or material points P filling a volume in space. The configuration κ of B describes the continuous mapping of points in B into a three dimensional space $\mathbb{R}^3$. The reference configuration κ_r is named Lagrange configuration and describes the matter at time $t = 0$ in an undeformed state.

$$\kappa_r : B \to \mathbb{R}^3$$
$$P \to \mathbf{X} = \mathbf{X}(P)$$

The deformed configuration κ_t, also known as Euler configuration describes the configuration of B at time t by:
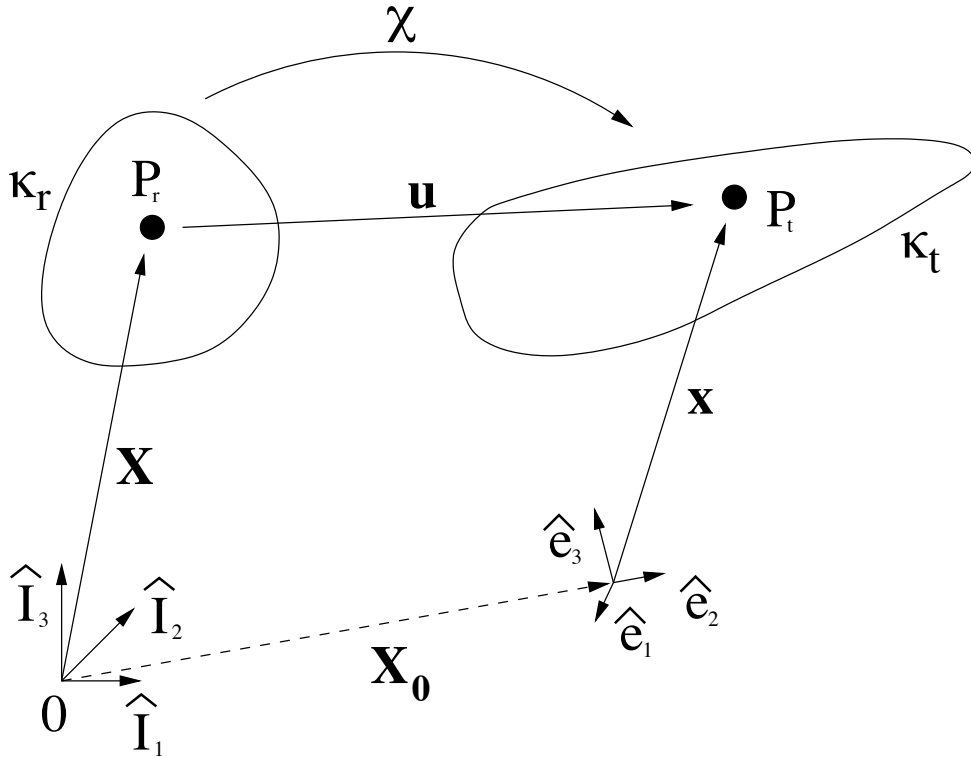
Figure A.1. Schematic of continuum mechanical configurations. The object to the left shows the continuum in the Lagrangian configuration κ_r at time $t = 0$, with the origin 0, the coordiante system $\hat{E}_i$. The left object displays the same continuum at a later time $t = t$ in the Eulerian configuration κ_t, with the coordiante system $\hat{e}_i$. The position of a material point in Lagrangian configuration P_t can be described by the vector $\mathbf{X}$ and the corresponding point in Eulerian configuration P_r by vector $\mathbf{x}$. The displacement vector $\mathbf{u}$ joins the points P_r and P_t. Vector $\mathbf{X_0}$ describes the displacement vector of the origin. The function χ maps the Lagrangian into the Euler configuration.

$$\kappa_t : \mathbf{X_0} \to \mathbb{R}^3$$
$$P \to \mathbf{x} = \mathbf{x}(P, t)$$

In general the configurations κ_r and κ_t are not closer defined, however more interest is given to the function χ, mapping the Lagrangian into the Euler configuration.

$$\chi : \mathbb{R}^3 \to \mathbb{R}^3$$
$$\mathbf{X} \to \mathbf{x} = \mathbf{x}(\mathbf{X}, t)$$

Both configurations are shown in fig. A.1.

A.3 Displacement Vector

The relationship between Lagrangian and Eulerian configuration is accomplished by the displacement vector $\mathbf{u}$ (fig. A.1). It joins the positions of the material points P_r and P_t by using $\mathbf{X}$ and $\mathbf{x}$ resulting in:

$$\mathbf{u} = \mathbf{x} - \mathbf{X} + \mathbf{X_0} \tag{A.1}$$

If the coordinate origins of Lagrangian and Eulerian configuration coincide ($\mathbf{X_0} = \mathbf{0}$), eq. A.1 results to:

$$\mathbf{u} = \mathbf{x} - \mathbf{X} \tag{A.2}$$

A.4 Deformation Gradient

Partial differentiation of eq. A.1 with respect to X_j produces the tensor $\frac{\partial x_i}{\partial X_j}$, which is called deformation gradient tensor $\mathbf{F}$:

$$\mathbf{F} = \nabla \mathbf{x}(\mathbf{X}, t)$$

$$\mathbf{F} = \begin{pmatrix} \frac{\partial x_1}{\partial X_1} & \frac{\partial x_2}{\partial X_1} & \frac{\partial x_3}{\partial X_1} \\ \frac{\partial x_1}{\partial X_2} & \frac{\partial x_2}{\partial X_2} & \frac{\partial x_3}{\partial X_2} \\ \frac{\partial x_1}{\partial X_3} & \frac{\partial x_2}{\partial X_3} & \frac{\partial x_3}{\partial X_3} \end{pmatrix}$$

With the aid of the deformation gradient tensor $\mathbf{F}$ a line element $d\mathbf{X}$ of the Lagrangian configuration can be transfered into the corresponding line element in the Eulerian configuration $d\mathbf{x}$.

$$d\mathbf{x} = \mathbf{F}d\mathbf{X}$$

Since in case of myocardial tissue the displacement should be reversible, $\mathbf{F}$ must be invertible, which leads to:

$$|\mathbf{F}| \neq 0, \tag{A.3}$$

With the so-called Jacobian determinant $J = |\mathbf{F}|$. The relationship of surface and volume elements transfered between configurations can be described by:

$$d\mathbf{s} = J(\mathbf{F}^{-1})^T d\mathbf{S}$$

with s and S a surface element in either configuration and

$$dv = JdV$$

with v and V a volume element in either configuration [212, 173, 213].

A.4.1 Polar Decomposition

The deformation gradient tensor $\mathbf{F}$ can be decomposed into a rotation tensor $\mathbf{R}$ and a right $\mathbf{U}$ or a left $\mathbf{V}$ stretch tensor.

$$\mathbf{F} = \mathbf{R}\,\mathbf{U} = \mathbf{V}\mathbf{R}$$

with $\mathbf{R}$ an orthonormal matrix and $\mathbf{U}$ and $\mathbf{V}$ symmetric, positive semidefinite matrices. The application of rotation before stretching and stretching before rotation is described in fig. A.2. A stretch free deformation can only be accomplished when $\mathbf{U} = \mathbf{V} = \mathbf{I}$, with $\mathbf{I}$ being the matrix description of the Kronecker delta δ, defined by

$$\delta_{ij} = \begin{cases} 1 \; for \; i = j \\ 0 \; for \; i \neq j \end{cases}$$

A.5 Tensor Arithmetic

The inverse of a square tensor or reciprocal matrix is defined as

$$\mathbf{A}\mathbf{A}^{-1} = \mathbf{I} \tag{A.4}$$

with $\mathbf{A}$ the matrix, $\mathbf{A}^{-1}$ the inverse matrix, and $\mathbf{I}$ the identity matrix. The inverse matrix exists under the condition that the Jacobian of $\mathbf{A}$ is $J \neq 0$.
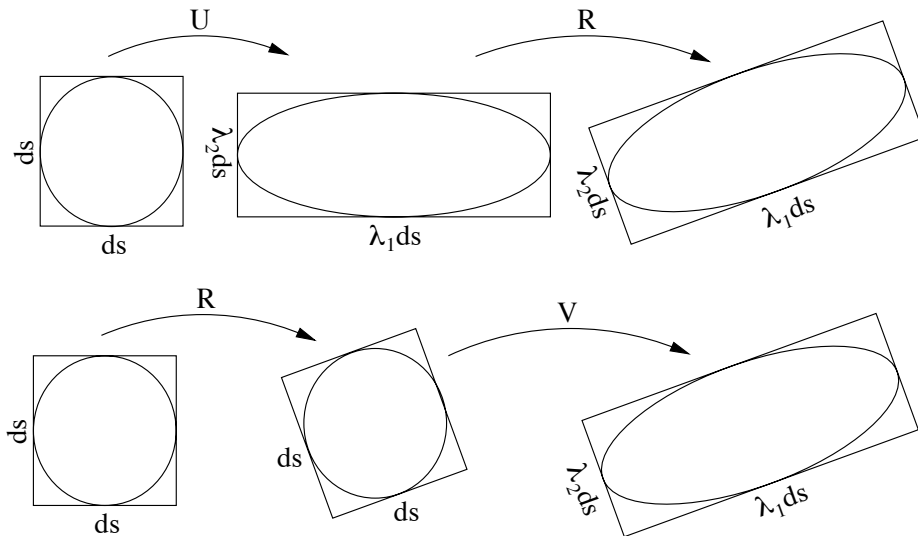
Figure A.2. Polar decomposition of deformation gradient tensor. The edges of the cube ds are aligned along the orthogonal principal axis of $\mathbf{U}$. The stretch factors λ_i represent the positive Eigenvalues of $\mathbf{U}$ and $\mathbf{V}$, respectively. The rotation is described by the tensor $\mathbf{R}$.

For a 3×3 matrix :

$$\mathbf{A} = \begin{bmatrix} a & b & c \\ d & e & f \\ g & h & i \end{bmatrix} \tag{A.5}$$

the inverse is

$$\mathbf{A}^{-1} = \frac{1}{|\mathbf{A}|} \begin{bmatrix} \begin{vmatrix} e & f \\ h & i \end{vmatrix} & \begin{vmatrix} c & b \\ i & h \end{vmatrix} & \begin{vmatrix} b & c \\ e & f \end{vmatrix} \\[1em] \begin{vmatrix} f & d \\ i & g \end{vmatrix} & \begin{vmatrix} a & c \\ g & i \end{vmatrix} & \begin{vmatrix} c & a \\ f & d \end{vmatrix} \\[1em] \begin{vmatrix} d & e \\ g & h \end{vmatrix} & \begin{vmatrix} b & a \\ h & g \end{vmatrix} & \begin{vmatrix} a & b \\ d & e \end{vmatrix} \end{bmatrix} \tag{A.6}$$

The transposed matrix $\mathbf{A}^T$ can be obtained by replacing all elements a_{ij} with a_{ji}. It results to a exchange of $\mathbf{A}$'s rows and columns. However, it must satisfy the identity:

$$\left(\mathbf{A}^T\right)^{-1} = \left(\mathbf{A}^{-1}\right)^T \tag{A.7}$$

A.6 Strain Tensor

The squared tensors $\mathbf{U}$ and $\mathbf{V}$ are used to describe the strain:

$$\mathbf{C} = \mathbf{U}^2 = \mathbf{F}^T\mathbf{F} \text{ right Cauchy-Green tensor}$$
$$\mathbf{B} = \mathbf{V}^2 = \mathbf{F}\mathbf{F}^T \text{ left Cauchy-Green tensor}$$

The right Cauchy-Green tensor transfers a squared length $d\mathbf{X}^2$ in Lagrangian configuration into the corresponding squared length $d\mathbf{x}^2$ in Eulerian configuration. For the inverse transformation the left Cauchy-Green tensor is applied.

$$d\mathbf{x}^2 = d\mathbf{X}\mathbf{C}d\mathbf{X}$$
$$d\mathbf{X}^2 = d\mathbf{x}\mathbf{B}^{-1}d\mathbf{x}$$

The difference $d\mathbf{x}^2 - d\mathbf{X}^2$ of two neighboring particles is used as the measure of deformation, which occurs in the vicinity of the particles between the configurations. If the difference is identical to zero, a rigid displacement occured. The difference can be expressed by:

$$d\mathbf{x}^2 - d\mathbf{X}^2 = d\mathbf{X}\mathbf{C}d\mathbf{X} - d\mathbf{X}\mathbf{I}d\mathbf{X}$$
$$= d\mathbf{X}(\mathbf{C} - \mathbf{I})d\mathbf{X}$$
$$= 2d\mathbf{X}\mathbf{E}d\mathbf{X}$$

resulting in the Green-Lagrangian finite strain tensor $\mathbf{E}$:

$$\mathbf{E} = \tfrac{1}{2}(\mathbf{C} - \mathbf{I}) \quad \text{Green-Lagrangian strain tensor} \tag{A.8}$$

Furthermore, the differences can be expressed by:

$$
\begin{aligned}
d\mathbf{x}^2 - d\mathbf{X}^2 &= d\mathbf{x}\mathbf{I}d\mathbf{x} - d\mathbf{x}\mathbf{B}^{-1}d\mathbf{x} \\
&= d\mathbf{x}(\mathbf{I} - \mathbf{B}^{-1})d\mathbf{x} \\
&= 2d\mathbf{x}\mathbf{A}d\mathbf{x}
\end{aligned}
$$

resulting in the Eulerian (or Almansi's) finite strain tensor $\mathbf{A}$:

$$\mathbf{A} = \tfrac{1}{2}(\mathbf{I} - \mathbf{B}^{-1}) \text{ Eulerian (or Almansi's) strain tensor} \tag{A.9}$$

The derivation of the tensors can be found in [212, 173, 213].

The Green-Lagrangian strain tensor $\mathbf{E}$ can also be described as a function of displacements $\mathbf{u}$. Therefore, eq. A.1 is differentiated by $\mathbf{X}$:

$$\frac{\partial \mathbf{u}}{\partial \mathbf{X}} = \frac{\partial \mathbf{x}}{\partial \mathbf{X}} - \frac{\partial \mathbf{X}}{\partial \mathbf{X}} + \frac{\partial \mathbf{X}_0}{\partial \mathbf{X}} = \mathbf{F} - \mathbf{I}$$

transformed to

$$
\begin{aligned}
\mathbf{F} &= \frac{\partial \mathbf{u}}{\partial \mathbf{X}} + \mathbf{I} \\
&= \nabla\mathbf{u} + \mathbf{I}
\end{aligned}
\tag{A.10}
$$

and substituted into eq. A.8:

$$\mathbf{E} = \frac{1}{2}(\mathbf{F}^T\mathbf{F} - \mathbf{I}) \tag{A.11}$$

$$\mathbf{E} = \frac{1}{2}(\nabla\mathbf{u} + (\nabla\mathbf{u})^T + (\nabla\mathbf{u})^T\nabla\mathbf{u})$$

The strain tensor describes the material independent change of the geometry of the object.

A.7 Stress Tensor

A.7.1 Cauchy Stress Tensor

The Cauchy stress tensor $\boldsymbol{\sigma}$ is defined for each point in the continuous medium and describes the forces per unit square. The components of the Cauchy stress tensor can be displayed with reference to the coordinate planes (fig. A.3). The components perpendicular to the planes $\boldsymbol{\sigma}_{11}, \boldsymbol{\sigma}_{22}, \boldsymbol{\sigma}_{22}$ are

called normal stresses, the others acting tangent to the surface are called shear stresses. It is a symmetric tensor of second order [214].

$$\sigma = \begin{pmatrix} \sigma_{11} & \sigma_{12} & \sigma_{13} \\ \sigma_{21} & \sigma_{22} & \sigma_{23} \\ \sigma_{31} & \sigma_{32} & \sigma_{33} \end{pmatrix}$$

A.7.2 First Piola-Kirchhoff Stress Tensor

The first Piola-Kirchhoff stress tensor $\mathbf{T}$ or Lagrangian stress tensor is a non-symmetric second order tensor. The tensor can be derived from the Cauchy stress tensor $\boldsymbol{\sigma}$:

$$\mathbf{T} = J(\mathbf{F}^{-1})\boldsymbol{\sigma}$$

with the Jacobian determinant J and the deformation gradient tensor $\mathbf{F}$.

A.7.3 Second Piola-Kirchhoff Stress Tensor

The second Piola-Kirchhoff stress tensor $\mathbf{S}$ is a symmetric tensor of second order. It is an extension of the first Piola-Kirchhoff stress tensor $\mathbf{T}$:

$$\mathbf{S} = \mathbf{T}(\mathbf{F}^{-1})^T = J(\mathbf{F}^{-1})\boldsymbol{\sigma}(\mathbf{F}^{-1})^T \tag{A.12}$$
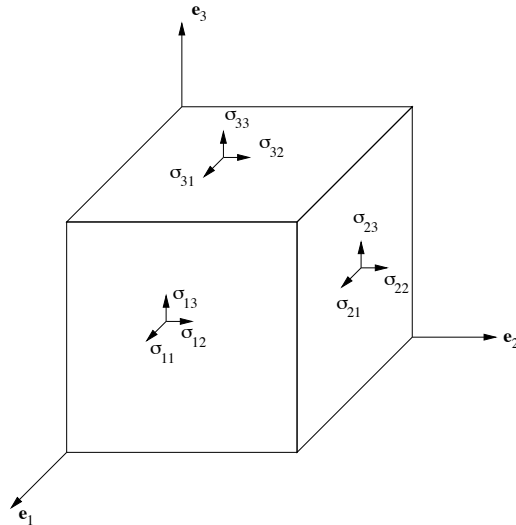
Figure A.3. Components of the Cauchy stress tensor. Any stress acting on the surface of an infinitesimal cubic element can be decomposed into the coordinate axes.

with the Jacobian determinant J, the deformation gradient tensor $\mathbf{F}$, and the Cauchy stress tensor $\boldsymbol{\sigma}$.

A.8 Energy Density Function

The stretch of an object results in material dependent strains. The strain dependent energy of an object can be described by energy density functions. The mathematical description of mechanical properties of the myocardium are mainly formulated as energy density functions (section 5.3). Hunter et al. [83] proposed the following energy density function:

$$\mathbf{W} = \sum_{i=1}^{3} \frac{k_i \mathbf{E}_{ii}^2}{(a_i - |\mathbf{E}_{ii}|)^{\beta_i}} \tag{A.13}$$

The anisotropy and inhomogeneity of the myocardium is modeled, with k_i, a_i und β_i describing the fiber, sheet, and sheet normal parameters and $\mathbf{E}_{ii}$ the components of the Green-Lagrangian strain tensor.
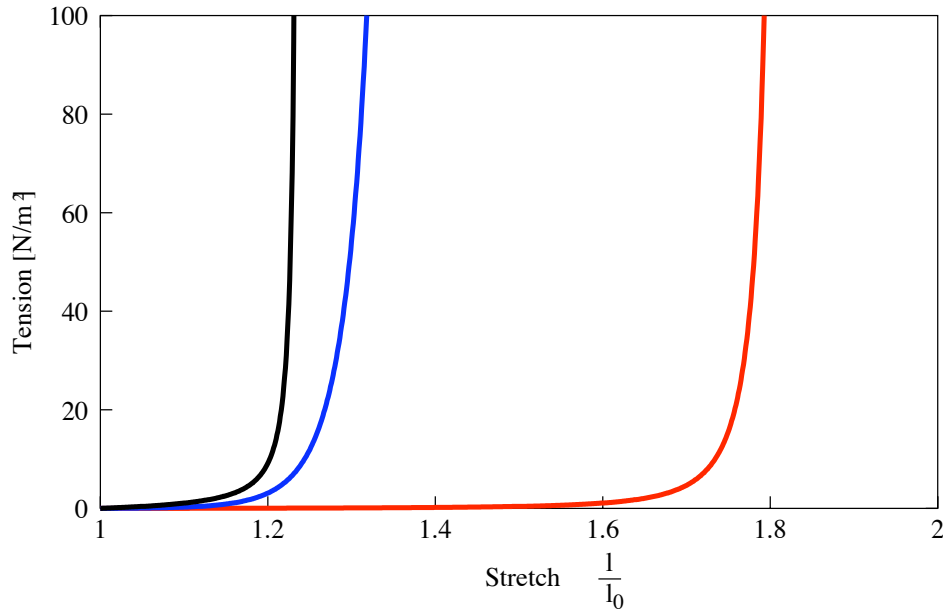
Figure A.4. Stress strain relationship of Hunter et al. [83]. This figure shows the stress strain relationship in fiber (red), sheet (blue), and sheet normal (black) direction.

A.9 Application of Energy Density Function

Various models describe the mechanical properties of the heart by energy density functions, depending on the Green-Lagrangian strain tensor $\mathbf{E}$.

In this work energy density function of Guccione et al. [80] are applied to model passive myocardial tissue. The following mathematical method describes the application of the energy density function $\mathbf{W}$.

The hybrid deformation model results in a step wise deformation of a cubic element. The displacement of the cubic vertices is used to calculate the deformation gradient tensor $\mathbf{F}$ (eq. A.10).

The differentiation of the energy density function $\mathbf{W}$ by $\mathbf{E}$ (Green-Lagrangian strain tensor eq. A.11)

$$\mathbf{S} = \frac{\partial \mathbf{W}}{\partial \mathbf{E}} \tag{A.14}$$

results in the second Piola-Kirchoff stress tensor $\mathbf{S}$.

Rearranging eq. A.12 to:

$$\boldsymbol{\sigma} = \frac{1}{J} \mathbf{F} \mathbf{S} \mathbf{F}^T \tag{A.15}$$

results in the Cauchy strain tensor $\boldsymbol{\sigma}$.

The components of the Cauchy stress tensor $\boldsymbol{\sigma}_{ij}$ can be used to compile a stress vector for each plane (fig. A.5) e. g. :

$$\boldsymbol{\sigma}_{W1} = \begin{pmatrix} \sigma_{11} \\ \sigma_{12} \\ \sigma_{13} \end{pmatrix}, \boldsymbol{\sigma}_{W2} = \begin{pmatrix} \sigma_{21} \\ \sigma_{22} \\ \sigma_{23} \end{pmatrix}, \boldsymbol{\sigma}_{W3} = \begin{pmatrix} \sigma_{31} \\ \sigma_{32} \\ \sigma_{33} \end{pmatrix} \tag{A.16}$$

From the stresses resulting force vectors can be computed by:

$$\mathbf{f}_i = A \boldsymbol{\sigma}_{Wi} \tag{A.17}$$

for each voxel plane derived from the energy density function $\mathbf{W}$. This force vector can be used in the spring-mass system to model material stress depending on material strain.
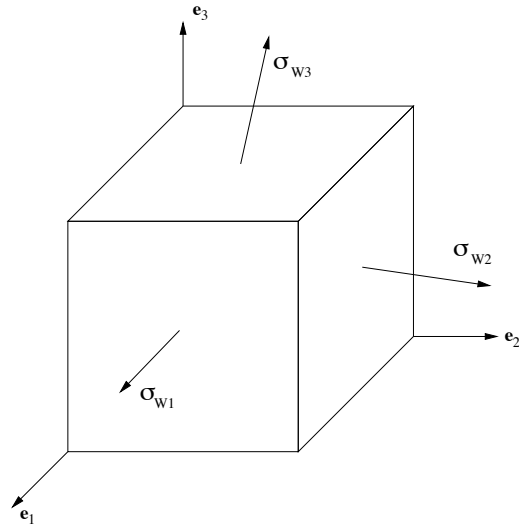
Figure A.5. Schematic of stress vectors on voxel surfaces.

B

Physical Units

Quantity	Symbol
Displacement vector	$\mathbf{u}$
Deformation gradient tensor	$\mathbf{F}$
Jacobian determinant	J
Rotation tensor	$\mathbf{R}$
Right stretch tensor	$\mathbf{U}$
Left stretch tensor	$\mathbf{V}$
Kronecker delta	δ
Identity matrix	$\mathbf{I}$
Right Cauchy-Green strain tensor	$\mathbf{C}$
Left Cauchy-Green strain tensor	$\mathbf{B}$
Green-Lagranginan finite strain tensor	$\mathbf{E}$
Eulerian (or Almansi's) finite strain tensor	$\mathbf{A}$
Cauchy stress tensor	$\boldsymbol{\sigma}$
First Piola-Kirchhoff stress tensor	$\mathbf{T}$
Second Piola-Kirchhoff stress tensor	$\mathbf{S}$
Energy Density Function	$\mathbf{W}$
Force	$\mathbf{f}$
surface area	A

Table B.1. Physical symbols

List of Figures

List of Tables

References

1. E. Keeve, S. Girod, R. Kikinis, and B. Girod, "Deformable modeling of facial tissue for craniofacial surgery simulation," *Comp. Aided Surg.*, vol. 3, no. 5, pp. 228–238, 1998.

2. E. Keeve, S. Girod, and B. Girod, "Craniofacial surgery simulation," in *Proceedings of the 4th International Conference on Visualization in Biomedical Computing VBC'96*, 1998.

3. D. Bourguignon and M.-P. Cani, "Controlling anisotropy in mass-spring systems," in *Computer Animation and Simulation '00, Proc. 11th Eurographics Workshop, Interlaken, Switzerland*, Springer Computer Science, pp. 113–123, Springer, Aug. 2000.

4. H. Gray and W. H. Lewis, *Anatomy of the human body*. Philadelphia: Lea & Febiger, 20 ed., 1918.

5. A. M. Katz, *Physiology of the Heart*, ch. 1. Structure of the heart and cardiac muscle, pp. 1–36. Raven Press, New York, 2nd ed., 1992.

6. E. Pierce, "Schematic illustration of blood flow." Wikipedia, The Free Encyclopedia, http://en.wikipedia.org/wiki/Image:Heart_labelled_large.png.

7. "Conduction system of the heart," 2003. Benjamin-Cummings Publishing Company.

8. W. Hort, "Untersuchungen über die Muskelfaserdehnung und das Gefüge des Myokards in der rechten Herzkammerwand des Meerschweinchens," *Virchows Arch. Pathol. Anat. Physiol. Klin. Med.*, vol. 359, pp. 694–731, 1957.

9. W. Hort, "Makroskopische und mikrometrische Untersuchungen am Myokard verschieden stark gefüllter linker Kammern," *Virchows Arch. Pathol. Anat. Physiol. Klin. Med.*, vol. 333, pp. 523–564, 1960.

10. D. D. Streeter, jr. and D. L. Bassett, "An engineering analysis of myocardial fiber orientation in pig's left ventricle in systole," *Anatomical Record*, vol. 155, pp. 503–512, 1966.

11. D. D. Streeter, H. M. Spotnitz, D. P. Patel, J. Ross Jr., and E. H. Sonnenblick, "Fiber orientation in the canine left ventricle during diastole and systole," *Circ. Res.*, vol. 24, pp. 339–347, Mar 1969.

12. D. D. Streeter, "Gross morphology and fiber geometry of the heart," in *Handbook of Physiology: The Cardiovascular System* (B. Bethesda, ed.), vol. I, pp. 61–112, American Physiology Society, 1979.

13. M. Nash, *Mechanics and Material Properties of the Heart using an Anatomically Accurate Mathematical Model*. PhD thesis, University of Auckland, Dep. of Engineering Science, New Zealand, 1998.

14. F. Schöeni-Affolter, "Schematic of skeletal muscle structure." Universität Freiburg, Schweiz, http://www.unifr.ch/histologie/elearningfree/allemand/biochemie/muskel/aufbau/d-aufbau.php.

15. A. Mc Murry and C. Castellion, *Fundamentals of General, Organic, and Biological Chemistry*. 3 ed., 1999.

16. R. Lynch, "Intercalated disc." www.colorado.edu/epob/epob1220lynch/image/figure8n.jpg.

17. F. H. Martini, *Fundamentals of Anatomy & Physiology*, vol. 5th Edition. Prentice Hall, Inc. Upper Saddle River, NJ: Benjamin-Cummings Publishing Company, 1998.

18. O. Dössel, *Bildgebende Verfahren in der Medizin*. Berlin: Springer, 1999.

19. W. A. Kalender, "ECG-Based Cardiac CT Imaging," 2006. Institute of Medical Physics, Friedrich-Alexander-University Erlangen-Nürnberg.

20. H. Morneburg, Siemens Aktiengesellschaft, ed., *Bildgebende Systeme für die medizinische Diagnostik*. Erlangen: Publicis MCD, 3 ed., 1995.

21. J. P. Hornak, *The Basics of MRI*. http://www.cis.rit.edu/htbooks/mri/, 2005.

22. M. J. Ackerman, "Viewpoint: The Visible Human Project," *J. Biocommunication*, vol. 18, no. 2, p. 14, 1991.

23. Institut für Biomedizinische Technik, Universität Karlsruhe, Germany, "MEET Man project."

24. "Visible human project." http://www.nlm.nih.gov/research/visible/visibleuman.html.

25. F. B. Sachse, C. D. Werner, M. Müller, and K. Meyer-Waarden, "Preprocessing of the Visible Man dataset for the generation of macroscopic anatomical models," in *Proc. First Users Conference of the National Library of Medicine's Visible Human Project*, 1996.

26. F. B. Sachse, M. Glas, M. Müller, and K. Meyer-Waarden, "Segmentation and tissue-classification of the Visible Man dataset using the computertomographic scans and the thin-section photos," in *Proc. First Users Conference of the National Library of Medicine's Visible Human Project*, 1996.

27. L. Zhukov and A. H. Barr, "Heart-muscle fiber reconstruction from diffusion tensor MRI," in *Proceedings of IEEE Visualization, 2003*, pp. 597 – 602, 19-24 Oct. 2003.

28. S. Köhler, K. Hiller, C. Waller, P. M. Jakob, W. R. Bauer, and A. Haase, "Visualization of myocardial microstructure using highresolution T*2 imaging at high magnetic field," *Magnetic Resonance in Medicine*, vol. 2, pp. 371–375, February 2003.

29. S. Köhler, K. Hiller, C. Waller, P. M. Jakob, W. R. Bauer, and A. Haase, "Investigation of the Microstructure of the Isolated Rat Heart: A Comparison Between T*2 and Diffusion Weighted MRI," *Magnetic Resonance in Medicine*, vol. 50, pp. 1144–1150, December 2003.

30. F. B. Sachse, C. Henriquez, G. Seemann, C. Riedel, C. D. Werner, R. C. Penland, B. Davis, and E. Hsu, "Modeling of fiber orientation in the ventricular myocardium with MR diffusion imaging," in *Proc. Computers in Cardiology*, vol. 28, pp. 617–620, Sep. 2001.

31. F. B. Sachse, *Computational Cardiology: Modeling of Anatomy, Electrophysiology, and Mechanics*. LNCS 2966, Heidelberg: Springer Press, 2004.

32. A. D. McCulloch, "Cardiac biomechanics," in *The Biomedical Engineering Handbook* (J. D. Bronzino, ed.), pp. 28–1–28–26, CRC Press, 2 ed., 2000.

33. M. A. Fernandez-Teran and J. M. Hurle, "Myocardial fiber architecture of the human heart ventricles," *The Anatomical Record*, vol. 204, pp. 137–147, 1982.

34. A. F. Grimm, K. V. Katele, and H.-L. Lin, "Fiber bundle direction in the mammalian heart," *Basic Res. Cardiol.*, vol. 71, pp. 381–388, 1976.

35. I. J. LeGrice, B. H. Smaill, L. Z. Chai, S. G. Edgar, J. B. Gavin, and P. J. Hunter, "Laminar structure of the heart: Ventricular myocyte arrangement and connective tissue architecture in the dog," *Am. J. Physiol.*, vol. 269, pp. H571–H582, 1995.

36. A. A. Young, L. J. LeGrice, M. A. Young, and B. H. Smaill, "Extended confocal microscopy of myocardial laminae and collagen network," *J. Microscopy*, vol. 192, pp. 139–150, Nov. 1998.

37. A. McCulloch, "Continuity 6, problem-solving environment for finite element analysis in bioengineeeing and physiology," 2006. University of California, San Diego, U.S.A, http://www.continuity.ucsd.edu.

38. P. M. F. Nielsen, I. J. LeGrice, P. J. Hunter, and B. H. Smaill, "Mathematical model of geometry and fibrous structure of the heart," *Am. J. Physiol.*, vol. 260, pp. H1365–H1378, 1991.

39. F. J. Vetter and A. McCulloch, "Three-dimensional analysis of regional cardiac function: A model of rabbit ventricular anatomy," *Prog. Biophys. Mol. Biol.*, vol. 69, pp. 157–183, 1998.

40. *Geo kompakt; Das Wunder Mensch*. Gruner + Jahr Hamburg, 2005.

41. R. Busse, "Gefäßsystem und Kreislaufregulation," in *Physiologie des Menschen* (R. F. Schmidt and G. Thews, eds.), ch. 24, pp. 498–561, Berlin, Heidelberg, New York: Springer, 1997.

42. R. M. Berne and M. N. Levy, *Cardiovascular physiology*. C. V. Mosby Company ed., 1967.

43. H. Antoni, "Funktionen des Herzens," in *Physiologie des Menschen* (R. F. Schmidt and G. Thews, eds.), ch. 19, pp. 461–504, Berlin, Heidelberg, New York: Springer, 1993.

44. O. Frank, "Die Grundform des arteriellen Pulses," *Zeitschrift für Biologie*, vol. 37, pp. 483–526, 1899.

45. K. Sagawa, R. K. Lie, and J. Schaefer, "Translation of Otto Frank's paper "Die Grundform des Arteriellen Pulses"," *Journal of Molecular & Cellular Cardiology*, vol. 22, pp. 253–277, Mar 1990.

46. J. Schrader, "Das Herz," in *Lehrbuch der Physiologie* (R. Klinke and S. Silbernagl, eds.), ch. 7, pp. 109–144, Stuttgart, New York: Thieme, 2001.

47. S. Silbernagl and A. Despopoulos, *Taschenbuch der Physiologie*. Stuttgart; New York: Georg Thieme Verlag, 4 ed., 1991.

48. W. Nernst, "Zur Kinetik der in Lösung befindlichen Körper: Theorie der Diffusion," *Z. Phys. Chem.*, pp. 613–637, 1888.

49. D. E. Goldman, "Potential, impedance, and rectification in membranes," *J. Gen. Physiol.*, vol. 27, pp. 37–60, 1943.

50. A. L. Hodgkin and B. Katz, "The effect of sodium ions on the electrical activity of the giant axon of a squid," *J. Physiol.*, vol. 108, pp. 37–77, 1949.

51. R. F. Schmidt, G. Thews, and F. Lang, *Physiologie des Menschen*. Berlin; Heidelberg; New York: Springer, 28 ed., 2000.

52. R. F. Schmidt, "Erregungsphysiologie des Herzens," in *Physiologie kompakt*, ch. 23, pp. 197–204, Berlin, Heidelberg, New York: Springer, 1999.

53. R. Klinke and S. Silbernagl, *Taschenatlas der Physiologie*. Stuttgart; New York: Georg Thieme Verlag, 5 ed., 2001.

54. J. R. Balser, "Biophysics of Normal and Abnormal Cardiac Sodium Channel Function," in *Cardiac Electrophysiology. From Cell to Bedside* (D. P. Zipes and J. Jalife, eds.), ch. 9, pp. 77–87, Philadelphia: W. B. Saunders Company, 4 ed., 2004.

55. S. Silbernagl and A. Despopoulos, "Nerv und Muskel, Arbeit," in *Taschenatlas der Physiologie*, ch. 2, pp. 42–76, Stuttgart: Georg Thieme Verlag, 2001.

56. O. Skipa, *Linear inverse problem of electrocardiography: epicardial potentials and transmembrane voltages*. PhD thesis, Universität Karlsruhe (TH), Institut für Biomedizinische Technik, 2004.

57. M. S. Spach, J. F. Heidlage, and P. C. Dolber, "The dual nature of anisotropic discontinous conduction in the heart," in *Cardiac Electrophysiology. From Cell to Bedside* (D. P. Zipes and J. Jalife, eds.), ch. 25, pp. 213–222, Philadelphia: W. B. Saunders Company, 3 ed., 1999.

58. A. G. Kléber, V. G. Fast, and S. Rohr, "Continuous and discontinuous propagation," in *Cardiac Electrophysiology. From Cell to Bedside* (D. P. Zipes and J. Jalife, eds.), ch. 24, pp. 213–222, Philadelphia: W. B. Saunders Company, 3 ed., 1999.

59. H. J. Jongsma and M. B. Rook, "Biophysics of cardiac gap junction channels," in *Cardiac Electrophysiology. From Cell to Bedside* (D. P. Zipes and J. Jalife, eds.), ch. 14, pp. 119–125, Philadelphia: W. B. Saunders Company, 3 ed., 1999.

60. S. Verheule, M. J. A. van Kempen, P. H. J. A. te Welscher, B. R. Kwak, and H. J. Jongsma, "Characterization of gap junction channels in adult rabbit atrial and ventricular myocardium," *Circ. Res.*, vol. 80, pp. 673–681, 1997.

61. M. Delmar, H. S. Duffy, P. L. Sorgen, S. M. Taffet, and D. C. Spray, "Molecular organization and regulation of the cardiac gap junction channel connexin43," in *Cardiac Electrophysiology. From Cell to Bedside* (D. P. Zipes and J. Jalife, eds.), ch. 8, pp. 66–76, Philadelphia: W. B. Saunders Company, 4 ed., 2004.

62. E. Carafoli, "Calcium signaling: A tale for all seasons," *Proc. Natl. Acad. Sci. USA*, vol. 99, no. 3, pp. 1115–1122, 2002.

63. Y. C. Fung, *Biomechanics: Mechanical Properties of Living Tissues.* New York, Berlin, Heidelberg: Springer, 1993.

64. J. M. Guccione, A. D. McCulloch, and L. K. Waldman, "Passive material properties of intact ventricular myocardium determined from a cylindrical model," *J. Biomechanical Engineering*, vol. 113, pp. 42–55, Feb. 1991.

65. R. J. Okamoto, M. J. Moulton, S. J. Peterson, D. Li, M. K. Pasque, and J. M. Guccione, "Epicardial suction: A new approach to mechanical testing of the passive ventricular wall," *J. Biomed. Engin.*, vol. 122, pp. 479–487, Oct. 2000.

66. M. R. Zile, M. K. Cowles, J. M. Buckley, K. Richardson, B. A. Cowles, C. F. Baicu, G. Cooper, and V. Gharpuray, "Gel stretch method: A new method to measure constitutive properties of cardiac muscle cells," *Am. J. Physiol.*, vol. 274, pp. H2188–H2202, 1998.

67. S. Dokos, I. J. LeGrice, B. H. Smaill, J. Kar, and A. A. Young, "A triaxial-measurement shear-test device for soft biological tissues," *J. Biomedical Engineering*, vol. 122, pp. 471–478, Oct. 2000.

68. S. Dokos, B. H. Smaill, A. A. Young, and I. J. LeGrice, "Shear properties of passive ventricular myocardium," *Am. J. Physiol.*, vol. 283, pp. H2650–H2659, 2003.

69. J. S. Rankin, C. E. Arentyen, P. A. McHale, D. Ling, and R. W. Anderson, "Viscoelastic properties of the diastolic left ventricle in the conscious dog," *Circ. Res.*, vol. 41, pp. 37–45, July 1976.

70. A. McCulloch and J. H. Omens, "Factors affecting the regional mechanics of the diastolic heart," in *Theory of Heart* (L. Glass, P. Hunter, and A. McCulloch, eds.), pp. 121–144, Berlin, Heidelberg, New York: Springer, 1991.

71. D. H. S. Lin and F. C. P. Yin, "A multiaxial constituive law for mammalian left ventricular myocardium in steady-state barium contracture or tetanus," *J. Biomechanical Engineering*, vol. 120, pp. 504–517, 1998.

72. E. H. Sonnenblick, "Series elastic and contractile elements in heart muscles: Changes in muscle length," *Am. J. Physiol.*, vol. 207, no. 6, pp. 1330–1338, 1964.

73. J. G. Pinto and Y. C. Fung, "Mechanical properties of the heart muscle in the passive state," *J. Biomechanics*, vol. 6, pp. 597–616, 1973.

74. R. F. Janz and A. F. Grimm, "Deformation of the Diastolic Left Ventricle - I. Nonlinear Elastic Effects," *Biophysical J.*, vol. 13, pp. 689–704, 1973.

75. R. F. Janz, B. R. Kubert, and T. F. Moriarty, "Deformation of the Diastolic Left Ventricle - II. Nonlinear Geometric Effects," *J. Biomechanics*, vol. 7, pp. 509–516, 1974.

76. N. R. Alpert, B. B. Hamrell, and W. Halpern, "Mechanical and biochemical correlates of cardiac hypertrophy," *Circ. Res.*, vol. 34,35, pp. II71–II82, 1974.

77. R. L. Kane, T. A. McMahon, R. L. Wagner, and W. H. Abelmann, "Ventricular elastic modulus as a function of age in the syrian golden hamster," *Circ. Res.*, vol. 38, pp. 74–80, Feb. 1975.

78. P. J. Hunter and B. H. Smaill, "The analysis of cardiac function: A continuum approach," *Prog. Biophys. Mol. Biol.*, vol. 52, pp. 101–164, 1988.

79. B. H. Smaill and P. J. Hunter, "Structure and function of the diastolic heart," in *Theory of Heart* (L. Glass, P. Hunter, and A. McCulloch, eds.), pp. 1–30, Berlin, Heidelberg, New York: Springer, 1991.

80. J. M. Guccione, "Finite element modeling of ventricular mechanics," in *Theory of Heart* (L. Glass, P. Hunter, and A. McCulloch, eds.), ch. 6, pp. 121–144, Berlin, Heidelberg, New York: Springer, 1991. ibt bibl. vorhanden.

81. V. P. Novak, F. C. P. Yin, and J. D. Humphrey, "Regional mechanical properties of passive myocardium," *J. Biomechanics*, vol. 27, no. 4, pp. 403–412, 1994.

82. P. J. Hunter, "Myocardial constitutive laws for continuum mechanics models of the heart," in *Molecular and Subcellular Cardiologgy: Effects of Structure and Function* (S. Sideman and R. Beyar, eds.), ch. 30, pp. 303–318, New York: Plenum Press, 1995.

83. P. Hunter, M. P. Nash, and G. P. Sands, "Computational electromechanics of the heart," in *Computational Biology of the Heart* (A. V. Panfilov and A. V. Holden, eds.), pp. 345–408, Chichester: John Wiley & Sons, 1997.

84. M. J. Moulton, L. L. Creswell, R. L. Actis, K. W. Myers, M. W. Vannier, B. A. Szabó, and M. K. Pasque, "An inverse approach to determining myocardial material properties," *J. Biomechanics*, vol. 28, no. 8, pp. 935–948, 1995.

85. C. E. Miller, M. A. Vanni, and B. B. Keller, "Characterization of passive embryonic myocardium by quasi-linear viscoelasticity theory," *J. Biomechanics*, vol. 30, no. 9, pp. 985–988, 1997.

86. J. H. Omens, S. M. Vaplon, B. Fazeli, and A. D. McCulloch, "Left ventricular geometric remodeling and residual stress in the rat heart," *J. Biomechanical Engineering*, vol. 120, pp. 715–719, 1998.

87. G. Seemann, D. L. Weiß, F. B. Sachse, and O. Dössel, "Electrophysiology and tension development in a transmural heterogeneous model of the visible female left ventricle," in *LNCS* (A. F. Franji, P. I. Radeva, A. Santos, and M. Hernandez, eds.), vol. 3504, pp. 172–182, 2005.

88. A. L. Hodgkin and A. F. Huxley, "A quantitative description of membrane current and its application to conduction and excitation in nerve," *J. Physiol.*, vol. 177, pp. 500–544, 1952.

89. D. Noble, "A modification of the Hodgkin-Huxley equation applicable to Purkinje fibre action and pacemaker potentials," *J. Physiol.*, vol. 160, pp. 317–352, 1962.

90. R. E. McAllister, D. Noble, and R. W. Tsien, "Reconstruction of the electrical activitity of cardiac Purkinje fibres," *J. Physiol.*, vol. 251, pp. 1–59, 1975.

91. G. W. Beeler and H. Reuter, "Reconstruction of the action potential of ventricular myocardial fibres," *J. Physiol.*, vol. 268, pp. 177–210, 1977.

92. D. DiFrancesco and D. Noble, "A model of cardiac electrical activity incorporating ionic pumps and concentration changes," *Phil. Trans. R. Soc. Lond.*, vol. 307, pp. 353–398, 1985.

93. D. W. Hilgemann and D. Noble, "Excitation-contraction coupling and extracellular calcium transients in rabbit atrium: Reconstruction of basic cellular mechanisms," *Proc. R. Soc. Lond.*, vol. 230, pp. 163–205, 1987.

94. Y. E. Earm and D. Noble, "A model of single atrial cell: Relation between calcium current and calcium release," *Proc. R. Soc. Lond.*, vol. 240, pp. 83–96, 1990.

95. C.-H. Luo and Y. Rudy, "A model of the ventricular cardiac action potential," *Circ. Res.*, vol. 68, no. 6, pp. 1501–1526, 1991.

96. C.-H. Luo and Y. Rudy, "A dynamic model of the ventricular cardiac action potential: I. Simulations of ionic currents and concentration changes," *Circ. Res.*, vol. 74, no. 6, pp. 1071–1096, 1994.

97. C.-H. Luo and Y. Rudy, "A dynamic model of the ventricular cardiac action potential: II. Afterdepolarizations, triggered activity, and potentiation," *Circ. Res.*, vol. 74, no. 6, pp. 1097–1113, 1994.

98. S. S. Demir, J. W. Clark, C. R. Murphey, and W. R. Giles, "A mathematical model of a rabbit sinoatrial node cell," *Am. J. Physiol.*, vol. 35, pp. 832–852, 1994.

99. S. Dokos, B. G. Celler, and N. H. Lovell, "Vagal control of sinoatrial rhythm: A mathematical model," *J. Theor. Biol.*, vol. 182, pp. 21–44, Sep. 1996.

100. S. S. Demir, B. O'Rourke, G. F. Tomaselli, E. Marbán, and R. L. Winslow, "Action potential variation in canine ventricle: A modeling study," in *Proc. Computers in Cardiology*, vol. 23, pp. 221–224, 1996.

101. M. Courtemanche, R. J. Ramirez, and S. Nattel, "Ionic mechanisms underlying human atrial action potential properties: Insights from a mathematical model," *Am. J. Physiol.*, vol. 275, no. 44, pp. H301–H321, 1998.

102. M. S. Jafri, J. J. Rice, and R. L. Winslow, "Cardiac Ca^{2+} dynamics: The roles of ryanodine receptor adapation and sarcoplasmic reticulum load," *Biophysical J.*, vol. 74, pp. 1149–1168, Mar. 1998.

103. D. Noble, A. Varghese, P. Kohl, and P. Noble, "Improved guinea-pig ventricular cell model incorporating a diadic space, I_{Kr} and I_{Ks}, and length- and tension-dependend processes," *Can. J. Cardiol.*, vol. 14, pp. 123–134, Jan. 1998.

104. A. Nygren, C. Fiset, L. Firek, J. W. Clark, D. S. Lindblad, R. B. Clark, and W. R. Giles, "Mathematical model of an adult human atrial cell," *Circ. Res.*, vol. 82, pp. 63–81, 1998.

105. L. Priebe and D. J. Beuckelmann, "Simulation study of cellular electric properties in heart failure," *Circ. Res.*, vol. 82, pp. 1206–1223, 1998.

106. R. L. Winslow, J. J. Rice, S. Jafri, E. Marbán, and B. O'Rourke, "Mechanisms of altered excitation-contraction coupling in canine tachycardia-induced heart failure, II model studies," *Circ. Res.*, vol. 84, pp. 571–586, 1999.

107. B. OŔourke, D. A. Kass, G. F. Tomaselli, S. Kaab, R. Tunin, and E. Marbán, "Mechanisms of altered excitation-contraction coupling in canine tachycardia-induced heart failure, I experimental studies," *Circ. Res.*, vol. 84, no. 5, pp. 562–570, 1999.

108. H. Zhang, A. V. Holden, I. Kodama, H. Honjo, M. Lei, T. Varghese, and M. R. Boyett, "Mathematical models of action potentials in the periphery and center of the rabbit sinoatrial node," *Am. J. Physiol.*, vol. 279, no. 1, pp. 397–421, 2000.

109. S. V. Pandit, R. B. Clark, W. R. Giles, and S. S. Demir, "A mathematical model of action potential heterogeneity in adult left ventricular myocytes," *Biophys. J.*, vol. 81, pp. 3029–3051, 2001.

110. J. L. Puglisi and D. M. Bers, "LabHEART: An interactive computer model of rabbit ventricular myocyte ion channels and Ca transport," *Am. J. Physiol.*, vol. 281, pp. C2049–C2060, 2001.

111. O. Bernus, R. Wilders, C. W. Zemlin, H. Verschelde, and A. V. Panfilov, "A computationally efficient electrophysiological model of human ventricular cells," *Am. J. Physiol.*, vol. 282, pp. H2296–H2308, 2002.

112. K. H. W. J. ten Tusscher, D. Noble, P. J. Noble, and A. V. Panfilov, "A model for human ventricular tissue," *Am. J. Physiol.*, vol. 286, pp. H1573–H1589, 2004.

113. V. Iyer, R. Mazhari, and R. L. Winslow, "A computational model of the human left-ventricular epicardial myocyte," *Biophys. J.*, vol. 87, no. 3, pp. 1507–1525, 2004.

114. P. Wach, R. Killmann, F. Dienstl, and C. Eichtinger, "A computer model of human ventricular myocardium for simulation of ECG, MCG, and activation sequence including reentry rhythms," *Basic Research in Cardiology*, vol. 84, no. 4, 1989.

115. R. Killmann, P. Wach, and F. Dienstl, "Three-dimensional computer model of the entire human heart for simulation of reentry and tachycardia: Gap phenomenon and Wolff-Parksinson-White syndrome," *Basic Research in Cardiology*, vol. 86, no. 5, pp. 485–501, 1991.

116. B. E. H. Saxberg and R. J. Cohen, "Cellular automata models of cardiac conduction," in *Theory of Heart* (L. Glass, P. Hunter, and A. McCulloch, eds.), pp. 437–476, Berlin, Heidelberg, New York: Springer, 1991.

117. D. Wei, O. Okazaki, K. Harumi, E. Harasawa, and H. Hosaka, "Comparative simulation of excitation and body surface electrocardiogram with isotropic and anisotropic computer heart models," *IEEE Transactions on Biomedical Engineering*, vol. 42, pp. 343–357, Apr. 1995.

118. A. V. Panfilov, "Three-dimensional wave propagation in mathematical models of ventricular fibrillation," in *Cardiac Electrophysiology. From Cell to Bedside* (D. P. Zipes and J. Jalife, eds.), ch. 31, pp. 271–277, Philadelphia: W. B. Saunders Company, 3 ed., 1999.

119. J. P. Keener and A. V. Panfilov, "The effects of geometry and fibre orientation on propagation and extracellular potentials in myocardium," in *Computational Biology of the Heart* (A. V. Panfilov and A. V. Holden, eds.), pp. 235–258, Chichester: John Wiley & Sons, 1997.

120. J. M. Rogers, "Modeling the cardiac action potential using b-spline surfaces," *IEEE Transactions on Biomedical Engineering*, vol. 47, pp. 784–791, June 2000.

121. M. Delorme, "An introduction to cellular automata," in *Cellular Automata* (M. Delorme and J. Mazoyer, eds.), ch. 1, pp. 5–49, Dordrecht: Kluwer, 1999.

122. T. A. Sudkamp, *Languages and Machines*. Reading, Massachusetts; Menlo Park, California: Addison-Wesley, 2 ed., 1997.

123. C. D. Werner, F. B. Sachse, and O. Dössel, "Electrical excitation propagation in the human heart," *Int. J. Bioelectromagnetism*, vol. 2, no. 2, 2000.

124. C. D. Werner, *Simulation der elektrischen Erregungsausbreitung in anatomischen Herzmodellen mit adaptiven zellulären Automaten*. PhD thesis, Universität Karlsruhe (TH), Institut für Biomedizinische Technik, 2001.

125. A. V. Hill, "The heat of shortening and the dynamic constants of muscle," *Proc. R. Soc. Lond.*, vol. B126, pp. 136–195, 1938.

126. A. F. Huxley, "Muscle structures and theories of contraction," *Prog. Biophys. and biophys. Chemistry*, vol. 7, pp. 255–318, 1957.

127. R. B. Panerai, "A model of cardiac muscle mechanics and energetics," *J. Biomechanics*, vol. 13, pp. 929–940, 1980.

128. J. N. Peterson, W. C. Hunter, and M. R. Berman, "Estimated time course of Ca^{2+} bound to tropononin C during relaxation in isolated cardiac muscle," *Am. J. Physiol.*, vol. 260, pp. H1013–H1024, 1991.

129. A. Landesberg and S. Sideman, "Coupling calcium binding to troponin C and cross-bridge cycling in skinned cardiac cells," *Am. J. Physiol.*, vol. 266, pp. H1260–H1271, 1994.

130. A. Landesberg and S. Sideman, "Mechanical regulation of cardiac muscle by coupling calcium kinetics with cross-bridge cycling: A dynamic model," *Am. J. Physiol.*, vol. 267, pp. H779–H795, 1994.

131. A. Landesberg, R. Beyar, and S. Sideman, "Intracellular control of contraction of the cardiac muscle," in *IFAC Modeling and Control in Biomedical Systems*, pp. 79–80, 1994.

132. P. J. Hunter, A. D. McCulloch, and H. E. D. J. ter Keurs, "Modelling the mechanical properties of cardiac muscle," *Prog. Biophys. Mol. Biol.*, vol. 69, pp. 289–331, 1998.

133. J. M. Guccione, I. Motabarzadeh, and G. I. Zahalak, "A distribution-moment model of deactivation in cardiac muscle," *J Biomech*, vol. 31, no. 11, pp. 1069–73, 1998.

134. J. J. Rice, R. L. Winslow, and W. C. Hunter, "Comparison of putative cooperative mechanisms in cardiac muscle: Length dependence and dynamic responses," *Am. J. Physiol.*, vol. 276, pp. H1734–H1754, 1999.

135. J. J. Rice, M. S. Jafri, and R. L. Winslow, "Modeling short-term interval-force relations in cardiac muscle," *Am. J. Physiol.*, vol. 278, pp. H913–H931, 2000.

136. M. Mlcek, J. Neumann, O. Kittnar, and V. Novak, "Mathematical model of the electromechanical heart contractile system - Regulatory subsystem physiological considerations," *Physiol. Res.*, vol. 50, pp. 425–432, 2001.

137. D. P. Nickerson, N. P. Smith, and P. J. Hunter, "A model of cardiac cellular electromechanis," *Phil. Trans. R. Soc. Lond.*, vol. 359, pp. 1159–1172, 2001.

138. K. Glänzel, F. B. Sachse, G. Seemann, C. Riedel, and O. Dössel, "Modeling force development in the sarcomere in consideration of electromechanical coupling," in *Biomedizinische Technik*, vol. 47-1/2, pp. 774–777, Sep. 2002.

139. F. B. Sachse, K. Glänzel, and G. Seemann, "Modeling of protein interactions involved in cardiac tension development," *Int. J. Bifurc. Chaos*, vol. 13, no. 12, pp. 3561–3578, 2003.

140. Y. Bengio, "Markovian models for sequential data," *Neural Computing Surveys*, vol. 2, pp. 129–162, 1999.

141. A. Krogh, M. Brown, I. Mian, K. Sjlander, and D. Haussler, "Hidden markov models in computational biology: Applications to protein modeling," *J. Mol. Biol.*, vol. 235, pp. 1501–1531, 1994.

142. F. B. Sachse, G. Seemann, K. Chaisaowong, and D. Weiß, "Quantitative reconstruction of cardiac electromechanics in human myocardium: Assembly of electrophysiological and tension generation models," *J. Cardiovasc. Electrophysiol.*, vol. 14, pp. S210–S218, Oct. 2003.

143. K. Glänzel, "Kraftentwicklung im Sarkomer unter Berücksichtigung elektromechanischer Kopplung," diploma thesis, Universität Karlsruhe (TH), Institut für Biomedizinische Technik, Sep. 2002.

144. F. B. Sachse, K. Glänzel, and G. Seemann, "Modeling of electro-mechanical coupling in cardiac myocytes: Feedback mechanisms and cooperativity," *LNCS 2674*, pp. 62–71, 2003.

145. H. Demiray, "A note on the elasticity of soft biological tissue," *J. Biomechanics*, vol. 5, pp. 309–311, 1972.

146. S. A. Glantz, "A constitutive equation for the passive properties of muscle," *J. Biomechanics*, vol. 7, pp. 137–145, 1974.

147. A. Needleman, S. A. Rabinowitz, D. K. Bogen, and T. A. McMahon, "A finite element model of the infarcted left ventricle," *J. Biomechanics*, vol. 16, no. 1, pp. 45–58, 1983.

148. J. D. Humphrey and F. C. P. Yin, "On constitutive relations and finite deformations of passive cardiac tissue: I. A pseudostrain energy function," *J. Biomechanical Engineering*, vol. 109, pp. 298–304, 1987.

149. A. Horowitz, I. Sheinman, Y. Lanir, M. Perl, and S. Sideman, "Nonlinear incompressible finite element for simulating loading on cardiac tissue - Part 1: Two dimensional formulation for thin myocardial stripes," *J. Biomechanical Engineering*, vol. 110, pp. 57–61, 1988.

150. A. Horowitz, Y. Lanir, F. C. P. Yin, M. Perl, I. Sheinman, and R. K. Strumpf, "Structural three-dimensional constitutive law for the passive myocardium," *J. Biomechanical Engineering*, vol. 110, pp. 200–207, 1988.

151. E. Nevo and Y. Lanir, "Structural finite deformation model of the left ventricle during diastole and systole," *J. Biomechanical Engineering*, vol. 111, pp. 342–349, 1989.

152. J. D. Humphrey, R. K. Strumpf, and F. C. P. Yin, "Determination of a constitutive relation for passive myocardium: I. A new functional form," *J. Biomechanical Engineering*, vol. 112, pp. 333–339, 1990.

153. J. D. Humphrey, R. K. Strumpf, and F. C. P. Yin, "Determination of a constitutive relation for passive myocardium: II. Parameter estimation," *J. Biomechanical Engineering*, vol. 112, pp. 340–346, 1990.

154. J. M. Huyghe, D. H. van Campen, T. Arts, and R. M. Heethaar, "The constitutive behaviour of passive heart muscle tissue: A quasi-linear viscoelastic formulation," *J. Biomechanical Engineering*, vol. 24, no. 9, pp. 840–849, 1991.

155. M. Yang and L. A. Taber, "The possible role of poroelasticity in the apparent viscoelastic behavior of passive cardiac muscle," *J. Biomechanics*, vol. 24, no. 7, pp. 587–597, 1991.

156. M. S. Sacks and C. J. Chuong, "A constitutive relation for passive right-ventricular free wall myocardium," *J. Biomechanics*, vol. 26, no. 11, pp. 1341–1345, 1993.

157. E. Nevo and Y. Lanir, "The effect of residual strain on the diastolic function of the left ventricle as predicted by a structural model," *J. Biomechanics*, vol. 27, no. 12, pp. 1433–1446, 1994.

158. J. M. Guccione, K. D. Costa, and A. D. McCulloch, "Finite element stress analysis of left ventricular mechanics in the beating dog heart," *J. Biomechanics*, vol. 28, no. 10, pp. 1167–1177, 1995.

159. K. May-Newman and A. McCulloch, "Homogenization modeling for the mechanics of perfused myocardium," *Prog. Biophys. Mol. Biol.*, vol. 69, pp. 463–481, 1998.

160. T. P. Usyk, R. Mazhari, and A. D. McCulloch, "Effect of laminar orthotropic myofiber architecture on regional stress and strain in the canine left ventricle," *J. Elasticity*, vol. 61, pp. 143–165, 2000.

161. J.-J. Wang, A. B. O'Brien, N. G. Shrive, K. H. Parker, and J. V. Tyberg, "Time-domain representation of ventricular-arterial coupling as a windkessel and wave system," *Am. J. Physiol.*, vol. 284, no. 4, pp. H1358–H1368, 2003.

162. J. Lighthill, *Waves in fluids*, ch. 2.2. Examples, including elastic tubes and open channels, pp. 94–100. Cambridge University Press, 1980.

163. N. Westerhof, P. Sipkema, G. C. van den Bos, and G. Elzinga, "Forward and backward waves in the arterial system," *Cardiovasc. Res.*, vol. 6, pp. 648–656, Nov 1972.

164. P. Verdonck, P. Segers, and D. De Mey, *Cardiac mechanics*. von Karman Institute for Fluid Dynamics, Brussel: VKI Lecture Series, Biological fluid dynamics ed., May 12-16 2003.

165. W. H. Gaasch, *Left ventricular diastolic dysfunction and heart failure*, ch. Passive elastic properties of the left ventricle, pp. 143–149. Lea & Febiger, w. h. gaasch and m. m. lewinter ed., 1994.

166. J. L. Weiss, J. W. Frederiksen, and M. L. Weisfeldt, "Hemodynamic determinants of the time-course of fall in canine left ventricular pressure," *J. Clin. Invest.*, vol. 58, pp. 751–760, Sep 1979.

167. R. H. Bartels, J. C. Beatty, and B. A. Barsky, *An instruction to splines for use in computer graphics and geomtric modeling*. 1987.

168. G. E. Farin, *Curves and surfaces for computer aided geometric design : a practical guide*. Boston : Academic Press, Inc., San Diego, second edition ed., 1990.

169. A. H. Barr, "Global and local deformations of solid primitives," in *SIGGRAPH '84: Proceedings of the 11th annual conference on Computer graphics and interactive techniques*, pp. 21 – 30, ACM Press, New York, 1984.

170. S. Coquillart, "Extended free-form deformation: a sculpturing tool for 3d geometric modeling," in *SIGGRAPH '90: Proceedings of the 17th annual conference on Computer graphics and interactive techniques*, ACM Press, New York, 1990.

171. W. M. Hsu, J. F. Hughes, and H. Kaufman, "Direct manipulation of free-form deformations," in *SIGGRAPH '92: Proceedings of the 19th annual conference on Computer graphics and interactive techniques*, no. 26 in 2, pp. 177–184, ACM Press, New York, 1992.

172. R. MacCracken and K. I. Joy, "Free-form deformations with lattices of arbitrary topology," in *SIG-GRAPH '96: Proceedings of the 23rd annual conference on Computer graphics and interactive techniques*, pp. 181–188, ACM Press, New York, 1996.

173. K.-J. Bathe, *Finite Element Procedures*. Upper Saddle River, New Jersey: Prentice Hall, 1996.

174. L. P. Nedel and D. Thalmann, "Real time muscle deformations using massspring systems," in *CGI '98: Proceedings of the Computer Graphics International 1998*, (Washington, DC, USA), p. 156, IEEE Computer Society, 1998.

175. L. P. Nedel, *Anatomic modeling of human bodies using physically-based muscle stimulation*. PhD thesis, LIG-Computer Graphics Lab, EPFL, Lausanne, Switzerland, June 1998.

176. W. Lin and R. A. Robb, "Simulation and interactive multi-dimensional visualization of cardiac dynamics using a patient-specific physics-based model," *Proceedings of the 14th International Congress & Exhibition*, vol. CARS 2000, 2000.

177. M. Desbrun and M.-P. Cani-Gascuel, "Active implicit surface for animation," in *Graphics Interface*, pp. 143–150, June 17-18 1998.

178. Y.-M. Kang, J.-H. Choi, H.-G. Cho, D.-H. Lee, and C.-J. Park, "Real-time animation technique for flexible and thin objects," in *Proc. of WSCG 2000, Pizen, Czech.*, pp. 322–329, 2000.

179. Y.-M. Kang, J.-H. Choi, H.-G. Cho, and C.-J. Park, "Fast and stable animation of cloth with an approximated implicit method," in *CGI '00: Proceedings of the International Conference on Computer Graphics*, p. 247, IEEE Computer Society, Washington, DC, USA, 2000.

180. Y. Zhang, E. C. Prakash, and E. Sung, "A physically-based model with adaptive refinement for facial animation," in *Computer Animation, 2001. The Fourteenth Conference on Computer Animation*, pp. 28–31, 7-8 Nov 2001.

181. F. Mazzella, *Automated acquisition of elastic properties of soft tissues for surgical simulation*. PhD thesis, Stanford-NASA National Biocomputation Center, 1999.

182. Y. Chen, Q. Zhu, and A. Kaufman, "Physically-based animation of volumetric objects," in *Proc. IEEE Computer Animation*, pp. 154–160, 1998.

183. Q.-H. Zhu, Y. Chen, and A. Kaufman, "Real-time biomechanically-based muscle volume deformation using FEM," *Computer Graphics Forum*, vol. 17, pp. 275–284, 1 August 1998.

184. J. T. Stern Jr., "Computer modelling of gross muscle dynamics," *J. Biomech.*, vol. 7, pp. 411–412, Sep 1974.

185. F. B. Sachse, G. Seemann, and C. D. Werner, "Modeling of electro-mechanics in left ventricle," in *Proc. Computers in Cardiology*, pp. 705–708, 2002.

186. P. J. Hunter, P. M. Nielsen, B. H. Smaill, I. J. LeGrice, and I. W. Hunter, "An anatomical heart model with applications to myocardial activation and ventricular mechanics," *Crit. Rev. Biomed. Eng.*, vol. 20, no. 5-6, pp. 403–426, 1992.

187. P. J. Hunter and B. E. Smail, "Electromechanics in anatomically based models of the heart," in *Cardiac Electrophysiology. From Cell to Bedside* (D. P. Zipes and J. Jalife, eds.), ch. 32, pp. 277–282, Philadelphia: W. B. Saunders Company, 3 ed., 1999.

188. A. McCulloch, L. Waldmann, and J. Rogers, "Large-scale finite element analysis of the beating heart," *Critical Reviews in Biomedical Engineering*, vol. 20, no. 5-6, pp. 427–449, 1992.

189. K. D. Costa, P. J. Hunter, J. S. Wayne, L. K. Waldmann, J. M. Guccione, and A. D. McCulloch, "A three-dimensional finite element method for large elastic deformations of ventricular myocardium: II - Prolate spheroidal coordinates," *J. Biomedical Engineering*, vol. 118, pp. 464–472, Nov. 1996.

190. L. G. Blümcke, "Entwicklung eines schnellen Verfahrens zur Berechnung der Deformation im Herzen ausgehend von makroskopischen Modellen der Kraftentwicklung," diploma thesis, Universität Karlsruhe (TH), Institut für Biomedizinische Technik, Sep. 2001.

191. E. Promayon, P. Baconnier, and C. Puech, "Physically-based deformations constrained in displacements and volume," in *Computer Graphics Forum (Proc. of Eurographics '96)* (J. Rossignac and F. Sillion, eds.), vol. 16, (Poitiers, France), pp. 155–164, Sep. 1996.

192. Y. Lee, D. Terzopoulos, and K. Walters, "Realistic modeling for facial animation," in *SIGGRAPH '95: Proceedings of the 22nd annual conference on Computer graphics and interactive techniques*, pp. 55–62, ACM Press, New York, 1995.

193. M. B. Mohr, L. G. Blümcke, G. Seemann, F. B. Sachse, and O. Dössel, "Volume modeling of myocard deformation with a spring mass system," in *Surgery Simulation and Soft Tissue Modeling* (N. Ayache and H. Delingette, eds.), vol. LNCS 2673, pp. 332–339, Berlin, Heidelberg, New York: Springer-Verlag GmbH, 2003. ISSN 0302-9743.

194. ANSYS, Inc., *ANSYS Theory Reference Manual*, 2004.

195. F. B. Sachse, "Modeling of the mammalian heart," Universität Karlsruhe (TH), Institut für Biomedizinische Technik, 2002. Habilitationsschrift.

196. R. Plonsey and R. C. Barr, "Mathematical modeling of electrical activity of the heart," *J. Electrocardiol.*, vol. 20, no. 3, pp. 219–226, 1987.

197. S. Miyazaki, T. Yasuda, S. Yokoi, and J. Toriwaki, "Modeling and implementation of elastic object manipulation in virtual space," *Electronics and Communications in Japan (Part III: Fundamental Electronic Science)*, vol. 81, no. 4, pp. 42–50, 1998.

198. T. Jakobsen, "Advanced character physics." Gamasutra, January 2003. IO Interactive, Copenhagen, Hitman.

199. L. Verlet, "Computer "Experiments" on Classical Fluids I. Thermodynamical Properties of Lennard-Jones Molecules," *Physical Review*, vol. 159, pp. 98–103, July 1967.

200. C. S. Henriquez, A. L. Muzikant, and C. K. Smoak, "Anisotropy, fiber curvature and bath loading effects on activation in thin and thick cardiac tissue preparations: Simulations in a three-dimensional bidomain model," *J. Cardiovasc. Electrophysiol.*, vol. 7, pp. 424–444, May 1996.

201. R. Schnell, "Druck-Volumen Beziehung im menschlichen Herzen. Implementierung in ein mechanisches Herzmodell," tech. rep., Universität Karlsruhe (TH), Institut für Biomedizinische Technik, 2005. Student Research Project.

202. M. Mohr, "Vergleich von mikroskopischen und makroskopischen Modellen der Deformation im Myokard," diploma thesis, Universität Karlsruhe (TH), Institut für Biomedizinische Technik, Sep. 2001.

203. M. B. Mohr, L. G. Blümcke, F. B. Sachse, G. Seemann, C. D. Werner, and O. Dössel, "Volumenbasierte Modellierung der Deformation im Myokard ausgehend von Modellen der Kraftentwicklung," in *Biomedizinische Technik*, vol. 47-1/2, pp. 225–228, Sep. 2002.

204. M. B. Mohr, L. G. Blümcke, G. Seemann, F. B. Sachse, and O. Dössel, "Modeling of myocardial deformation with an extended spring mass system," in *Biomedizinische Technik*, vol. 48-1, pp. 6–7, 2003.

205. M. B. Mohr, L. G. Blümcke, F. B. Sachse, G. Seemann, and O. Dössel, "Hybrid deformation model of myocardium," in *Proc. CinC*, vol. 30, pp. 319–322, 2003.

206. M. B. Mohr, G. Seemann, F. B. Sachse, and O. Dössel, "Deformation simulation in an elastomechanical ventricular model," in *Proc. CinC*, pp. 777–780, 2004.

207. M. B. Mohr, G. Seemann, F. B. Sachse, and O. Dössel, "Enhancing numerical stability of an electromechanical ventricular model," *Biomedizinische Technik*, vol. 50 Suppl 1, no. Part 1, pp. 548–549, 2005.

208. M. B. Mohr, R. R. Schnell, G. Seemann, F. B. Sachse, and O. Dössel, "Incorporating blood pressure load into an elastomechanical ventricular model," in *Computers in Cardiology, Lyon, France*, 25-28 Sep 2005.

209. B. Jung, *Neue kernspintomographische Techniken für funktionelle Untersuchung des Herzmuskels*. PhD thesis, Albert-Ludwigs-Universität, Freiburg i. Brsg., 2005.

210. E. Nagel, M. Stuber, M. Lakatos, M. Scheidegger, P. Boesiger, and O. Hess, "Cardiac rotation and relaxation after anterolateral myocardial infarction," *Coronary Artery Disease*, vol. 11, pp. 261–7, May 2000.

211. S. Masood and G. Z. Yang, "Macroscopic structure and physiology of the normal and diseased heart," tech. rep., Department of Computing, Imperial College of Science, Technology and Medicine, London, UK, 2001.

212. R. Greve, "Kontinuumsmechanik," tech. rep., Fachbereich Mechanik (AG3), TU Darmstadt, 2000. Vorlesungsskript.

213. G. E. Mase, *Schaum's Outline of Theory and Problems of Continuum Mechanics*. New York, San Francisco, Washington: McGraw-Hill, 1970.

214. D. C. Kay, *Schaum's Outline of Theory and Problems of Tensor Calculus*. New York, San Francisco, Washington: McGraw-Hill, 1988.

Danksagung

Curriculum Vitae

Matthias B. Mohr

1973	Born in Bad Dürkheim, Germany, at October 16th
1984 – 1990	High school: Thomas Mann Gymnasium, Stutensee, Germany
1990 – 1991	High school: Fenwick, Oak Park, Illinois, U.S.A.
1991 – 1994	High school: Thomas Mann Gymnasium, Stutensee, Germany, with "Abitur"
Oct. 1994 – Sep. 2001	Studies of electrical engineering and information technology at the Universität Karlsruhe (TH) Research University · founded 1825 , Karlsruhe, Germany
	Specialization in: Biomedical Engineering Degree: Diplom-Ingenieur Diploma thesis: "Vergleich von mikroskopischen und makroskopischen Modellen der Deformation im Myokard" (Comparison of microscopic and macroscopic models of myocardial deformation) at the Institute of Biomedical Engineering at the Universität Karlsruhe (TH) Research University · founded 1825 , Karlsruhe, Germany
since Jan. 2002	Scientific employee at the Institute of Biomedical Engineering at the Universität Karlsruhe (TH) Research University · founded 1825 , Karlsruhe, Germany
Practical work experience	
Jun. 1992 – Sep. 1997	Forschungszentrum Karlsruhe (science and engineering research institutions), Institute for Applied Computer Science, Germany
May 1999 – Sep. 1999	Siemens Medical, Research and Development, Erlangen, Germany
Additional Education	
Jun. 2004 – Nov.2005	Education in academic teaching skills for faculty members. Awarded with the "Baden-Württemberg Certificate"

Publications

First Author

- M. B. Mohr and F. B. Sachse and G. Seemann and C. D. Werner and O. Dössel, "Vergleich von mikroskopischen und makroskopischen Modellen der Kraftentwicklung und Deformation im Myokard," in *Biomedizinische Technik*, vol. 46-1, pp. 524-525, Sep. 2001

- M. B. Mohr, "Vergleich von mikroskopischen und makroskopischen Modellen der Deformation im Myokard," *Diploma Thesis*, Institut für Biomedizinische Technik, Universität Karlsruhe (TH), Sep. 2001

- M. B. Mohr, L. G. Blümcke, F. B. Sachse, G. Seemann, C. D. Werner, and O. Dössel, "Volumen-basierte Modellierung der Deformation im Myokard ausgehend von Modellen der Kraftentwicklung," in *Biomedizinische Technik*, vol. 47-1/2, pp. 225–228, Sep. 2002.

- M. B. Mohr, L. G. Blümcke, G. Seemann, F. B. Sachse, and O. Dössel, "Volume modeling of myocard deformation with a spring mass system," *LNCS 2673*, pp. 332–339, Springer-Verlag, 2003, ISSN 0302-9743.

- M. B. Mohr, L. G. Blümcke, F. B. Sachse, G. Seemann, and O. Dössel, "Hybrid deformation model of myocardium," *Proc. Computers in Cardiology*, vol. 30, pp. 319–322, 2003.

- M. B. Mohr, L. G. Blümcke, G. Seemann, F. B. Sachse, and O. Dössel, "Modeling of myocardial deformation with an extended spring mass system," *Biomedizinische Technik*, vol. 48-1, pp. 6–7, 2003.

- M. B. Mohr, G. Seemann, F. B. Sachse, and O. Dössel, "Deformation simulation in an elastomechanical ventricular model," *Proc. Computers in Cardiology*, pp. 777–780, 2004.

- M. B. Mohr and G. Seemann and F. B. Sachse and O. Dössel, "Enhancing numerical stability of an electromechanical ventricular model," *Biomedizinische Technik*, vol. 50-Suppl 1, pp. 548–549, Sep. 2005.

- M. B. Mohr, R. R. Schnell, G. Seemann, F. B. Sachse, and O. Dössel, "Incorporating blood pressure load into an elastomechanical ventricular model," *Computers in Cardiology*, in press, Sep 2005.

Co-author

- F. B. Sachse, G. Seemann, M. B. Mohr, L. G. Blümcke, and C. D. Werner, "Models of the human heart for simulation of clinical interventions," in *Proc. CARS*, pp. 43–48, 2002.

- F. B. Sachse and L. G. Blümcke and M. Mohr and K. Glänzel and J. Häfner and C. Riedel and G. Seemann and O. Skipa and C. D. Werner and O. Dössel, "Comparison of Macroscopic Models of Excitation and Force Propagation in the Heart," *Biomedizinische Technik*, vol. 47-1/2, pp. 217–220, Sep. 2002

- K. Chaisaowong and F. B. Sachse and G. Seemann and M. Mohr and O. Dössel, "Modeling of human cardiac force development: Quantitative description from myofilament to myocardium" *Biomedizinische Technik*, vol. 48-1, pp. 466–467, Sep. 2003

- F. B. Sachse and G. Seemann and M. B. Mohr and Arun V. Holden, " Mathematical Modeling of Cardiac Electro-Mechanics: From Protein to Organ," *Int. J. Bifurc. Chaos*, vol. 13, no. 12, pp. 3747–3755, 2003

- F. B. Sachse and G. Seemann and K. Chaisaowong and M. B. Mohr, "Modeling of electro-mechanics of human cardiac myocytes: Parameterization with numerical minimization techniques," *Proc. 25th Conf. IEEE EMBS*, pp. 2810–2813, 2003

- F. B. Sachse and G. Seemann and M. B. Mohr, "Electro-mechanics in biventriculer models," *Proc. Computers in Cardiology*, vol. 31, pp. 537–540, 2004

- M. Reumann and M. B. Mohr and O. Dössel and Anke Diez "Vorlesung, Übung und Tutorium im Koordinierten Zusammenspiel, Ein Lehr-/Lernpaket schnüren - Grundlagenvorlesungen in der Elektrotechnik," *Neues Handbuch Hochschullehre*, Bonn (Raabe-Verlag), in press

Supervised Diploma Theses and Student Research Projects

- K. Chaisaowong, "Modeling of human cardiac force development:quantitative description from myofilament to myocardium," Diploma Thesis, Institut für Biomedizinische Technik, Universität Karlsruhe (TH), Jun. 2004.

- R. R. Schnell, "Druckvolumen Beziehung im menschlichen Herzen Implementierung in ein mechanisches Herzmodell," *Student Research Project*, Institut für Biomedizinische Technik, Universität Karlsruhe (TH), Sep. 2005

Administrative Work at the Institute of Biomedical Engineering

Teaching

- Excercise lecture for "Lineare elektrische Netze" (linear electrical networks) (2002/2003)
- Education of student tutors: "Tutorenschulung - didaktische Grundlagen und Kompetenzen" (fundamentals in didactics and teaching skills) (2005)

Teaching Assistance

- Excercise lecture for "Lineare elektrische Netze" (linear electrical networks) (2004/2005)

Oral Examination Assistance

- "Anatomie und Physologie" (anatomy and physiology)
- "Electromagnetics and Numerical Calculation of Fields"

Other Responsibilities

- Web administrator, Common Gateway Interfaces
- Administration of online exam admission
- Administration of in-house Wiki
- Administration of in-house source code documentation
- Administration of in-house source code linux compatibility
- Administration of in-house application software documentation
- Coaching of students